APORTACIONES AL CONTROL NO LINEAL DE CORRIENTE APLICADO A ACCIONAMIENTOS DE INDUCCIÓN DE SEIS FASES

TESIS DOCTORAL

UNIVERSIDAD NACIONAL DE ASUNCIÓN
Facultad de Ingeniería
Laboratorio de Sistemas de Potencia y Control
Doctorado en Ingeniería Electrónica
Énfasis Electrónica de Potencia

APORTACIONES AL CONTROL NO LINEAL DE CORRIENTE APLICADO A ACCIONAMIENTOS DE INDUCCIÓN DE SEIS FASES

Magno Elias Ayala Silva
Autor

Nombre del Tutor
Jorge Esteban Rodas Benítez – Facultad de Ingeniería, Paraguay

Nombre del Cotutor
Raúl Igmar Gregor Recalde – Facultad de Ingeniería, Paraguay

Nombre del Cotutor Internacional
Jesús Doval-Gandoy – Universidad de Vigo, España

2020

TRIBUNAL EXAMINADOR

PRESIDENTE

SILVIA ARRUA, Universidad Nacional de Asunción, Paraguay

SECRETARIO

JORGE RODAS, Universidad Nacional de Asunción, Paraguay

VOCALES

HANG SENG CHE, University of Malaya, Malaysia

PAT WHEELER, University of Nottingham, United Kingdom

JESÚS DOVAL-GANDOY, Universidad de Vigo, España

ALEJANDRO GÓMEZ-YEPES, Universidad de Vigo, España

IGNACIO GONZÁLEZ PRIETO, Universidad de Málaga, España

RAÚL GREGOR, Universidad Nacional de Asunción, Paraguay

Junio 2020
Campus Universitario, San Lorenzo, Paraguay

RESUMEN

Las máquinas multifásicas (mayor a tres fases) se han vuelto ampliamente reconocidas como alternativas a los típicos esquemas trifásicos en numerosas aplicaciones, principalmente en aquellas en las que se requieren mayor fiabilidad y disponibilidad (funcionamiento en post-falta). Algunos ejemplos de la adopción de esta tecnología apunta por un lado al sector industrial, y por otro a sistemas de tracción eléctrica, entre los que se destacan los vehículos eléctricos. Así mismo, recientemente se ha explorado su uso en aplicaciones de energías renovables entre los que se destaca la generación eólica.

Desde el punto de vista del control, las estrategias de control aplicadas a máquinas multifásicas, han evolucionado en los últimos años, desde la extensión de los métodos de control escalar, vectorial y control directo de par, utilizados en las máquinas trifásicas, a métodos más sofisticados, tales como los controles no lineales, como el control deslizante y el control predictivo.

La técnica de control deslizante se basa en la selección de una trayectoria definida por una superficie relacionada al comportamiento del sistema, típicamente se utiliza el error de seguimiento de la variable a controlar. Ésta técnica posee características muy atractivas que han motivado su estudio en aplicaciones en máquinas eléctricas, tales como robustez, alta velocidad de respuesta y estabilidad garantizada. Este controlador genera un esfuerzo de control en forma de voltaje para la máquina multifásica y para sintetizar dicho valor en los convertidores de potencia, se requiere una etapa de modulación. El principal problema al aplicar el control deslizante es el fenómeno chattering que produce oscilaciones de alta frecuencia en el actuador del sistema y en algunos casos, produce inestabilidad. La solución a este fenómeno aplicado a máquinas de inducción asimétricas hexafásicas será abordado en esta Tesis, siendo esta solución una de las aportacionaes de esta Tesis Doctoral.

Por otro lado, para el caso de la implementación del control predictivo aplicado a las máquinas multifásicas es necesario realizar la predicción o cálculo del comportamiento futuro del sistema, pudiéndose utilizar dicha información para obtener los valores óptimos que minimizan una función de costo o reducen el error de una determinada variable del sistema. La ejecución del algoritmo del controlador predictivo se basa en tres pasos: estimación de las variables no medibles por medio de un observador, la predicción del comportamiento futuro de los estados del sistema y la optimización de las salidas, de acuerdo a las restricciones impuestas como consigna de control. Teniendo en cuenta su aplicación a máquinas multifásicas por medio de convertidores electrónicos de potencia, el comportamiento de la salida de dichos controladores es del tipo discreto, por ello se plantea una etapa de modulación para optimizar el comportamiento del sistema con el control predictivo. Algunos problemas existentes al aplicar el control predictivo es una generación de armónicos indeseados en la corriente y problemas de estabilidad a mayores velocidades mecánicas que se serán abordados en esta Tesis como aporaciones al estado del arte del control predictivo aplicado al accionamiento multifásico.

Teniendo en cuenta el enfoque del control aplicado a máquinas multifásicas, los aportes de esta Tesis Doctoral se aplican tanto al control deslizante como al control predictivo, aplicados a la máquina de inducción asimétrica de hexafásica. En primer lugar, se centra en la aplicación del control de modo deslizante y una variante aplicado a máquinas de inducción asimétricas hexafásicas. En segundo lugar, se realiza la aplicación del control predictivo basado en el modelo aplicado a la misma máquina junto a un análisis de estabilidad del mismo. Luego, se realiza un análisis comparativo de la eficiencia a partir de los algoritmos de control no lineal de corriente. Los resultados obtenidos, considerando la eficiencia, son comparados entre sí, mediante un análsis cuantitativo.

Los aportes han sido analizados y evaluadas a través de pruebas experimentales en una bancada de ensayos basado en el accionamiento de asimétrico hexafásico, sobre el cual se validan experimentalmente las aportaciones.

MAGNO ELIAS AYALA SILVA

Junio, 2020. San Lorenzo, Paraguay.

SUMMARY

Multiphase machines (more than three phases) have become widely recognized as alternatives to the typical three-phase schemes in many applications, mainly in the variables in which greater reliability and availability (operation in post-fault) are required. Some examples of the adoption of this technology point on one hand to the industrial sector, and on the other to electrical traction systems, among which are electric vehicles. Likewise, its use in renewable energy applications has recently been explored, i.e. wind power generation systems.

From a control point of view, control strategies applied to multiphase machines, have evolved in recent years, from the extension of scalar, vector and direct torque control methods used in three-phase machines, to more sophisticated methods, such as non-linear controls, such as the sliding mode and predictive control.

The sliding mode control process is based on the selection of a path defined by a surface related to the behavior of the system, typically the tracking error of the variable to be controlled is used. This technique has very attractive characteristics that have motivated its study in applications in electrical machines, such as robustness, high response speed and guaranteed stability. This controller generates a control effort in the form of voltage for the multiphase machine and to synthesize its value in the power converters, a modulation stage is required. The main problem when applying the sliding control is the chattering phenomenon that produces high frequency oscillations in the system actuator and, in some cases, produces instability. The solution to this phenomenon applied to six-phase asymmetrical induction machines will be addressed in this Thesis, being this solution one of the contributions of this Doctoral Thesis.

On the other hand, in the case of the implementation of the predictive control applied to multiphase machines, it is necessary to predict or calculate the future behavior of the system, and this information can be used to obtain the optimal values that minimize a cost function or reduce the error of a certain variable of the system. The execution of the predictive controller algorithm is based on three steps: estimation of the non-measurable variables by means of an observer, prediction of the future behavior of the system states and optimization of the outputs, according to the restrictions imposed as a control setpoint. Taking into account its application to multiphase machines by means of electronic power converters, the behavior of the output of these controllers is of the discrete type, therefore a modulation stage is proposed to optimize the behavior of the system with predictive control. Some existing problems when applying predictive control is a generation of undesired harmonics in the currents and stability problems at higher mechanical speeds that will be addressed in this Thesis as contributions to the state of the art of predictive control applied to multiphase drives.

Taking into account the control approach applied to multiphase machines, the contributions of this Doctoral Thesis apply to both the sliding control and the predictive control, applied to the six-phase asymmetrical induction machine. First, it focuses on the application of the sliding mode control and a variant applied to six-phase asymmetrical induction machines. Secondly, the application of model predictive control applied to the same machine is carried out together with an analysis of its stability. Then, a comparative analysis of the efficiency is carried out from the non-linear current control algorithms. The obtained results, taking into account the efficiency, are compared to each other, by means of a quantitative analysis.

The contributions have been analyzed and evaluated through experimental tests in a test bench based of the asymmetrical six-phase drive, on which the contributions are experimentally validated.

MAGNO ELIAS AYALA SILVA

June, 2020. San Lorenzo, Paraguay.

AGRADECIMIENTOS

Antes que todo, doy a gracias a Dios, por darme fuerzas para cumplir mis objetivos y ayudarme a llegar hasta este punto, por su apoyo incondicional.

A mis tutores, Raúl Gregor y Jorge Rodas, quienes me han brindado apoyo y me guiaron durante todo el proceso del Doctorado. Aprecio mucho que hayan compartido conmigo sus experiencias y conocimientos, fueron invaluables para mí. A mi tutor internacional, Jesús Doval-Gandoy, por su completa vocación a la docencia e investigación, su apoyo total durante mi estancia en la Universidad de Vigo, su sabiduría y su amistad.

A mis compañeros del LSPyC de la FIUNA y del APET de la Universidad de Vigo, por su apoyo técnico y su amistad durante la duración del Doctorado y la estancia en la Universidad de Vigo. A los profesores del Doctorado, que solo con sus conocimientos avanzados ya te inspiran a seguir sus ejemplos, particularmente resaltando a Marco Rivera, que es un digno ejemplo de docente-investigador.

En el ámbito personal, a mis padres Magno y Sonia, por los principios y valores que me enseñaron durante toda mi vida, además a mis abuelas Angélica y Ladislaa por su apoyo incondicional desde siempre. A mis hermanos Martín y Matias, por su apoyo incondicional, además a toda mi familia extiendo mis agradecimientos. Por último, al amor de mi vida Fátima Gabriela por todo su amor y apoyo desde que nos conocimos.

A todos mis amigos y colegas, que me apoyaron en todo momento, especialmente para lidiar con los momentos de mucho esfuerzo y estrés.

Magno Elias Ayala Silva

AGRADECIMIENTOS INSTITUCIONALES

Al Consejo Nacional de Ciencia y Tecnología (CONACYT) del Paraguay por el apoyo económico a través del proyecto de investigación 14-INV-101, el programa de Doctorado POSG16-05 y del programa de vinculación de científicos y tecnólogos PVCT 16-90.

A la Facultad de Ingeniería y Politécnica de la Universidad Nacional de Asunción (FIUNA-FPUNA) y al Laboratorio de Sistemas de Potencia y Control (LSPyC) por el permiso institucional para realizar estancias de investigación en la Universidad de Vigo.

Magno Elias Ayala Silva

Dedicado a:
mis padres Magno y Sonia,
hermanos Martín y Matías,
abuelas Angélica y
Ladislaa
y a mi novia Fátima
Gabriela

ÍNDICE GENERAL

PARTE II ANÁLISIS DE CONTENIDO

PARTE III PUBLICACIONES

ÍNDICE DE FIGURAS

ÍNDICE DE TABLAS

ACRÓNIMOS

AC	Corriente alterna.
A/D	Analógico/Digital.
DC	Corriente continua.
DSMC	Control de modo deslizante discreto.
DSTC	Control super torcido discreto.
CCS-MPC	Control predictivo de estado continuo.
DTC	Control directo de par.
DRFOC	Control vectorial directo de campo rotórico orientado.
FCS-MPC	Control predictivo de estados finitos.
FF	Factor de forma.
FOC	Control de campo orientado.
FPO	Operaciones de punto flotante.
HOSM	Control de modo deslizante de alto orden.

IRFOC	Control vectorial indirecto de campo rotórico orientado.
KF	Filtro de Kalman.
LO	Observador de Luenberger.
MI	Máquina de inducción.
MIAH	Máquina de inducción asimétrica hexafásica.
MPC	Control predictivo por modelo.
MSE	Error cuadrático medio.
PCC	Control predictivo de corriente.
PI	Proporcional integral.
PWM	Modulación por ancho de pulsos.
RFOC	Control de campo rotórico orientado.
RMS	Valor cuadrático medio.
SMC	Control de modo deslizante.
STC	Control super torcido.
SVM	Modulación por espacio vectorial.
TDE	Estimador con tiempo de retardo.
THD	Distorsion ármonica total.
VSD	Descomposición de espacio vectorial.
VSI	Inversor con fuente de voltaje.

PARTE I

GENERALIDADES

CAPÍTULO 1

JUSTIFICACIÓN Y METODOLOGÍA

1.1 Introducción

Las aplicaciones más atractivas para máquinas multifásicas son de tracción en vehículos eléctricos, vehículos híbridos, aeronaves eléctricas y otros. En aplicaciones industriales o en las citadas anteriormente, las máquinas multifásicas son operadas bajos régimenes de velocidad variable, por lo que es requerido un convertidor electrónico de potencia [1, 2]. Desde el punto de vista de sistemas de generación de energía eléctrica utilizando fuentes renovables, las áreas más activas de investigación son las pequeñas centrales hidráulicas y las eólicas [3–5]. En estas centrales se utilizan principalmente generadores trifásicos de inducción justificado principalmente por su alta viabilidad, bajo costo, construcción simple, robustez y bajo mantenimiento [3]. Sin embargo, no es conveniente su aplicación para generación de alta potencia (hasta 10 MW) ya que no puede operar con fallas de una o más fases en el estator, además produce un alto rizado en el par de torsión con alta amplitud y baja frecuencia y también una alta vibración mecánica [3, 6]. Por eso, en los últimos años el interés de las máquinas multifásicas (cantidad de fases > 3) en la comunidad académica e industrial ha incrementado debido a sus características propias como bajo rizado de par de torsión, mayor distribución de potencia por fase y mejor tolerancia a fallos en comparación a las máquinas trifásicas accionadas con convertidores de potencia [6, 7].

Entre las máquinas multifásicas más estudiadas se encuentra la asimétrica hexafásica [8–12]. La presente Tesis se centra en el estudio de esta máquina particular por el hecho de ser la más utilizada [13]. Para poder controlar las variables físicas de la máquina de inducción asimétrica hexafásica (MIAH) se propusieron varias estrategias de control en las últimas décadas, algunos son el control de campo orientado (FOC) utilizando un control de corriente interno de lazo cerrado, otro es el control directo de par (DTC) [14]. Sin embargo, el DTC tiene algunas desventajas como control débil del par de torsión a baja velocidad, pulsaciones notorias de par de torsión y flujo magnético y un comportamiento de frecuencia de conmutación variable [15]. Por otro lado, el control vectorial indirecto de campo rotórico orientado (IRFOC) tiene un buen comportamiento de corriente, pero contiene un lazo externo de velocidad, cuatro lazos internos de corriente, un control de flujo magnético y algunos modelos de transformación para distintos sub-espacios espaciales de referencia. Por ello, el costo computacional y la complejidad de la implementación del sistema de control es incrementado [16–19].

En los últimos años, debido a los avances tecnológicos y la creación de microcontroladores más veloces con capacidad de cálculos complejos, la implementación de sistemas de control no lineales, como control de modo deslizante (SMC) [20, 21], control difuso [22, 23], control adaptativo [24, 25] y control predictivo por modelo (MPC) [26, 27] se han vuelto viables. Particularmente el SMC y el MPC han ganado mayor interés, debido a sus distintas propiedades como características de desacoplamiento intrínseco, rápida respuesta dinámica y alto ancho de banda. Dentro del MPC, se puede optar por el control predictivo de estados finitos (FCS-MPC). Con esta técnica el control de corriente tiene una precisión bastante evidente y una actuación muy buena desde el punto de vista de respuesta dinámica. Desde el punto de vista de rizado de corriente, el FCS-MPC produce una alta distorsión debido a un grupo finito de posibilidades [28] y además tiene inconvenientes relacionado a la estabilidad a velocidades altas. Sin embargo, se puede agregar un modulador para obtener una respuesta a frecuencia fija de conmutación y disminuir el rizado de corriente. Por el lado del SMC, este posee mucha robustez y rápida velocidad de respuesta, es fácil de diseñar y no tiene mucho costo computacional. Es necesario incluir una etapa de modulación para sintetizar el esfuerzo de control requerido. Se debe considerar también una limitación del SMC que se denomina chattering que consiste en oscilaciones de alta frecuencia en el actuador y puede perjudicar el desempeño del sistema e incluso lograr inestabilizarlo. En esta Tesis se presentan variantes tanto del SMC como el MPC aplicado a la MIAH donde se abordan las limitaciones y se consideran soluciones, además se discuten las distintas características de los controladores propuestos.

1.2 Motivación

La principal motivación que ha impulsado esta Tesis es el desarrollo de aportes al estado de arte de algoritmos de control no lineal aplicados a los accionamientos de inducción multifásicos en los sistemas de tracción, específicamente la asimétrica hexafásica, teniendo en cuenta que en las últimas décadas, ha habido grandes avances en el área de máquinas multifásicas, especialmente en aplicaciones de tracción y generación eléctrica. Para su correspondiente aplicación, es necesario el uso de convertidores electrónicos de potencia, por ello el estudio de los mismos y las diversas técnicas de control no lineales propuestas es un tema muy relevante para el estudio de las máquinas multifásicas, el cual también es abordado en esta Tesis Doctoral.

1.3 Objetivos

El objetivo de esta Tesis es el desarrollo teórico y experimental de algoritmos de control no lineales aplicados al accionamiento multifásico centrado en las máquinas de inducción asimétricas hexafásicas. En concreto, se pueden enumerar los siguientes apartados:

- Diseñar nuevos esquemas de control no lineales, basados en la teoría de control deslizante, aplicados en accionamientos de máquinas de inducción asimétricas hexafásicas.
- Validar los nuevos esquemas de control no lineales, basados en la teoría de control deslizante, aplicados en accionamientos de máquinas de inducción asimétricas hexafásicas.
- Diseñar nuevos esquemas de control no lineales, basados en la teoría de control predictivo, aplicados en accionamientos de máquinas de inducción asimétricas hexafásicas.
- Validar los nuevos esquemas de control no lineales, basados en la teoría de control predictivo, aplicados en accionamientos de máquinas de inducción asimétricas hexafásicas.
- Desarrollar un análisis de estabilidad para las técnicas de control predictivo propuestas y validadas aplicados en accionamientos de máquinas de inducción asimétricas hexafásicas.

1.4 Organización del Documento

En la Parte I se detallan las generalidades del trabajo. Se realiza una presentación del mismo, sus fundamentos, objetivos y la organización del documento (Capítulo 1). Posteriormente, se describe al estado del arte de los accionamientos multifásicos enfocado en el modelado, y los distintos métodos de control de corriente y velocidad (Capítulo 2).

En la Parte II se discuten los aportes realizados en los trabajos de investigación realizados (Capítulo 3). Primero se detallan los aportes relacionados con las técnicas de control de modo deslizante para el control interno de corriente de una máquina multifásica y posteriormente se evalúan variantes del control predictivo aplicado a la máquina multifásica. Finalmente se exponen las conclusiones alcanzadas y se presentan futuros trabajos en la línea de investigación planteada en esta Tesis Doctoral (Cápitulo 4).

La Parte III se compone de los cinco artículos basados en ideas originales, desarrollados y publicados durante la realización de la investigación en los accionamientos de máquinas de inducción asimétrica hexafásicas y otros cinco con autoría pero que no representan las contribuciones de esta Tesis Doctoral. Los primeros cinco artículos son los que representan los aportes principales de esta Tesis Doctoral. El primero se basa en el control deslizante aplicado a una máquina hexafásica respectivamente con resultados experimentales. El segundo es una nueva versión del control deslizante aplicado a la máquina de inducción asimétrica hexafásica validado por resultados experimentales. El tercero se concentra en múltiples técnicas de control predictivo con modulaciones en la salida del inversor, un análisis y distintos resultados de comportamiento de los mismos basados en resultados experimentales. El cuarto artículo es aporte de nuevas versiones de la técnica de control predictivo validadas por resultados experimentales. El quinto realiza un análisis teórico y experimental de la estabilidad del control predictivo y sus variantes. El sexto y séptimo es una técnica de modulación del control predictivo que no representa un aporte a esta Tesis y se valida por resultados experimentales. El octavo es una propuesta del control deslizante validado por resultados de simulación. El noveno artículo es una comparativa entre dos técnicas no lineales aplicado a la máquina de inducción hexafásica con resultados de simulación. Por último, el décimo artículo es una comparativa entre técnicas de modulación aplicadas con el control predictivo a la máquina hexafásica validadas por resultados de simulación.

CAPÍTULO 2

MODELADO Y CONTROL DE MÁQUINAS DE INDUCCIÓN ASIMÉTRICAS HEXAFÁSICAS

2.1 Introducción

En este capítulo se desarrollará el modelado de la MIAH. Se aboradará primeramente la representación del sistema en tiempo continuo para posteriormente desarrollar las ecuaciones que rigen el modelo de la MIAH en tiempo discreto utilizando la notacion de variables de estado. Se introduce la técnica de descomposición de espacio vectorial (VSD) describiendo las ecuaciones que rigen el modelo de la MIAH en el sistema de referencia estacionario ($\alpha - \beta$) y dinámico ($d - q$). El modelado del sistema global (accionamineto y actuador) contempla además la representación matricial del modelo del inversor con fuente de voltaje (VSI). El capítulo concluye con una taxonomía de las técnicas de control aplicadas a la MIAH y una descripción de aquellas que resultan útiles en el marco de las aportaciones de esta Tesis Doctoral.

2.1.1 Modelo de Máquinas de Inducción de Bobinados Distribuidos

Las máquinas de inducción (MI) constituyen unos de los dispositivos electromecánicos más utilizados en aplicaciones industriales por su bajo costo de producción y mantenimiento. La teoría general de máquinas eléctricas y sistemas multifásicos dispone de suficientes herramientas para definir el modelo del sistema, considerando un número arbitrario de fases [29]. La generalización de Fortescue y Clarke son la base para los modelos vectoriales utilizados actualmente. Esta generalización diferencia entre máquinas con un número de fases correspondiente a un múltiplo de tres [30, 31] y máquinas con un número arbitrario par o impar de fases [32–34].

Entre las máquinas multifásicas más estudiadas, desde el punto de vista del modelado matemático, se encuentran las máquinas de cinco y seis fases [30–34], aunque para el caso de las máquinas simétricas son preferibles los diseños con números de fases impar frente a aquellas que poseen números pares de fases. Esto se debe a que en los casos de distribución simétrica y con número par de fases se producirá un rizado de par electromagnético idéntico al de una máquina con la mitad del número de fases, perdiéndose una de las principales ventajas que se deriva del uso de un accionamiento multifásico. Cuando el número de fases es múltiplo de tres y par, además de ser asimétrica con neutros aislados se obtiene el mismo número de sub-espacios (grado de libertad para el control) que en máquinas simétricas con número de fases menor pero ofreciendo una mejor distribución de potencia por fase. Particularmente, las máquinas con devanados múltiplos de tres son de mayor interés para aplicaciones de alta potencia [35].

Consideraciones para el Modelado El proceso de modelado de las máquinas de inducción multifásicas está generalmente sujeto a varias consideraciones, las cuales se aplican también al caso de la MIAH y se describen a continuación [36, 37].

- Todos los bobinados en el estator de la MIAH son iguales. Mientras que el rotor es del tipo jaula de ardilla que puede ser modelado como n cargas inductivas interconectadas en paralelo por los anillos que sostienen a las barras que lo conforman.
- El entrehierro de la MIAH se considera uniforme y de espesor constante, y su variación debido a las excentricidades del rotor o por las ranuras del estator y del rotor son despreciables.
- La característica de magnetización del material ferromagnético se supone que es lineal. Por lo tanto, los efectos de la saturación magnética no son considerados.
- Las inductancias de fuga y la resistencia de los devanados del estator y del rotor se consideran constantes. Se ignoran sus variaciones debidas a cambios de frecuencia o temperatura.

- Las variables del rotor se encuentran proyectadas al estator mediante la relación de transformación del acoplamiento estator–rotor.

- Se desprecian las variaciones debidas a la variaciones de frecuencia, temperatura y humedad, al envejecimiento de los componentes eléctricos.

Modelo Definido en Función a las Variables de Fase de una MIAH La MIAH está compuesta de dos sistemas trifásicos conectados en estrella y desfasados entre sí en 30°, por lo que también se lo suele denominar dual-trifásico. Ésta posee dos neutros para ambos sistemas trifásicos, inicialmente aislados entre sí. La **Figura 2.1** muestra la disposición de las bobinas de los sistemas trifásicos y su correspondiente desfasaje, además de los neutros N y N'.

Debido a que todos los bobinados distribuidos de la MIAH tienen una naturaleza del tipo resistiva-inductiva, la ecuación de equilibrio de voltaje de cada fase, tanto del estator como del rotor, sigue esta ecuación:

$$v = Ri + \frac{d\psi}{dt} \tag{2.1}$$

donde v, i y ψ representan los valores instantáneos de las magnitudes de voltaje, corriente y flujo magnético respectivamente, a la vez que R representa la resistencia del bobinado. La MIAH posee seis fases, tanto en el estator como en el rotor, y las ecuaciones que

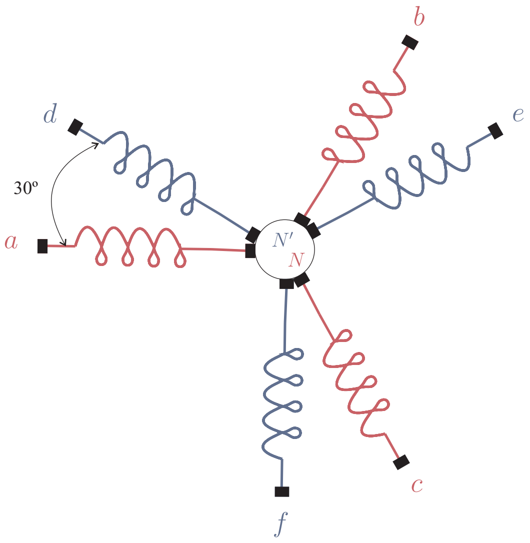

Figura 2.1 Disposición de las bobinas de la MIAH.

representan el equilibro de tensión, tanto en el estator como en el rotor, puede representarse en forma matricial utilizando las siguientes ecuaciones:

$$v_s = R_s i_s + \frac{d}{dt}\psi_s \tag{2.2}$$

$$v_r = R_r i_r + \frac{d}{dt}\psi_r \tag{2.3}$$

donde $v_s = [v_{sa},\, v_{sd},\, v_{sb},\, v_{se},\, v_{sc}, v_{sf}]^T$ y $v_r = [v_{ra},\, v_{rd},\, v_{rb},\, v_{re},\, v_{rc},\, v_{rf}]^T$ son los vectores columna que representan los voltajes del estator y del rotor, respectivamente, $i_s = [i_{sa},\, i_{sd},\, i_{sb},\, i_{se},\, i_{sc},\, i_{sf}]^T$ e $i_r = [i_{ra},\, i_{rd},\, i_{rb},\, i_{re},\, i_{rc},\, i_{rf}]^T$ representan los vectores que representan las corrientes de las fases del estator y del rotor, respectivamente y $\psi_s = [\psi_{sa},\, \psi_{sd},\, \psi_{sb},\, \psi_{se},\, \psi_{sc},\, \psi_{sf}]^T$ y $\psi_r = [\psi_{ra},\, \psi_{rd},\, \psi_{rb},\, \psi_{re},\, \psi_{rc},\, \psi_{rf}]^T$ son los vectores que representan las flujos del estator y del rotor, respectivamente. Las resistencias del estator y rotor están representados por R_s y R_r las cuales son matrices diagonales con sus respectivos valores. Por último, se tiene en cuenta que los bobinados del rotor en la máquina de inducción tipo jaula de ardilla están cortocircuitadas. Por tanto, los voltajes en el rotor en (2.3) son nulas. Las matrices de flujo magnético se encuentran definidas tal como se describe en las siguientes ecuaciones:

$$\psi_s = L_s i_s + L_{sr} i_r \tag{2.4}$$

$$\psi_r = L_r i_r + L_{rs} i_s \tag{2.5}$$

donde L_s y L_r son las matrices de inductancia del estator y rotor, respectivamente y L_{sr} y L_{rs} son las inductancias mutuas del estator a rotor y rotor a estator, respectivamente. Bajo las consideraciones antes mencionadas, las matrices de inductancia del estator y del rotor sólo poseen coeficientes constantes y son matrices 6×6:

$$L_s = \begin{bmatrix} L_{s11} & L_{s12} & L_{s13} & L_{s14} & L_{s15} & L_{s16} \\ L_{s21} & L_{s22} & L_{s23} & L_{s24} & L_{s25} & L_{s26} \\ L_{s31} & L_{s32} & L_{s33} & L_{s34} & L_{s35} & L_{s36} \\ L_{s41} & L_{s42} & L_{s43} & L_{s44} & L_{s45} & L_{s46} \\ L_{s51} & L_{s52} & L_{s53} & L_{s54} & L_{s55} & L_{s56} \\ L_{s61} & L_{s62} & L_{s63} & L_{s64} & L_{s65} & L_{s66} \end{bmatrix} \tag{2.6}$$

$$L_r = \begin{bmatrix} L_{r11} & L_{r12} & L_{r13} & L_{r14} & L_{r15} & L_{r16} \\ L_{r21} & L_{r22} & L_{r23} & L_{r24} & L_{r25} & L_{r26} \\ L_{r31} & L_{r32} & L_{r33} & L_{r34} & L_{r35} & L_{r36} \\ L_{r41} & L_{r42} & L_{r43} & L_{r44} & L_{r45} & L_{r46} \\ L_{r51} & L_{r52} & L_{r53} & L_{r54} & L_{r55} & L_{r56} \\ L_{r61} & L_{r62} & L_{r63} & L_{r64} & L_{r65} & L_{r66} \end{bmatrix} \tag{2.7}$$

Se considera que todos los devanados individuales de las fases en el estator son iguales y que los devanados se encuentran distribuidos simétricamente, las inductancias de fase son iguales, $L_{s11} = L_{s22} = L_{s33} = L_{s44} = L_{s55} = L_{s66}$, y las inductancias mutuas en el estator cumplen con la siguiente condición $L_{sij} = L_{sji}$, donde $i \neq j$ y también $i = j = [1,\ 2,\ 3,\ 4,\ 5,\ 6]$.

La posición relativa de los devanados del rotor con relación a los devanados del estator y viceversa depende directamente del ángulo del rotor θ_r, el cual varía debido a la posición angular del rotor y hace que los coeficientes de las matrices L_{sr} y L_{rs} varíen en el tiempo. La velocidad eléctrica del rotor (ω_r) se obtiene de la siguiente ecuación:

$$\theta_r(t) = \int_0^t \omega_r dt \tag{2.8}$$

Según las consideraciones hechas al inicio de esta sección, ambos flujos, generados en el estator y en el rotor, son sinusoidales y la matriz de inductancia mutua del estator a rotor L_{sr} es:

$$L_{sr} = M \begin{bmatrix} \cos(\sigma_1) & \cos(\sigma_6) & \cos(\sigma_5) & \cos(\sigma_4) & \cos(\sigma_3) & \cos(\sigma_2) \\ \cos(\sigma_2) & \cos(\sigma_1) & \cos(\sigma_6) & \cos(\sigma_5) & \cos(\sigma_4) & \cos(\sigma_3) \\ \cos(\sigma_3) & \cos(\sigma_2) & \cos(\sigma_1) & \cos(\sigma_6) & \cos(\sigma_5) & \cos(\sigma_4) \\ \cos(\sigma_4) & \cos(\sigma_3) & \cos(\sigma_2) & \cos(\sigma_1) & \cos(\sigma_6) & \cos(\sigma_5) \\ \cos(\sigma_5) & \cos(\sigma_4) & \cos(\sigma_3) & \cos(\sigma_2) & \cos(\sigma_1) & \cos(\sigma_6) \\ \cos(\sigma_6) & \cos(\sigma_5) & \cos(\sigma_4) & \cos(\sigma_3) & \cos(\sigma_2) & \cos(\sigma_1) \end{bmatrix} \tag{2.9}$$

donde M representa la inductancia de magnetización. La inductancia mutua del rotor a estator se obtiene de $L_{rs} = L_{sr}^T$. El ángulo σ_k se define de la siguiente manera:

$$\sigma_k = \theta_r - (k-1)\varphi \tag{2.10}$$

donde $k = [1,\, 2,\, 3,\, 4,\, 5,\, 6]$ y φ representa el desfasaje angular entre dos devanados consecuentes del estator. Las ecuaciones (2.2) y (2.3) se pueden plantear de la siguiente forma:

$$v_s = R_s i_s + L_s \frac{d}{dt} i_s + L_{sr} \frac{d}{dt} i_r \tag{2.11}$$

$$v_r = R_r i_r + L_r \frac{d}{dt} i_r + L_{rs} \frac{d}{dt} i_s \tag{2.12}$$

De esta manera, por medio de (2.2)-(2.12) se describe por completo el comportamiento eléctrico de la MIAH, representada en variables de fase. A causa de que sólo hay un grado de libertad en el movimiento del rotor, la ecuación que relaciona el par de torsión y los parámetros mecánicos de la máquina con respecto a la velocidad mecánica es:

$$T_e - T_L = J_m \frac{d\omega_{rm}}{dt} + B_m \omega_{rm} \tag{2.13}$$

donde T_e representa el par electromagnético generado por la máquina, T_L el par de torsión de la carga mecánica, J_m el coeficiente de inercia, B_m el coeficiente de fricción mecánica y ω_{rm} la velocidad mecánica angular. Al mismo tiempo, se puede relacionar ω_{rm} con la velocidad eléctrica ω_r por esta relación:

$$\omega_r = P \omega_{rm} \tag{2.14}$$

donde P representa el par de polos magnéticos de la MIAH. De esta manera la ecuación (2.13) puede ser reescrita de la siguiente manera:

$$T_e - T_L = \frac{J_m}{P} \frac{d\omega_r}{dt} + \frac{B_m}{P} \omega_r \tag{2.15}$$

El T_e desarrollado por la MIAH relaciona el subsistema electromagnético con el subsistema mecánico y es responsable de la conversión electromecánica de la energía. En general, T_e viene dado por la siguiente ecuación:

$$T_e = \frac{P}{2} \begin{bmatrix} i_s & i_r \end{bmatrix} \frac{d}{d\theta_r} \begin{bmatrix} L_s & L_{sr} \\ L_{rs} & L_r \end{bmatrix} \begin{bmatrix} i_s \\ i_r \end{bmatrix} \tag{2.16}$$

Como L_s y L_r no dependen de ω_r, la ecuación (2.16) se reduce a:

$$T_e = P i_s^T \frac{dL_{sr}}{d\theta_r} i_r \tag{2.17}$$

Esto equivale a que T_e en la MIAH es dependiente directamente de la interacción entre los bobinados del estator y del rotor. Finalmente, el modelo matemático completo, tanto eléctrico como electromecánico, de la MIAH es representado por medio de las ecuaciones (2.2)-(2.17). Este modelo matemático se compone de trece ecuaciones diferenciales, de los cuales doce representan el equilibrio de voltaje en el estator y el rotor, y la última denota la ecuación mecánica de equilibrio. En consecuencia, estas ecuaciones conforman un sistema no lineal basado en ecuaciones diferenciales, con coeficientes variantes en el tiempo debido a la inductancia mutua entre estator a rotor. Aunque es posible resolver el modelo completo directamente, en función de las variables de fase, gracias a la elevada capacidad computacional existente en las actuales computadoras (ordenadores), esto implicaría un costo computacional muy elevado, resultando una implementación muy costosa. Por tanto, se han propuesto varias trasnformaciones de las variables de fase para convertir el modelo de variables de fase a otro más simplificado.

Tranformación de Clarke En el modelo descrito anteriormente, con el enfoque basado en las variables de fase, cada variable eléctrica queda definida en un espacio de dimensión 6. Luego, aplicando la transformación de Clarke, por medio de la matriz cuadrada $\mathbf{C}$ representada por (2.19), de orden 6, se consigue reemplazar el conjunto de 6 variables en un nuevo conjunto de 6 variables, y al mismo tiempo descompone el vector de espacio de 6 dimensiones en 3 sub-espacios bidimensionales. Como los sub-espacios y ejes que constituyen el nuevo espacio son ortogonales, el cual constituye la principal propiedad de esta transformación, estos sub-espacios estarán completamente desacoplados entre sí, con lo que se consigue una importante simplificación en el modelo de la MIAH [38]. La transformación aplicada se indica en la siguiente ecuación:

$$g_{\alpha\beta} = \mathbf{C} g_{1-6} \tag{2.18}$$

donde $g_{\alpha\beta} = [g_\alpha,\, g_\beta,\, g_x,\, g_y,\, g_{z_1},\, g_{z_2}]^T$ representa el vector columna de las magnitudes eléctricas de voltaje, corriente o flujo que designan tanto al estator como al rotor luego de la transformación, mientras que $g_{1-6} = [g_1,\, g_2,\, g_3,\, g_4,\, g_5,\, g_6]^T$ corresponde al vector columna en función a las variables de fase. Como se satisface la condición que $\mathbf{C}^{-1} = \mathbf{C}^T$, se puede asumir que $g_{1,\,2,\,3,\,4,\,5,\,6} = \mathbf{C}^T g_{\alpha\beta}$.

$$\mathbf{C} = k \begin{bmatrix} 1 & \cos(\phi) & \cos(4\phi) & \cos(5\phi) & \cos(8\phi) & \cos(9\phi) \\ 0 & \sin(\phi) & \sin(4\phi) & \sin(5\phi) & \sin(8\phi) & \sin(9\phi) \\ 1 & \cos(5\phi) & \cos(8\phi) & \cos(\phi) & \cos(4\phi) & \cos(9\phi) \\ 0 & \sin(5\phi) & \sin(8\phi) & \sin(\phi) & \sin(4\phi) & \sin(9\phi) \\ 1 & 0 & 1 & 0 & 1 & 0 \\ 0 & 1 & 0 & 1 & 0 & 1 \end{bmatrix} \tag{2.19}$$

donde $\phi = \frac{\pi}{6}$ y $k = \frac{2}{6}$ que representa a la magnitud encargada de mantener invariante a la amplitud (voltaje-corriente) [39].

Luego de la aplicación de esta transformación al modelo en variables de fase (2.11)-(2.15) y despreciando las pérdidas, el modelo desacoplado de Clarke se describe mediante el conjunto de ecuaciones de voltaje (2.20)-(2.27).

$$v_{\alpha s} = R_s i_{\alpha s} + \frac{d\psi_{\alpha s}}{dt} = R_s i_{\alpha s} + L_s \frac{di_{\alpha s}}{dt} + L_m \frac{d}{dt}(i'_{\alpha r}\cos(\theta) - i'_{\beta r}\sin(\theta)) \quad (2.20)$$

$$v_{\beta s} = R_s i_{\beta s} + \frac{d\psi_{\beta s}}{dt} = R_s i_{\beta s} + L_s \frac{di_{\beta s}}{dt} + L_m \frac{d}{dt}(i'_{\alpha r}\sin(\theta) + i'_{\beta r}\cos(\theta)) \quad (2.21)$$

$$v_{\alpha r} = 0 = R_r i'_{\alpha r} + \frac{d\psi'_{\alpha r}}{dt} = R_r i'_{\alpha r} + L_r \frac{di'_{\alpha r}}{dt} + L_m \frac{d}{dt}(i_{\alpha s}\cos(\theta) + i_{\beta s}\sin(\theta)) \quad (2.22)$$

$$v_{\beta r} = 0 = R_r i'_{\beta r} + \frac{d\psi'_{\beta r}}{dt} = R_r i'_{\beta r} + L_r \frac{di'_{\beta r}}{dt} + L_m \frac{d}{dt}(-i_{\alpha s}\sin(\theta) + i_{\beta s}\cos(\theta)) \quad (2.23)$$

$$v_{xs} = R_s i_{xs} + \frac{d\psi_{xs}}{dt} = R_s i_{xs} + L_{ls} \frac{di_{xs}}{dt} \quad (2.24)$$

$$v_{ys} = R_s i_{ys} + \frac{d\psi_{ys}}{dt} = R_s i_{ys} + L_{ls} \frac{di_{ys}}{dt} \quad (2.25)$$

$$v_{z_1 s} = R_s i_{z_1 s} + \frac{d\psi_{z_1 s}}{dt} = R_s i_{z_1 s} + L_{ls} \frac{di_{z_1 s}}{dt} \quad (2.26)$$

$$v_{z_2 s} = R_s i_{z_2 s} + \frac{d\psi_{z_2 s}}{dt} = R_s i_{z_2 s} + L_{ls} \frac{di_{z_2 s}}{dt} \quad (2.27)$$

donde $L_m = 3M$ es la inductancia mutua, $L_s = L_m + L_{ls}$ la inductancia del estator y $L_r = L_m + L_{lr}$ la inductancia del rotor.

Las ecuaciones (2.20)-(2.23) representan las componentes del estator y rotor del sub-espacio $(\alpha - \beta)$, en las cuales se mapea la componente fundamental del flujo y, por lo tanto, es el sub-espacio vinculado a la conversión de energía electromecánica. En los demás sub-espacios ortogonales $(x - y)$ y $(z_1 - z_2)$ sólo se encuentran las variables de estator, al considerar el devanado de la MIAH del tipo distribuido. Particularmente, en el sub-espacio ($z_1 - z_2$) se representan los componentes homopolares, que de parte del rotor no tendrán en ningún caso corriente ya que se encuentran cortocircuitadas. Además, el modelo de la MIAH a estudiar será con los dos neutros aislados entre sí, por lo que la corriente en el estator en este sub-espacio será nula.

Luego de la aplicación de la transformación, las variables del rotor y del estator en las ecuaciones (2.20)-(2.23) se encuentran referidas a marcos de referencias distintos, como se aprecia en la **Figura 2.2**. Las variables del estator se encuentran referidas a un marco de referencia estacionario ($\alpha - \beta$), mientras que las variables del rotor se encuentran referidas a un marco de referencia fijado al rotor ($\alpha' - \beta'$) que se encuentra desfasado del sub-espacio ($\alpha - \beta$) por θ y va girando a una velocidad ω_r. Se deben representar todas las variables con respecto a un único marco de referencia para simplificar el modelo en estado estacionario. Para ello, es necesario aplicar una transformación a las variables del rotor utilizando la matriz de rotación $\mathbf{R}(\theta)$.

$$g_r = \mathbf{R}(\theta) g_r' \tag{2.28}$$

donde $g_r = [g_{\alpha r}, g_{\beta r}, g_{xr}, g_{yr}, g_{z_1 r}, g_{z_2 r}]^T$ y $g_r' = [g_{\alpha r}', g_{\beta r}', g_{xr}', g_{yr}', g_{z_1 r}', g_{z_2 r}']^T$. La matriz $\mathbf{R}(\theta)$ se denota como:

$$\mathbf{R}(\theta) = \begin{bmatrix} \cos(\theta) & -\sin(\theta) & 0 & 0 & 0 & 0 \\ \sin(\theta) & \cos(\theta) & 0 & 0 & 0 & 0 \\ 0 & 0 & 1 & 0 & 0 & 0 \\ 0 & 0 & 0 & 1 & 0 & 0 \\ 0 & 0 & 0 & 0 & 1 & 0 \\ 0 & 0 & 0 & 0 & 0 & 1 \end{bmatrix} \tag{2.29}$$

$$\mathbf{R}(\theta)^{-1} = \mathbf{R}(\theta)^T \tag{2.30}$$

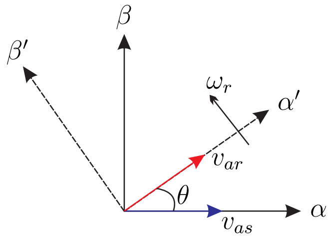

Figura 2.2 Sistema de referencia estacionario ($\alpha - \beta$) y ($\alpha' - \beta'$).

La aplicación de esta transformación en el rotor sólo afecta a sus componentes en el sub-espacio ($\alpha - \beta$). Finalmente, el modelo de la MIAH en este sub-espacio, con todas sus variables referenciadas respecto al marco de referencia estacionario, es descrito por las siguientes ecuaciones:

$$v_{\alpha s} = R_s i_{\alpha s} + \frac{d\psi_{\alpha s}}{dt} = R_s i_{\alpha s} + L_s \frac{di_{\alpha s}}{dt} + L_m \frac{di_{\alpha r}}{dt} \tag{2.31}$$

$$v_{\beta s} = R_s i_{\beta s} + \frac{d\psi_{\beta s}}{dt} = R_s i_{\beta s} + L_s \frac{di_{\beta s}}{dt} + L_m \frac{di_{\beta r}}{dt} \tag{2.32}$$

$$v_{\alpha r} = 0 = R_r i_{\alpha r} + \frac{d\psi_{\alpha r}}{dt} = R_r i_{\alpha r} + L_r \frac{di_{\alpha r}}{dt} + L_m \frac{di_{\alpha s}}{dt} + \omega_r (L_m i_{\beta s} + L_r i_{\beta r}) \tag{2.33}$$

$$v_{\beta r} = 0 = R_r i_{\beta r} + \frac{d\psi_{\beta r}}{dt} = R_r i_{\beta r} + L_r \frac{di_{\beta r}}{dt} + L_m \frac{di_{\beta s}}{dt} - \omega_r (L_m i_{\alpha s} + L_r i_{\alpha r}) \tag{2.34}$$

El T_e, definido en base a las nuevas variables, se calcula aplicando las transformaciones descritas en (2.18) y (2.28) a (2.17) con lo que se obtiene la siguiente ecuación:

$$T_e = 3PL_m(i_{\alpha r} i_{\beta s} - i_{\beta r} i_{\alpha s}) \tag{2.35}$$

donde el factor 3 no aparecerá si se aplica la transformación invariante en potencia [40].

Transformada Rotacional o de Park Existen otras simplificaciones que pueden ser conseguidas cuando las variables son definidas respecto a otros marcos de referencias dinámicos, seleccionados apropiadamente para el control. Los cambios de marco de referencia se obtienen mediante transformaciones matriciales aplicadas al modelo desacoplado de Clarke. Como el estator y el rotor se encuentran acoplados sólo en el sub-espacio ($\alpha - \beta$), las transformaciones a marcos de referencia dinámicos sólo afectarán a las variables eléctricas definidas en el mismo. La transformación se define de tal forma que el nuevo conjunto de bobinados del estator y del rotor, los cuales reemplazarán a los bobinados en ($\alpha - \beta$), giren a la misma velocidad angular, también llamada marco de referencia dinámico ($d - q$). Además, el movimiento relativo entre los bobinados del estator y del rotor queda eliminado, consiguiendo así un conjunto de ecuaciones diferenciales con coeficientes constantes [38, 40].

Como en una MIAH el entrehierro es constante y todas las inductancias de los bobinados del estator y del rotor también son constantes, la elección de la velocidad de giro del marco de referencia dinámico es arbitraria. Para el desarrollo del modelo, se denota a la velocidad de giro del marco de referencia dinámico como ω_a, cuya posición instantánea respecto al marco estacionario está definida por la coordenada θ_a, que se relaciona a su vez con la velocidad de la siguiente forma:

$$\theta_a(t) = \int_0^t \omega_a dt \tag{2.36}$$

el cual será utilizada para la transformación rotacional de las variables estatóricas. Del mismo modo, el rotor también se encuentra girando a una velocidad ω_r y su coordenada respecto al marco de referencia estacionario se encuentra dada por la variable θ, tal como muestra la **Figura 2.3**. Sin embargo, la coordenada del rotor respecto al marco de referencia $(d-q)$ está definida por la posición θ_r que depende en cada instante de tiempo de la velocidad relativa entre el marco de referencia dinámico y el rotor ω_{sl} (deslizamiento) de acuerdo con la siguiente ecuación:

$$\theta_r = \theta_a - \theta = \int_0^t (\omega_a - \omega_r) dt = \int_0^t \omega_{sl} dt \tag{2.37}$$

El segundo eje del marco de referencia dinámico, el cual es perpendicular al eje d, es denominado q. Así, la transformación de las variables de estator y rotor se detalla mediante la siguiente ecuación:

$$g_{dq} = \mathbf{D} g_{\alpha\beta} \tag{2.38}$$

donde $g_{dq} = [g_d, g_q, g_x, g_y, g_{z_1}, g_{z_2}]^T$ y $g_{\alpha\beta} = [g_\alpha, g_\beta, g_x, g_y, g_{z_1}, g_{z_2}]^T$. La matriz $\mathbf{D}$ se denota como:

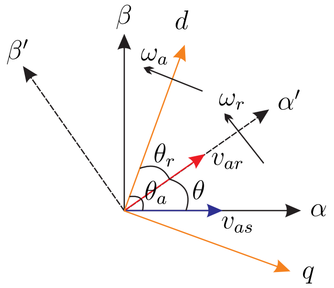

Figura 2.3 Sistema de referencia dinámico $(d-q)$.

$$\mathbf{D}_s = \begin{bmatrix} \cos(\theta_a) & -\sin(\theta_a) & 0 & 0 & 0 & 0 \\ \sin(\theta_a) & \cos(\theta_a) & 0 & 0 & 0 & 0 \\ 0 & 0 & 1 & 0 & 0 & 0 \\ 0 & 0 & 0 & 1 & 0 & 0 \\ 0 & 0 & 0 & 0 & 1 & 0 \\ 0 & 0 & 0 & 0 & 0 & 1 \end{bmatrix} \tag{2.39}$$

$$\mathbf{D}_r = \begin{bmatrix} \cos(\theta_r) & -\sin(\theta_r) & 0 & 0 & 0 & 0 \\ \sin(\theta_r) & \cos(\theta_r) & 0 & 0 & 0 & 0 \\ 0 & 0 & 1 & 0 & 0 & 0 \\ 0 & 0 & 0 & 1 & 0 & 0 \\ 0 & 0 & 0 & 0 & 1 & 0 \\ 0 & 0 & 0 & 0 & 0 & 1 \end{bmatrix} \tag{2.40}$$

siendo $\mathbf{D}_s$ la matriz de transformación para las variables de estator y $\mathbf{D}_r$ la matriz de transformación para las variables de rotor. La transformación de rotación sólo aplica a las ecuaciones en el sub-espacio $(\alpha - \beta)$, mientras que las ecuaciones en los sub-espacios $(x - y)$ y $(z_1 - z_2)$ no varían [38]. También se puede afirmar que $g_{\alpha\beta} = \mathbf{D}^T g_{dq}$ ya que se cumple esta condición $\mathbf{D}^{-1} = \mathbf{D}^T$.

El modelo matemático resultante, luego de la aplicación de la transformación propuesta en (2.38)-(2.40) se encuentra definido por el siguiente conjunto de ecuaciones de equilibrio de voltaje:

$$v_{ds} = R_s i_{ds} + L_s \frac{di_{ds}}{dt} + L_m \frac{di_{dr}}{dt} - \omega_a (L_s i_{qs} + L_m i_{qr}) \tag{2.41}$$

$$v_{qs} = R_s i_{qs} + L_s \frac{di_{qs}}{dt} + L_m \frac{di_{qr}}{dt} + \omega_a (L_s i_{ds} + L_m i_{dr}) \tag{2.42}$$

$$v_{dr} = 0 = R_r i_{dr} + L_m \frac{di_{ds}}{dt} + L_r \frac{di_{dr}}{dt} - \omega_{sl} (L_m i_{qs} + L_r i_{qr}) \tag{2.43}$$

$$v_{qr} = 0 = R_r i_{qr} + L_m \frac{di_{qs}}{dt} + L_r \frac{di_{qr}}{dt} + \omega_{sl} (L_m i_{ds} + L_r i_{dr}) \tag{2.44}$$

$$v_{xs} = R_s i_{xs} + L_{ls} \frac{di_{xs}}{dt} \tag{2.45}$$

$$v_{ys} = R_s i_{ys} + L_{ls}\frac{di_{ys}}{dt} \tag{2.46}$$

$$v_{z_1s} = R_s i_{z_1s} + L_{ls}\frac{di_{z_1s}}{dt} \tag{2.47}$$

$$v_{z_2s} = R_s i_{z_2s} + L_{ls}\frac{di_{z_2s}}{dt} \tag{2.48}$$

Por último, el T_e se define de manera similar al caso anterior (2.35):

$$T_e = 3PL_m(i_{dr}i_{qs} - i_{qr}i_{ds}) \tag{2.49}$$

Algunas representaciones alternativas relacionando a los flujos magnéticos del estator y rotor son las siguientes:

$$T_e = 3P(\psi_{ds}i_{qs} - \psi_{qs}i_{ds}) = 3P\frac{L_m}{L_r}(\psi_{dr}i_{qs} - \psi_{qr}i_{ds}) \tag{2.50}$$

2.1.2 Modelo de los Convertidores Electrónicos de Potencia

Existen diferentes topologías de convertidores de potencia multifásicos entre las que se encuentra el convertidor multinivel [41–44] y el matricial [28, 45, 46]. No obstante, la topología más popular tanto en sistemas trifásicos como multifásicos sigue siendo el de dos niveles y dos etapas corriente alterna/corriente continua (AC/DC) - corriente continua/corriente alterna (DC/AC). Estas etapas consisten por lo general en un rectificador no controlado y un VSI, respectivamente; acoplados eléctricamente por un bus de corriente continua denominada comúnmente DC–link. El sistema descrito posee la capacidad de operar en un amplio rango de frecuencias en su salida y de generar, mediante un adecuado algoritmo de control, una salida con valor medio sinusoidal conjuntamente con una pequeña cantidad de armónicos de bajo orden.

El modelo del VSI es de utilidad para la formulación y extensión de las técnicas de control propuestas en esta Tesis. Inicialmente se obtiene el modelo escalar del VSI; posteriormente, se aplican a éste transformaciones descritas en la sección anterior para definir el modelo vectorial que resulta de mayor interés para la descripción de las distintas estrategias de control descritas posteriormente.

Modelo Escalar del VSI de 6 ***fases asimétrico*** En la **Figura 2.4** se muestra un esquema del VSI de 6 ramas y dos niveles. Se considera que el DC–link es alimentado con una fuente de voltaje V_{dc} de DC con un punto medio 0. El VSI está compuesto de 12 interruptores electrónicos de potencia, un par por cada rama. La salida del VSI corresponde a cada

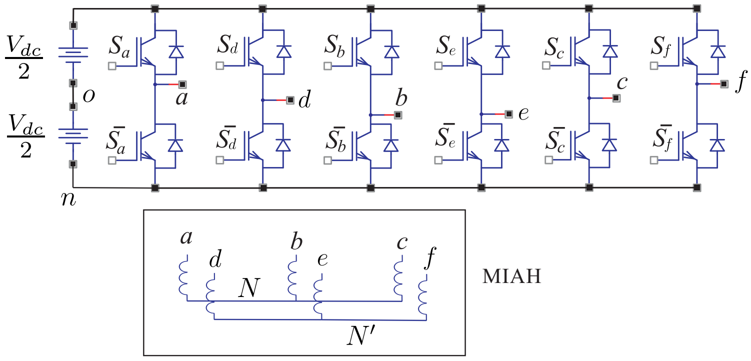

Figura 2.4 Diagrama esquemático del VSI de 6 fases y dos niveles.

punto medio (a, d, b, e, c, f) entre estos interruptores. Se asume, por simplicidad, que la salida del VSI alimenta a una carga balanceada en conexión estrella con predominancia inductiva (característica dominante en las MIAH). Los voltajes de fase se definen por las variables V_{sk} y $V_{sk'}$ siendo $k = [a,\ b,\ c]$ y $k' = [d,\ e,\ f]$.

Para el esquema presentado, a fin de evitar cortocircuitos, en cada rama sólo puede ser activado un interruptor de potencia a la vez. Cuando ambos interruptores de una rama se encuentran desactivados no se tiene ningún tipo de control sobre la carga por lo que este estado también debe ser evitado. Las condiciones especificadas se cumplen en el esquema presentado en la **Figura 2.4**, utilizando señales de disparos complementarias para cada par de interruptores en una determinada rama. Así, el estado de cada rama (S_k y $S_{k'}$) puede definirse utilizando la lógica binaria, ($S_k \in [0,\ 1]$ y $S_{k'} \in [0,\ 1]$); de manera que $S_k = 1$ implica que el interruptor superior se encuentran activado y el inferior desactivado, mientras que el caso opuesto se verifica cuando $S_k = 0$ (interruptor inferior activado y superior desactivado). Esto permite que en la salida del VSI se disponga de dos niveles de voltaje ($\pm\frac{V_{dc}}{2}$ respecto al punto medio del DC–link (o). La función de conmutación del VSI puede definirse utilizando el vector de conmutación $[S_a,\ S_d,\ S_b,\ S_e,\ S_c,\ S_f]^T$.

Los voltajes v_{kn} y $v_{k'n}$ respecto al bus negativo del DC–link (n) pueden ser definidos basándose en el estado de conmutación de sus ramas, como se indica en la siguiente ecuación:

$$\begin{aligned} v_{kn} &= V_{dc} S_k \\ v_{k'n} &= V_{dc} S_{k'} \end{aligned} \tag{2.51}$$

Por otra parte, los voltajes v_{kn} y $v_{k'n}$ se encuentran relacionados con los voltajes de fase (v_{kN} y $v_{kN'}$) y los voltajes entre el bus negativo del DC–link y los puntos comunes del conexionado en estrella (v_{Nn} y $v_{N'n}$), con estas ecuaciones:

$$\begin{aligned} v_{kn} &= v_{kN} + v_{Nn} \\ v_{k'n} &= v_{kN'} + v_{N'n} \end{aligned} \tag{2.52}$$

Para el caso estudiado con carga balanceada, la suma de los voltajes de fase debe ser igual a cero. Sumando todas las ecuaciones que se obtienen en cada fase con la expresión obtenida en (2.52) en conjunto con (2.51), se llega a que los voltajes v_{Nn} y $v_{N'n}$ pueden definirse a partir de los estados de conmutación de la siguiente forma:

$$\begin{aligned} v_{Nn} &= \frac{1}{3}(v_{an} + v_{bn} + v_{cn}) \\ v_{N'n} &= \frac{1}{3}(v_{dn} + v_{en} + v_{fn}) \end{aligned} \tag{2.53}$$

Reemplazando esta igualdad en (2.52), los voltajes quedan determinados por las siguientes ecuaciones:

$$\begin{aligned} v_{kN} &= v_{kn} - v_{Nn} = V_{dc}S_k - \frac{1}{3}(v_{an} + v_{bn} + v_{cn}) \\ v_{k'N'} &= v_{k'n} - v_{N'n} = V_{dc}S_{k'} - \frac{1}{3}(v_{dn} + v_{en} + v_{fn}) \end{aligned} \tag{2.54}$$

El voltaje generado por el VSI puede tomar 5 valores distintos comprendidos entre $\frac{2V_{dc}}{3}$ y $\frac{-2V_{dc}}{3}$ con pasos de $\frac{V_{dc}}{3}$. Por simplicidad, los voltajes de fase definidos en (2.54) en función de los estados de conmutación pueden expresarse utilizando matrices, como se indica a continuación [47]:

$$\mathbf{M} = \frac{1}{3}\begin{bmatrix} 2 & 0 & -1 & 0 & -1 & 0 \\ 0 & 2 & 0 & -1 & 0 & -1 \\ -1 & 0 & 2 & 0 & -1 & 0 \\ 0 & -1 & 0 & 2 & 0 & -1 \\ -1 & 0 & -1 & 0 & 2 & 0 \\ 0 & -1 & 0 & -1 & 0 & 2 \end{bmatrix} \tag{2.55}$$

$$\begin{bmatrix} v_{aN} \\ v_{dN'} \\ v_{bN} \\ v_{eN'} \\ v_{cN} \\ v_{fN'} \end{bmatrix} = V_{dc}\mathbf{M} \begin{bmatrix} S_a \\ S_d \\ S_b \\ S_e \\ S_c \\ S_f \end{bmatrix} \tag{2.56}$$

Los voltajes en modo común del VSI se definen como el voltaje del punto común del conexionado en estrella (N y N') con respecto al punto medio del DC-link (o) y se los puede considerar de la siguiente manera:

$$\begin{aligned} v_{No} &= v_{Nn} - \frac{V_{dc}}{2} = \frac{1}{3}(v_{an} + v_{bn} + v_{cn}) - \frac{V_{dc}}{2} \\ v_{N'o} &= v_{N'n} - \frac{V_{dc}}{2} = \frac{1}{3}(v_{dn} + v_{en} + v_{fn}) - \frac{V_{dc}}{2} \end{aligned} \tag{2.57}$$

Estas últimas ecuaciones indican que el VSI de dos niveles con 6 fases asimétrico, y en las condiciones de carga descritas, presenta 4 valores distintos de voltaje en modo común comprendidas desde $+\frac{V_{dc}}{2}$ hasta $-\frac{V_{dc}}{2}$ con paso incremental de $\frac{V_{dc}}{3}$. Esto corresponde a 2 niveles de magnitud en voltaje.

Modelo Vectorial del VSI de* 6 *fases asimétrico Con el fin facilitar y simplificar el análisis del modelo matemático del convertidor, se utiliza la matriz de transformación de Clarke para un VSI de 6 fases descrita en (2.19). El vector de dimensión 6 que se encuentra definido por las componentes en variables de fase $[v_{aN},\, v_{dN'},\, v_{bN},\, v_{eN'},\, v_{cN},\, v_{fN'}]^T$, luego de la transformación, quedará representado por el vector que contiene a las componentes bidimensionales de cada sub-espacio y las homopolares $[v_\alpha,\, v_\beta,\, v_x,\, v_y,\, v_{z_1},\, v_{z_2}]^T$. Los voltajes obtenidos, luego de aplicar (2.19) a (2.56), se calculan mediante la siguiente ecuación:

$$\begin{bmatrix} v_\alpha \\ v_\beta \\ v_x \\ v_y \\ v_{z_1} \\ v_{z_2} \end{bmatrix} = \mathbf{C}V_{dc}\mathbf{M} \begin{bmatrix} S_a \\ S_d \\ S_b \\ S_e \\ S_c \\ S_f \end{bmatrix} \tag{2.58}$$

El modelo del VSI de 6 fases asimétrico queda caracterizado por $2^6 = 64$ vectores posibles de activación (60 activos y 4 nulos). Estos vectores son proyectados en los sub-espacios $(\alpha - \beta)$ y $(x - y)$ como se muestran en la **Figura 2.5**, donde todos los posibles estados son identificados por dos números octales correspondientes a los números binarios $[S_a S_d S_b]$ y $[S_e S_c S_f]$ respectivamente. Además, para la MIAH con neutros aislados, los vectores de voltaje en el sub-espacio $(z_1 - z_2)$ son nulos, por lo que no tienen ninguna influencia en la técnicas de control aplicadas. Los vectores espaciales en los sub-espacios $(\alpha - \beta)$ y $(x - y)$ presentan 49 vectores relevantes y 15 repetidos o redundantes, ilustrados en la **Figura 2.5**.

2.2 Control de la MIAH

El desarrollo de nuevos métodos de control (lineal y no lineal) para accionamientos eléctricos multifásicos se ha convertido en uno de los tópicos que ha ganado mayor interés en los últimos años [8, 16, 48, 49]. La mayoría de las investigaciones se enfocan en la adaptación de los métodos de control de sistemas convencionales, siendo el FOC el más empleado. Desde el punto de vista de los sistemas multifásicos se debe destacar la popularidad de los sistemas formados por MIAH. Por lo que la mayoría de esfuerzos en la adaptación de los métodos de control convencionales han sido referidos a este tipo de sistemas. A continuación se presenta los esquemas de control aplicados hasta la fecha a las MIAH.

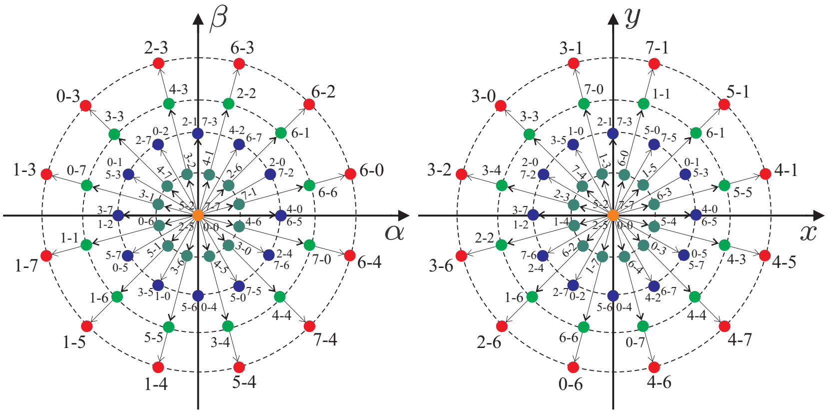

Figura 2.5 Proyecciones de los vectores de voltaje en los sub-espacios $(\alpha - \beta)$ (izq) y $(x - y)$ (der) para una MIAH con neutros aislados.

2.2.1 Control Escalar v/f

Esta es una de las estrategias de control más sencillas y menos costosas aplicadas a las MIAH. Se define como una estrategia de control de velocidad basada en que la velocidad del rotor se encuentra cerca de la velocidad eléctrica de la MIAH y en que la ecuación que representa al voltaje de una fase a puede ser expresada como:

$$v_{as} = R_s i_{as} + \frac{d\psi_{as}}{dt} \tag{2.59}$$

Para condiciones de régimen permanente a velocidades intermedias y altas, el término de flujo magnético domina al término resistivo en (2.59), por ello, la magnitud del voltaje aplicado está relacionada a la magnitud del flujo magnético del estator ($\wedge_s$) de esta forma:

$$v_s = \omega_r \wedge_s \tag{2.60}$$

donde se sugiere que para mantener el enlace de flujo constante (para evitar la saturación), la magnitud del voltaje de estator debe ser proporcional a la frecuencia.

La **Figura 2.6** presenta una posible implementación del control escalar v/f aplicado al control de una MIAH. La entrada del sistema es denominada ω_{rm}^* y se lo conecta a un saturador para reducir los transitorios al limitar la tasa de cambio de ω_{rm}^*. La salida del saturador es multiplicada por $\frac{P}{2}$, donde P es el número de polos para obtener la velocidad eléctrica ω_r^* que posee la unidad de medida de rad/s. Luego, ω_r^* es multiplicado por el factor de cambio v/f denominado $\frac{v_b}{\omega_b}$, donde v_b es la tasa de cambio de voltaje y ω_b es la tasa de cambio de frecuencia en rad/s con el fin de formar un voltaje con valor cuadrático medio (RMS) línea-neutro de comando denominado v_s. El voltaje v_s es multiplicado por $\sqrt{2}$ para obtener la referencia de voltaje en el eje q denominado v_{qs}^*. El voltaje de referencia en el eje d es puesto a 0. Además, la velocidad eléctrica ω_r^* es integrada para obtener la posición del marco de referncia síncrono θ_r. La integracion que determina θ_r es reiniciada de forma periódica al llegar a un valor múltiplo de 2π para mantener limitado a θ_r. Por último, los comandos en los ejes d y q se utilizan junto a alguna técnica de modulación (modulación por ancho de pulsos (PWM) siendo la más popular) para obtener una salida deseada en el VSI [40].

Las ventajas de este control es que es simple y que es relativamente de bajo costo ya que se trata de un control en lazo abierto, y la velocidad puede ser controlada (al menos por un grado de control) sin realimentación. La principal desventaja en su aplicación es que al ser de tipo lazo abierto, existirá un error entre la referencia y la salida, particularmente de forma más notoria a bajas velocidades [40].

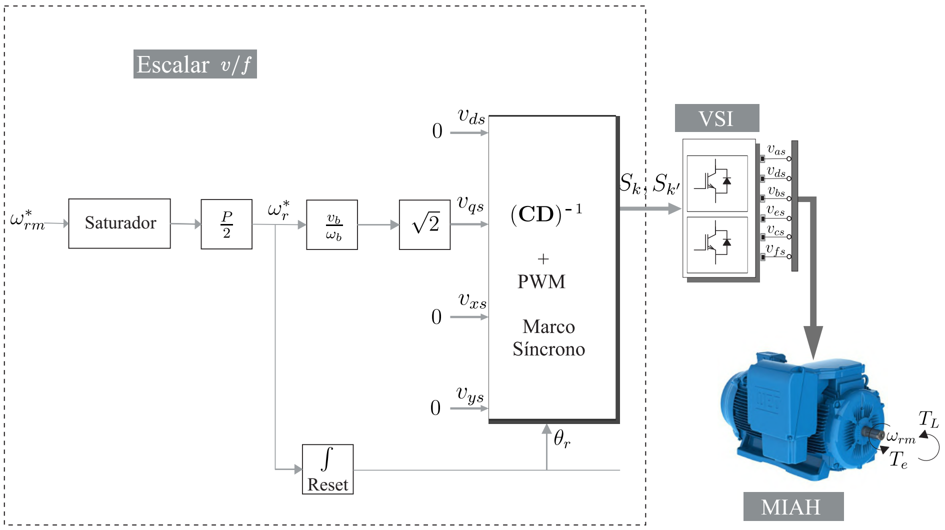

Figura 2.6 Diagrama en bloques del control escalar v/f aplicado al control de la MIAH.

2.2.2 Control de Campo Orientado (FOC)

El FOC es una estrategia de control que ha sido extendida a MIAH donde la generación de par y los componentes magnéticos que producen el flujo del estator se controlan de manera independiente (desacoplados). Los principios fundamentales del FOC, el cual permite una conversión matemática de una máquina de inducción hexafásica de AC a su modelo equivalente DC (Transformada de Clarke-Park), fueron establecidos a inicios de la década de 1970 y desde la década de 1980 ha sido objeto de numerosos estudios llegando al día de hoy a su estado de madurez [50].

El esquema de control FOC aplicado a una MIAH se basa en el modelo matemático. El modelo de dicha máquina en jaula de ardilla, con los bobinados del rotor cortocircuitados, está descrito por (2.41)-(2.50). El marco de referencia en el cual se ejecuta el control corresponde al marco de referencia del flujo del rotor, por tanto, el FOC generalmente se lo conoce como control de campo rotórico orientado (RFOC). El marco de referencia se caracteriza por las siguientes expresiones [40]:

$$\theta_a = \theta_r \tag{2.61}$$

$$\omega_a = \omega_r \tag{2.62}$$

$$\omega_r = \frac{d\theta_r}{dt} \tag{2.63}$$

La orientación necesaria para este control, se consigue alineando el eje d del sistema de referencia síncrono con el vector del flujo rotórico ψ_r. De esta manera se tienen:

$$\psi_{dr} = \psi_r \tag{2.64}$$

$$\psi_{qr} = 0 \tag{2.65}$$

$$\frac{d\psi_{qr}}{dt} = 0 \tag{2.66}$$

Las ecuaciones de los voltajes del rotor (2.43)-(2.44) en este marco de referencia se describen mediante el siguiente conjunto de ecuaciones:

$$0 = R_r i_{dr} + \frac{d\psi_{dr}}{dt} - \omega_{sl}\psi_{qr} \tag{2.67}$$

$$0 = R_r i_{qr} + \frac{d\psi_{qr}}{dt} + \omega_{sl}\psi_{dr} \tag{2.68}$$

Las componentes de corriente del rotor en los ejes $(d-q)$ pueden ser expresados en función del flujo del rotor, considerando la relación de (2.50), de la siguiente manera:

$$i_{dr} = \frac{(\psi_{dr} - L_m i_{ds})}{L_r} \tag{2.69}$$

$$i_{qr} = -\left(\frac{L_m}{L_r}\right) i_{qs} \tag{2.70}$$

Sustituyendo (2.69) en (2.67) y (2.70) en (2.68) completa el modelo del control RFOC:

$$\psi_r + \tau_r \frac{d\psi_r}{dt} = L_m i_{ds} \tag{2.71}$$

$$\omega_{sl}\psi_r\tau_r = L_m i_{qs} \tag{2.72}$$

$$T_e = P\left(\frac{L_m}{L_r}\right)\psi_r i_{qs} \tag{2.73}$$

donde $\tau_r = \frac{L_r}{R_r}$ representa la constante de tiempo del rotor.

El par electromagnético representado por (2.73) muestra que el mismo puede controlarse modificando la corriente de referencia del estator i_{qs} y manteniendo constante el flujo del rotor ψ_r por debajo del sincronismo. Analizando (2.71) se puede afirmar que el flujo del rotor es independiente de la corriente i_{qs} encargada de la producción del par y que el valor del flujo del rotor se determina únicamente mediante la corriente del estator i_{ds}. Habitualmente el valor de referencia de i_{ds} es establecido a su valor nominal (referencia de flujo constante e igual al máximo posible por debajo de la velocidad de sincronismo del accionamiento electromecánico de la MIAH), mientras que i_{qs} es controlada independientemente. Cabe mencionar que las corrientes i_{qs} e i_{ds} son corrientes DC en estado estacionario, lo que facilita su regulación. Reescribiendo (2.73) en función del deslizamiento y reemplazando i_{qs} por el obtenido de (2.72) se obtiene la siguiente ecuación:

$$T_e = P\left(\frac{\psi_r^2}{R_r}\right)\omega_{sl} \tag{2.74}$$

Para el control RFOC es necesario determinar el ángulo del flujo del rotor, y de acuerdo a la forma de determinar dicho ángulo. La estrategia RFOC puede clasificarse en dos categorías: control vectorial directo de campo rotórico orientado (DRFOC) y el IRFOC. En el caso del DRFOC, dicho ángulo es medido mediante sensores de flujo insertados en el accionamiento electromecánico en la MIAH o estimado a partir de la medida directa de los voltajes y las corrientes, mientras que en el IRFOC el ángulo del flujo del rotor se fuerza a partir de la posición angular del rotor ϕ_r integrada de ω_r y del ángulo de deslizamiento ϕ_{sl} impuesto para garantizar el desacople entre la componente de corriente de estator que regula el flujo y el par. Teniendo en cuenta (2.61), (2.62), (2.63) y (2.72) se tiene:

$$\omega_{sl}^* = \frac{L_m i_{qs}^*}{\tau_r \psi_r^*} \tag{2.75}$$

$$\phi_r = \int \omega_r dt = \int (\omega - \omega_{sl}^*) dt = \phi - \int \omega_{sl}^* dt \tag{2.76}$$

Aunque ambos métodos comparten el mismo principio de funcionamiento, el IRFOC presenta una mayor sencillez, menor dependencia de los parámetros de la MIAH, además de requerir un menor número de sensores, lo que ha hecho que sea la opción más popular del FOC [40].

El diagrama en bloque del RFOC para una MIAH se representa en la **Figura 2.7**, donde se resalta tanto el método de control IRFOC como el DRFOC. El esquema de control es prácticamente idéntico al tradicional trifásico, con la diferencia que se consideran las corrientes en el sub-espacio $(x - y)$. Luego de aplicar la matriz de transformación de

Clarke para obtener los sub-espacios desacoplados, se implementan controladores de corriente. Además se puede apreciar en la **Figura 2.7** el esquema de control, el cual se basa en dos bucles de control externos encargados de la regulación de la velocidad mecánica ω_{rm} y del flujo del rotor ψ_r, así como de una serie de bucles internos de control de corriente (comúnmente se utilizan los controladores proporcional integral (PI)), cuyo número es función del número de fases de la máquina a controlar. Su empleo proporciona al sistema una cierta robustez ante la principal desventaja de este método de control: la necesidad de conocer los parámetros de la MIAH para conseguir una correcta orientación. La salida de los bucles de corriente proporciona los valores de referencia de los voltajes en el sistema de referencia $(d-q)$. Para el control del convertidor, por lo general, estos voltajes se suelen transformar al sistema de referencia de fase, aplicándose posteriormente alguna técnica de modulación.

La estrategia de control RFOC es el caso más estudiado en el campo del control de accionamientos multifásicos y los recientes avances en las investigaciones se centran en el control de corriente [7]. La estrategia IRFOC es la más utilizada [48, 51–53], por ser la más sencilla de aplicar ya que requiere de menor cantidad de sensores.

Como alternativa a los controladores internos de corriente (PI) en el IRFOC se consideran técnicas de control no lineales tales como el SMC [20, 54], control difuso [55], MPC [56], entre otros. La **Figura 2.8** engloba la clasificación de los controladores más

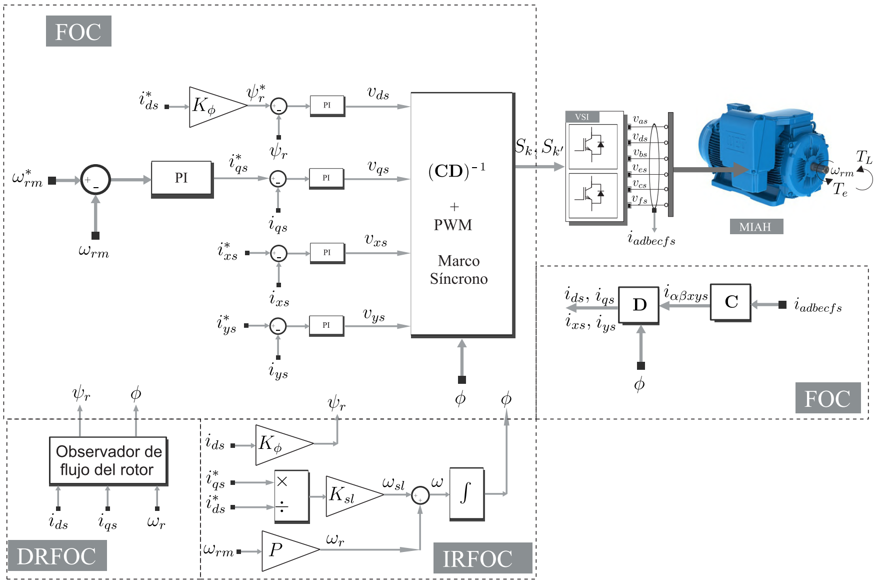

Figura 2.7 Diagrama en bloques del control vectorial para una MIAH.

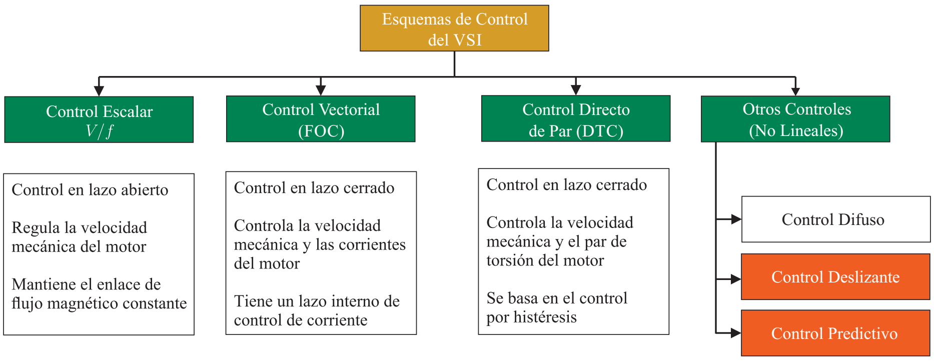

Figura 2.8 Clasificación de los controladores más utilizados aplicado al control de convertidores de potencia hexafásicos.

utilizados aplicado al control de convertidores de potencia hexafásicos. Esta Tesis se centra en el control SMC y MPC, cuyos conceptos y aplicaciones al control de accionamientos eléctricos convencionales y multifásicos serán abordadas detalladamente en las siguientes secciones. Cabe mencionar que ambos controles son utilizados para el control interno de corriente siguiendo el esquema del IRFOC con el bucle externo de velocidad con control PI.

2.2.3 Control Avanzado de Convertidores Hexafásicos

En esta sección se describirán los controladores no lineales aplicados en la actualidad a MIAH conectados a VSI de potencia.

Control Deslizante El control deslizante se asegura que la dinámica deseada del sistema es insensible contra variación de parámetros y perturbaciones externas. Mientras que los límites inferior y superior de los parámetros del modelo y de las perturbaciones existentes, es posible diseñar un control deslizante preciso y con tiempo transitorio finito. Algunos desafíos para el control deslizante son: que en primer lugar, la mayoría de los sistemas están gobernados por un grupo de ecuaciones diferenciales fuertemente correlacionadas y en segundo lugar, existe una cantidad de parámetros desconocidos. Por ello, el control deslizante se encarga de desacoplar y reducir el orden del sistema y presenta una robustez contra perturbaciones y parámetros desconocidos [57, 58].

En la teoría del control deslizante, la trayectoria del sistema está localizada en un espacio de menor dimensión que el del sistema original. El orden de las ecuaciones diferenciales descritas por la moción deslizante es reducida a $(n - m)$, donde n es la dimensión del sistema y m es la dimensión de la entrada de control (esfuerzo de control).

En este caso, el diseño de la unidad de control se reduce a dos sub-problemas más simples: seleccionar una superficie deslizante de orden $(n-m)$ con el fin de asignar las dinámicas deseadas y diseñar una función de control discontinua en el sub-espacio de dimensión n que impone la trayectoria de la superficie deslizante para las variables controladas. Los controladores deslizantes presentan también un fenómeno denominado chattering, que consisten en oscilaciones de amplitud finita y alta frecuencia en la estructura controlada. Este fenómeno puede causar baja precisión en el control, movimiento indeseado de partes móviles e incluso daño irreversible al sistema controlado. El chattering es la mayor obstáculo y desventaja para los SMC [58, 59].

Por otra parte, se encuentra el SMC de segundo orden, el cual es de comportamiento asintótico. En este controlador, la derivada de la superficie deslizante seleccionada es continua, a diferencia del control deslizante de primer orden. Esto aumenta el orden del sistema de manera artificial. Este controlador prioriza la reducción de la derivada del error. Basado en el SMC de segundo orden, el control torcido es definido como una forma especial que asegura convergencia en un tiempo finito. Sin embargo, solo es aplicable para sistemas con una sola entrada. Este algoritmo presenta una entrada de control limitada continuamente dependiendo del tiempo con un efecto discontinuo en la derivada de la entrada de control. Si las condiciones son suficientes, este controlador garantiza convergencia en tiempo finito con error y la derivada del error a cero. Por último se considera el control super torcido (STC), que es una versión mejorada del anterior, donde este no necesita información del tiempo de la derivada del error del sistema, simplificando su diseño pero con las mismas prestaciones [57–59]. La ley de seguimiento del SMC está dado por:

$$\sigma = x^{*} - x \tag{2.77}$$

$$u = -\rho \, sign(\sigma) \tag{2.78}$$

donde u es la señal de control, ρ es la ganancia del SMC y σ es la superficie deslizante definida por el error de seguimiento de la variable a controlar.

La **Figura 2.9** representa la clasificación del control de modo deslizante aplicado a los convertidores de potencia hexafásicos. El SMC Y STC son los propuestos en esta Tesis y serán descritos de manera más detallada en el siguiente capítulo.

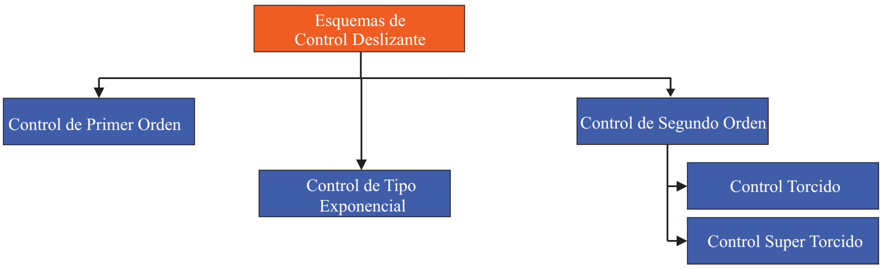

Figura 2.9 Clasificación del control de modo deslizante aplicado a los convertidores de potencia hexafásicos.

En la **Figura 2.10** se representa el diagrama de bloques simplificado del SMC, teniendo en cuenta un sistema con una variable $x[k|k]$, siendo k la muestra correspondiente, y un VSI de dos niveles que se conecta a una MIAH.

Control Predictivo El control predictivo cubre una amplia variedad de controladores que pueden encontrar aplicaciones en el control de convertidores de potencia. Existen varios modelos de control predictivo, tal como se muestra en la **Figura 2.11**, como el control deadbeat, control predictivo basado en histéresis, control predictivo basado en la trayectoria y el MPC [56, 60–62].

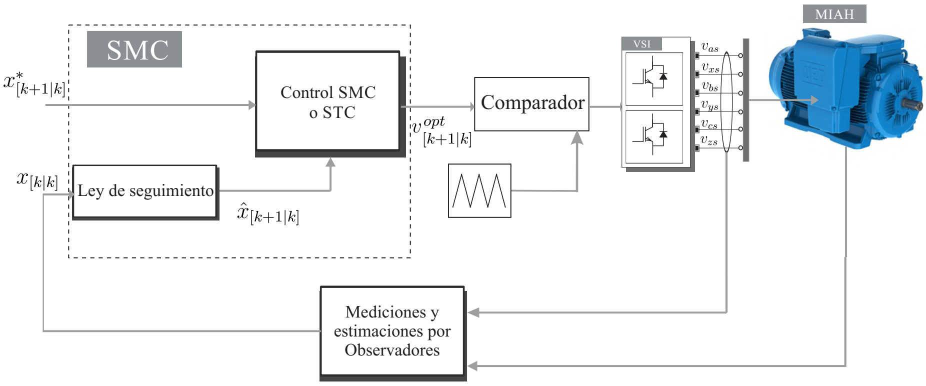

Figura 2.10 Diagrama en bloques del SMC aplicado al control de convertidores de potencia hexafásicos.

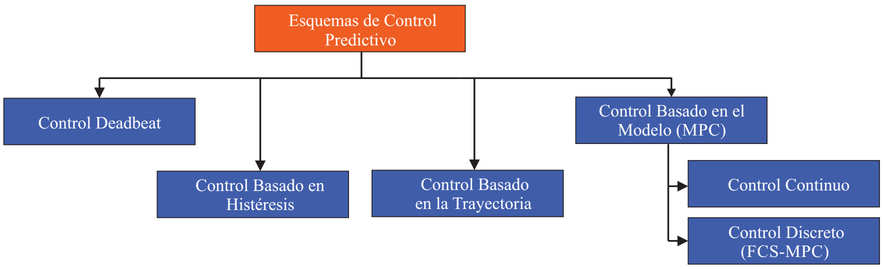

Figura 2.11 Clasificación del control predictivo aplicado a los convertidores de potencia hexafásicos.

La principal característica del MPC se centra en el uso del modelo matemático del sistema dinámico para predecir el comportamiento futuro de las variables del sistema. A partir de la predicción de la variable del sistema a ser controlada, se ejerce un esfuerzo de control basado en la actuación óptima por medio de la minimización de una función de costo. Existes diferentes formas de definir la función de costo dependiendo del sistema a controlar [56,60]. Entre las más utilizadas está la definición de la función de costo como el error cuadrático entre la variable controlada medida y su referencia. Esta estructura tiene numerosas ventajas: los conceptos son muy intuitivos y fáciles de entender; puede ser aplicado para una gran variedad de sistemas; se puede considerar un sistema con múltiples variables; los tiempos muertos pueden ser compensados; la inclusión de fenómenos no lineales al sistema es sencilla; el controlador resultante es fácil de implementar [60,61].

Sin embargo, posee algunas desventajas como el alto costo computacional debido a los cálculos que debe realizar el MPC en comparación a un controlador clásico como el PI. La precisión del modelo matemático influye directamente en el desempeño del MPC, por ello en caso de modificación de parámetros en el tiempo, es requerido un algoritmo que adapte dichos cambios para mantener la eficiencia del MPC [60,61]. Es por eso que el MPC es aplicado a convertidores electrónicos de potencia y se clasifica en dos categorías: control predictivo de estado continuo (CCS-MPC) y FCS-MPC [56,61]. Al tener en cuenta la naturaleza discreta de los VSI, es posible reducir el problema de optimización, permitiendo una implementación en tiempo real. Al considerar el número finito de estados de conmutación del VSI y los procesadores veloces disponibles, el cálculo de la optimización por medio de la evaluación en tiempo real de cada estado de conmutación es factible [56]. Por todo lo antes mencionado, esta Tesis también abordará al FCS-MPC como alternativa al bucle interno de corriente PI basado en el esquema IRFOC, aplicado a la MIAH.

En la **Figura 2.12** se representa el diagrama de bloques simplificado del FCS-MPC, teniendo en cuenta un sistema con una variable $x[k|k]$, siendo k la muestra correspondiente, y un VSI de dos niveles que se conecta a una MIAH. Como objetivo principal, el controlador trata que la variable $\hat{x}[k+1|k]$ obtenida del modelo del FCS-MPC se acerque al valor de referencia $x^*[k+1|k]$, donde el optimizador del FCS-MPC (función de costo) seleccionará un estado de conmutación óptimo que cumpla con la premisa predeterminada.

$$g = \|x^* - \hat{x}\|^2 \tag{2.79}$$

donde g es la función de costo que se calcula por medio del error cuadrático del error de seguimiento de la variable a controlar.

Para la aplicación de la técnica FCS-MPC a una MIAH por medio de un VSI de dos niveles, se considerará a la corriente como variable a controlar, es decir, se aplicará un control predictivo de corriente (PCC) a la MIAH. Primeramente se modelará matemáticamente a la MIAH con una representación en espacio de estado, cuyas variables de estado serán las corrientes de estator y rotor de los sub-espacios $(\alpha - \beta)$ y $(x - y)$. Para ello, se utilizarán las transformaciones de las ecuaciones en el marco de referencia general a los sub-espacios $(\alpha - \beta)$ y $(x - y)$ descritos en (2.31)-(2.35). En la **Figura 2.4** se puede apreciar la conexión entre la MIAH con el VSI de dos niveles a utilizar. Por otro lado, se consideran los voltajes en el estator de los sub-espacios $(\alpha - \beta)$ y $(x - y)$ para la MIAH en la **Figura 2.5**. Estos vectores de voltaje son los posibles estados de conmutación que el PCC debe seleccionar considerando la minimización del error representado en la función de costo. Teniendo en cuenta la principal ventaja del FCS-MPC, que es la limitada cantidad de estados de conmutación, se logra optimizar el algoritmo en términos de costo computacional y simplicidad, evitando el uso de un modulador. Sin embargo, el problema es que solo se puede seleccionar un número finito de estados de conmutación, generando

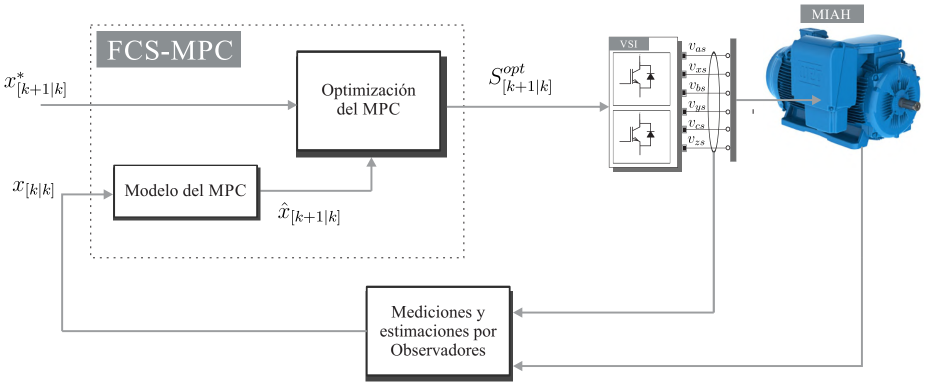

Figura 2.12 Diagrama en bloques del FCS-MPC aplicado al control de convertidores de potencia hexafásicos.

mayor distorsión y grandes rizados de voltaje y corriente para una baja frecuencia de muestreo. La frecuencia de conmutación variable ocasionada por la naturaleza del control predictivo produce un grupo de ármonicos propagado en el espectro de frecuencia, condicionando el rendimiento del sistema en término de calidad de energía [60, 63]. En [62] y los aportes presentados en el siguiente capítulo se proponen nuevos esquemas de FCS-MPC con modulaciones de distintas clases, como PWM, modulación por espacio vectorial (SVM) y aplicación de varios vectores por algún patrón de selección. El control MPC será descrito de manera más detallada en el siguiente capítulo.

2.3 Conclusiones del Capítulo

En el presente capítulo se describieron las ecuaciones que rigen el modelo matemático de la MIAH haciendo especial énfasis en la representación del modelo en tiempo discreto ya que esto forma parte fundamental de las aportaciones de esta Tesis Doctoral. El capítulo ha abordado además la descripción matricial del VSI para lo cual se ha presentado el modelo matemático del convertidor de potencia. El capítulo concluye con una taxonomía de las técnicas de control comúmente aplicadas a las MIAH y presenta una descripción de dos controladores no lineales que conforman el punto focal de las aportaciones de esta Tesis Doctoral. En el siguiente capítulo se abordará una descripción del diseño de los controladores no lineales y sus variantes propuestas en esta Tesis Doctoral.

PARTE II

ANÁLISIS DE CONTENIDO

CAPÍTULO 3

DISCUSIÓN DE LAS APORTACIONES

Las aportaciones de esta Tesis Doctoral se centran en el desarrollo de algoritmos de control no lineal aplicados a una MIAH con bobinados distribuidos. Estas aportaciones se basan en dos técnicas denominadas control predictivo basado en el modelo y control de modo deslizante. A partir de estas técnicas, durante el desarrollo de la Tesis Doctoral se han propuesto variantes con la finalidad de mejorar las prestaciones de los algoritmos de control, las cuales estarán presentadas en este capítulo. El desarrollo de estas variantes han sido abordadas primeramente mediante propuestas teóricas implementadas inicialmente a nivel de simulaciones, utilizando la herramienta computacional MATLAB/Simulink, para posteriormente validar estos resultados teóricos con resultados experimentales obtenidos a partir de la bancada de ensayos. Estas variantes fueron analizadas teniendo en cuenta varias figuras de mérito con el fin de validar su desempeño. Al mismo tiempo, varios análisis de estabilidad se tuvieron en cuenta para las técnicas propuestas. En el presente capítulo se presentarán las aportaciones realizadas en la presente Tesis Doctoral, las cuales por motivo de simplicidad serán divididas en este documento en dos secciones, la primera aborda las aportaciones realizadas al control en modo deslizante y la segunda las aportaciones realizadas al control predictivo.

3.1 Control de Modo Deslizante

Las aportaciones realizadas al control en modo deslizante se sustentan en los siguientes artículos publicados en revistas internacionales arbitradas e indexadas, con factor de impacto definido:

1. Y. Kali, **M. Ayala**, J. Rodas, M. Saad, J. Doval-Gandoy, R. Gregor, K. Benjelloun, ”Current Control of a Six-Phase Induction Machine Drive based on Discrete-Time Sliding Mode with Time Delay Estimation,” Energies, vol. 12, no, 1, 2019, DOI 10.3390/en12010170. (Impact Factor 2.707). [Cont-1]

Considerando los controladores no lineales, el SMC es uno de los más utilizados y ha recibido atención especial de la comunidad de automatización debido a tres propiedades muy valiosas, robustez contra incertidumbres, simplicidad en el diseño y convergencia en tiempo finito [59, 64]. Este método obliga a las variables de estado del sistema a alcanzar, en tiempo finito, la superficie deslizante seleccionada por el usuario (*superficie conmutada*) incluso en la presencia de incertidumbres usando entradas discontinuas [59]. Para asegurar un alto desempeño, las ganancias conmutadas deben ser seleccionadas lo más grande posible para rechazar el efecto de incertidumbres limitadas. Sin embargo, esta elección causa un gran defecto del SMC, conocido como el fenómeno chattering [65, 66]. Este fenómeno tiene un impacto indeseado en los actuadores del sistema. Puede llevar al deterioro del sistema controlado y/o a la inestabilidad. Una vez que el problema fue identificado, muchos trabajos intentaron resolverlo. Alguno de esos trabajos son los siguientes:

- La sustitución de una función signo discontinua para sistemas lienales [67]. Este método es el SMC basado en una capa limitada. Esta proposición permite la reducción del fenómeno chattering. Sin embargo, la convergencia en tiempo finito ya no es garantizada. Esto es muy requerido cuando el tiempo de convergencia crítico es requerido.

- Observador basado en SMC [68,69]. El problema de diseñar un controlador no lineal robusto es reducido a diseñar un observador robusto no lineal. En otras palabras, si las incertidumbres definidas no son estimadas de manera precisa, el desempeño obtenido no será satisfactorio.

- Control de modo deslizante de alto orden (HOSM) [70–72]. La idea consiste en hacer al término del control conmutado en un control derivativo, que hace que la entrada de control sea continua. Este método da mejores desempeños ya que permite mayor precision y reduce el fenómeno chattering. Sin embargo, este enfoque requiere cierta información, como la primera derivada de la superficie deslizante seleccionada que no necesariamente están disponibles en mediciones complicando la implementación.

Recientemente, un método interesante que consiste en combinar el SMC con estimador con tiempo de retardo (TDE) para sistemas no lineales ha sido desarrollado [73, 74]. El método propuesto ha sido probado de manera exitorsa en un robot manipulador. La idea básica es estimar las incertidumbres definidas que se asumen ser Lipschitz usando estados anteriores y la información de la entrada. Entonces, los términos estimados son añadidos al controlador equivalente con el fin de incluir una pequeña ganancia conmutada en el controlador discontinuo.

El modelo en tiempo discreto del sistema representado en espacio de estados es modelado por las siguientes ecuaciones [75]:

$$\mathbf{X}(k+1) = \mathbf{A}\,\mathbf{X}(k) + \mathbf{B}\,\mathbf{u}(k) + \mathbf{n}(k) \tag{3.1}$$

$$\mathbf{Y}(k) = \mathbf{E}\,\mathbf{X}(k) \tag{3.2}$$

siendo k la muestra actual. En las ecuaciones recientes, las corrientes de estator y rotor son el vector de estado:

$$\mathbf{X}(k) = [i_{s\alpha}(k),\, i_{s\beta}(k),\, i_{sx}(k),\, i_{sy}(k), i_{r\alpha}(k),\, i_{r\beta}(k)]^T \tag{3.3}$$

mientras que los voltajes de estator representan al vector de entrada:

$$\mathbf{u}(k) = [u_{s\alpha}(k),\, u_{s\beta}(k),\, u_{sx}(k),\, u_{sy}(k)]^T \tag{3.4}$$

y las corrientes de estator como el vector de salida:

$$\mathbf{Y}(k) = [i_{s\alpha}(k),\, i_{s\beta}(k),\, i_{sx}(k),\, i_{sy}(k)]^T \tag{3.5}$$

Los voltajes de estator tienen una naturaleza discreta debido al modelo del VSI y su relación entre ellos es representado por:

$$V_{\mathrm{dc}}\,\mathbf{C}\,\mathbf{M} = [u_{s\alpha}(k),\, u_{s\beta}(k),\, u_{sx}(k),\, u_{sy}(k)]^T \tag{3.6}$$

donde V_{dc} es el DC-link y el modelo del VSI es el basado en (2.55):

$$\mathbf{M} = \frac{1}{3}\begin{bmatrix} 2 & 0 & -1 & 0 & -1 & 0 \\ 0 & 2 & 0 & -1 & 0 & -1 \\ -1 & 0 & 2 & 0 & -1 & 0 \\ 0 & -1 & 0 & 2 & 0 & -1 \\ -1 & 0 & -1 & 0 & 2 & 0 \\ 0 & -1 & 0 & -1 & 0 & 2 \end{bmatrix} \mathbf{S}^T \tag{3.7}$$

donde $\mathbf{S} = [S_a,\ S_d,\ S_b,\ S_e,\ S_c,\ S_f]$ es el vector de las activaciones con $S_i \in \{0,\ 1\}$.

3.1.1 Lazo de Control Externo de Velocidad

Un controlador PI de dos grados de libertad con una etapa de saturación es introducido en [76]. Este controlador es utilizado en el lazo externo de velocidad, basado en el método IRFOC. En este lazo, la salida del regulador PI es usada como la referencia de corriente dinámica $i_{sq}^*(k)$. Además, la frecuencia de deslizamiento $\omega_{sl}(k)$ es obtenida desde las referencias de corriente $i_{sd}^*(k), i_{sq}^*(k)$ en el sub-espacio dinámico y los parámetros eléctricos de la MIAH, como en la **Figura 3.1**. La siguiente ecuación en el plano s representa al controlador de velocidad.

$$i_{sq}^* = K_p e + \frac{K_i e}{s} - \frac{K_i \omega^*}{s+\alpha} \tag{3.8}$$

donde K_p, K_i y α son parámetros del controlador basados en el diseño en [76], e es el error de la velocidad de referencia y la medida ω^* es la velocidad de referencia. El lazo externo de velocidad es usado con todos los controladores de corriente propuestos en esta Tesis Doctoral.

3.1.2 Lazo Interno de Control de Corriente

El lazo interno tiene como fin el control de las corrientes estatóricas. Para este propósito, el control de modo deslizante discreto (DSMC) con TDE serán desarrollados para asegurar la convergencia en tiempo finito de las corrientes estatóricas en los sub-espacios $(\alpha - \beta)$ y $(x-y)$ a sus respectivas referencias con alta precisión incluso si algunas variables de estado no son medibles (por ejemplo: corrientes rotóricas) y en la presencia de incertidumbres. En primer lugar, el sistema discreto, descrito en (3.1), se descompone en tres sub-sistemas

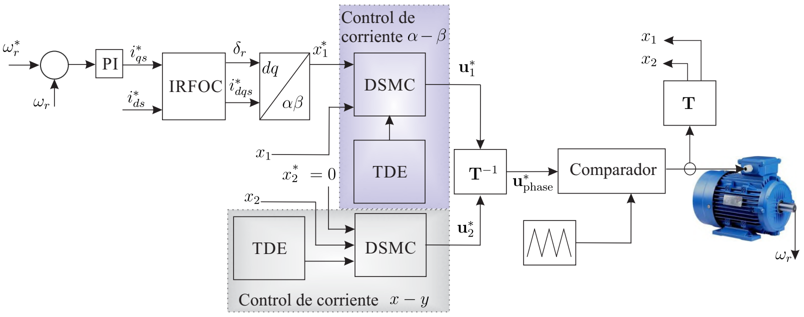

Figura 3.1 Diagrama en bloques del sistema basado en IRFOC y DSMC con TDE.

como sigue:

$$\mathbf{x}_1(k+1) = \mathbf{A}_1\,\mathbf{x}_1(k) + \overline{\mathbf{A}}_1\,\mathbf{x}_3(k) + \mathbf{B}_1\,\mathbf{u}_1(k) + \eta_1(k) \tag{3.9}$$

$$\mathbf{x}_2(k+1) = \mathbf{A}_2\,\mathbf{x}_2(k) + \mathbf{B}_2\,\mathbf{u}_2(k) + \eta_2(k) \tag{3.10}$$

$$\mathbf{x}_3(k+1) = \mathbf{A}_3\,\mathbf{x}_1(k) + \overline{\mathbf{A}}_3\,\mathbf{x}_3(k) + \mathbf{B}_3\,\mathbf{u}_1(k) + \eta_3(k) \tag{3.11}$$

donde las corrientes estatóricas y rotóricas son parte del vector de estado:

$$\mathbf{x}_1(k) = \left[i_{s\alpha}(k),\, i_{s\beta}(k)\right]^T \tag{3.12}$$

$$\mathbf{x}_2(k) = \left[i_{sx}(k),\, i_{sy}(k)\right]^T \tag{3.13}$$

$$\mathbf{x}_3(k) = \left[i_{r\alpha}(k),\, i_{r\beta}(k)\right]^T \tag{3.14}$$

mientras que los voltajes de estator representan el vector de entrada:

$$\mathbf{u}_1(k) = \left[u_{s\alpha}(k),\, u_{s\beta}(k)\right]^T \tag{3.15}$$

$$\mathbf{u}_2(k) = \left[u_{sx}(k),\, u_{sy}(k)\right]^T \tag{3.16}$$

y $\eta_1(k) = [n_1(k),\, n_2(k)]^T$, $\eta_2(k) = [n_3(k),\, n_4(k)]^T$ y $\eta_3(k) = [n_5(k),\, n_6(k)]^T$ denota los vectores de incertidumbre. Las matrices $\mathbf{A}_1$, $\overline{\mathbf{A}}_1$, $\mathbf{A}_2$, $\mathbf{A}_3$, $\overline{\mathbf{A}}_3$, $\mathbf{B}_1$, $\mathbf{B}_2$ y $\mathbf{B}_3$ son definidas como siguen:

$$\mathbf{A}_1 = \begin{bmatrix} a_{11} & a_{12} \\ a_{21} & a_{22} \end{bmatrix},\ \mathbf{A}_2 = \begin{bmatrix} a_{33} & 0 \\ 0 & a_{44} \end{bmatrix},\ \mathbf{A}_3 = \begin{bmatrix} a_{51} & a_{52} \\ a_{61} & a_{62} \end{bmatrix},\ \overline{\mathbf{A}}_1 = \begin{bmatrix} a_{15} & a_{16} \\ a_{25} & a_{26} \end{bmatrix}$$

$$\overline{\mathbf{A}}_3 = \begin{bmatrix} a_{55} & a_{56} \\ a_{65} & a_{66} \end{bmatrix}, \mathbf{B}_1 = \begin{bmatrix} b_1 & 0 \\ 0 & b_1 \end{bmatrix}, \mathbf{B}_2 = \begin{bmatrix} b_2 & 0 \\ 0 & b_2 \end{bmatrix}, \mathbf{B}_3 = \begin{bmatrix} b_3 & 0 \\ 0 & b_3 \end{bmatrix}$$

donde:

$$\begin{array}{ll} a_{11} = a_{22} = 1 - T_s\, c_2\, R_s & a_{12} = -a_{21} = T_s\, c_4 L_m\, \omega_{r(k)} \\ a_{15} = a_{26} = T_s\, c_4\, R_r & a_{16} = -a_{25} = T_s\, c_4 L_r\, \omega_{r(k)} \\ a_{33} = a_{44} = 1 - T_s\, c_3\, R_s & a_{52} = -a_{61} = -T_s\, c_5\, L_m\, \omega_{r(k)} \\ a_{55} = a_{66} = 1 - T_s\, c_5\, R_r & a_{51} = a_{62} = T_s\, c_4\, R_s \\ a_{56} = -a_{65} = -c_5\, \omega_{r(k)}\, T_s\, L_r & b_1 = T_s\, c_2 \\ b_2 = T_s\, c_3 & b_3 = -T_s\, c_4 \end{array}$$

siendo T_s el tiempo de muestreo y c_1 a c_5 son definidos como: $c_1 = L_s L_r - L_m^2$, $c_2 = \frac{L_r}{c_1}$, $c_3 = \frac{1}{L_{ls}}$ $c_4 = \frac{L_m}{c_1}$ $c_5 = \frac{L_s}{c_1}$. Los parámetros eléctricos del sistema son R_s, R_r, $L_r = L_{lr} + L_m$, $L_s = L_{ls} + L_m$ y L_m.

Control de las Corrientes Estatóricas en el Sub-espacio ($\alpha - \beta$) Para lograr el objetivo de control, se asume que $\mathbf{x}_1^*(k) = i_{s\phi}^*(k) = \left[i_{s\alpha}^*(k), i_{s\beta}^*(k) \right]^T$ es el vector de las referencias deseadas con $\phi \in \{\alpha, \beta\}$ y $\mathbf{e}_\phi(k) = \mathbf{x}_1(k) - \mathbf{x}_1^*(k) = i_{s\phi}(k) - i_{s\phi}^*(k)$ es el vector del error de seguimiento. Como el grado relativo de las corrientes estatóricas en el sub-espacio ($\alpha - \beta$) es igual a 1, entonces, la superficie deslizante [59] es seleccionada como el error de la variable como sigue:

$$\sigma(k) = \mathbf{e}_\phi(k) \tag{3.17}$$

En el diseño de DSMC, las siguientes condiciones deben ser satisfechas para lograr un movimiento ideal deslizante:

$$\sigma(k) = 0, \qquad \sigma(k+1) = 0 \tag{3.18}$$

donde $\sigma(k+1)$ se computa como:

$$\begin{aligned} \sigma(k+1) &= \mathbf{e}_\phi(k+1) = \mathbf{x}_1(k+1) - \mathbf{x}_1^*(k+1) \\ &= \mathbf{A}_1\, \mathbf{x}_1(k) + \overline{\mathbf{A}}_1\, \mathbf{x}_3(k) + \mathbf{B}_1\, \mathbf{u}_1(k) + \eta_1(k) - \mathbf{x}_1^*(k+1) \end{aligned} \tag{3.19}$$

El control obtenido al colocar $\sigma(k+1) = 0$ no asegura la robustez y la convergencia en tiempo finito. Por estas razones, la siguiente ley de seguimiento es seleccionada:

$$\sigma(k+1) = \Lambda\,\sigma(k) - T_s\,\rho\,\mathrm{sign}(\sigma(k)) \tag{3.20}$$

donde $\Lambda = \mathrm{diag}(\lambda_1, \lambda_2)$ con $0 < \lambda_i < 1$ for $i = 1, 2$, $\rho \in R^{2\times 2}$ es una matriz diagonal positiva y $\mathrm{sign}(\sigma(k)) = [\mathrm{sign}(\sigma_1(k)), \mathrm{sign}(\sigma_2(k))]^T$ con:

$$\mathrm{sign}(\sigma_i(k)) = \begin{cases} 1, & \text{if } \sigma_i(k) > 0 \\ 0, & \text{if } \sigma_i(k) = 0 \\ -1, & \text{if } \sigma_i(k) < 0 \end{cases} \tag{3.21}$$

Entonces, al usar (3.19) y (3.20), la ley del DSMC para las corrientes estatóricas en el sub-espacio $(\alpha - \beta)$ es obtenido por:

$$\begin{aligned} \mathbf{u}_1(k) = -\mathbf{B}_1^{-1} \Big[& \mathbf{A}_1\,\mathbf{x}_1(k) + \overline{\mathbf{A}}_1\,\mathbf{x}_3(k) + \eta_1(k) - \mathbf{x}_1^*(k+1) \\ & -\Lambda\,\sigma(k) + T_s\,\rho\,\mathrm{sign}(\sigma(k)) \Big] \end{aligned} \tag{3.22}$$

El desempeño de control podría no ser satisfactorio ya que la ecuación anterior está en términos de las corrientes rotóricas $\mathbf{x}_3(k)$ que no son medibles y el vector de incertidumbre $\eta_1(k)$. Asumiendo que $\mathbf{x}_3(k)$ y $\eta_1(k)$ no fluctúa enormemente entre dos tiempos de muestreo, el método TDE [71, 77] puede ser usado para obtener una aproximación como:

$$\begin{aligned} \overline{\mathbf{A}}_1\,\hat{\mathbf{x}}_3(k) + \hat{\eta}_1(k) &\cong \overline{\mathbf{A}}_1\,\mathbf{x}_3(k-1) + \eta_1(k-1) \\ &= \mathbf{x}_1(k) - \mathbf{A}_1\,\mathbf{x}_1(k-1) - \mathbf{B}_1\,\mathbf{u}_1(k-1) \end{aligned} \tag{3.23}$$

Definición 3.1 *Para un sistema discreto, un modo quasi-deslizante es considerado para la trayectoria en la cercanía de la superficie deslizante, tal que $|\sigma(k)| < \varepsilon$, y donde $\varepsilon > 0$ es el ancho de banda del modo quasi-deslizante. Con el fin de asegurar una convergencia del modo quasi-deslizante, las condiciones dadas en [71, 78] que son necesarias y suficientes deben ser verificadas para cada superficie deslizante, por ejemplo:*

$$\begin{cases} \sigma_i(k) > \varepsilon & \Rightarrow -\varepsilon \le \sigma_i(k+1) < \sigma_i(k) \\ \sigma_i(k) < -\varepsilon & \Rightarrow \sigma_i(k) < \sigma_i(k+1) \le \varepsilon \\ |\sigma_i(k)| \le \varepsilon & \Rightarrow |\sigma_i(k+1)| \le \varepsilon \end{cases} \tag{3.24}$$

Teorema 3.1 *Si la siguiente condición es satisfecha para $i = 1, 2$:*

$$\rho_i > \frac{1}{T_s}\delta_i. \tag{3.25}$$

Entonces, el método DSMC con TDE para las corrientes estatóricas en el sub-espacio $(\alpha-\beta)$ (3.9) *son dadas por:*

$$\begin{aligned}\mathbf{u}_1(k) = -\mathbf{B}_1^{-1}\Big[&\mathbf{A}_1\,\mathbf{x}_1(k) + \overline{\mathbf{A}}_1\,\hat{\mathbf{x}}_3(k) + \hat{\eta}_1(k) - \mathbf{x}_1^*(k+1)\\ &-\Lambda\,\sigma(k) - T_s\,\rho\,\mathrm{sign}(\sigma(k))\Big]\end{aligned} \tag{3.26}$$

asegura un modo quasi-deslizante. Además, cada trayectoria del sistema alcanzará sus correspondientes superficies deslizantes (3.17) *como máximo* $k_i^{'}+1$ *pasos, donde para* $i = 1, 2$*:*

$$k_i^{'} = \frac{|\sigma_i(0)|}{T_s\,\rho_i - \delta_i} \tag{3.27}$$

Sustituyendo el controlador obtenido en tiempo discreto (3.26) a la ecuación (3.19) lleva a:

$$\sigma(k+1) = \Lambda\,\sigma(k) + \mathbf{E}(k) - T_s\,\rho\,\mathrm{sign}(\sigma(k)) \tag{3.28}$$

donde $\mathbf{E}(k) = \overline{\mathbf{A}}_1\,(x_3(k) - \hat{x}_3(k)) + (\eta_1(k) - \hat{\eta}_1(k))$ es el error del TDE limitado tal que para $i = 1, 2$:

$$|E_i(k)| < \delta_i \tag{3.29}$$

Ahora, se elige $\varepsilon = T_s\,\rho_i + \delta_i$. Por lo tanto, la ecuación (3.24) puede ser escrita como:

$$\begin{aligned}&\sigma_i(k) > T_s\,\rho_i + \delta_i \Rightarrow -T_s\,\rho_i - \delta_i \le \sigma_i(k+1) < \sigma_i(k)\\ &\sigma_i(k) < -T_s\,\rho_i - \delta_i \Rightarrow \sigma_i(k) < \sigma_i(k+1) \le T_s\,\rho_i + \delta_i\\ &|\sigma_i(k)| \le T_s\,\rho_i + \delta_i \Rightarrow |\sigma_i(k+1)| \le T_s\,\rho_i + \delta_i.\end{aligned} \tag{3.30}$$

1. Considere el primer caso donde $\sigma_i(k) > T_s\,\rho_i + \delta_i$, then $\sigma_i(k) > 0$, $\mathrm{sign}(\sigma_i(k)) = 1$ y:

   $$\begin{aligned}&\sigma_i(k+1) = \lambda_i\,\sigma_i(k) + E_i(k) - T_s\,\rho_i\\ &\sigma_i(k+1) - \sigma_i(k) = E_i(k) + (\lambda_i - 1)\,\sigma_i(k) - T_s\,\rho_i.\end{aligned} \tag{3.31}$$

   Si la condición en (3.25) es satisfecha, entonces $\sigma_i(k+1) - \sigma_i(k) < 0 \Rightarrow \sigma_i(k+1) < \sigma_i(k)$.

   Además, $-T_s\,\rho_i - \delta_i \le \sigma_i(k+1)$ puede ser escrita como:

   $$\lambda_i\,\sigma_i(k) + E_i(k) - T_s\,\rho_i \ge -T_s\,\rho_i - \delta_i. \tag{3.32}$$

Por lo tanto:

$$\sigma_i(k) \geq \frac{1}{\lambda_i}\left(E_i(k) - \delta_i\right) \tag{3.33}$$

ya que $\sigma_i(k) > 0$ y $(E_i(k) - \delta_i) < 0$, entonces, la desigualdad arriba siempre es verdadera.

2. Considere el segundo caso donde $\sigma_i(k) < -T_s\,\rho_i - \delta_i$. Esto implica $\sigma_i(k) < 0$ y $\operatorname{sign}(\sigma_i(k)) = -1$. Entonces, se vuelve a escribir $\sigma_i(k) < \sigma_i(k+1)$ como sigue:

$$\begin{aligned} \sigma_i(k) &< \lambda_i\,\sigma_i(k) + E_i(k) + T_s\,\rho_i \\ (1-\lambda_i)\,\sigma_i(k) &< E_i(k) + T_s\,\rho_i \end{aligned} \tag{3.34}$$

el cual siempre es verdad ya que $\rho_i > \frac{1}{T_s}\delta_i$.

Además, $\sigma_i(k+1) < T_s\,\rho_i + \delta_i$ puede ser reescrita como:

$$\lambda_i\,\sigma_i(k) + E_i(k) + T_s\,\rho_i < T_s\,\rho_i + \delta_i. \tag{3.35}$$

Ya que $\sigma_i(k) < 0$ y $\delta_i > E_i(k)$. Entonces, es obvio que la desigualdad en (3.9) es siempre verdadera.

3. Considere el tercer caso donde $|\sigma_i(k)| \leq \varepsilon$, entonces:

   a. si $\sigma_i(k) > 0$, entonces $|\sigma_i(k)| \leq \varepsilon$ se vuelve:

$$0 < \sigma_i(k) < \varepsilon. \tag{3.36}$$

   Multiplicando (3.36) por λ_i y sumando $E_i(k) - T_s\,\rho_i$ a tods las partes lleva a:

$$\begin{gathered} E_i(k) - T_s\,\rho_i < \sigma_i(k+1) < E_i(k) - T_s\,\rho_i + \lambda_i\,\varepsilon \\ -\varepsilon < \sigma_i(k+1) < \varepsilon \\ |\sigma_i(k+1)| \leq \varepsilon \end{gathered} \tag{3.37}$$

   b. si $\sigma_i(k) < 0$, entonces $|\sigma_i(k)| \leq \varepsilon$ se vuelve:

$$-\varepsilon < \sigma_i(k) < 0. \tag{3.38}$$

   Nuevamente, multiplicando (3.38) por λ_i y sumando $E_i(k) + T_s\,\rho_i$ a todas las partes da:

$$\begin{aligned} E_i(k) + T_s\,\rho_i - \lambda_i\,\varepsilon < \sigma_i(k+1) &< E_i(k) + T_s\,\rho_i \\ -\varepsilon < \sigma_i(k+1) &< \varepsilon \\ |\sigma_i(k+1)| &\leq \varepsilon \end{aligned} \tag{3.39}$$

Por lo tanto:

$$|\sigma_i(k+1)| < \varepsilon = T_s\,\rho_i + \delta_i. \tag{3.40}$$

Ya que las condiciones en (3.30) son encontradas, la existencia de un modo quasi-deslizante ha sido establecido. Consecuentemente, el método propuesto DSMC con TDE en (3.26) es estable.

Ahora, se demostrará por contradicción considerando en (3.28) que la ecuación (3.27) es verdadera. Para esta parte, se asume que $\sigma_i(0) \neq 0$ y $\mathrm{sign}(\sigma_i(0)) = \mathrm{sign}(\sigma_i(1)) = \cdots = \mathrm{sign}(\sigma_i(k^{'}+1))$.

1. Considere el primer caso donde $\sigma_i(0) > 0$ y $\sigma_i(m) > 0$ para todo $m \leq (k_i^{'}+1)$. Entonces:

$$\begin{aligned} \sigma_i(1) &= \lambda_i\,\sigma_i(0) + E_i(0) - T_s\,\rho_i \\ &\leq \sigma_i(0) + E_i(0) - T_s\,\rho_i \\ \sigma_i(2) &\leq \sigma_i(1) + E_i(1) - T_s\,\rho_i \\ &\leq \sigma_i(0) + E_i(0) + E_i(1) - 2\,T_s\,\rho_i \\ &\vdots \\ \sigma_i(m) &\leq \sigma_i(m-1) + E_i(m-1) - T_s\rho_i \\ &\leq \sigma_i(0) + \sum_{j=0}^{m-1} E_i(j) - m\,T_s\,\rho_i \\ &\leq |\sigma_i(0)| + m\left[\delta_i - T_s\,\rho_i\right]. \end{aligned} \tag{3.41}$$

Por lo tanto, es obvio que $k_i^{'}$ asegura:

$$|\sigma_i(0)| + k_i^{'}\left[\delta_i - T_s\,\rho_i\right] = 0. \tag{3.42}$$

Luego:

$$\begin{aligned}\sigma_i(k_i^{'}+1) &\leq |\sigma_i(0)| + (k_i^{'}+1)\,[\delta_i - T_s\,\rho_i] \\ &< |\sigma_i(0)| + k_i^{'}\,[\delta_i - T_s\,\rho_i] = 0\end{aligned} \tag{3.43}$$

el cual es contradictorio por le hecho que $\sigma_i(m) > 0,\ \forall\, m \leq (k_i^{'}+1)$.

2. Considere el segundo caso donde $\sigma_i(0) < 0$ y $\sigma_i(m) < 0$ para todo $m \leq (k_i^{'}+1)$. Entonces:

$$\begin{aligned}\sigma_i(1) &= \lambda_i\,\sigma_i(0) + E_i(0) + T_s\,\rho_i \\ &\geq \sigma_i(0) + E_i(0) + T_s\,\rho_i \\ \sigma_i(2) &\geq \sigma_i(1) + E_i(1) + T_s\,\rho_i \\ &\geq \sigma_i(0) + E_i(0) + E_i(1) + 2\,T_s\,\rho_i \\ &\vdots \\ \sigma_i(m) &\geq \sigma_i(m-1) + E_i(m-1) + T_s\,\rho_i \\ &\geq \sigma_i(0) + \sum_{j=0}^{m-1} E_i(j) + m\,T_s\,\rho_i \\ &\geq -|\sigma_i(0)| + m\,[T_s\,\rho_i - \delta_i]\end{aligned} \tag{3.44}$$

Una vez más, es obvio que $k_i^{'}$ verifica que:

$$-|\sigma_i(0)| + k_i^{'}\,[T_s\,\rho_i - \delta_i] = 0. \tag{3.45}$$

Luego sigue:

$$\begin{aligned}\sigma_i(k_i^{'}+1) &\geq -|\sigma_i(0)| + (k_i^{'}+1)\,[T_s\,\rho_i - \delta_i] \\ &> -|\sigma_i(0)| + k_i^{'}\,[T_s\,\rho_i - \delta_i] = 0\end{aligned} \tag{3.46}$$

el cual es contradictorio por el hecho que $\sigma_i(m) < 0,\ \forall\, m \leq (k_i^{'}+1)$.

Esto concluye la prueba del Teorema 3.1.

Control de las Corrientes Estatóricas en el Sub-espacio ($x - y$) En esta sección, la misma metodología utilizada anteriormente en las corrientes estatóricas $\mathbf{x}_1(k)$ será adoptado para el control de las corrientes en el sub-espacio $(x-y)$. En este caso, la superficie deslizante es seleccionada como sigue:

$$\sigma^{"}(k) = \mathbf{e}_{s_{xy}}(k) = \mathbf{x}_2(k) - \mathbf{x}_2^{*}(k) \tag{3.47}$$

donde $\mathbf{x}_2^*(k) = [i_{sx}^*(k),\ i_{sy}^*(k)]^T$ es la corriente $(x-y)$ deseada y $\mathbf{e}_{s_{xy}}(k)$ denota el error de seguimiento variable. Por lo tanto, $\sigma^{"}(k+1)$ es computado como sigue:

$$\begin{aligned}\sigma^{"}(k+1) &= \mathbf{e}_{s_{xy}}(k+1) = \mathbf{x}_2(k+1) - \mathbf{x}_2^*(k+1) \\ &= \mathbf{A}_2\,\mathbf{x}_2(k) + \mathbf{B}_2\,\mathbf{u}_2(k) + \eta_2(k) - \mathbf{x}_2^*(k+1).\end{aligned} \tag{3.48}$$

El controlador en tiempo discreto es obtenido al resolver lo siguiente:

$$\sigma^{"}(k+1) = \Gamma\,\sigma^{"}(k) - T_s\,\varrho\,\mathrm{sign}(\sigma^{"}(k)) \tag{3.49}$$

donde $\Gamma = \mathrm{diag}(\Gamma_1, \Gamma_2)$ with $0 < \Gamma_i < 1$ for $i = 1, 2$, $\varrho \in R^{2\times 2}$ es una matriz diagonal positiva y $\mathrm{sign}(\sigma^{"}(k)) = \left[\mathrm{sign}(\sigma_1^{"}(k)), \mathrm{sign}(\sigma_2^{"}(k))\right]^T$ y al sustituir el vector de incertidumbre $\eta_2(k)$ por la estimación del método TDE:

$$\begin{aligned}\hat{\eta}_2(k) &\cong \eta_2(k-1) \\ &= \mathbf{x}_2(k) - \mathbf{A}_2\,\mathbf{x}_2(k-1) - \mathbf{B}_2\,\mathbf{u}_2(k-1).\end{aligned} \tag{3.50}$$

Teorema 3.2 *Si las ganancias del controlador son elegidas para* $i = 1, 2$ *como sigue:*

$$\varrho_i > \frac{1}{T_s}\delta_i^{"} \tag{3.51}$$

con $\delta_i^{"} > 0$ *es el límite superior del error del TDE* $E^{"}(k) = \eta_2(k) - \hat{\eta}_2(k)$*. Entonces, el siguiente método DSMC con TDE para las corrientes estatóricas en el sub-espacio* $(x-y)$ (3.10) *asegura un movimiento quasi-deslizante:*

$$\mathbf{u}_2(k) = -\mathbf{B}_2^{-1}\left[\mathbf{A}_2\,\mathbf{x}_2(k) + \hat{\eta}_2(k) - \mathbf{x}_2^*(k+1) - \Gamma\,\sigma^{"}(k) + T_s\,\varrho\,\mathrm{sign}(\sigma^{"}(k))\right]. \tag{3.52}$$

El análisis de estabilidad es similar al descrito para las corrientes estatóricas en el sub-espacio $(\alpha - \beta)$.

3.1.3 Análisis Experimental de las Aportaciones al SMC

La técnica propuesta DSMC es probada en una bancada experimental para validar su desempeño. Esta bancada consiste en una MIAH alimentada por dos VSI trifásicos convencionaels, siendo equivalente a un VSI hexafásico, usando una fuente DC contante como fuente de energía. El VSI hexafásico es controlador por una plataforma de tiempo real para prototipo denominada dSPACE MABXII DS1401, con Simulink version 8.2. Los resultados obtenidos son capturados y procesados usando un algoritmo de MATLAB versión R2013b. Los parámetros de la MIAH fueron obtenidos utilizando métodos convencionales en el tiempo con AC y pruebas con alimentación por VSI [79, 80]. Estos resultados son listados en la **Tabla 3.1**. Cabe mencionar que la misma bancada, con las mismas condiciones, fue utilizada para comprobar el desempeño de los aportes presentados más adelante.

Las pruebas experimentales fueron realizadas con sensores de corriente LA 55-P s, los cuales tienen un ancho de banda de frecuencias desde DC hasta 200 kHz. Las mediciones de corriente fueron convertidas a digital utilizando un conversor Analógico/Digital (A/D) de 16 bits. La posición mecánica de la MIAH fue obtenida mediante un encoder incremental con 1024 ppr y la velocidad rotórica es estimada de esas mediciones. Finalmente un freno por corrientes parásitas de 5 HP es usado para introducir una carga mecánica a la MIAH. Un diagrama en bloques de la bancada experimental es mostrado en la **Figura 3.2**, incluyendo algunas fotografías del equipamiento.

El desempeño de la técnica DSMC es analizada en condiciones transitorias y de régimen permanente. Los resultados experimentales analizan el desempeño del controlador en términos de error cuadrático medio (MSE) entre la las corrientes estatóricas de referencia y medidas en los sub-espacios $(\alpha-\beta)$, $(x-y)$ y $(d-q)$. El RMS de las corrientes en el sub-espacio $(d-q)$ es usado para calcular los correspondientes factor de forma (FF). Además, la distorsion ármonica total (THD) de las corrientes $(\alpha-\beta)$ son obtenidas así como el MSE entre la velocidad rotórica de referencia y medida para la evaluación de la técnica. El MSE es definido como:

$$\mathrm{MSE}(i_{s\Phi}) = \sqrt{\frac{1}{N}\sum_{k=1}^{N}(i_{s\Phi}(k) - i_{s\Phi}^{*}(k))^2} \qquad (3.53)$$

donde N es el número de muestras analizadas, $i_{s\Phi}^{*}$ las corrientes estatóricas de referencia, $i_{s\Phi}$ las corrientes estatóricas medidas y $\Phi \in \{\alpha,\ \beta,\ x,\ y,\ d,\ q\}$. Por otro lado, el THD es calculado como sigue:

Tabla 3.1 Parámetros de la MIAH.

Parámetro	Valor	Parámetro	Valor	Parámetro	Valor
R_r (Ω)	6.9	L_r (mH)	626.8	P_w (kW)	2
R_s (Ω)	6.7	ω_{nom} (rpm)	2540	J_i (kg.m^2)	0.07
L_{ls} (mH)	5.3	L_s (mH)	654.4	B_i (kg.m^2/s)	0.0004
L_m (mH)	614	P	1	V_{dc} (V)	400

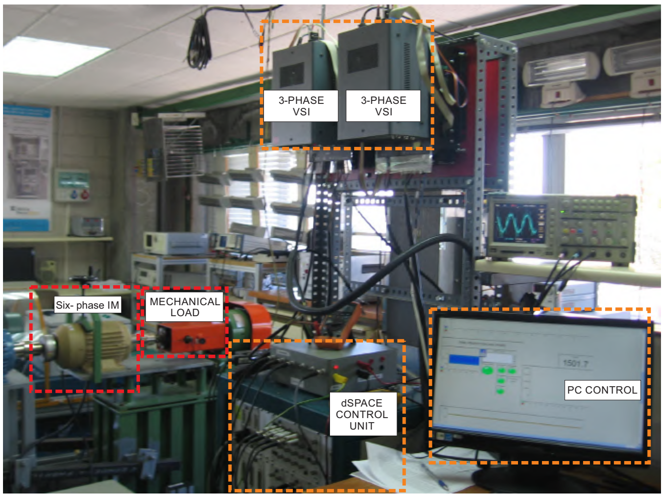

Figura 3.2 Diagrama en bloques de la bancada experimental incluyendo la MIAH, el VSI hexafásico, el dSPACE y la carga mecánica.

$$\mathrm{THD}(i_s) = \sqrt{\frac{1}{i_{s1}^2}\sum_{j=2}^{N}(i_{sj})^2} \tag{3.54}$$

donde i_{s1} son las corrientes fundamentales estatóricas y i_{sj} son las corrientes harmónicas estatóricas. Por último, el FF es computado como:

$$\mathrm{FF}(i_{dqs}) = \frac{i_{dqs-RMS}}{i_{dqs-mean}}. \tag{3.55}$$

Un valor fijo de corriente d ($i_{ds}^* = 1$ A) ha sido utilizado. Para incluir una carga mecánica a la MIAH, el freno por corrientes parásitas fue fijado a 1.65 A. Además, las ganancias seleccionadas para el DSMC con TDE para seguimiento de las corrientes estatóricas son:

$$\lambda = \mathrm{diag}(0.5, 0.5), \qquad \rho_1 = \rho_2 = 100,$$

$$\Gamma = \mathrm{diag}(0.9, 0.9), \qquad \varrho_1 = \varrho_2 = 100.$$

Las corrientes de referencia estatóricas en el sub-espacio $(x - y)$ son fijadas a cero ($i_{xs}^* = i_{ys}^* = 0\ A$) con el fin de reducir las pérdidas en el cobre. Las frecuencias de muestreo utilizadas en las pruebas son de 8 kHz y 16 kHz. Tres puntos de operación son considerados para la velocidad rotórica: 500 rpm, $1\,000$ rpm y $1\,500$ rpm para el análisis en régimen permanente. Para la respuesta transitoria, un cambio escalón en la velocidad rotórica es considerado desde 500 a -500 rpm (en este caso es una condición de reversa).

La técnica propuesta DSMC es probada bajo diferentes puntos de operación en régimen permanente y condiciones transitorias. La **Tabla 3.2** muestra los resultados experimentales obtenidos para diferentes velocidades rotóricas y frecuencias de muestreo, relacionando al MSE de las corrientes estatóricas en los sub-espacios $(\alpha - \beta)$, $(x - y)$ y $(d - q)$. Los resultados muestran un buen desempeño del DSMC aplicado a la MIAH en términos de seguimiento de corriente en sus correspondientes sub-espacios, especialmente en el seguimiento en $(\alpha - \beta)$. La **Tabla 3.3** muestra los resultados de THD de las corrientes estatóricas en $(\alpha - \beta)$, el RMS del rizado y FF de las corrientes en $(d - q)$ y el MSE entre la velocidad rotórica de referencia y la medida. Los resultados presentan una reducción en el THD de las corrientes estatóricas a mayor frecuencia de muestreo y velocidad rotórica. En términos de RMS de rizado y FF, hay una reducción significativa a mayor frecuencia de muestreo en todas las pruebas a distintas velocidades rotóricas. Sin embargo el MSE de la velocidad rotórica tiene mejor desempeño a baja velocidad rotórica y frecuencia de muestreo, pero no es significativo.

La **Figura 3.3** presenta las trayectorias polares de las corrientes estatóricas en los sub-espacios $(\alpha - \beta)$ y $(x - y)$ a diferentes velocidades rotóricas. Las pruebas fueron desarrolladas con la misma carga mecánica, por lo que la amplitud de las corrientes en $(\alpha - \beta)$ son proporcionales a la velocidad rotórica. Las figuras muestran que las corrientes en $(x - y)$ son reducidas casi a la misma ración en cada caso y el seguimiento de las corrientes en $(\alpha - \beta)$ es buena. Por otro lado, las **Figuras 3.4** y textbf3.5 reportan la

Tabla 3.2 Análisis de desempeño de corrientes estatóricas en $(\alpha - \beta)$, $(x - y)$, $(d - q)$, MSE (A) para tres diferentes velocidades (rpm).

Frecuencia de muestreo a 8 kHz						
ω_m^*	MSE$_\alpha$	MSE$_\beta$	MSE$_x$	MSE$_y$	MSE$_d$	MSE$_q$
500	0.2502	0.2602	0.1875	0.1729	0.2494	0.2609
1000	0.2937	0.3021	0.2326	0.2280	0.3039	0.2919
1500	0.3000	0.3050	0.2491	0.2456	0.3327	0.2689
		Frecuencia	de muestreo	16 kHz		
ω_m^*	MSE$_\alpha$	MSE$_\beta$	MSE$_x$	MSE$_y$	MSE$_d$	MSE$_q$
500	0.1867	0.1883	0.1931	0.1851	0.1830	0.1919
1000	0.1797	0.1779	0.2078	0.1975	0.1795	0.1780
1500	0.1731	0.1786	0.2342	0.2291	0.1767	0.1750

Tabla 3.3 Análisis de desempeño de corrientes estatóricas ($\alpha - \beta$), THD ($\%$), ($d - q$), RMS de rizado (A) y FF, velocidad rotórica (ω_m), MSE (rpm), a diferentes velocidades rotóricas (rpm).

Frecuencia de muestreo a 8 kHz							
ω_m^*	THD$_\alpha$	THD$_\beta$	Rizado$_q$	Rizado$_d$	FF$_q$	FF$_d$	MSE$_{\omega_m}$
500	29.6198	30.7074	0.2598	0.2492	1.0811	1.0300	1.3432
1000	17.8543	18.0026	0.2890	0.3005	1.0203	1.0405	2.2250
1500	17.8761	18.0059	0.2593	0.3194	1.0084	1.1389	2.4146
Frecuencia de muestreo a 16 kHz							
ω_m^*	THD$_\alpha$	THD$_\beta$	Rizado$_q$	Rizado$_d$	FF$_q$	FF$_d$	MSE$_{\omega_m}$
500	21.6914	22.6592	0.1895	0.1829	1.0466	1.0164	1.6508
1000	15.3291	14.8507	0.1751	0.1783	1.0087	1.0151	2.8814
1500	11.1020	11.2140	0.1707	0.1712	1.0040	1.0134	3.1855

prueba dinámica, que consiste en el desempeño transitorio del DSMC con una respuesta escalón en la corriente de referencia del eje q (i_{qs}^*). La respuesta dinámica es generada por medio de una condición reversa de la velocidad mecánica del rotor (ω_m) de 500 a -500 rpm. Las **Figuras 3.4(a)** y **3.5(a)** muestran un sobrepico de $42\ \%$ y $70\ \%$ respectivamente, y un tiempo de establecimiento de 1.3 ms y 1.4 ms respectivamente presentando, en ambos casos, respuestas muy rápidas.

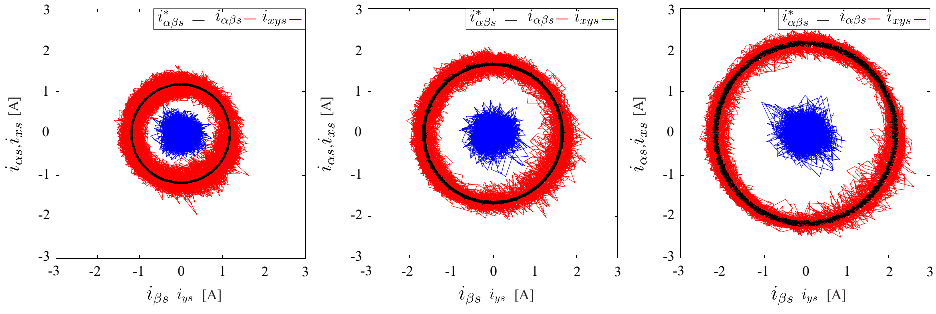

(a) (b) (c)

Figura 3.3 Corrientes estatóricas en los sub-espacios ($\alpha-\beta$) y ($x-y$) para diferentes velocidades rotóricas ω_m: (a) 500 rpm; (b) 1 000 rpm; (c) 1 500 rpm.

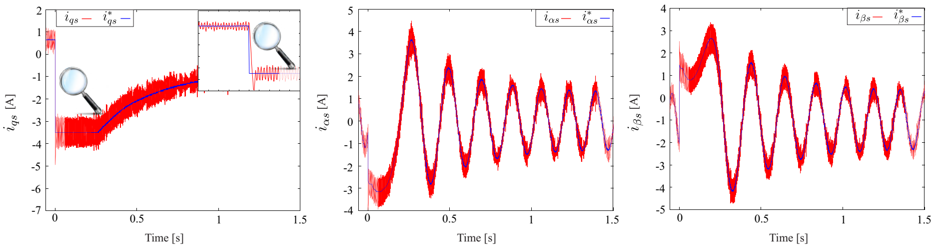

(a) (b) (c)

Figura 3.4 Respuesta transitoria de las corrientes estatóricas de una respuesta escalón de 500 rpm a -500 rpm para ω_m a una frecuencia de muestreo de 8 kHz: (a) i_{qs}; (b) $i_{\alpha s}$; (c) $i_{\beta s}$.

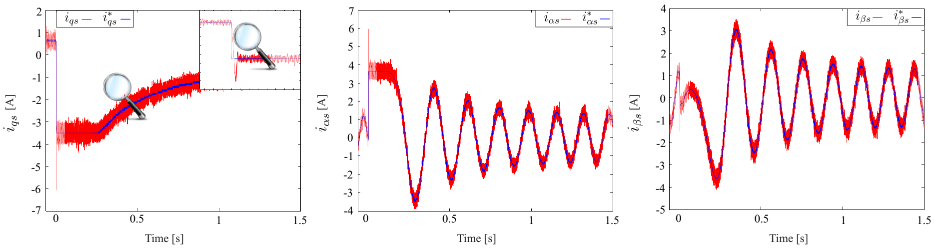

(a) (b) (c)

Figura 3.5 Respuesta transitoria de las corrientes estatóricas de una respuesta escalón de 500 rpm a -500 rpm para ω_m a una frecuencia de muestreo de 16 kHz: (a) i_{qs}; (b) $i_{\alpha s}$; (c) $i_{\beta s}$.

3.1.4 Discusión de los Resultados

Un control de velocidad basado en la estrategia de IRFOC con un control interno robusto denominado DSMC con TDE para corrientes estatóricas en los sub-espacios $(\alpha - \beta)$ y $(x - y)$ fue propuesta. Por un lado, el método TDE permite una simple manera de estimar precisamente las incertidumbres, perturbaciones y las corrientes rotóricas no medidas. Por otro lado, el DSMC cancela el efecto del error del TDE, asegurando robustez y entrega gran precisión y rápida convergencia. La eficiencia del controlador DSMC ha sido confirmado con una implementación en tiempo real de una MIAH. La técnica propuesta provee gran desempeño en el proceso dinámico como en régimen permanente.

3.2 Control Super Torcido

Las aportaciones realizadas al control super torcido se sustentan en los siguientes artículos publicados en revistas internacionales arbitradas e indexadas, con factor de impacto definido:

2. Y. Kali, **M. Ayala**, J. Rodas, M. Saad, J. Doval-Gandoy, R. Gregor, K. Benjelloun, "Time Delay Estimation based Discrete-Time Super-Twisting Current Control for a Six-Phase Induction Motor ", IEEE Transactions on Power Electronics, 2020. (R2). (Impact Factor 7.224). [Cont-2]

A pesar de la gran popularidad del convencional SMC, muchos trabajos han intentado mejorar las limitaciones mencionadas anteriormente [73, 81–83]. La técnica más atractiva es el HOSM [84]. En esta sección se describirá al HOSM diseñado, denominado control super torcido discreto (DSTC).

3.2.1 Lazo de Control Interno de Corriente

En este lazo interno, un algoritmo basado en el DSTC con TDE será desarrollado paraq asegurar que las corrientes estatóricas $(i_{s\alpha}(k), i_{s\beta}(k))$ en el sub-espacio $(\alpha - \beta)$ puedan seguir de manera precisa las deseadas referencias incluso si las corrientes rotóricas no son medibles y para forzar a las corrientes estatóricas $(i_{sx}(k), i_{sy}(k))$ en el sub-espacio $(x - y)$ sean 0 A con el fin de minimizar las pérdidas. En primer lugar, se define la superficie conmutada como sigue:

$$\mathbf{S}(k) = \mathbf{e}(k). \tag{3.56}$$

Ahora, se computará $\mathbf{S}(k+1)$ como:

$$\begin{aligned} \mathbf{S}(k+1) &= \mathbf{e}(k+1) \\ &= \mathbf{y}(k+1) - \mathbf{y}^*(k+1) \\ &= \mathbf{C}\chi(k+1) - \mathbf{y}^*(k+1) \\ &= \mathbf{CA}\chi(k) + \mathbf{CBv}(k) + \mathbf{Cp}(k) - \mathbf{y}^*(k+1) \\ &= \overline{\mathbf{A}}\mathbf{y}(k) + \overline{\mathbf{B}}\mathbf{v}(k) + \mathbf{P}(k) - \mathbf{y}^*(k+1) \end{aligned} \tag{3.57}$$

donde:

$$\overline{\mathbf{A}} = \begin{bmatrix} a_{11} & a_{12} & 0 & 0 \\ a_{21} & a_{22} & 0 & 0 \\ 0 & 0 & a_{33} & 0 \\ 0 & 0 & 0 & a_{44} \end{bmatrix} \tag{3.58}$$

$$\overline{\mathbf{B}} = \begin{bmatrix} b_1 & 0 & 0 & 0 \\ 0 & b_1 & 0 & 0 \\ 0 & 0 & b_2 & 0 \\ 0 & 0 & 0 & b_2 \end{bmatrix} \tag{3.59}$$

$$\mathbf{P}(k) = \begin{bmatrix} p_1(k) + a_{15}\, i_{r\alpha}(k) + a_{16}\, i_{r\beta}(k) \\ p_2(k) + a_{25}\, i_{r\alpha}(k) + a_{26}\, i_{r\beta}(k) \\ p_3(k) \\ p_4(k) \end{bmatrix} \tag{3.60}$$

Por otra parte, la forma discreta del DSTC es como sigue:

$$\begin{aligned} \mathbf{S}(k+1) &= \mathbf{Q}_1\mathbf{S}(k) - T_s\boldsymbol{\Gamma}_1\mathrm{sig}^{0.5}(\mathbf{S}(k)) + T_s\mathbf{W}(k) \\ \mathbf{W}(k+1) &= \mathbf{Q}_2\mathbf{W}(k) - T_s\boldsymbol{\Gamma}_2\,\mathrm{sign}(\mathbf{S}(k)) \end{aligned} \tag{3.61}$$

donde $\mathbf{Q}_1 = \mathrm{diag}(Q_{11}, \cdots, Q_{14})$ y $\mathbf{Q}_2 = \mathrm{diag}(Q_{21}, \cdots, Q_{24})$ son matrices diagonales donde los elementos son elegidos de forma que $Q_{ji} \in R^+$ y $Q_{ji} < 1$ para $j = 1, 2$ y $i = 1, \cdots, 4$, $\boldsymbol{\Gamma}_1 = \mathrm{diag}(\Gamma_{11}, \cdots, \Gamma_{14})$ and $\boldsymbol{\Gamma}_2 = \mathrm{diag}(\Gamma_{21}, \cdots, \Gamma_{24})$ son matrices diagonales positivas, $\mathrm{sign}(\mathbf{S}(k)) = [\mathrm{sign}(S_1(k)), \cdots, \mathrm{sign}(S_4(k))]^T$ y el término $\mathrm{sig}^{0.5}(\mathbf{S}(k)) = \left[|S_1(k)|^{0.5}\mathrm{sign}(S_1(k)), \cdots, |S_4(k)|^{0.5}\mathrm{sign}(S_4(k))\right]^T$ con:

$$\mathrm{sign}(S_i(k)) = \begin{cases} 0, & \text{if } S_i(k) = 0 \\ -1, & \text{if } S_i(k) < 0 \\ 1, & \text{if } S_i(k) > 0 \end{cases} \tag{3.62}$$

Combinando (3.57) usando (3.61) llega a la siguiente ley de control:

$$\begin{aligned} \mathbf{v}(k) = -\overline{\mathbf{B}}^{-1} \big[&\overline{\mathbf{A}}\mathbf{y}(k) - \mathbf{y}^*(k+1) + \mathbf{P}(k) - \mathbf{Q}_1\mathbf{S}(k) \cdots \\ &\cdots + T_s\boldsymbol{\Gamma}_1\mathrm{sig}^{0.5}(\mathbf{S}(k)) - T_s\mathbf{W}(k)\big] \end{aligned} \tag{3.63}$$

El desempeño de control podría no ser satisfactorio ya que el vector $\mathbf{P}(k)$ de las perturbaciones y las corrientes rotóricas no medibles son desconocidas. Entonces, asumiendo que durante dos tiempos de muestreo consecutivos, las variaciones de los elementos $\mathbf{P}(k)$ no son muy grandes, entonces:

$$|P_i(k) - P_i(k-1)| \leq T_s \rho_i < \infty \tag{3.64}$$

Por lo tanto, el método TDE [21] puede ser usado para aproximar como sigue:

$$\hat{\mathbf{P}}(k) \cong \mathbf{P}(k-1) = \mathbf{y}(k) - \overline{\mathbf{A}}\mathbf{y}(k-1) - \overline{\mathbf{B}}\mathbf{v}(k-1) \tag{3.65}$$

Teorema 3.3 *Considere a la MIAH descrita en* (3.1) *y* (3.2)*. Entonces, el control DSTC con TDE para las corrientes estatóricas son dados por:*

$$\begin{aligned} \mathbf{v}(k) &= \overline{\mathbf{B}}^{-1}\Big[\mathbf{y}^*(k+1) - \overline{\mathbf{A}}\mathbf{y}(k) - \hat{\mathbf{P}}(k) \cdots \\ &\qquad \cdots + \mathbf{Q}_1\mathbf{S}(k) - T_s\mathbf{\Gamma}_1 \mathrm{sig}^{0.5}(\mathbf{S}(k)) + T_s\mathbf{W}(k)\Big] \\ \mathbf{W}(k+1) &= \mathbf{Q}_2\mathbf{W}(k) - T_s\mathbf{\Gamma}_2\,\mathrm{sign}(\mathbf{S}(k)) \end{aligned} \tag{3.66}$$

asegura la convergencia del error a una bola b que tiene un radio r_b menor a:

$$r_b \leq \frac{\left(\left(\dfrac{\bar{\phi}_1}{2}\right)^2 \|\overline{\Theta}^{-1}\|^2 + \bar{\phi}_2\right)}{r} \tag{3.67}$$

si las siguientes condiciones son encontradas para $i = 1:4$:

$$\Gamma_{1i} > 0, \;\; \Gamma_{2i} > \frac{(1+Q_{2i})}{T_s}\rho_i. \tag{3.68}$$

En primer lugar, se sustituye el cotrol discreto propuesto por (3.66) en (3.57):

$$\begin{aligned} \mathbf{S}(k+1) &= \mathbf{Q}_1\mathbf{S}(k) - T_s\mathbf{\Gamma}_1\mathrm{sig}^{0.5}(\mathbf{S}(k)) + T_s\mathbf{W}(k) + \mathbf{\Delta P}(k) \\ \mathbf{W}(k+1) &= \mathbf{Q}_2\mathbf{W}(k) - T_s\mathbf{\Gamma}_2\,\mathrm{sign}(\mathbf{S}(k)) \end{aligned} \tag{3.69}$$

donde $\mathbf{\Delta P}(k) = \mathbf{P}(k) - \mathbf{P}(k-1)$ es el error del TDE. La dinámica del error en la ecuación anterior puede ser escrita para $i = 1, \cdots, 4$ como sigue:

$$\begin{aligned} S_i(k+1) =& Q_{1i}S_i(k) - T_s\Gamma_{1i}|S_i(k)|^{0.5}\mathrm{sign}(S_i(k)) \\ & + \Delta P_i(k) + T_s W_i(k) \\ W_i(k+1) =& Q_{2i}W_i(k) - T_s\Gamma_{2i}\mathrm{sign}(S_i(k)) \end{aligned} \tag{3.70}$$

Para demostrar la convergencia, se introduce una nueva variable definida por $Z_i(k) = W_i(k) + T_s^{-1}\Delta P_i(k)$ tal que (3.70) pueda ser escrita como:

$$\begin{aligned} S_i(k+1) =& Q_{1i}S_i(k) - T_s\Gamma_{1i}|S_i(k)|^{0.5}\text{sign}(S_i(k)) + T_sZ_i(k) \\ Z_i(k+1) =& Q_{2i}Z_i(k) - T_s\Gamma_{2i}\text{sign}(S_i(k)) + \zeta_i(k) \end{aligned} \tag{3.71}$$

donde

$$\zeta_i(k) = T_s^{-1}(\Delta P_i(k+1) - Q_{2i}\Delta P_i(k)) \tag{3.72}$$

Ahora, se define $\eta_i(k) = [S_i(k), Z_i(k)]^T$, entonces, la ecuación (3.70) puede ser escrita en forma de matriz:

$$\eta_i(k+1) = \Psi\eta_i(k) + \Phi(k)\text{sign}(S_i(k)) \tag{3.73}$$

donde Ψ y $\Phi(k)$ son definidas como:

$$\begin{aligned} \Psi &= \begin{bmatrix} Q_{1i} & T_s \\ 0 & Q_{2i} \end{bmatrix} \\ \Phi(k) &= \begin{bmatrix} -T_s\Gamma_{1i}|S_i(k)|^{0.5} \\ -T_s\Gamma_{2i} + \zeta_i(k)\text{sign}(S_i(k)) \end{bmatrix} \end{aligned} \tag{3.74}$$

Ahora, se considera la siguiente función discreta candidata de Lyapunov:

$$V(k) = \eta_i^T(k)L\eta_i(k) \tag{3.75}$$

donde $L = L^T \in R^{2\times 2}$ es una matriz definida simétrica positiva. Entonces, uno puede implicar:

$$\begin{aligned} \Delta V(k) &= V(k+1) - V(k) \\ &= \eta_i^T(k+1)L\eta_i(k+1) - \eta_i^T(k)L\eta_i(k) \end{aligned} \tag{3.76}$$

Combinando (3.73) con (3.76) y usando la matriz de desigualdad Λ [85] $A^TB + B^TA \leq A^T\Lambda A + B^T\Lambda^{-1}B$ se obtiene:

$$\begin{aligned} \Delta V(k) =& \eta_i^T(k)(\Psi^TL\Psi - L)\eta_i(k) + \Phi^T(k)L\Phi(k) \\ &+ 2\eta_i^T(k)\Psi^TL\Phi(k)\text{sign}(S_i(k)) \\ \leq& \eta_i^T(k)(\Psi^TL\Psi - L)\eta_i(k) + \Phi^T(k)L\Phi(k) \\ &+ \eta_i^T(k)(\Psi^TL\Lambda L\Psi)\eta_i(k) + \Phi^T(k)\Lambda^{-1}\Phi(k) \\ \leq& \eta_i^T(k)(\Psi^T(L + L\Lambda L)\Psi - (1-r)L)\eta_i(k) \\ &+ \Phi^T(k)(L + \Lambda^{-1})\Phi(k) - rV(k) \\ \leq& -\eta_i^T(k)\Theta\eta_i(k) + \Phi^T(k)R\Phi(k) - rV(k) \end{aligned} \tag{3.77}$$

donde $0 < r < 1$, $R = L + \Lambda^{-1}$ y Θ es una matriz simétrica definida positiva (2×2) que resuelve la matriz de desigualdad [86] tal que: $\Psi^T(L + L\Lambda L)\Psi - (1-r)L = -\Theta$. Ahora, se expande el término $\Phi^T(k)R\Phi(k)$ como sigue:

$$\Phi^T(k)R\Phi(k) = \phi_1|S_i(k)| + \phi_2|S_i(k)|^{0.5} + \phi_3 \tag{3.78}$$

donde ϕ_1, ϕ_2 y ϕ_3 son computados como sigue:

$$\begin{aligned}
\phi_1 =& T_s^2\Gamma_{1i}^2 R_{11} \\
\phi_2 =& 2T_s\Gamma_{1i}R_{21}(T_s\Gamma_{2i} - \zeta_i(k)sign(S_i(k))) \\
\phi_3 =& R_{22}(T_s\Gamma_{2i} - \zeta_i(k)sign(S_i(k)))^2
\end{aligned} \tag{3.79}$$

De otra manera $\zeta_i(k)$ está limitado por:

$$\begin{aligned}
\zeta_i(k) &= T_s^{-1}(\Delta P_i(k+1) - Q_{2i}\Delta P_i(k)) \\
&\leq T_s^{-1}|\Delta P_i(k+1) - Q_{2i}\Delta P_i(k)| \\
&\leq T_s^{-1}\left(|\Delta P_i(k+1)| + |Q_{2i}\Delta P_i(k)|\right) \\
&\leq T_s^{-1}\left(T_s\rho_i + Q_{2i}T_s\rho_i\right) \\
&\leq (1+Q_{2i})\rho_i
\end{aligned} \tag{3.80}$$

Por lo tanto, si Γ_{2i} es elegida como en (3.68), el término ϕ_2 será siempre positivo tal que $\phi_2|S_i(k)|^{0.5} \leq \phi_2(1 + |S_i(k)|)$ y la siguiente desigualdad pueda ser establecida:

$$\begin{aligned}
\Phi^T(k)R\Phi(k) \leq& \phi_1|S_i(k)| + \phi_2(1 + |S_i(k)|) + \phi_3 \\
\leq& (\phi_1 + \phi_2)|S_i(k)| + \phi_2 + \phi_3 \\
\leq& \bar{\phi}_1|S_i(k)| + \bar{\phi}_2
\end{aligned} \tag{3.81}$$

donde $\bar{\phi}_1$ y $\bar{\phi}_2$ son computados como sigue:

$$\begin{aligned}
\bar{\phi}_1 =& T_s^2\Gamma_{1i}^2 R_{11} + 2T_s\Gamma_{1i}R_{21}(T_s\Gamma_{2i} + (1+Q_{2i})\rho_i) \\
\bar{\phi}_2 =& 2T_s\Gamma_{1i}R_{21}(T_s\Gamma_{2i} + (1+Q_{2i})\rho_i) \\
&+ R_{22}\big(T_s\Gamma_{2i} + (1+Q_{2i})\rho_i\big)^2
\end{aligned} \tag{3.82}$$

Substituyendo (3.81) en (3.77) y usando la descomposición Choleskii, $\Delta V(k)$ se vuelve:

$$\begin{aligned}
\Delta V(k) \leq& -\eta_i^T(k)\Theta\eta_i(k) + \bar{\phi}_1|S_i(k)| + \bar{\phi}_2 - rV(k) \\
\leq& -\|\overline{\Theta}\eta_i(k)\|^2 + \bar{\phi}_1\|\overline{\Theta\Theta}^{-1}\eta_i(k)\| + \bar{\phi}_2 - rV(k) \\
\leq& -\star^T\star + \left(\frac{\bar{\phi}_1}{2}\right)^2\|\overline{\Theta}^{-1}\|^2 + \bar{\phi}_2 - rV(k) \\
\leq& \left(\frac{\bar{\phi}_1}{2}\right)^2\|\overline{\Theta}^{-1}\|^2 + \bar{\phi}_2 - rV(k) \\
V(k+1) \leq& \left(\left(\frac{\bar{\phi}_1}{2}\right)^2\|\overline{\Theta}^{-1}\|^2 + \bar{\phi}_2\right) + (1-r)V(k)
\end{aligned} \tag{3.83}$$

donde $\overline{\Theta}^2 = \Theta$ y $\star = \left(\|\overline{\Theta}\eta_i(k)\| - \frac{\bar{\phi}_1}{2}\|\overline{\Theta}^{-1}\|\right)$. La solución a la desigualdad discreta lineal está dada por:

$$V(k+1) \leq \left(\left(\frac{\bar{\phi}_1}{2}\right)^2 \|\overline{\Theta}^{-1}\|^2 + \bar{\phi}_2\right) \sum_{i=1}^{k+1} (1-r)^{i-1} + (1-r)^{k+1} V(0) \tag{3.84}$$

Considere el caso donde k va a ∞, entonces puede concluirse lo siguiente:

$$\lim_{k \to +\infty} V(k) \leq \frac{\left(\left(\frac{\bar{\phi}_1}{2}\right)^2 \|\overline{\Theta}^{-1}\|^2 + \bar{\phi}_2\right)}{r} \tag{3.85}$$

Por lo tanto, el DSTC asegura la convergencia de las trayectorias es una bola b que tiene un radio r_b más pequeño que:

$$r_b \leq \frac{\left(\left(\frac{\bar{\phi}_1}{2}\right)^2 \|\overline{\Theta}^{-1}\|^2 + \bar{\phi}_2\right)}{r} \tag{3.86}$$

Esto concluye la prueba.

3.2.2 Análisis Experimental de las Aportaciones al STC

La técnica propuesta DSTC es probada en una bancada experimental para validar su desempeño. Esta bancada es la misma utilizada en la sección anterior.

Figuras de mérito La técnica propuesta es evaluada por medio del MSE entre la referencia y la medición de las corrietes estatóricas, el MSE de la velocidad rotórica, el RMS del rizado de las corrientes estatóricas en el sub-espacio $(d - q)$ y el THD de las corrientes estatóricas en el sub-espacio $(\alpha - \beta)$. El rizado RMS de las corrientes $(d - q)$ se calculan de la siguiente manera:

$$\text{RMS}(rizado_\theta) = \sqrt{RMS(i_{s\theta})^2 - Mean(i_{s\theta})^2} \tag{3.87}$$

donde $i_{s\theta}$ las corrientes estatóricas en el sub-espacio $(d - q)$ y $Mean$ es el valor medio de dichas corrientes $(d - q)$.

Análisis en régimen permanente Las frecuencias de muestreo seleccionadas son 8 kHz y 16 kHz. El freno por corrientes parásitas es calibrado para obtener una corriente q a 1.4 A para la MIAH. Para el análisis en régimen permanente, tres velocidades mecánicas son designadas: 500 rpm, 1 000 rpm y 1 500 rpm. La **Tabla 3.4** muestra los resultados obtenidos para distintas frecuencias de muestreo y velocidades mecánicas, presentado como el MSE de las corrientes estatóricas en todos los sub-espacios. Los datos muestran buen desempeño del DSTC con TDE aplicado a la máquina en términos de control de corriente en todos los sub-espacios, especialmente en el seguimiento de las corrientes $(\alpha - \beta)$. La **Tabla 3.5** presenta el RMS del rizado de las corrientes $(d - q)$, el THD de las corrientes $(\alpha - \beta)$ y el MSE de la velocidad mecánica. Los resultados muestran un

Tabla 3.4 Prueba de corrientes estatóricas en régimen permanente $(d-q)$, $(\alpha-\beta)$, $(x-y)$, MSE (A) para tres distintas velocidades mecánicas de referencia (rpm).

Frecuencia de muestreo a 8 kHz						
ω_m^*	MSE_d	MSE_q	MSE_α	MSE_β	MSE_x	MSE_y
500	0.0416	0.0621	0.0537	0.0520	0.0383	0.0383
1000	0.0649	0.0791	0.0670	0.0773	0.0474	0.0443
1500	0.1145	0.1395	0.1262	0.1290	0.1109	0.0995
Frecuencia de muestreo a 16 kHz						
ω_m^*	MSE_d	MSE_q	MSE_α	MSE_β	MSE_x	MSE_y
500	0.1343	0.1377	0.1341	0.1379	0.1598	0.1456
1000	0.1300	0.1393	0.1341	0.1353	0.1805	0.1591
1500	0.1274	0.1358	0.1320	0.1313	0.1785	0.1766

Tabla 3.5 Prueba de corrientes estatóricas en régimen permanente: THD (%) en $(\alpha-\beta)$, RMS de rizado (A) en $(d-q)$, MSE (rpm) de la velocidad rotórica (ω_m), a tres distintas velocidades mecánicas de referencia (rpm).

Frecuencia de muestreo a 8 kHz					
ω_m^*	THD_α	THD_β	Rizado_d	Rizado_q	MSE_{ω_m}
500	4.3418	4.0378	0.0322	0.0514	1.7722
1000	3.8585	5.5634	0.0452	0.0491	2.1242
1500	9.5917	9.9925	0.0957	0.1016	3.8799
Frecuencia de muestreo a 16 kHz					
ω_m^*	THD_α	THD_β	Rizado_d	Rizado_q	MSE_{ω_m}
500	12.8828	13.6806	0.1336	0.1332	1.8619
1000	13.1770	13.3089	0.1276	0.1323	2.5163
1500	12.6697	12.9736	0.1227	0.1269	3.6441

bajo THD a baja frecuencia de muestreo y baja velocidad mecánica, ya que altas frecuencias de muestreo amplifican las perturbaciones. Para los resultados del RMS del rizado, hay una mejora significativa a baja frecuencia de muestreo en las tres velocidades mecánicas probadas. Por último para la velocidad mecánica, un mejor desempeño es obtenido a baja frecuencia de muestreo y baja velocidad mecánica, pero no es muy significativo en comparación a las otras pruebas.

Además, la **Figura 3.6** muestra la representación polar de las corrientes estatóricas para las tres velocidades mecánicas. El análisis fue realizado para una corriente q de referencia fija, por lo que las amplitudes de las corrientes estatóricas en $(\alpha-\beta)$ se mantienen a distintas velocidades mecánicas.

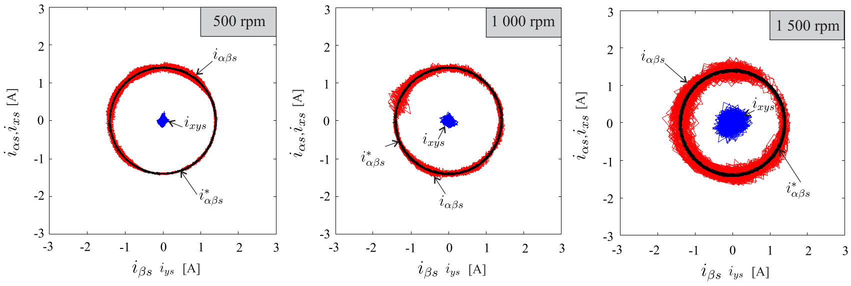

Figura 3.6 Corrientes estatóricas en los sub-espacios $(\alpha-\beta)$ y $(x-y)$ para distintas velocidades mecánicas a la frecuencia de muestreo de 8 kHz.

Las figuras presentan a las corrientes $(x-y)$ donde se puede notar que son bastante reducidas en todos los casos, resaltando las pruebas a baja frecuencia de muestreo. Por otro lado, el seguimiento de las corrientes en $(\alpha-\beta)$ es bueno, presentando mayor rizado a mayor frecuencia de muestreo, mostrando una relación directa entre las perturbaciones y la frecuencia de conmutación.

Análisis Dinámico Luego, para una prueba transitoria, que consiste en un cambio escalón en la referencia de la corriente estatórica q (i^*_{qs}) fue producida por una condición reversa (500 to -500 rpm). La **Figura 3.7** reporta la prueba. Las **Figuras 3.7(a)** y **3.7(b)** presentan el tiempo de establecimiento a un valor aproximado de 1.9 ms y 1.8 ms respectivamente y un sobrepico de 42.1 % y 68 % respectivamente, presentando una respuesta muy rápida en ambos casos.

Al mismo tiempo, otras pruebas transitorias fueron desarrolladas para observar el desempeño del controlador con un cambio escalón de -500 rpm a 1000 rpm y luego un segundo cambio escalón de 1000 rpm a -500 rpm. El único notable efecto es el cambio en las corrientes $(\alpha-\beta)$ cambian de amplitud de 4.25 A a 1.2 A como se muestran en la **Figura 3.8**. En la misma figura, se puede apreciar la respuesta rápida dinámica del controlador y un buen seguimiento del controlador DSTC con TDE.

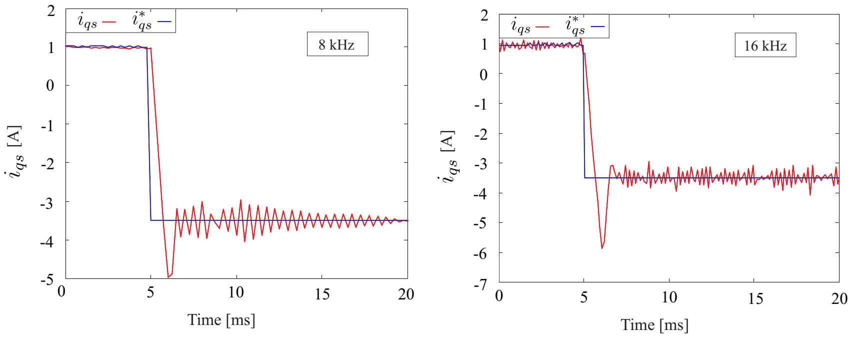

Figura 3.7 Comportamiento dinámico de la corriente i_{qs} por una condición reversa de 500 rpm a -500 rpm para ω_m a frecuencias de muestreo de 8 y 16 kHz.

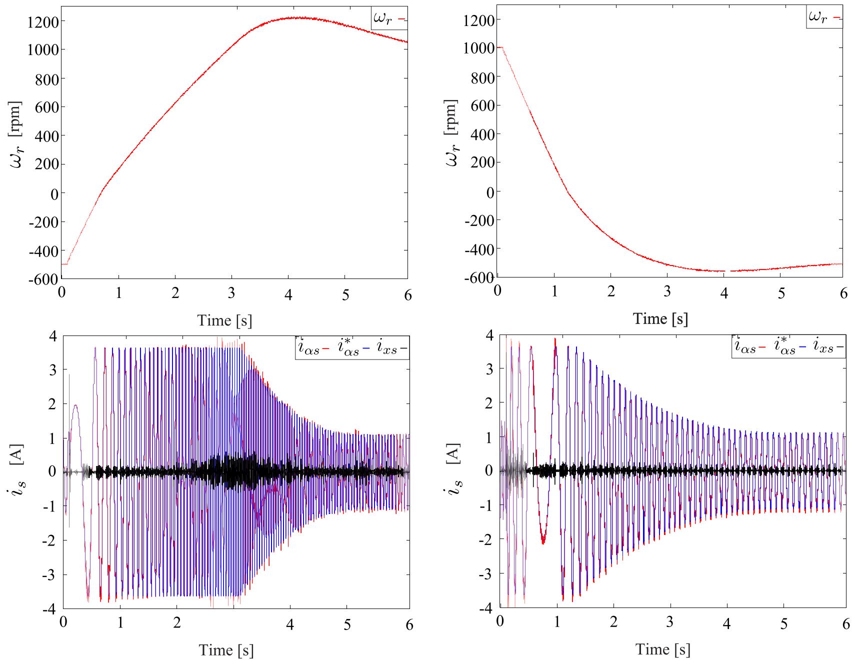

Figura 3.8 Respuesta transitoria de corrientes estatóricas para diferentes velocidades rotóricas de referencia ω_r^*: en primer lugar de -500 a 1000 rpm, luego de 1000 a -500 rpm.

En adición, los valores del MSE son MSE$_\alpha = 0.1539$ A, MSE$_\beta = 0.1655$ A, MSE$_x = 0.1192$ A y MSE$_y = 0.1145$ A para el primer cambio escalón y MSE$_\alpha = 0.0779$ A, MSE$_\beta = 0.0734$ A, MSE$_x = 0.0654$ A y MSE$_y = 0.0651$ A para el segundo cambio escalón.

Respuesta a Perturbaciones En segundo lugar, para mostrar la robustez del método propuesto, se prueba a condición en régimen permanente para una velocidad de 1000 rpm con la introducción de un cambio escalón en el par de carga desde el vación (sin carga) a la carga nominal y viceversa. Los resultados de estas pruebas son vistos en la **Figura 3.9**. Se puede notar una alta precisión en el seguimiento de las corrientes estatóricas en el sub-espacio $\alpha - \beta$. Los resultados obtenidos son muy similares para la prueba a 1000 rpm donde los valores obtenidos de MSE para el primer caso son: MSE$_\alpha = 0.0555$ A, MSE$_\beta = 0.0684$ A, MSE$_x = 0.0398$ A y MSE$_y = 0.0419$ A, mientras que los valores para la segunda prueba son: MSE$_\alpha = 0.0647$ A, MSE$_\beta = 0.0776$ A, MSE$_x = 0.0424$ A y MSE$_y = 0.0513$ A.

Sensibilidad de Parámetros Por otro lado, la **Figura 3.10** presenta el desempeño del control con un cambio de valor del 25% de la L_m nominal para determinar la robustez del control ante incertidumbres. Los resultados muestran que a baja velocidad, el desempeño es prácticamente idéntico al nominal, mostrando una gran robustez para este particular cambio. A mayores velocidades rotóricas los resultados muestran un deterioro del seguimiento de corriente a aproximadamente 21 %

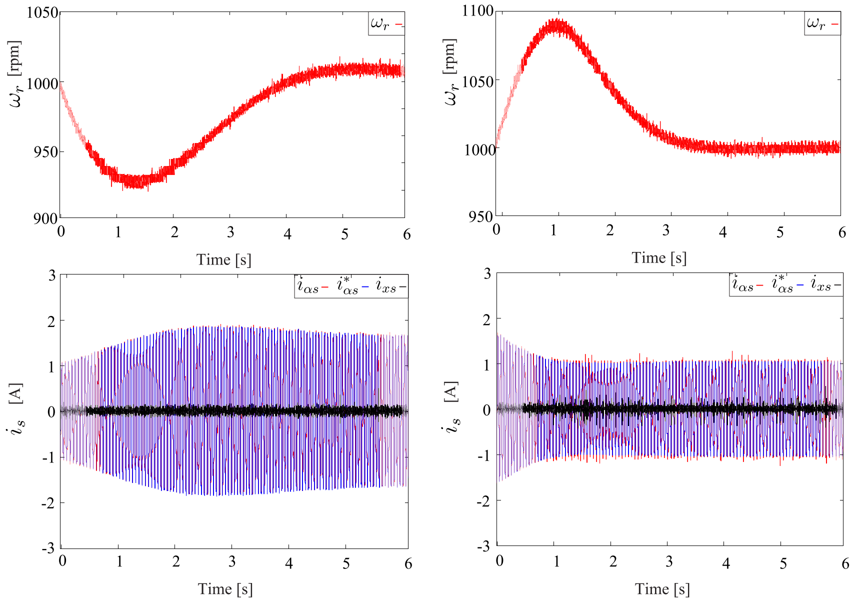

Figura 3.9 Respuesta en régimen permanente de las corrientes estatóricas para una velocidad de referencia $\omega_r^* = 1000$ rpm con un cambio escalón de par de carga desde vacío (sin carga) a carga nominal y luego de carga nominal a vacío.

y 60 %, comparado al valor nominal de L_m, para 1000 y 1500 rpm respectivamente, mostrando un incremento en la sensibilidad en estos puntos de operación.

Las pruebas transitorias analizadas, considerando la variación del 25% del valor nominal de L_m, prueban la habilidad de rechazar perturbaciones y las dinámicas desconocidas. Los resultados obtenidos se muestran en la **Figura 3.11**. Un buen desempeño, similar al caso nominal, es obtenido. Esto es confirmado por los valores de MSE. Para las pruebas con variación se obtuvieron los siguientes resultados: $\text{MSE}_\alpha = 0.1916$ A, $\text{MSE}_\beta = 0.2016$ A, $\text{MSE}_x = 0.1665$ A y $\text{MSE}_y = 0.1525$ A mientras que los valores del segundo caso son: $\text{MSE}_\alpha = 0.0835$ A, $\text{MSE}_\beta = 0.0769$ A, $\text{MSE}_x = 0.0712$ A y $\text{MSE}_y = 0.0683$ A. Estos valores son prácticamente iguales a los primeros análisis transitorios, mostrando una buena robustez del controlador en estado transitorio basado en condición reversa de la MIAH a frecuecia de muestreo de 8 kHz.

Análisis comparativo con el DSMC La **Tabla 3.6** presenta un análisis comparativo del desempeño del algoritmo DSTC con TDE comparado con el DSMC con TDE, propuesto en [21], en términos de %, donde valor positivo $(+)$ y negativo $(-)$ significan mejora o deterioro respectivamente,

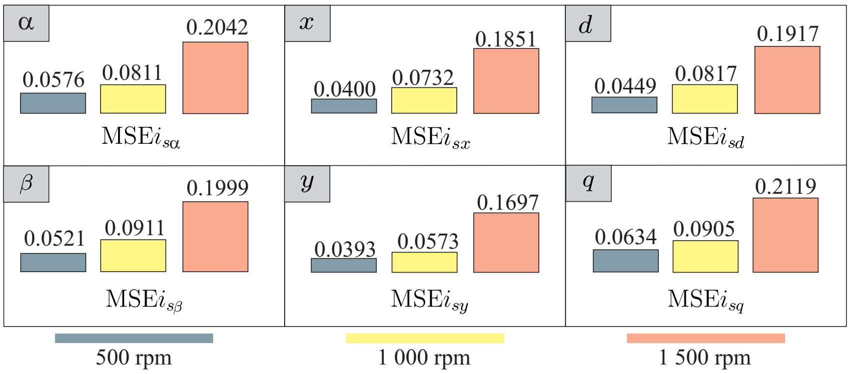

Figura 3.10 Análisis de desempeño de corrientes estatóricas MSE (A) bajo una variación del 25 % de L_m.

y es calculado como sigue:

$$\text{Imp (\%)} = 100\frac{\text{DSMC}_{\text{valor}} - \text{DSTC}_{\text{valor}}}{\text{DSMC}_{\text{valor}}} \tag{3.88}$$

donde valor puede ser el MSE de las corrientes estatóricas en los sub-espacios $(\alpha - \beta)$ y $(x - y)$, el THD de las corrientes estatóricas $(\alpha - \beta)$ o el RMS de rizado de las corrientes en el sub-espacio $(d - q)$. La **Figura 3.12** resume la comparativa entre el DSMC con TDE y el DSTC con TDE utilizando el valor medio del MSE en cada sub-espacio para diferentes velocidades rotóricas a una frecuencia de muestreo de 8 kHz.

Tabla 3.6 Análisis comparativo (%) de DSTC y DSMC a diferentes velocidades (rpm).

ω_m^*	$\mathrm{MSE}_{\alpha\beta}$	MSE_{xy}	$\mathrm{RMSripple}_d$	$\mathrm{RMSripple}_q$	$\mathrm{THD}_{\alpha\beta}$
Frecuencia de muestreo a 8 kHz (DSTC)					
500	79.29	78.75	87.08	80.22	86.11
1000	75.90	80.09	84.96	83.01	73.72
1500	57.82	57.47	70.04	60.82	45.42
Frecuencia de muestreo a 16 kHz (DSTC)					
500	27.47	19.25	26.95	29.71	40.11
1000	24.66	16.21	28.44	24.44	12.24
1500	25.14	23.35	28.33	25.66	-14.91

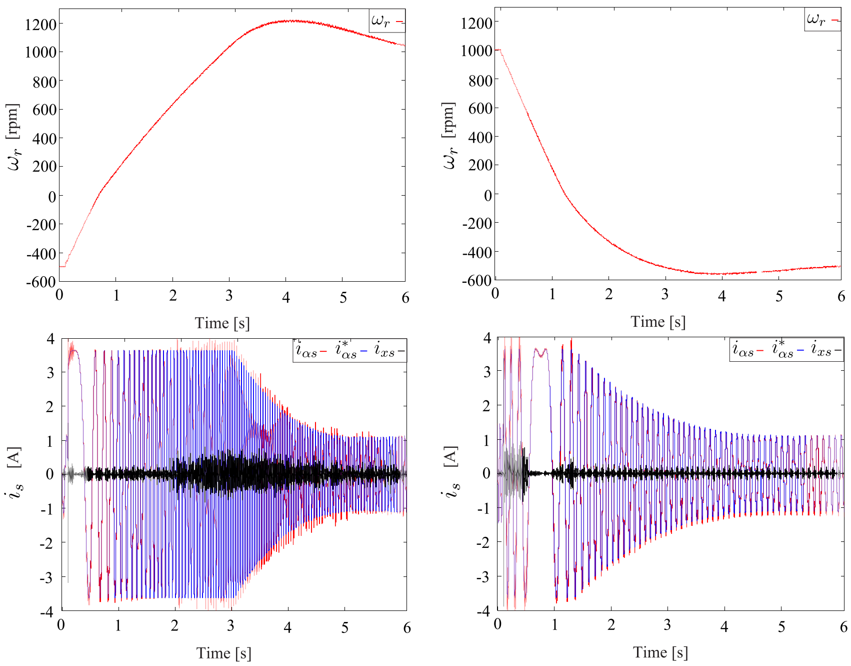

Figura 3.11 Respuesta transitoria de las corrientes estatóricas para diferentes velocidades rotóricas de referencia ω_r^* con una variación del 25 % de L_m: de -500 a 1000 rpm, y luego de 1000 a -500 rpm.

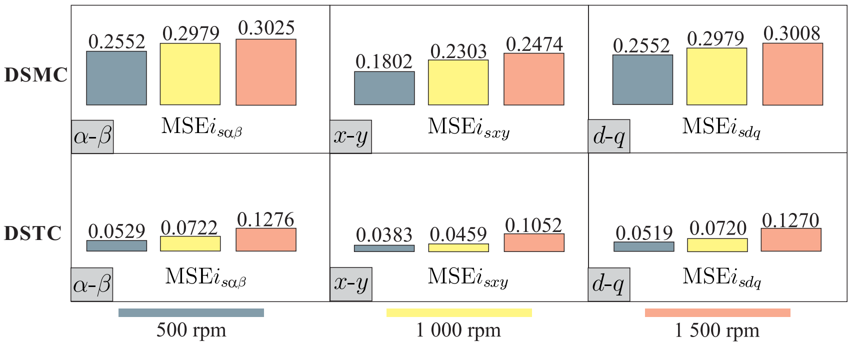

Figura 3.12 Comparativa del desempeño (MSE (A)) de corrientes estatóricas en los sub-espacios $(\alpha - \beta)$, $(x - y)$ y $(d - q)$ para una frecuencia de muestreo de 8 kHz.

3.2.3 Discusión de los Resultados

Un control interno de corriente robusto basado en DSTC con TDE fue presentado para controlar las corrientes estatóricas en los sub-espacios $(\alpha - \beta)$ y $(x - y)$ de una MIAH con un control externo de velocidad. Como los resultados presentados, el DSTC con TDE presenta un comportamiento óptimo en seguimiento de corriente con bajo contenido armónico, asegurando robustez y dinámicas rápidas, en términos de tiempo de establecimiento y sobrepico, y una rápida convergencia en todos los puntos de operación. En resumen, el DSTC con TDE es una opción óptima, a baja frecuencia de muestreo y bajas velocidades y una buena alternativa para velocidades altas en aplicaciones industriales.

3.3 Control Predictivo Basado en el Modelo

Las aportaciones realizadas al control predictivo basado en modelo se sustentan en los siguientes artículos publicados en revistas internacionales arbitradas e indexadas, con factor de impacto definido:

3. **M. Ayala**, J. Doval-Gandoy, J. Rodas, R. Gregor, O. González, "Current Control Designed with Model Based Predictive Control for Six-Phase Motor Drives," ISA Transactions, vol. 98, DOI: 10.1016/j.isatra.2019.08.052, pp. 496-504, Mar. 2020. (Impact Factor 4.343). [Cont-3]
4. **M. Ayala**, J. Doval-Gandoy, J. Rodas, O. González, R. Gregor, M. Rivera, "A Novel Modulated Model Predictive Control Applied to Six-Phase Induction Motor Drives", IEEE Transactions on Industrial Electronics, DOI: 10.1109/TIE.2020.2984425, 2020. (Impact Factor 7.503). [Cont-4]
5. **M. Ayala**, J. Doval-Gandoy, O. González, J. Rodas, R. Gregor, M. Rivera, "Stability Analysis of Modulated Model Predictive Controllers Applied to Six-Phase Induction Motor Drives", IEEE Transactions on Industrial Electronics, pp. 1-10, 2020. (R1). (Impact Factor 7.503). [Cont-5]

El control MPC ha ganado mucha atención en los últimos años como alternativa a controladores lineales convencionales [7,60,87]. Las estrategias MPC son identificadas por el requisito de definir un modelo del sistema con el fin de predecir los valores futuros para las variables de estado. Una vez obtenidos dichos valores, el MPC utiliza un criterio de optimización basado en la minimización de una función de costo que describe el comportamiento deseado del sistema en cada tiempo de muestreo. El MPC tiene una respuesta dinámica rápida y puede ser aplicado a distintos sistemas, tales como convertidores AC-DC [88], convertidores conectados a red [89,90], máquinas síncronas de imanes permanentes [91,92] y máquinas de inducción [93,94]. El MPC es clasificado por un control continuo y por un control discreto. Este último es más aplicado en sistemas con naturaleza discreta, como sistemas trifásicos y multifásicos con topologías VSI, siendo la más utilizada la de dos niveles [91–94]. La **Figura 2.5** muestra las 64 posibilidades los cual consisten en 49 vectores diferentes (48 vectores + 1 vector nulo) en los sub-espacios $(\alpha - \beta)$ y $(x - y)$.

3.3.1 FCS-MPC Clásico aplicado a una MIAH (PC1)

Esta técnica es utilizada con un filtro de Kalman (KF) para estimar las corrientes rotóricas propuesto en [33]. Teniendo en cuenta el modelo discreto de la MIAH en (3.1) y (3.2), se puede estimar la predicción de la futura variable estado $\hat{\mathbf{X}}(k+1|k)$:

$$\hat{\mathbf{X}}(k+1|k) = \mathbf{X}(k) + \mathrm{f}\left(\mathbf{X}(k),\ \mathbf{u}(k),\ T_s,\ \omega_r(k)\right) \tag{3.89}$$

Observador de Orden Reducido La representación en espacio de estado (3.1) tiene seis variables de estado, donde solo las corrientes estatóricas pueden ser medidas. Los voltajes de estator son fácilmente calculados a partir de (3.6), donde los comandos de conmutación generan el voltaje de salida del VSI. Por otro lado, las corrientes rotóricas no pueden ser medidas directamente. Esto se resuelve con un observador de orden reducido. Estos observadores estiman los valores no medibles del vector de estado. Este es un problema recientemente solucionado mediante la aplicación del observador de Luenberger (LO) y KF, donde el KF muestra mejores resultados debido a que la ganancia del observador son computadas de forma online considerando los ruidos de proceso y medición de la MIAH. Por otra parte, las ganancias de LO no son optimizadas y tienen una configuración determinística [95, 96]. Por ello, un observador de orden reducido KF es implementada con PC1 para la estimación de las corrientes rotóricas, teniendo en cuenta ruidos de proceso y medición con valor medio cero tipo Gaussianos. La dinámica de error del observador KF es presentado:

$$e(k+1) = \mathbf{\Omega}(k)e(k) = \left\{ \begin{bmatrix} a_{55} & a_{56} \\ a_{65} & a_{66} \end{bmatrix} - \mathbf{K}(k) \begin{bmatrix} a_{15} & a_{16} \\ a_{25} & a_{26} \end{bmatrix} \right\} e(k) \tag{3.90}$$

donde $e(k)$ es el error entre la estimación y el valor real de las corrientes rotóricas mientras que $\mathbf{K}(k)$ es la ganancia del KF. Para una rápida convergencia a cero, los autovalores de $\mathbf{\Omega}(k)$ deben encontrarse dentro del círculo unitario. Puede ser considerado que la dinámica de las corrientes rotóricas es lenta facilitando al KF la convergencia. Una descripción detallada de la convergencia y dinámica del observador de orden reducido KF (y LO) puede ser consultado en [33, 95].

Función de Costo El diseño para la función de costo puede garantizar la optimización de variables importantes tales como la minimización del rizado de par de la MIAH, pérdidas de conmutación del VSI y reducción del contenido armónico [60]. Como consecuencia, al incluir más términos en la función de costo el controlador puede incluir otras variables o restricciones. En PC1 el parámetro es el error de seguimiento de las corrientes estatóricas predichas para el siguiente tiempo de muestreo. Por ello, la función de costo es determinada:

$$\begin{aligned} J(k+2|k) =&\| i_{\alpha s}(k+2)^{*} - \hat{i}_{\alpha s}(k+2|k) \|^{2} + \| i_{\beta s}(k+2)^{*} - \hat{i}_{\beta s}(k+2|k) \|^{2} \\ &+ \lambda_{xy} \left(\| i_{xs}(k+2)^{*} - \hat{i}_{xs}(k+2|k) \|^{2} + \| i_{ys}(k+2)^{*} - \hat{i}_{ys}(k+2|k) \|^{2} \right) \end{aligned} \tag{3.91}$$

Al usar (3.92), una predicción de segundo horizonte en las corrientes estatóricas $\hat{i}_s(k+2|k)$ es computado para compensar el retardo del sistema [60]. La trayectoria deseada de referencia de las corrientes estatóricas es representada por $i_s(k+2)^*$. El factor de peso es un tópico actual y algunos trabajos han presentado aportes sobre este tema [97–99]. Típicamente, en máquinas multifásicas, λ_{xy} permite priorizar las corrientes estatóricas en el sub-espacio $(\alpha - \beta)$ [33, 53].

$$\hat{\mathbf{X}}(k+2|k) = \mathbf{A}(k)\mathbf{X}(k+1) + \mathbf{B}(k)\mathbf{u}(k+1) + \mathbf{H}\mathbf{n}(k) \tag{3.92}$$

Considerando el costo computacional, 49 vectores de voltaje no redundantes son seleccionados por PC1 siendo el número de iteraciones realizado en cada tiempo de muestreo. En cada iteración hay 48 operaciones de punto flotante (FPO) relacionados al cálculo de la predicción, la minimización de la función de costo y el proceso de predicción de segundo horizonte, dando un total de 2352 FPO, mientras que el KF tiene 450 FPO. La **Figura 3.13** muestra el diagrama en bloques del FCS-MPC aplicado a la MIAH.

3.3.2 FCS-MPC con PWM (PC2)

PC1 selecciona un vector óptimo $\mathbf{S}^{opt}$ al minimizar la función de costo en (3.91). A diferencia de PC1, PC2 presentado en [100], usa el vector óptimo combinando con la teoría VSD para obtener ciclos de trabajo como sigue:

$$\tau = \frac{1}{2} + \frac{3}{4}\mathbf{M}_{[\mathbf{S}^{opt}]} \tag{3.93}$$

donde $\tau = [\tau_a,\, \tau_b,\, \tau_c,\, \tau_d,\, \tau_e,\, \tau_f]^T$ y $\mathbf{M}_{[\mathbf{S}^{opt}]}$ el modelo ideal del VSI en (3.7) con el vector óptimo seleccionado. Los ciclos de trabajo, definidos como τ, están relacionados con las fases del

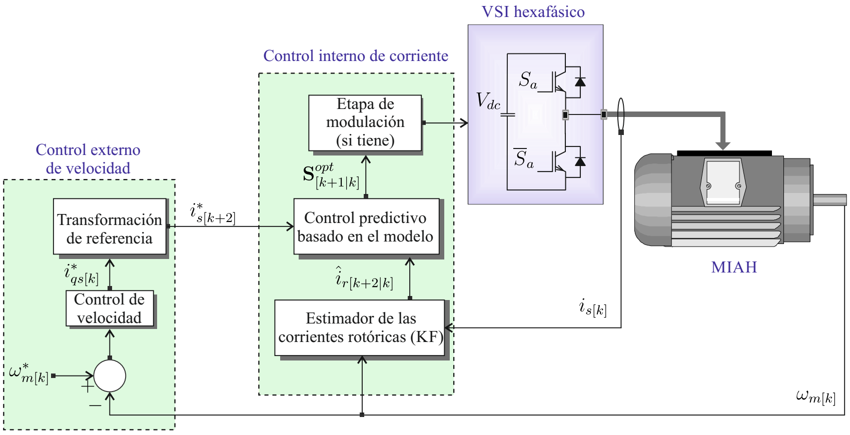

Figura 3.13 Diagrama en bloques del FCS-MPC aplicado a la MIAH.

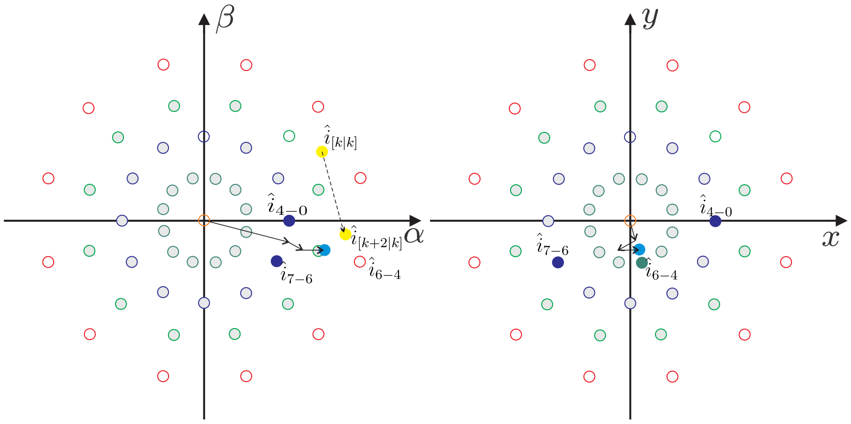

Figura 3.14 Predicciones de corrientes estatóricas proyectados por PC2 en los sub-espacios $(\alpha - \beta)$ y $(x - y)$.

VSI y están normalizadas entre 0 y 1. $\mathbf{S}^{opt}$ produce un cierto nivel de voltaje por cada fase y esta técnica, a través del cálculo de los ciclos de trabajo, permite al VSI para generar un valor similar de voltaje (75% del valor del vector óptimo) con una combinación de vectores espaciales. Esta técnica puede ser considerada como la aplicación de varios vectores para lograr reducir la amplitud de la amplitud del vector de voltaje con el fin de minimizar las corrientes estatóricas en el sub-espacio $(x - y)$ en un tiempo de muestreo mostrado en (con un ejemplo para el vector óptimo $6 - 4$) la **Figura 3.14**. Teniendo en cuenta el costo computacional, es un poco mayor a PC1, ya que la etapa de modulación tiene 90 FPO.

3.3.3 FCS-MPC con Reducción de Carga Computacional (PC3)

PC3 es una de las técnicas propuestas en esta Tesis y está basado en el convencional PC1, que selecciona el vector óptimo a través de la minimización de la función de costo en (3.91) para un tiempo de muestreo, y una técnica de vector restringido será aplicada en el siguiente tiempo de muestreo. El objetivo principal de esta técnica es reducir las corrientes estatóricas en el sub-espacio $(x - y)$ limitando la selección de vectores a una determinada región dependiendo del vector seleccionado anteriormente, con el fin de priorizar un vector óptio que generará un voltaje opuesto en el sub-espacio $(x - y)$. Sin embargo, esta técnica limitará la regulación de las corrientes estatóricas en el sub-espacio $(\alpha - \beta)$ debido a que PC3 restringe los vectores para reducir las corrientes $(x - y)$ [27, 101].

Como se muestra en la **Figura 3.15**, el sub-espacio $(x - y)$ puede ser dividido en cuatro regiones, donde cada región contiene 12 vectores de voltaje no redundantes. PC3 operará como un convencional PC1, donde el vector óptimo será seleccionado por la minimización de la función de

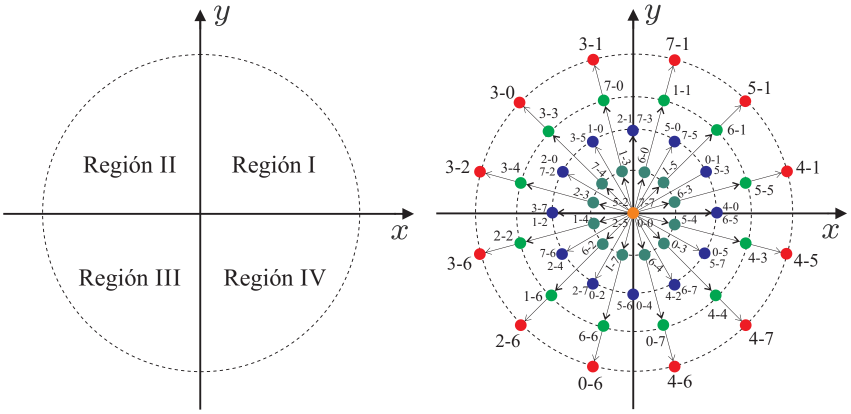

Figura 3.15 Vectores espaciales de voltaje en el sub-espacio $(x - y)$ determinado por PC3 para una MIAH.

costo. Entonces, el algoritmo reducirá los posibles vectores para el próximo tiempo de muestreo, a la región opuesta del anterior vector óptimo.

PC3 es una técnica de vectores de voltaje restringidos, por lo que el costo computacional es reducido debido a la limitación en las iteraciones en comparación a PC1, siendo un total de 61 iteraciones en dos tiempos de muestreo. Esta técnica reduce el costo computacional a aproximadamente 888 FPO en cada tiempo de muestreo.

3.3.4 FCS-MPC con Reducción Computacional y Etapa PWM (PC4)

PC4 es una combinación entre PC2 y PC3, donde hay una restricción de vectores de voltaje seleccionados y una modulación PWM aplicada en la etapa final del control, como se muestre en la **Figura 3.16**. El objetivo principal de esta técnica es mejorar la reducción de las corrientes estatóricas en el sub-espacio $(x - y)$ al combinar las dos técnicas y aún logrando una reducción del costo computacional similar a PC3, solo agregando 90 FPO por la etapa de modulación.

3.3.5 M2PC (PC5)

Esta técnica consiste en la determinación de cada sector del VSI hexafásico en el sup-espacio $(\alpha - \beta)$, siendo 48 sectores en total, que están compuestos de dos vectores activos adyacentes y un vector nulo (VZ), como se muestra en la **Figura 3.17**. Está técnica, basada en SVM, estima la predicción de dos vectores activos que conforman los 12 sectores externos en cada tiempo de muestreo y analiza sus respectivas funciones de costo (J_0, J_1 y J_2) de forma separada. Cada predicción es evaluada en (3.91) donde la única diferencia es el cálculo del vector de voltaje de entrada $\mathbf{u}(k)$ [31, 75].

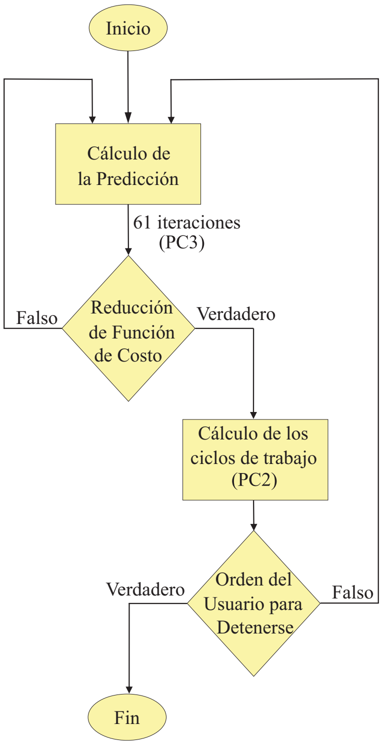

Figura 3.16 Diagrama en bloques del control PC4.

El objetivo principal de esta técnica de modulación es conseguir cualquier vector de voltaje en el sub-espacio ($\alpha - \beta$) usando los vectores largos (VL) y el VZ, cubriendo todo el espacio vectorial, y al mismo tiempo, considerar que los vectores externos son los más pequeños en el sub-espacio ($x - y$), logrando una reducción de las corrientes estatóricas en el sub-espacio ($x - y$) [26].

Los ciclos de trabajo, para los dos vectores activos d_1 y d_2, son obtenidos al resolver las siguientes ecuaciones, relacionados a sus respectivas funciones de costo (24 para cada tiempo de muestreo):

$$d_0 = \frac{\sigma}{\sqrt{J_0}} \qquad d_1 = \frac{\sigma}{\sqrt{J_1}} \qquad d_2 = \frac{\sigma}{\sqrt{J_2}} \tag{3.94}$$

$$d_0 + d_1 + d_2 = 1 \tag{3.95}$$

donde d_0 es el ciclo de trabajo del vector nulo. Entonces, es posible calcular la expresión de σ y los ciclos de trabajo para cada vector están dados por:

$$J_T = \sqrt{J_1}\sqrt{J_2} + \sqrt{J_0}\sqrt{J_1} + \sqrt{J_0}\sqrt{J_2} \tag{3.96}$$

$$d_0 = \frac{\sqrt{J_1}\sqrt{J_2}}{J_T} \tag{3.97}$$

$$d_1 = \frac{\sqrt{J_0}\sqrt{J_2}}{J_T} \tag{3.98}$$

$$d_2 = \frac{\sqrt{J_0}\sqrt{J_1}}{J_T} \tag{3.99}$$

Considerando estas ecuaciones, la función de costo final, que es calculada para 12 iteraciones durante T_s, es considerada como:

$$G_{[k+2|k]} = d_1\sqrt{J_1} + d_2\sqrt{J_2} \tag{3.100}$$

Los dos vectores, que reducen $G_{[k+2|k]}$, son seleccionados y aplicado al VSI hexafásico en el siguiente tiempo de muestreo. Luego de calcular los ciclos de trabajo para los dos vectores a ser aplicados, es necesario proponer una ecuación que relacione los ciclos de trabajo y los vectores de voltaje seleccionados, con el fin de implementar un PWM simétrico:

$$\tau_i = \frac{d_0}{2} + d_1 v_{1(i)} + d_2 v_{2(i)} \tag{3.101}$$

donde $i = [a, d, b, e, c, f]$ y τ_i es el ciclo de trabajo por fase (pata). Esta variable es comparada con una forma de onda triangular para obtener el PWM simétrico para cada transistor, consiguiendo una frecuencia fija de conmutación igual a la frecuencia de muestreo.

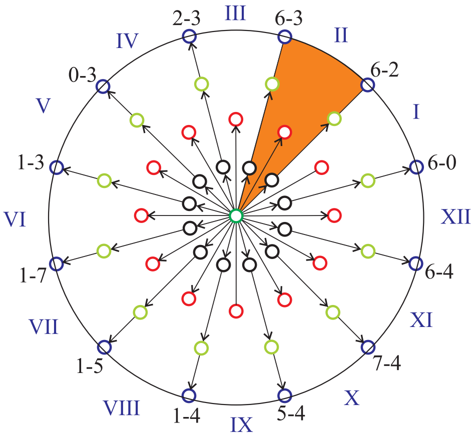

Figura 3.17 Sectores disponibles en un VSI hexafásico.

3.3.6 N-M2PC (PC6)

Así como el M2PC, N-M2PC está basado también en SVM y es un aporte de esta Tesis. La principal diferencia es que M2PC solo usa 2 VL por sector y N-M2PC usa 4 que incluyen 2 vectores medios (VM) y 2 VL. La principal meta de esta modulación es mejorar más el error en régimen permanente de las corrientes estatóricas en el sub-espacio $(d - q)$ al incluir los vectores adyacentes VM por sector con el fin de evitar el uso de VZ el cual limita el rango de voltaje. Esto es debido a que el vector óptimo deseado está dentro del sector correspondiente y la cierta combinación de vectores puede representar ese particular vector óptimo. Sin embargo, VZ reduce el rango con su ciclo de trabajo, limitando la capacidad del controlador en el seguimiento de las corrientes estatóricas en el sub-espacio $(\alpha - \beta)$, debido a que el ciclo de trabajo de VZ incrementa cuando las corrientes en $(x - y)$ buscan reducirse con M2PC. En resumen, N-M2PC no tiene la misma limitación que M2PC, ya que este no utilizar VZ y los vectores usados pueden obtener cualquier punto en el área superior del sub-espacio $(\alpha - \beta)$.

Los ciclos de trabajo, para los cuatro vectores activos d_1, d_2, d_3 y d_4, son obtenidos al resolver las siguientes ecuaciones:

$$d_1 = \frac{\sigma}{\sqrt{J_1}} \quad d_2 = \frac{\sigma}{\sqrt{J_2}} \quad d_3 = \frac{\sigma}{\sqrt{J_3}} \quad d_4 = \frac{\sigma}{\sqrt{J_4}} \tag{3.102}$$

$$d_1 + d_2 + d_3 + d_4 = 1 \tag{3.103}$$

donde J_1, J_2, J_3 y J_4 son las correspondientes funciones de costo (3.91) de los vectores para cada sector. Así como en M2PC, es posible calcular la expresión para σ y los ciclos de trabajo para cada vector son dados por:

$$J_{T1} = \sqrt{J_1}\sqrt{J_3}\sqrt{J_4} + \sqrt{J_2}\sqrt{J_3}\sqrt{J_4} \tag{3.104}$$

$$J_{T2} = \sqrt{J_1}\sqrt{J_2}\sqrt{J_4} + \sqrt{J_1}\sqrt{J_2}\sqrt{J_3} \tag{3.105}$$

$$d_1 = \frac{\sqrt{J_2}\sqrt{J_3}\sqrt{J_4}}{J_{T1} + J_{T2}} \tag{3.106}$$

$$d_2 = \frac{\sqrt{J_1}\sqrt{J_3}\sqrt{J_4}}{J_{T1} + J_{T2}} \tag{3.107}$$

$$d_3 = \frac{\sqrt{J_1}\sqrt{J_2}\sqrt{J_4}}{J_{T1} + J_{T2}} \tag{3.108}$$

$$d_4 = \frac{\sqrt{J_1}\sqrt{J_2}\sqrt{J_3}}{J_{T1} + J_{T2}} \tag{3.109}$$

N-M2PC evalúa todos los 12 sectores, como se aprecia en la **Figura 3.18**, al calcular las funciones de costo correspondientes (48 en total), luego los ciclos de trabajo para cada vector son calculados como en M2PC, por último, la función de costo final es computado como sigue:

$$G_{[k+2|k]} = d_1\sqrt{J_1} + d_2\sqrt{J_2} + d_3\sqrt{J_3} + d_4\sqrt{J_4} \tag{3.110}$$

Se puede notar que los VM usados para obtener los 12 sectores son los redundantes, dando la posibilidad para seleccionar cada uno de los vectores con el fin de lograr un cierto patrón de

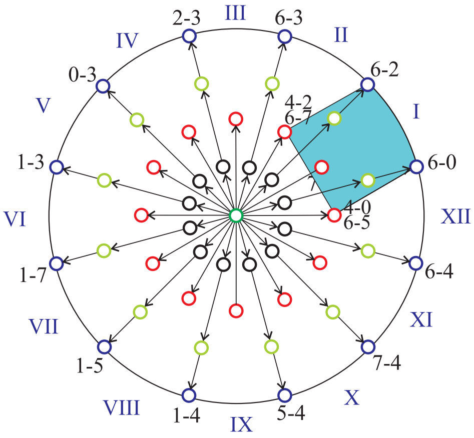

Figura 3.18 Sectores disponibles para N-M2PC para el VSI hexafásico.

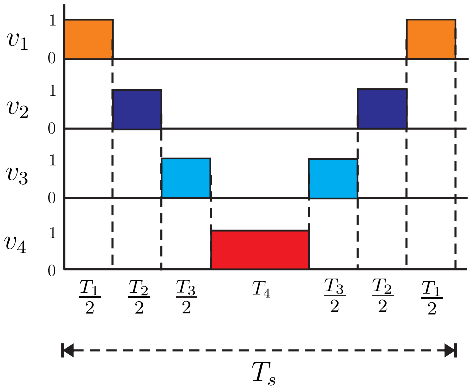

Figura 3.19 Patrón de conmutación para los vectores óptimos seleccionados.

conmutación, como el mostrado en la **Figura 3.19**. Esto permite el uso de una simple ecuación para calcular los ciclos de trabajo $\tau_{(i)}$ para cada transistor de cada pata del VSI, como sigue:

$$\tau_{(i)} = d_1 v_{1(i)} + d_2 v_{2(i)} + d_3 v_{3(i)} + d_4 v_{4(i)} \tag{3.111}$$

donde $\tau_{(i)}$ está normalizado entre 0 and 1, para los transistores de cada pata del VSI. Por último, una forma de onda triangular es usada para aplicar el valor de $\tau_{(i)}$ en los correspondientes transistores.

3.3.7 Análisis de Estabilidad del FCS-MPC

El análisis de estabilidad del MPC es el último aporte de esta Tesis. Ejemplos de variantes de MPC son bastante conocidos en la literatura, los cuales presentan propiedades comunes que permiten formalizar el análisis de estabilidad [102]. Una función candidata de Lyapunov es comúnmente considerada como un método popular para probar la estabilidad del MPC. Otro enfoque considerado, presentado en [27, 103, 104] consiste en estimar una cierta ganancia $\mathbf{L}(k)$ con el fin de obtener una matriz estable $(\mathbf{A}(k) - \mathbf{B}(k)\mathbf{L}(k))$ cuyos autovalores sean menores a 1. El segundo método es más práctico debido a su simplicidad y al considerar que MPC tiene un número finito de esfuerzo de control, por ejemplo: 49 vectores de voltaje en el caso de la MIAH. Para una limitada corriente de referencia (debido a criterios de seguridad), existe un número finito de $\mathbf{L}(k)$ que a través de la minimización de la función de costo puede mostrar un comportamiento similar en términos de estabilidad local al analizar distintos escenarios, tales como valores típicos de velocidades rotóricas y frecuencias de muestreo (F_s).

$$\mathbf{u}(k) = -\mathbf{L}(k)\mathbf{X}(k) \tag{3.112}$$

donde $\mathbf{L}(k)$ es seleccionado como sigue:

$$\mathbf{L}(k) = \begin{bmatrix} L_1 & L_2 & 0 & 0 & L_3 & L_4 \\ -L_2 & L_1 & 0 & 0 & -L_4 & L_3 \\ 0 & 0 & L_5 & L_6 & 0 & 0 \\ 0 & 0 & -L_6 & L_5 & 0 & 0 \end{bmatrix}$$

Es considerado un rango limitado de $[-3.5, 3.5]$ A para variables de estado ($\mathbf{X}(k)$), considerando el teorema de separación los autovalores en lazo cerrado son la unión de las variables observadas y realimentadas asumiendo variables medidas en su totalidad, y valores finitos del vector de entrada ($\mathbf{u}(k)$), por ejemplo: 49 distintos valores para la MIAH, un número finito de $\mathbf{L}(k)$ es encontrado por medio de una búsqueda exhaustiva, como se muestra en la **Tabla 3.7**. Al mismo tiempo, la **Tabla 3.8** presenta el máximo valor de velocidad rotórica estable (autovalores dentro del círculo unitario) a distintas frecuencias de muestreo para PC1, PC5 y PC6. Cabe mencionar que PC2, PC3 y PC4 no son tenidos en cuenta por su alta similitud en términos de estabilidad con PC1, por lo que solo PC1 será evaluada junto a PC5 y PC6. Por último, los autovalores de la matriz $(\mathbf{A}(k) - \mathbf{B}(k)\mathbf{L}(k))$ a

Tabla 3.7 Rango de valores de distintas ganancias ($\mathbf{L}(k)$) para PC1, PC5 y PC6.

Ganancias	PC1	PC5	PC6
L_1	$[-10, 10]$	$[-10, 10]$	$[-10, 10]$
L_2	$[-40, 40]$	$[-40, 40]$	$[-40, 40]$
L_3	$[-155, -150]; [-80, -70]$	$[-150, 10]$	$[-760, -300]$
L_4	$[-40, 40]$	$[-40, 40]$	$[-40, 40]$
L_5	$[-10, 10]$	$[-10, 10]$	$[-10, 10]$
L_6	$[-40, 40]$	$[-40, 40]$	$[-40, 40]$

Tabla 3.8 Análisis teórico de estabilidad de PC1, PC5 y PC6 y sus máximas velocidades estables (rpm).

F_s (kHz)	PC1	PC5	PC6
	Máxima Velocidad Estable		
2	700	850	250
2.5	850	1000	550
4	1100	1300	1250
5	1250	1400	1650
7.5	1600	1700	2800
8	1700	1850	2850
10	1900	2000	3000
12.5	2400	2300	3000
15	2600	2600	3000
16	2700	2700	3000
17.5	2800	2800	3000
20	3000	3000	3000

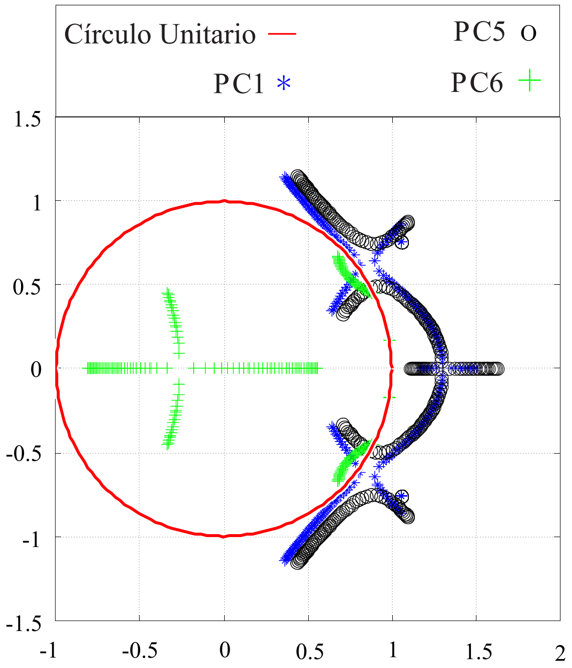

Figura 3.20 Autovalores de $(\mathbf{A}(k) - \mathbf{B}(k)\mathbf{L}(k))$ matrix a 10 kHz de frecuencia de muestreo y velocidad rotórica de 2500 rpm para PC1, PC5 y PC6.

10 kHz de frecuencia de muestreo y velocidad rotórica de 2500 rpm para las tres técnicas mostradas en la **Figura 3.20** donde, a esas condiciones, PC6 es el único controlador cuyos autovalores se encuentran dentro del círculo unitario.

3.3.8 Análisis Experimental de las Aportaciones al FCS-MPC

Las técnicas propuestas (PC1, PC2, PC3, PC4, PC5 y PC6) fueron probadas en la misma bancada experimental, que las secciones anteriores, para validar su desempeño. Los parámetros son los mismos que en la **Tabla 3.1**. La función de costo definida en 3.91) con λ_{xy} = 0.05 fue seleccionda para evaluar el desempeño de PC1, PC2, PC3, PC4 y PC5, ya que la influencia en su desempeño es mínima, dando más prioridad al seguimiento de las corrientes estatóricas en el sub-espacio $(\alpha - \beta)$ sobre la reducción de las corrientes $(x - y)$. En cuanto a PC6, fue seleccionada λ_{xy} = 0.1, ya que este no usa el vector nulo y la reducción de las corrientes en el sub-espacio $(x - y)$ es realizado por la combinación de cuatro vectores activos. Cabe mencionar que estos valores de λ_{xy} fueron seleccionados por un método heurístico buscando una solución sub-óptima. Los ruidos de proceso y medición fueron calculados por medio de un método de autocovanizanza mediante mínimos cuadrados, con el fin de sintonizar el KF de manera óptima, por medio de la colección de datos de la operación en lazo cerrado del sistema y usando dicho método propuesto en [95].

Análisis de Régimen Permanente En primer lugar, se realiza una comparativa entre PC1 a PC6, en las mismas condiciones de carga mecánica mediante un freno por corrientes de Foucault de 5 CV a diferentes velocidades rotóricas (ω_m). **Tabla 3.9** reporta los resultados experimentales obtenidos para PC1, a distintas velocidades rotóricas y frecuencias de muestreo, respecto al MSE y THD de las corrientes estatóricas en los sub-espacios $(\alpha - \beta)$ y $(x - y)$. Los resultados demuestran un buen seguimiento de las corrientes de referencia en el sub-espacio $(\alpha - \beta)$, pero una limitada reducción de las corrientes estatóricas en el sub-espacio $(x - y)$. La **Tabla 3.10** expone los resultados para PC2, considerando el MSE y THD de las corrientes estatóricas. Para PC2, hay una mejora en la reducción de las corrientes estatóricas en $(x - y)$ sobre PC1 de un 24 $\%$ en promedio, pero hay un decremento del seguimiento de las corrientes en $(\alpha - \beta)$ en un 21 $\%$ aproximadamente. La **Tabla 3.11** muestra los resultados del desempeño del sistema con PC3. Por la comparativa entre PC3 y PC1, hay una mejora del 13 $\%$ en promedio con respecto a la reducción de las corrientes estatóricas en el sub-espacio $(x - y)$, sin embargo, muestra un decremento en el seguimiento de las corrients en $(\alpha - \beta)$ en un 41 $\%$. Por último se presenta en la **Tabla 3.12** los resultados para PC4 a diferentes velocidades rotóricas y frecuencias de muestreo. Si los resultados son comparados con PC1, hay una mejora del 30 $\%$ en promedio para la reducción de las corrientes estatóricas en el sub-espacio $(x - y)$ y un decremento del seguimiento en las corrientes $(\alpha - \beta)$ en un 52 $\%$.

Las **Tablas 3.13** y **3.14** muestran los resultados del desempeño del sistema con PC5 y PC6 respectivamente. En ambos casos hay una notoria reducción de las corrientes $(x - y)$ en comparación con PC1 en un 79 $\%$ y 67 $\%$ en promedio respectivamente, mostrando una superioridad de ambas técnicas con respecto a las demás. En cuanto al seguimiento de las corrientes en $(\alpha - \beta)$, PC5 muestra una notoria mejora en comparación a PC1 a baja frecuencia de muestreo en aproximadamente un

Tabla 3.9 Análisis de desempeño de las corrientes estatóricas ($\alpha - \beta$), ($x - y$), MSE (A), THD ($\%$) para PC1 a diferentes velocidades rotóricas (rpm).

Frecuencia de muestreo a 12 kHz						
ω_m^*	MSE$_\alpha$	MSE$_\beta$	MSE$_x$	MSE$_y$	THD$_\alpha$	THD$_\beta$
500	0.0856	0.0874	0.6008	0.5859	8.31	8.64
1000	0.0975	0.0952	0.7127	0.7293	6.84	6.87
1500	0.0988	0.1006	0.7344	0.7140	5.86	6.06
Frecuencia de muestreo a 16 kHz						
ω_m^*	MSE$_\alpha$	MSE$_\beta$	MSE$_x$	MSE$_y$	THD$_\alpha$	THD$_\beta$
500	0.0717	0.0730	0.4707	0.4747	8.90	8.96
1000	0.0853	0.0855	0.5505	0.5538	6.20	6.17
1500	0.0783	0.0790	0.5736	0.5710	4.40	4.47
Frecuencia de muestreo a 20 kHz						
ω_m^*	MSE$_\alpha$	MSE$_\beta$	MSE$_x$	MSE$_y$	THD$_\alpha$	THD$_\beta$
500	0.0641	0.0661	0.4137	0.4103	6.48	7.14
1000	0.0745	0.0791	0.4764	0.4813	5.46	5.83
1500	0.0726	0.0737	0.4701	0.4649	4.10	4.32

Tabla 3.10 Análisis de desempeño de las corrientes estatóricas ($\alpha - \beta$), ($x - y$), MSE (A), THD ($\%$) para PC2 a diferentes velocidades rotóricas (rpm).

Frecuencia de muestreo a 12 kHz						
ω_m^*	MSE$_\alpha$	MSE$_\beta$	MSE$_x$	MSE$_y$	THD$_\alpha$	THD$_\beta$
500	0.1259	0.1095	0.4862	0.4796	13.20	11.52
1000	0.1100	0.1010	0.5360	0.5380	7.66	7.10
1500	0.1539	0.1465	0.5092	0.5547	10.19	9.67
Frecuencia de muestreo a 16 kHz						
ω_m^*	MSE$_\alpha$	MSE$_\beta$	MSE$_x$	MSE$_y$	THD$_\alpha$	THD$_\beta$
500	0.0827	0.0807	0.3801	0.3652	9.83	9.38
1000	0.0927	0.0886	0.4086	0.4058	6.75	6.53
1500	0.1102	0.1075	0.4685	0.4627	5.23	5.34
Frecuencia de muestreo a 20 kHz						
ω_m^*	MSE$_\alpha$	MSE$_\beta$	MSE$_x$	MSE$_y$	THD$_\alpha$	THD$_\beta$
500	0.0944	0.0877	0.3262	0.3139	10.75	10.23
1000	0.1072	0.1025	0.3566	0.3677	7.59	7.10
1500	0.1114	0.1096	0.4202	0.4271	5.74	5.63

Tabla 3.11 Análisis de desempeño de las corrientes estatóricas $(\alpha - \beta)$, $(x - y)$, MSE (A), THD (%) para PC3 a diferentes velocidades rotóricas (rpm).

Frecuencia de muestreo a 12 kHz						
ω_m^*	MSE$_\alpha$	MSE$_\beta$	MSE$_x$	MSE$_y$	THD$_\alpha$	THD$_\beta$
500	0.1699	0.1749	0.4996	0.5063	16.25	16.80
1000	0.2162	0.2203	0.5759	0.5867	12.99	13.07
1500	0.2734	0.2722	0.6339	0.6288	11.45	11.89
Frecuencia de muestreo a 16 kHz						
ω_m^*	MSE$_\alpha$	MSE$_\beta$	MSE$_x$	MSE$_y$	THD$_\alpha$	THD$_\beta$
500	0.1419	0.1386	0.3983	0.4023	14.55	15.01
1000	0.1798	0.1826	0.4800	0.4792	11.24	11.12
1500	0.2133	0.2195	0.5225	0.5345	9.98	9.96
Frecuencia de muestreo a 20 kHz						
ω_m^*	MSE$_\alpha$	MSE$_\beta$	MSE$_x$	MSE$_y$	THD$_\alpha$	THD$_\beta$
500	0.1101	0.1223	0.3525	0.3547	11.34	12.74
1000	0.1444	0.1557	0.4051	0.4197	9.33	10.11
1500	0.1935	0.1827	0.4504	0.4648	8.33	8.58

Tabla 3.12 Análisis de desempeño de las corrientes estatóricas $(\alpha - \beta)$, $(x - y)$, MSE (A), THD (%) para PC4 a diferentes velocidades rotóricas (rpm).

Frecuencia de muestreo a 12 kHz						
ω_m^*	MSE$_\alpha$	MSE$_\beta$	MSE$_x$	MSE$_y$	THD$_\alpha$	THD$_\beta$
500	0.2544	0.2125	0.3685	0.3844	22.32	17.70
1000	0.2627	0.2528	0.4467	0.4587	13.80	13.36
1500	0.3440	0.3262	0.4961	0.4908	17.42	16.71
Frecuencia de muestreo a 16 kHz						
ω_m^*	MSE$_\alpha$	MSE$_\beta$	MSE$_x$	MSE$_y$	THD$_\alpha$	THD$_\beta$
500	0.1716	0.1605	0.3057	0.2980	14.23	13.30
1000	0.2113	0.1934	0.3909	0.3742	10.62	9.85
1500	0.2882	0.2846	0.4814	0.4773	9.82	9.58
Frecuencia de muestreo a 20 kHz						
ω_m^*	MSE$_\alpha$	MSE$_\beta$	MSE$_x$	MSE$_y$	THD$_\alpha$	THD$_\beta$
500	0.1641	0.1463	0.2856	0.2695	15.28	13.51
1000	0.1937	0.1817	0.3376	0.3545	11.30	10.49
1500	0.2895	0.2719	0.4689	0.4668	10.31	9.62

Tabla 3.13 Análisis de desempeño de las corrientes estatóricas $(\alpha - \beta)$, $(x - y)$, MSE (A), THD $(\%)$ para PC5 a diferentes velocidades rotóricas (rpm).

Frecuencia de muestreo a 8 kHz						
ω_m^*	MSE$_\alpha$	MSE$_\beta$	MSE$_x$	MSE$_y$	THD$_\alpha$	THD$_\beta$
500	0.0562	0.0592	0.1241	0.1130	5.33	5.45
1000	0.0861	0.0903	0.1485	0.1545	7.35	7.41
1500	0.1039	0.0958	0.1960	0.1944	8.18	8.14
Frecuencia de muestreo a 16 kHz						
ω_m^*	MSE$_\alpha$	MSE$_\beta$	MSE$_x$	MSE$_y$	THD$_\alpha$	THD$_\beta$
500	0.1046	0.1094	0.1332	0.1334	10.55	10.67
1000	0.1037	0.1059	0.1401	0.1417	10.14	10.20
1500	0.0972	0.0986	0.1038	0.1069	8.08	8.12

Tabla 3.14 Análisis de desempeño de las corrientes estatóricas $(\alpha - \beta)$, $(x - y)$, MSE (A), THD $(\%)$ para PC6 a diferentes velocidades rotóricas (rpm).

Frecuencia de muestreo a 8 kHz						
ω_m^*	MSE$_\alpha$	MSE$_\beta$	MSE$_x$	MSE$_y$	THD$_\alpha$	THD$_\beta$
500	0.1977	0.1998	0.2490	0.2553	15.74	15.82
1000	0.2135	0.2159	0.2659	0.2684	14.37	14.47
1500	0.1983	0.1924	0.3012	0.2956	18.02	17.94
Frecuencia de muestreo a 16 kHz						
ω_m^*	MSE$_\alpha$	MSE$_\beta$	MSE$_x$	MSE$_y$	THD$_\alpha$	THD$_\beta$
500	0.1004	0.1003	0.2009	0.2130	9.95	9.95
1000	0.1051	0.1049	0.2091	0.2064	9.75	9.71
1500	0.1030	0.1097	0.2172	0.2125	9.74	9.82

47 $\%$ en promedio, sin embargo a mayor frecuencia de muestreo y mayores velocidades su capacidad de reduce en un 23 $\%$. Por otra parte, PC6 tiene un decremento en capacidad de seguimiento de las corrientes en $(\alpha - \beta)$ con respecto a PC1 en un 50 $\%$ y 25 $\%$ en promedio para baja y alta frecuencia de muestreo respectivamente.

La **Figura 3.21** expone las trayectorias polares de las corrientes estatóricas en los sub-espacios $(\alpha - \beta)$ y $(x - y)$. Los resultados obtenidos para PC1, PC2, PC3, PC4, PC5 y PC6 son mostrados en la **Figura 3.21(a)**, **3.21(b)**, **3.21(c)**, **3.21(d)**, **3.21(e)** y **3.21(f)** respectivamente. Las operaciones

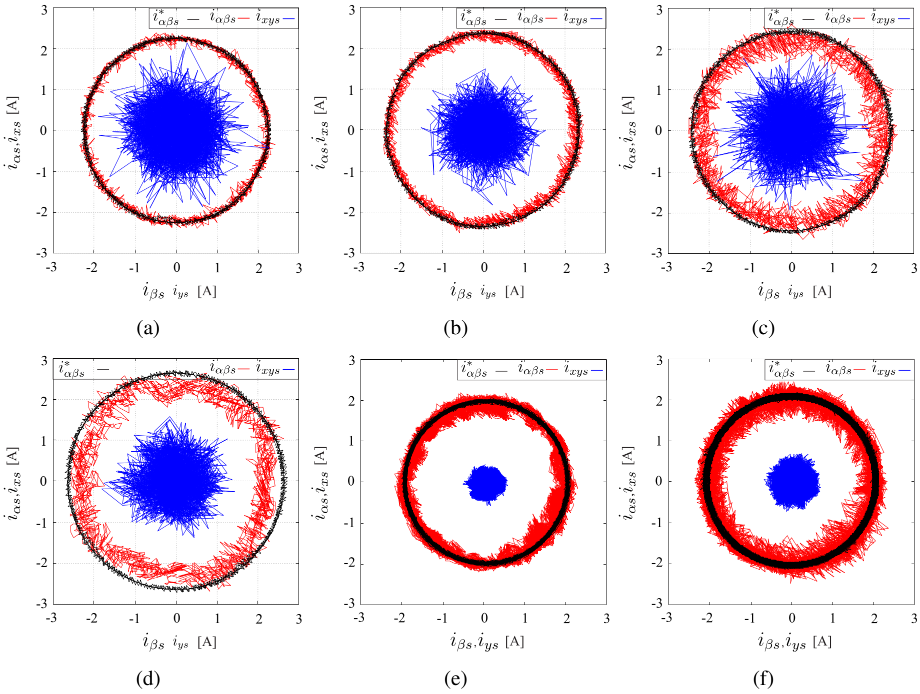

(a) (b) (c)

(d) (e) (f)

Figura 3.21 Corrientes estatóricas en los sub-espacios $(\alpha - \beta)$ y $(x - y)$ para una velocidad rotórica de 1500 rpm para: (a) PC1; (b) PC2; (c) PC3; (d) PC4; (e) PC5; (f) PC6.

fueron realizadas con distintas corrientes parásitas para obtener una misma amplitud de las corrientes $(\alpha - \beta)$ a distintas velocidades mecánicas.

Por otra parte, la **Tabla 3.15** muestra el costo computacional de las seis técnicas predictivas probadas en términos de FPO, donde PC2 tiene el más alto costo, mientras que PC5 tiene el menor costo computacional.

Análisis Transitorio Para una condición transitoria, un cambio escalón en la velocidad mecánica es realizad desde 500 a -500 rpm (condición reversa). La **Figura 3.22** expone una prueba dinámica (efecto en la corriente i^*_{qs}), el cual consiste en el comportamiento transitorio de todas las técnicas analizadas. Las **Figuras 3.22(a)**, **3.22(b)**, **3.22(c)**, **3.22(d)**, **3.22(e)** y **3.22(f)** muestran el compor-

Tabla 3.15 Costo computacional de todas las técnicas probadas en términos de FPO.

MPC	PC1	PC2	PC3	PC4	PC5	PC6
FPO	2 802	2 892	1 914	2 004	1968	2736

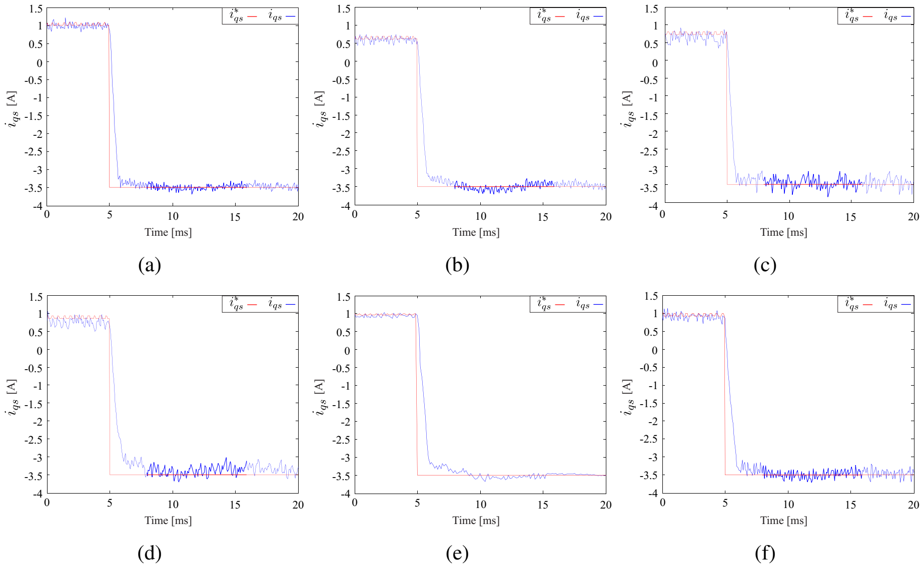

(a) (b) (c) (d) (e) (f)

Figura 3.22 Respuesta escalón transitoria de i_{qs} de un cambio escalón de velocidad ω_m de 500 a -500 rpm.: (a) PC1; (b) PC2; (c) PC3; (d) PC4; (e) PC5; (f) PC6.

tamiento transitorio para PC1, PC2, PC3, PC4, PC5 y PC6 respectivamente donde los tiempos de respuesta son aproximadamente 1 ms, 3.5 ms, 1 ms, 3.5 ms, 4 ms y 3 ms respectivamente.

Análisis de Estabilidad En todos los casos, el voltaje DC es considerado a 700 V. Las frecuencias de muestreo, en todas las pruebas son de 2.5 kHz, 5 kHz, 7.5 kHz, 10 kHz, 12.5 kHz, 15 kHz,

Tabla 3.16 Análisis de estabilidad de PC1, PC5 y PC6 considerando sus máximas velocidades estables (rpm).

F_s (kHz)	PC1	PC5	PC6
	Máxima Velocidad Estable		
2.5	400	700	300
5	900	1100	1400
7.5	1200	1400	2800
10	1800	2000	3000
12.5	2250	2300	3000
15	2600	2600	3000
17.5	3000	2800	3000
20	3000	3000	3000

Tabla 3.17 Frecuencia de conmutación promedio (kHz) de PC1, PC5 y PC6 a sus velocidades máximas estables (rpm) y frecuencias de muestreo (kHz).

F_s (kHz)	PC1	PC5	PC6
	Frecuencia de Conmutación Promedio		
2.5	0.7	2.5	0.4
5	1.4	5	0.8
7.5	2.1	7.5	1.1
10	2.5	10	1.4
12.5	3.2	12.5	1.6
15	3.5	15	1.9
17.5	3.7	17.5	2
20	4.2	20	2.2

17.5 kHz y 20 kHz. La **Tabla 3.16** muestra los resultados experimentales obtenidos a diferentes frecuencias de muestreo para PC1, PC5 y PC6, respecto a sus máximas velocidades rotóricas estables, presentando resultados similares al análisis teórico. Al mismo tiempo, la **Tabla 3.17** presenta la frecuencia de conmutación promedio a diferentes frecuencias de muestreo para PC1, PC5 y PC6. Por último, la **Figura 3.23(a)** y **Figura 3.23(b)** muestran los gráficos de tendencia de las máximas velocidades rotóricas estables y la frecuencia de conmutación promedio para PC1, PC5 y PC6 a diferentes frecuencias de muestreo. Los resultados muestran que PC6 tiene el mejor desempeño en términos de estabilidad local con la máxima velocidad rotórica de la MIAH, donde a baja frecuencia de muestreo los desempeños no son muy diferentes entre PC1 y PC5, pero a mayor frecuencia de muestreo, PC6 puede operar en todo el rango de velocidad nominal de la MIAH, pero para

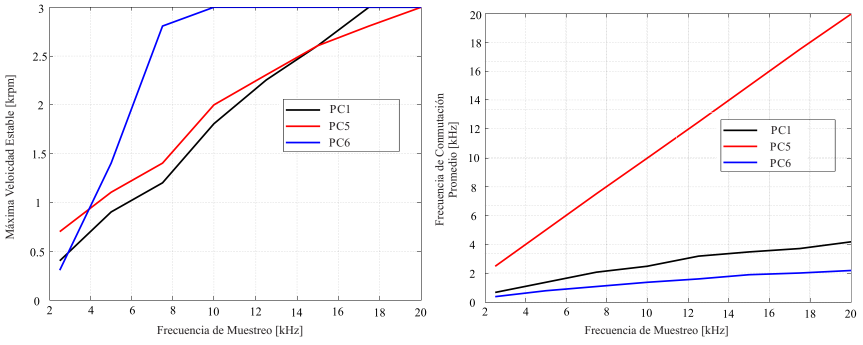

(a) (b)

Figura 3.23 Gráfico de tendencias de PC1, PC5 y PC6 con respecto a diferentes velocidades de muestreo y la: (a)velocidad mecánica rotórica; (b)frecuencia de conmutación promedio.

PC1 y PC5, tienden a mejorar linealmente la estabilidad local a mayores frecuencias de muestreo donde PC1 tiene una pendiente más pronunciada que PC5. Sin embargo, PC1 y PC6 son técnicas de frecuencia de conmutación variable, por lo que la frecuencia de conmutación es más baja que con PC5, donde PC6 tiene casi la mitad del valor de frecuencia de conmutación promedio que PC1, empeorando su desempeño en términos de THD de corrientes estatóricas pero mejorando las pérdidas de conmutación en el VSI hexafásico.

3.3.9 Discusión de los Resultados

Un control interno de corriente robusto basado en seis variantes del MPC con KF fueron presentados para controlar las corrientes estatóricas en los sub-espacios $(\alpha - \beta)$ y $(x - y)$ de una MIAH con un control externo de velocidad. Como se presentan en los resultados, PC5 es una excelente alternativa en términos de seguimiento de las corrientes en $(\alpha - \beta)$ y reducción de las corrientes en $(x - y)$. Sin embargo, existe una limitación en términos de altas velocidades mecánicas, donde PC5 empeora en su desempeño, debido al uso del vector nulo y además al poseer una frecuencia de conmutación fija y mayor a los demás controladores, este tiene mayores pérdidaes de conmutación. Por otra parte, PC6 prueba ser una gran alternativa a los demás controles, especialmente a mayores velocidades mecánicas, donde su frecuencia de conmutación es baja, probando tener menos pérdidas de conmutación pero logrando un buen desempeño en términos de MSE y THD de las corrientes estatóricas, además de ser un control robusto con comportamiento estable incluso a altas velocidades. En condición transitoria, los resultados muestran un buen comportamiento en términos de velocidad de respuesta, donde PC1 y PC3 son los más rápidos, seguido por PC6. En resumen, PC5 presenta un excelente desempeño para ser una gran alternativa a controles clásicos en bajas velocidades mecánicas (hasta 1500 rpm (25 Hz, 1 par de polos) y PC6 prueba ser una gran alternativa para mayores velocidades (encima de 1500 rpm) para aplicaciones industriales.

3.4 Conclusiones del Capítulo

Se han presentado con detalles las aportaciones realizadas en el marco de esta Tesis Doctoral. Los resultados experimentales muestran que los controles DSMC y DSTC son válidas alternativas para el control de la MIAH en aplicaciones industriales de baja y media velocidad, siendo DSTC una versión más robusta y con mejores prestaciones. Al mismo tiempo, de las técnicas FCS-MPC propuestas se pueden resaltar al PC5 y PC6 como válidas alternativas para bajas y altas velocidades de operación respectivamente, siendo PC6 la mejor versión considerando la estabilidad absoluta del sistema. Como producto se ha logrado la publicación de 5 artículos en revistas internacionales arbitradas e indexadas del primer cuartil (Q1), y se ha colaborado en materia de difusión de los resultados de la investigación en 4 conferencias internacionales arbitradas e indexadas.

CAPÍTULO 4

CONCLUSIONES Y TRABAJOS FUTUROS

4.1 Conclusiones

Esta Tesis Doctoral ha abordado el desarrollo de algoritmos de control no lineales aplicados a la MIAH. Las principales contribuciones han sido puestas de manifiesto en el Capítulo 3. Sin embargo a modo realizar una síntesis de las aportaciones, en el presente apartado se resumen las principales conclusiones:

- Se propuso nuevos esquemas de control no lineales, basados en la teoría de control deslizante, empleados en MIAH. Este objetivo fue logrado por medio de las contribuciones [Cont-1] y [Cont-2].

- Se validaron los nuevos esquemas de control no lineales, basados en la teoría de control deslizante, empleados en MIAH. Se observó que el método de control que ha sido denominado DSTC se constituye como una alternativa para aplicaciones industriales de baja velocidad, arrojando como resultado un desempeño óptimo con mucha robustez contra las perturbaciones externas. Este objetivo fue logrado por medio de las contribuciones [Cont-1] y [Cont-2].

- Se diseñaron nuevos esquemas de control no lineales, basados en la teoría de control predictivo, empleados en MIAH. Este objetivo fue logrado por medio de las contribuciones [Cont-3] y [Cont-4].
- Se validaron los nuevos esquemas de control no lineales, basados en la teoría de control predictivo, empleados en MIAH. Se comprobó teórica y experimentalmente que el método de control, que ha sido denominado M2PC es una propuesta válida para aplicaciones industriales en las cuales se requiere que el accionamiento opere a baja velocidad. En contraparte, el método denominado N-M2PC, ha arrojado buenos resultados a alta velocidad, demostrando un excelente desempeño dinámico y un mayor margen de estabilidad, analizado desde el punto de vista de los puntos de operación del sistema. Este objetivo fue logrado por medio de las contribuciones [Cont-3] y [Cont-4].
- Se ha desarrollado una propuesta válida para el análisis de estabilidad de las técnicas de control predictivo propuestas, y se ha validado esta propuesta mediante resultados experimentales. Este objetivo fue logrado por medio de la contribución [Cont-5].
- Los resultados obtenidos han dado como resultado varios artículos en conferencias internacionales y en revistas internacionales indexadas de alto impacto (Q1). La **Tabla 4.1** contiene un resumen de los artículos. Estas publicaciones validan las aportaciones realizadas en el marco de esta Tesis Doctoral.

Producción/Actividad	Número
Artículos de revista internacional Q1 como autor principal	3
Artículos de revista internacional Q1 como co-autor	3
Artículos de conferencia internacional como autor principal	1
Artículos de conferencia internacional como co-autor	3
Participación en proyectos de I+D	2
Realización de estancia internacional	1
Disertación en congresos nacionales e internacionales	2
Revisión de artículos científicos	12

Tabla 4.1 Resumen de cantidad de publicaciones logradas en revistas y conferencias internacionales arbitradas e indexadas, y otros logros.

4.2 Trabajos Futuros

El desarrollo de controladores no lineales aplicado a los accionamientos de máquinas de inducción asimétricas hexafásicas es un tema de investigación que ha sido escasamente abordado en la literatura. Por dicho motivo existen varios tópicos que pueden profundizarse dentro de esta línea, entre los que se citan los más relevantes que se desprende de esta Tesis Doctoral:

- Validar los desempeños de las técnicas de control abordadas en el marco de esta Tesis Doctoral, en la zona de debilitamiento de campo.
- Extender el estudio de las técnicas de control abordadas en el marco de esta Tesis Doctoral a máquinas de inducción multifásicas con distinta topologia, como la simétrica hexafásica.
- Extender el estudio de las técnicas de control abordadas en el marco de esta Tesis Doctoral, a algoritmos de control post-falta.
- Extender el estudio teórico y experimental de las técnicas de control abordadas en el marco de esta Tesis Doctoral, al control tipo sin sensor de velocidad en máquinas multifásicas.

REFERENCIAS

1. E. Levi, “Advances in converter control and innovative exploitation of additional degrees of freedom for multiphase machines,” *IEEE Trans. Ind. Electron.*, vol. 63, no. 1, pp. 433–448, 2016.
2. I. Subotic, N. Bodo, E. Levi, B. Dumnic, D. Milicevic, and V. Katic, “Overview of fast on-board integrated battery chargers for electric vehicles based on multiphase machines and power electronics,” *Elect. Power Appl.*, vol. 10, no. 3, pp. 217–229, 2016.
3. C. Kalaivani and K. Rajambal, “Modeling and analysis of multiphase induction generator,” in *Proc. ICCPCT*. IEEE, 2016, pp. 1–6.
4. M. Tsili and S. Papathanassiou, “A review of grid code technical requirements for wind farms,” *IET Renewable power generation*, vol. 3, no. 3, pp. 308–332, 2009.
5. H. Jadhav and R. Roy, “A comprehensive review on the grid integration of doubly fed induction generator,” *International Journal of Electrical Power & Energy Systems*, vol. 49, pp. 8–18, 2013.
6. M. J. Duran and F. Barrero, “Recent advances in the design, modeling, and control of multiphase machines: Part II,” *IEEE Trans. Ind. Electron.*, vol. 63, no. 1, pp. 459–468, 2016.
7. F. Barrero and M. J. Duran, “Recent advances in the design, modeling, and control of multiphase machines: Part I,” *IEEE Trans. Ind. Electron.*, vol. 63, no. 1, pp. 449–458, 2016.

8. R. Gregor, J. Rodas, D. Gregor, and F. Barrero, *Reduced-order observer analysis in MBPC techniques applied to the six-phase induction motor drives*. INTECH Open Science, 2015.
9. H. S. Che et al., "Post fault operation of an asymmetrical six-phase induction machine with single and two isolated neutral points," *IEEE Trans. Power Electron.*, vol. 29, no. 10, pp. 5406–5416, 2014.
10. H. S. Che et al, "Operation of a six-phase induction machine using series connected machine-side converters," *IEEE Trans. Ind. Electron.*, vol. 61, no. 1, pp. 595–605, 2014.
11. G. K. Singh, "A six-phase synchronous generator for stand-alone renewable energy generation: Experimental analysis," *Energy*, vol. 36, no. 3, pp. 1768–1755, 2011.
12. G. K. Singh, A. S. Kumar, and R. P. Saini, "Performance evaluation of series compensated self-excited six-phase induction generator for standalone renewable energy generation," *Energy*, vol. 35, no. 1, pp. 288–297, 2010.
13. E. Levi, R. Bojoi, F. Profumo, H. Toliyat, and S. Williamson, "Multiphase induction motor drives–a technology status review," *Elect. Power Appl.*, vol. 1, no. 4, pp. 489–516, 2007.
14. R. Gregor and J. Rodas, "Speed sensorless control of dual three-phase induction machine based on a luenberger observer for rotor current estimation," in *Proc. IECON*. IEEE, 2012, pp. 3653–3658.
15. A. Taheri and M. Mohammadbeigi, "Speed sensor-less estimation and predictive control of six-phase induction motor using extended kalman filter," in *Proc. PEDSTC*. IEEE, 2014, pp. 13–18.
16. A. G. Yepes, A. Vidal, J. Malvar, O. López, and J. Doval-Gandoy, "Tuning method aimed at optimized settling time and overshoot for synchronous proportional-integral current control in electric machines," *IEEE Trans. Power Electron.*, vol. 29, no. 6, pp. 3041–3054, 2014.
17. F. Baneira, J. Doval-Gandoy, A. G. Yepes, O. Lopez, and D. Pérez-Estévez, "Control strategy for multiphase drives with minimum losses in the full torque operation range under single open-phase fault," *IEEE Trans. Power Electron.*, vol. 32, no. 8, pp. 6275–6285, 2016.
18. A. G. Yepes, J. Doval-Gandoy, and H. Toliyat, "Multifrequency current control for multiphase machines with antiwindup, distortion-free saturation and full DC-link utilization," in *Proc. ECCE*. IEEE, 2018, pp. 776–783.
19. I. G. Prieto, M. Duran, P. Entrambasaguas, and M. Bermudez, "Field oriented control of multiphase drives with passive fault-tolerance," *IEEE Trans. Ind. Electron.*, 2019.
20. Y. Kali, J. Rodas, M. Saad, R. Gregor, K. Bejelloun, and J. Doval-Gandoy, "Current control based on super-twisting algorithm with time delay estimation for a five-phase induction motor drive," in *Proc. IEMDC*, Miami, FL, US, 2017.
21. Y. Kali, M. Ayala, J. Rodas, M. Saad, J. Doval-Gandoy, R. Gregor, and K. Benjelloun, "Current control of a six-phase induction machine drive based on discrete-time sliding mode with time delay estimation," *Energies*, vol. 12, no. 1, Jan. 2019.

22. Z. El-Barbary, “Fuzzy logic based controller for five-phase induction motor drive system,” *Alexandria Engineering Journal*, vol. 51, no. 4, pp. 263–268, 2012.
23. Z. Liu, Z. Zheng, and Y. Li, “Enhancing fault-tolerant ability of a nine-phase induction motor drive system using fuzzy logic current controllers,” *IEEE Trans. Energy Conversion*, vol. 32, no. 2, pp. 759–769, 2017.
24. L. Guo and L. Parsa, “Model reference adaptive control of five-phase ipm motors based on neural network,” *IEEE Trans. Ind. Electron.*, vol. 59, no. 3, pp. 1500–1508, 2011.
25. A. Hajary, S. G. Seifossadat, R. Kianinezhad, A. Saffarian, and S. S. Mortazavi, “An adaptive PI control design for multi-phase machines in healthy and faulty operations,” *COMPEL*, 2019.
26. O. Gonzalez, M. Ayala, J. Doval-Gandoy, J. Rodas, R. Gregor, and M. Rivera, “Predictive-fixed switching current control strategy applied to six-phase induction machine,” *Energies*, vol. 12, no. 12, p. 2294, 2019.
27. M. Ayala, J. Doval-Gandoy, J. Rodas, O. Gonzalez, and R. Gregor, “Current control designed with model based predictive control for six-phase motor drives,” *ISA transactions*, 2019.
28. M. Vijayagopal, P. Zanchetta, L. Empringham, L. De Lillo, L. Tarisciotti, and P. Wheeler, “Modulated model predictive current control for direct matrix converter with fixed switching frequency,” in *Proc. EPE*, 2015, pp. 1–10.
29. M. d. R. Correa, C. Jacobina, C. Da Silva, A. Lima, and E. Da Silva, “Six-phase ac drive system with reduced common-mode voltage,” in *Proc. IEMDC*, vol. 3. IEEE, 2003, pp. 1852–1858.
30. M. Ayala, O. Gonzalez, J. Rodas, R. Gregor, and J. Doval-Gandoy, “A speed-sensorless predictive current control of multiphase induction machines using a Kalman filter for rotor current estimator,” in *Proc. ESARS/ITEC*, Toulouse, France, 2016.
31. M. Ayala, J. Rodas, R. Gregor, J. Doval-Gandoy, O. Gonzalez, M. Saad, and M. Rivera, “Comparative study of predictive control strategies at fixed switching frequency for an asymmetrical six-phase induction motor drive,” in *Proc. IEMDC*, Miami, FL, US, 2017.
32. J. Rodas et al., “Model predictive current controller using kalman filter for fault-tolerant five-phase wind energy conversion systems,” in *Proc. ICIEA*. IEEE, 2016, pp. 1–6.
33. J. Rodas, F. Barrero, M. R. Arahal, C. Martin, and R. Gregor, “On-line estimation of rotor variables in predictive current controllers: A case study using five-phase induction machines,” *IEEE Trans. Ind. Electron.*, vol. 63, no. 9, pp. 5348–5356, 2016.
34. O. Gonzalez et al., “Predictive current control with kalman filter observer for a five-phase induction machine operating at fixed switching frequency,” in *Proc. ICIEA*. IEEE, 2017.
35. J. Riveros, “Aportaciones en el control de máquinas multifásicas,” Ph.D. dissertation, Universidad de Sevilla, 2013.
36. D. White and H. Woodson, *Electromechanical Energy Conversion*. Ed. New York: John Wiley & Sons, 1968.

37. B. Wilamowski and J. Irwin, *Power Electronics and Motor Drives*. CRC Press, 2018.
38. Y. Zhao and T. Lipo, “Space vector PWM control of dual three-phase induction machine using vector space decomposition,” *IEEE Trans. Ind. Electron.*, vol. 31, no. 5, pp. 1100–1109, 1995.
39. J. Rodas, “Aplicación de estimadores on-line de variables rotóricas para la mejora de las prestaciones en variadores de velocidad multifásicos,” Ph.D. dissertation, Universidad de Sevilla, 2016.
40. P. C. Krause, O. Wasynczuk, S. D. Sudhoff, and S. Pekarek, *Analysis of electric machinery and drive systems*. John Wiley & Sons, 2013, vol. 75.
41. O. Lopez, J. Alvarez, J. Doval-Gandoy, and F. D. Freijedo, “Multilevel multiphase space vector pwm algorithm with switching state redundancy,” *IEEE Trans. Ind. Electron.*, vol. 56, no. 3, pp. 792–804, 2009.
42. O. Lopez, E. Levi, F. Freijedo, and J. Doval-Gandoy, “Number of switching state vectors and space vectors in multilevel multiphase converters,” *Electron. letters*, vol. 45, no. 10, pp. 524–525, 2009.
43. J. Alvarez, O. Lopez, F. D. Freijedo, and J. Doval-Gandoy, “Digital parameterizable vhdl module for multilevel multiphase space vector pwm,” *IEEE Trans. Ind. Electron.*, vol. 58, no. 9, pp. 3946–3957, 2011.
44. J. I. Leon, O. Lopez, L. G. Franquelo, J. Doval-Gandoy, S. Vazquez, J. Alvarez, and F. D. Freijedo, “Multilevel multiphase feedforward space-vector modulation technique,” *IEEE Trans. Ind. Electron.*, vol. 57, no. 6, pp. 2066–2075, 2010.
45. S. Toledo et al., “Predictive current control with reactive power minimization in six-phase wind energy generator using multi-modular direct matrix converter,” in *Proc. ANDESCON*. IEEE, 2016.
46. F. Gavilan, D. Caballero, S. Toledo, E. Maqueda, R. Gregor, J. Rodas, M. Rivera, and I. Araujo-Vargas, “Predictive power control strategy for a grid-connected 2L-VSI with fixed switching frequency,” in *Proc. ROPEC*. IEEE, 2016, pp. 1–6.
47. N. Mohan, T. M. Undeland, and W. P. Robbins, *Power electronics: converters, applications, and design*. John Wiley & Sons, 2003.
48. H. Guzman, M. J. Duran, F. Barrero, L. Zarri, B. Bogado, I. G. Prieto, and M. R. Arahal, “Comparative study of predictive and resonant controllers in fault-tolerant five-phase induction motor drives,” *IEEE Trans. on Ind. Electron.*, vol. 63, no. 1, pp. 606–617, 2016.
49. J. Riveros, B. Bogado, J. Prieto, F. Barrero, S. Toral, and M. Jones, “Multiphase machines in propulsion drives of electric vehicles,” in *Proc. EPE/PEMC*, 2010, pp. T5–201.
50. J. D. Irwin, *Power electronics and motor drives*. CRC Press, 2011.
51. M. Mengoni, L. Zarri, A. Tani, G. Serra, and D. Casadei, “Sensorless multiphase induction motor drive based on a speed observer operating with third-order field harmonics,” in *Proc. ECCE*. IEEE, 2011, pp. 68–74.

52. S. Bozhko, S. Peresada, S. Kovbasa, and M. Zhelinskyi, “Robust indirect field oriented control of induction generator,” in *Proc. ESARS-ITEC*. IEEE, 2016, pp. 1–6.

53. C. Martin, M. Arahal, F. Barrero, and M. Duran, “Five-phase induction motor rotor current observer for finite control set model predictive control of stator current,” *IEEE Trans. Ind. Electron.*, vol. 63, no. 7, pp. 4527–4538, 2016.

54. M. Moutchou, A. Abbou, and H. Mahmoudi, “Mras-based sensorless speed backstepping control for induction machine, using a flux sliding mode observer,” *Turkish Journal of Electrical Engineering & Computer Sciences*, vol. 23, no. 1, pp. 187–200, 2015.

55. A. Boulkroune, S. Issaouni, and H. Chekireb, “Adaptive neuro-fuzzy controller of induction machine drive with nonlinear friction,” in *Nature-Inspired Computing for Control Systems*. Springer, 2016, pp. 169–192.

56. S. Vazquez, J. Rodriguez, M. Rivera, L. G. Franquelo, and M. Norambuena, “Model predictive control for power converters and drives: Advances and trends,” *IEEE Trans. on Ind. Electron.*, vol. 64, no. 2, pp. 935–947, 2017.

57. V. I. Utkin and H.-C. Chang, “Sliding mode control on electro-mechanical systems,” *Mathematical problems in Engineering*, vol. 8, no. 4-5, pp. 451–473, 2002.

58. H. Brandtstädter, “Sliding mode control of electromechanical systems,” Ph.D. dissertation, Technische Universität München, 2009.

59. V. Utkin, J. Guldner, and J. Shi, *Sliding mode control in electromechanical systems*. Taylor-Francis, 1999.

60. J. Rodriguez and P. Cortes, *Predictive control of power converters and electrical drives*. John Wiley & Sons, 2012, vol. 40.

61. J. Rodriguez, M. P. Kazmierkowski, J. R. Espinoza, P. Zanchetta, H. Abu-Rub, H. A. Young, and C. A. Rojas, “State of the art of finite control set model predictive control in power electronics,” *IEEE Trans. Ind. Informatics*, vol. 9, no. 2, pp. 1003–1016, 2013.

62. P. Gonçalves, S. Cruz, and A. Mendes, “Finite control set model predictive control of six-phase asymmetrical machines—An Overview,” *Energies*, vol. 12, no. 24, p. 4693, 2019.

63. P. Karamanakos, T. Geyer, N. Oikonomou, F. D. Kieferndorf, and S. Manias, “Direct model predictive control: A review of strategies that achieve long prediction intervals for power electronics,” *IEEE Ind. Electron. Mag.*, vol. 8, no. 1, pp. 32–43, 2014.

64. V. Utkin, *Sliding mode in control and optimization*. Springer-Verlag, Berlin, 1992.

65. L. Fridman, “An averaging approach to chattering,” *IEEE Trans. Autom. Control*, vol. 46, pp. 1260–1265, 2001.

66. I. Boiko and L. Fridman, “Analysis of chattering in continuous sliding-mode controllers,” *IEEE Trans. Autom. Control*, vol. 50, pp. 1442–1446, 2005.

67. K. D. Young, V. I. Utkin, and U. Ozguner, “A control engineer’s guide to sliding mode control,” *IEEE Trans. Control Syst. Technol.*, vol. 7, no. 3, pp. 328–342, 1999.

68. S. Drakunov and V. Utkin, “Sliding mode observers. tutorial,” in *34th IEEE Conference on Decision and Control*, vol. 4, 1995, pp. 3376–3378.

69. X.-G. Yan and C. Edwards, “Nonlinear robust fault reconstruction and estimation using a sliding mode observer,” *Automatica*, vol. 43, no. 9, pp. 1605 – 1614, 2007. [Online]. Available: http://www.sciencedirect.com/science/article/pii/S0005109807001719

70. A. Levant, “Higher-order sliding modes, differentiation and output-feedback control,” *Int. J. Contr.*, vol. 76, no. 9-10, pp. 924–941, 2003.

71. Y. Kali, M. Saad, K. Benjelloun, and A. Fatemi, “Discrete-time second order sliding mode with time delay control for uncertain robot manipulators,” *Robotics and Autonomous Systems*, vol. 94, pp. 53 – 60, 2017.

72. Y. Kali, M. Saad, K. Benjelloun, and C. Khairallah, “Super-twisting algorithm with time delay estimation for uncertain robot manipulators,” *Nonlinear Dynamics*, vol. 93, no. 2, pp. 557–569, Jul 2018.

73. Y. Kali, M. Saad, K. Benjelloun, and M. Benbrahim, “Sliding mode with time delay control for MIMO nonlinear systems with unknown dynamics,” in *Proc. RASM*, 2015, pp. 1–6.

74. Y. Kali, J. Rodas, R. Gregor, M. Saad, and K. Benjelloun, “Attitude tracking of a tri-rotor uav based on robust sliding mode with time delay estimation,” in *Proc. ICUAS*, June 2018, pp. 346–351.

75. O. Gonzalez, M. Ayala, J. Rodas, R. Gregor, G. Rivas, and J. Doval-Gandoy, “Variable-speed control of a six-phase induction machine using predictive-fixed switching frequency current control techniques,” in *Proc. PEDG*, 2018, pp. 1–6.

76. L. Harnefors, S. Saarakkala, and M. Hinkkanen, “Speed control of electrical drives using classical control methods,” *IEEE Trans. Ind. Appl.*, vol. 49, no. 2, pp. 889–898, 2013.

77. J. H. Jung, P. Chang, and S. H. Kang, “Stability analysis of discrete time delay control for nonlinear systems,” in *2007 American Control Conference*, July 2007, pp. 5995–6002.

78. S. Qu, X. Xia, and J. Zhang, “Dynamics of discrete-time sliding-mode-control uncertain systems with a disturbance compensator,” *IEEE Trans. Ind. Electron.*, vol. 61, no. 7, pp. 3502–3510, 2014.

79. A. G. Yepes, J. A. Riveros, J. Doval-Gandoy, F. Barrero, O. López, B. Bogado, M. Jones, and E. Levi, “Parameter identification of multiphase induction machines with distributed windings Part 1: Sinusoidal excitation methods,” *IEEE Trans. Energy Conv.*, vol. 27, no. 4, pp. 1056–1066, 2012.

80. J. A. Riveros, A. G. Yepes, F. Barrero, J. Doval-Gandoy, B. Bogado, O. Lopez, M. Jones, and E. Levi, “Parameter identification of multiphase induction machines with distributed windings Part 2: Time-domain techniques,” *IEEE Trans. Energy Conv.*, vol. 27, no. 4, pp. 1067–1077, 2012.

81. C. J. Fallaha, M. Saad, H. Y. Kanaan, and K. Al-Haddad, “Sliding-mode robot control with exponential reaching law,” *IEEE Trans. Ind. Electron.*, vol. 58, no. 2, pp. 600–610, Feb. 2011.

82. J. Yu, J. Liu, Z. Wu, and H. Fang, “Depth control of a bioinspired robotic dolphin based on sliding-mode fuzzy control method,” *IEEE Trans. Ind. Electron.*, vol. 65, no. 3, pp. 2429–2438, Mar. 2018.
83. Y. Kali, M. Saad, and K. Benjelloun, *Control of Robot Manipulators Using Modified Backstepping Sliding Mode*. Singapore: Springer Singapore, 2019, pp. 107–136.
84. A. Levant, “Sliding order and sliding accuracy in sliding mode control,” *Int. J. Control*, vol. 58, no. 6, pp. 1247–1263, 1993.
85. A. S. Poznyak, “Chapter 12 - miscellaneous,” in *Advanced Mathematical Tools for Automatic Control Engineers: Deterministic Techniques*, A. S. Poznyak, Ed. Oxford: Elsevier, 2008, pp. 213 – 227.
86. I. Salgado, I. Chairez, B. Bandyopadhyay, L. Fridman, and O. Camacho, “Discrete-time non-linear state observer based on a super twisting-like algorithm,” *IET Control Theory Appl.*, vol. 8, no. 10, pp. 803–812, Jul. 2014.
87. M. Arahal, F. Barrero, S. Toral, M. Duran, and R. Gregor, “Multi-phase current control using finite-state model-predictive control,” *Control Eng. Prac.*, vol. 17, no. 5, pp. 579–587, 2009.
88. S.-K. Kim, D.-K. Choi, K.-B. Lee, and Y. I. Lee, “Offset-free model predictive control for the power control of three-phase AC/DC converters,” *IEEE Trans. Ind. Electron.*, vol. 62, no. 11, pp. 7114–7126, 2015.
89. J. A. Rohten, J. R. Espinoza, J. A. Muñoz, M. A. Pérez, P. E. Melin, J. J. Silva, E. E. Espinosa, and M. Rivera, “Model predictive control for power converters in a distorted three-phase power supply,” *IEEE Trans. Ind. Electron.*, vol. 63, no. 9, pp. 5838–5848, 2016.
90. G. Mirzaeva, G. C. Goodwin, B. P. McGrath, C. Teixeira, and M. Rivera, “A generalized MPC framework for the design and comparison of VSI current controllers,” *IEEE Trans. Ind. Electron.*, vol. 63, no. 9, pp. 5816–5826, 2016.
91. E. Fuentes, C. A. Silva, and R. M. Kennel, “MPC implementation of a quasi-time-optimal speed control for a PMSM drive, with inner modulated-FS-MPC torque control,” *IEEE Trans. Ind. Electron.*, vol. 63, no. 6, pp. 3897–3905, 2016.
92. M. Preindl, “Robust control invariant sets and Lyapunov-based MPC for IPM synchronous motor drives,” *IEEE Trans. Ind. Electron.*, vol. 63, no. 6, pp. 3925–3933, 2016.
93. P. Karamanakos, P. Stolze, R. M. Kennel, S. Manias, and H. du Toit Mouton, “Variable switching point predictive torque control of induction machines,” *IEEE Trans. Emerg. Sel. Topics Power Electron.*, vol. 2, no. 2, pp. 285–295, 2014.
94. Y. B. Zbede, S. M. Gadoue, and D. J. Atkinson, “Model predictive MRAS estimator for sensorless induction motor drives,” *IEEE Trans. Ind. Electron.*, vol. 63, no. 6, pp. 3511–3521, 2016.
95. J. Rodas, C. Martin, M. R. Arahal, F. Barrero, and R. Gregor, “Influence of covariance-based ALS methods in the performance of predictive controllers with rotor current estimation,” *IEEE Trans. Ind. Electron.*, vol. 64, no. 4, pp. 2602–2607, 2017.

96. C. Martín, M. R. Arahal, F. Barrero, and M. J. Durán, “Multiphase rotor current observers for current predictive control: A five-phase case study,” *Control Eng. Prac.*, vol. 49, pp. 101–111, 2016.
97. C. S. Lim, E. Levi, M. Jones, N. A. Rahim, and W. P. Hew, “FCS-MPC-based current control of a five-phase induction motor and its comparison with PI-PWM control,” *IEEE Trans. Ind. Electron.*, vol. 61, no. 1, pp. 149–163, 2013.
98. M. Novak, T. Dragicevic, and F. Blaabjerg, “Weighting factor design based on artificial neural network for finite set MPC operated 3L-NPC converter,” in *Proc. APEC).* IEEE, 2019, pp. 77–82.
99. B. Majmunović, T. Dragičević, and F. Blaabjerg, “Multi objective modulated model predictive control of stand-alone voltage source converters,” *IEEE Journal of Emerging and Selected Topics in Power Electronics*, 2019.
100. R. Gregor, J. Rodas, J. Munoz, M. Ayala, O. Gonzalez, and D. Gregor, “Predictive-fixed switching frequency technique for 5-phase induction motor drives,” in *Proc. SPEEDAM*, Capri, Italy, 2016.
101. M. J. Duran, J. Prieto, F. Barrero, and S. Toral, “Predictive current control of dual three-phase drives using restrained search techniques,” *IEEE Trans. Ind. Electron.*, vol. 58, no. 8, pp. 3253–3263, 2010.
102. D. Q. Mayne, J. B. Rawlings, C. V. Rao, and P. O. Scokaert, “Constrained model predictive control: Stability and optimality,” *Automatica*, vol. 36, no. 6, pp. 789–814, 2000.
103. R. P. Aguilera and D. E. Quevedo, “On stability and performance of finite control set MPC for power converters,” in *Proc. PRECEDE.* IEEE, 2011, pp. 55–62.
104. R. Aguilera and D. Quevedo, “Stability analysis of quadratic MPC with a discrete input alphabet,” *IEEE Trans. Automatic Control*, vol. 58, no. 12, pp. 3190–3196, 2013.

PARTE III

PUBLICACIONES

En este apéndice se realiza una recopilación de los artículos publicados en el marco de esta Tesis, en el siguiente orden:

1. Yassine Kali, **Magno Ayala**, Jorge Rodas, Maarouf Saad, Jesus Doval-Gandoy, Raul Gregor and Khalid Benjelloun, ”Current Control of a Six-Phase Induction Machine Drive Based on Discrete-Time Sliding Mode with Time Delay Estimation”, Energies, pp. 1-17, DOI: 10.3390/en12010170, 2019.
2. Yassine Kali, **Magno Ayala**, Jorge Rodas, Maarouf Saad, Jesus Doval-Gandoy, Raul Gregor and Khalid Benjelloun, ”Time Delay Estimation based Discrete-Time Super-Twisting Current Control for a Six-Phase Induction Motor”, IEEE Transactions on Power Electronics, pp. 1-8, 2020. (R2)
3. **Magno Ayala**, Jesus Doval-Gandoy, Jorge Rodas, Osvaldo González and Raul Gregor, ”Current control designed with model based predictive control for six-phase motor drives”, ISA Transactions, pp. 1-9, DOI: 10.1016/j.isatra.2019.08.052, 2019.

4. **Magno Ayala**, Jesus Doval-Gandoy, Jorge Rodas, Osvaldo González, Raul Gregor and Marco Rivera, ”A Novel Modulated Model Predictive Control Applied to Six-Phase Induction Motor Drives”, IEEE Transactions on Industrial Electronics, pp. 1-10, 2020, DOI: 10.1109/TIE.2020.2984425.
5. **Magno Ayala**, Jesus Doval-Gandoy, Osvaldo González, Jorge Rodas, Raul Gregor and Marco Rivera, ”Stability Analysis of Modulated Model Predictive Controllers Applied to Six-Phase Induction Motor Drives”, IEEE Transactions on Industrial Electronics, pp. 1-10, 2020. (R1)
6. Osvaldo González, **Magno Ayala**, Jesus Doval-Gandoy, Raul Gregor and Gustavo Rivas, ”Variable-Speed Control of a Six-Phase Induction Machine using Predictive-Fixed Switching Frequency Current Control Techniques”, Proc. PEDG, Charlotte, US, pp. 1-6, DOI: 10.1109/PEDG.2018.8447837, 2018.
7. Osvaldo González, **Magno Ayala**, Jesus Doval-Gandoy, Jorge Rodas, Raul Gregor and Marco Rivera, ”Predictive-Fixed Switching Current Control Strategy Applied to Six-Phase Induction Machine”, Energies, pp. 1-14, DOI: 10.3390/en12122294, 2019.
8. Yassine Kali, Jorge Rodas, **Magno Ayala**, Maarouf Saad, Raul Gregor, Khalid Benjelloun, Jesus Doval-Gandoy and Graham Goodwin, ”Discrete-Time Sliding Mode with Time Delay Estimation of a Six-Phase Induction Motor Drive”, Proc. IECON, Washington, US, pp. 1-6, DOI: 10.1109/IECON.2018.8591293, 2018.
9. **Magno Ayala**, Osvaldo González, Jorge Rodas, Raul Gregor, Yassine Kali and Pat Wheeler, ”Comparative Study of Non-linear Controllers Applied to a Six-Phase Induction Machine”, Proc. ESARS-ITEC, Nottingham, England, United Kingdom, pp. 1-6, DOI: 10.1109/ESARS-ITEC.2018.8607288, 2018.
10. Osvaldo González, **Magno Ayala**, Carlos Romero, Jorge Rodas, Raúl Gregor, Larizza Delorme, Ignacio González-Prieto, Mario Durán and Marco Rivera, ”Comparative Assessment of Model Predictive Current Control Strategies applied to Six-Phase Induction Machine”, Proc. ICIT, Buenos Aires, Argentina, pp. 1-7, 2020.

ARTÍCULO 1

CURRENT CONTROL OF A SIX-PHASE INDUCTION MACHINE DRIVE BASED ON DISCRETE-TIME SLIDING MODE WITH TIME DELAY ESTIMATION

- Yassine Kali, **Magno Ayala**, Jorge Rodas, Maarouf Saad, Jesus Doval-Gandoy, Raul Gregor and Khalid Benjelloun, "Current Control of a Six-Phase Induction Machine Drive Based on Discrete-Time Sliding Mode with Time Delay Estimation", Energies, pp. 1-17, DOI: 10.3390/en12010170, 2019.

energies

MDPI

Article

Current Control of a Six-Phase Induction Machine Drive Based on Discrete-Time Sliding Mode with Time Delay Estimation

Yassine Kali [1,*], Magno Ayala [2], Jorge Rodas [2], Maarouf Saad [1], Jesus Doval-Gandoy [3], Raul Gregor [2] and Khalid Benjelloun [4]

[1] Power Electronics and Industrial Control Research Group (GRÉPCI), École de Technologie Supérieure, Montreal H3C 1K3, QC, Canada; maarouf.saad@etsmtl.ca
[2] Laboratory of Power and Control Systems (LSPyC), Facultad de Ingeniería, Universidad Nacional de Asunción, Luque 2060, Paraguay; mayala@ing.una.py (M.A.); jrodas@ing.una.py (J.R.); rgregor@ing.una.py (R.G.)
[3] Applied Power Electronics Technology Research Group (APET), Universidad de Vigo, 36310 Vigo, Spain; jdoval@uvigo.es
[4] Electrical Engineering Department, Ecole Mohammadia d'Ingénieurs, University of Mohammed V, Rabat 765, Morocco; bkhalid@emi.ac.ma
* Correspondence: y.kali88@gmail.com; Tel.: +1-514-443-8118

Received: 22 November 2018; Accepted: 29 December 2018; Published: 5 January 2019

Abstract: This paper proposes a robust nonlinear current controller that deals with the problem of the stator current control of a six-phase induction motor drive. The current control is performed by using a state-space representation of the system, explicitly considering the unmeasurable states, uncertainties and external disturbances. To estimate these latter effectively, a time delay estimation technique is used. The proposed control architecture consists of inner and outer loops. The inner current control loop is based on a robust discrete-time sliding mode controller combined with a time delay estimation method. As said before, the objective of the time delay estimation is to reconstruct the unmeasurable states and uncertainties, while the sliding mode aims is to suppress the estimation error, to ensure robustness and finite-time convergence of the stator currents to their desired references. The outer loop is based on a proportional-integral controller to control the speed. The stability of the current closed-loop system is proven by establishing sufficient conditions on the switching gains. Experimental work has been conducted to verify the performance and the effectiveness of the proposed robust control scheme for a six-phase induction motor drive. The results obtained have shown that the proposed method allows good performances in terms of current tracking, in their corresponding planes.

Keywords: multiphase induction machine; time delay estimation; sliding mode control; field-oriented control; current control

1. Introduction

Multiphase drives have received significant interest from the power electronics, control, machines and drives communities due to their good features in comparison with traditional three-phase drives. The features include lower torque ripple, lower current/power per phase and fault-tolerant capabilities without adding extra hardware [1–3]. Currently, multiphase drives are extensively used in several applications where high power is required such as ships, wind energy generation systems and electric vehicles [3,4]. In the literature, most of the developed and published control techniques for multiphase Induction Machine (IM) drives are an extension of the ones designed for the three-phase machines such as Proportional-Resonant (PR) [5], Proportional-Integral (PI) Pulse-Width Modulation (PWM) [6], Direct Torque Control (DTC) [7], Predictive Torque Control (PTC) [8], sensorless [9,10] and Model Predictive Control (MPC) [11,12], among others. Recently, the above-mentioned controllers have been extended for multiphase machines under fault situations [13–16]. However, few published papers have considered robust nonlinear controllers and intelligent techniques such as backstepping [17,18], Sliding Mode Control (SMC) [19–21], fuzzy logic [22] and others.

Among the above-mentioned nonlinear controllers, SMC is one of the most widely used and has received particular attention from the automation community due to its three highly-valued properties, namely robustness against matched uncertainties, simplicity of design and finite-time convergence [23,24]. This method forces the system states to reach in finite time the user-selected sliding surface (switching surface) even in the presence of the matched uncertainties using discontinuous inputs [24]. To ensure high performances, the switching gains should be chosen as large as possible to reject the effect of the bounded uncertainties. However, this choice causes the major drawback of SMC, well-known under the name of the chattering phenomenon [25,26]. The latter has an unpleasant impact on system actuators. It can lead to deterioration of the controlled system and/or instability. Once this problem has been identified, many works that tried to solve it were published, and among them, we cite the following:

- The substitution of the discontinuous signum function by linear ones [27]. This method is the well-known SMC based on a boundary layer. This proposition allows the reduction of the chattering phenomenon. However, the finite-time convergence feature is no longer guaranteed. The latter is very desirable when critical convergence time is required.
- Observer-based SMC [28,29]. The issue of designing a robust nonlinear controller in this technique is reduced to the issue of designing a robust nonlinear observer. In other words, if the matched uncertainties are not accurately estimated, the performances obtained will not be satisfactory.
- Higher Order Sliding Mode (HOSM) [30–32]. The idea consists of making the switching control term act on the control input derivative, which makes the control input fed into the system continuous. This method gives better performances since it allows higher precision and reduces the chattering phenomenon. However, this approach requires some information, as the first time derivative of the selected sliding surface is not always available for measurements, making the implementation difficult.

Recently, an interesting method that consists of combining SMC with the Time Delay Estimation (TDE) method for uncertain nonlinear systems [33,34] has been developed. The proposed method has been successfully tested on a redundant robot manipulator. The basic idea is to estimate the matched uncertainties that are assumed to be Lipschitz using delayed states and input information. Then, the estimated terms are added to the equivalent controller in order to allow a small choice of the switching gains of the discontinuous controller.

Nevertheless, real-time implementation is generally performed through discrete systems [35]. For this reason, the development of the controller should be done in discrete-time. Consequently, it is suitable for use with a discrete-time model of the six-phase IM during the design procedure since after discretization, the inherent properties of the sliding mode approach can no longer be maintained.

In summary, the aim of this paper is to develop a robust Discrete-time SMC (DSMC) combined with the TDE method for the inner current control loop of an Indirect Rotor Field-Oriented Control (IRFOC) of a six-phase IM drive. The developed controller works for all multiphase machines in several applications as more electric aircraft, ship propulsion, battery-powered electric vehicles, electric traction and hybrid electric vehicles. Experimental validation is presented to show the effectiveness of the current controller in transient and steady-state conditions. The rest of the paper is organized as follows. The mathematical discrete-time model of the considered system is presented in Section 2, while the proposed controller design and detailed stability analysis are explained in Section 3. Experimental results are presented in Section 4. Finally, Section 5 draws some conclusions.

2. Six-Phase IM and VSI Model

The considered system shown in Figure 1 consists of the asymmetrical six-phase IM fed by two two-Level (2L) Voltage Source Inverter (VSI). After using the Vector Space Decomposition (VSD) approach, the decoupling transformation **T** gives the $\alpha - \beta$ subspace, which is related to the flux/torque producing components and the loss-producing $x - y$subspace and a zero-sequence subspace. Then, by using an amplitude-invariant transformation matrix, **T** is defined as follows:

$$\mathbf{T} = \frac{1}{3}\begin{bmatrix} 1 & \frac{\sqrt{3}}{2} & -\frac{1}{2} & -\frac{\sqrt{3}}{2} & -\frac{1}{2} & 0 \\ 0 & \frac{1}{2} & \frac{\sqrt{3}}{2} & \frac{1}{2} & -\frac{\sqrt{3}}{2} & -1 \\ 1 & -\frac{\sqrt{3}}{2} & -\frac{1}{2} & \frac{\sqrt{3}}{2} & -\frac{1}{2} & 0 \\ 0 & \frac{1}{2} & -\frac{\sqrt{3}}{2} & \frac{1}{2} & \frac{\sqrt{3}}{2} & -1 \\ 1 & 0 & 1 & 0 & 1 & 0 \\ 0 & 1 & 0 & 1 & 0 & 1 \end{bmatrix}. \tag{1}$$

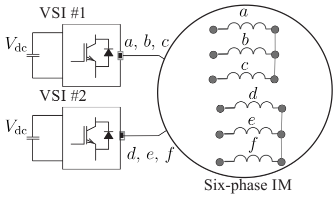

Figure 1. Scheme of the six-phase induction machine drive.

The discrete-time model of the system in state-space representation is represented by the following equations [36]:

$$\mathbf{X}(k+1) = \mathbf{A}\,\mathbf{X}(k) + \mathbf{B}\,\mathbf{u}(k) + \mathbf{n}(k) \tag{2}$$

$$\mathbf{Y}(k) = \mathbf{C}\,\mathbf{X}(k) \tag{3}$$

In the equations above, the stator and rotor currents are the state vector:

$$\mathbf{X}(k) = \left[i_{s\alpha}(k),\ i_{s\beta}(k),\ i_{sx}(k),\ i_{sy}(k), i_{r\alpha}(k),\ i_{r\beta}(k)\right]^T \tag{4}$$

while the stator voltages represent the input vector:

$$\mathbf{u}(k) = \left[u_{s\alpha}(k),\ u_{s\beta}(k),\ u_{sx}(k),\ u_{sy}(k)\right]^T \tag{5}$$

and the stator currents the output vector:

$$\mathbf{Y}(k) = \left[i_{s\alpha}(k),\ i_{s\beta}(k),\ i_{sx}(k),\ i_{sy}(k)\right]^T \tag{6}$$

and $\mathbf{n}(k)$ is the (6×1) uncertain vector. The stator voltages have a discrete nature due to the VSI model, and the relationship between them is represented as:

$$V_{\mathrm{dc}}\,\mathbf{T}\,\mathbf{M} = \left[u_{s\alpha}(k),\ u_{s\beta}(k),\ u_{sx}(k),\ u_{sy}(k)\right]^T \tag{7}$$

where V_{dc} is the DC-bus voltage, and the VSI model is:

$$\mathbf{M} = \frac{1}{3}\begin{bmatrix} 2 & 0 & -1 & 0 & -1 & 0 \\ 0 & 2 & 0 & -1 & 0 & -1 \\ -1 & 0 & 2 & 0 & -1 & 0 \\ 0 & -1 & 0 & 2 & 0 & -1 \\ -1 & 0 & -1 & 0 & 2 & 0 \\ 0 & -1 & 0 & -1 & 0 & 2 \end{bmatrix}\mathbf{S}^T \tag{8}$$

where $\mathbf{S} = \left[S_a,\, S_b,\, S_c,\, S_d,\, S_e,\, S_f\right]$ is the vector of the gating signals with $S_i \in \{0,\,1\}$. Moreover, the matrices $\mathbf{A} \in R^{6\times 6}$, $\mathbf{B} \in R^{6\times 4}$ and $\mathbf{C} \in R^{4\times 6}$ are defined by:

$$\mathbf{A} = \begin{bmatrix} a_{11} & a_{12} & 0 & 0 & a_{15} & a_{16} \\ a_{21} & a_{22} & 0 & 0 & a_{25} & a_{26} \\ 0 & 0 & a_{33} & 0 & 0 & 0 \\ 0 & 0 & 0 & a_{44} & 0 & 0 \\ a_{51} & a_{52} & 0 & 0 & a_{55} & a_{56} \\ a_{61} & a_{62} & 0 & 0 & a_{65} & a_{66} \end{bmatrix} \tag{9}$$

$$\mathbf{B} = \begin{bmatrix} b_1 & 0 & 0 & 0 \\ 0 & b_1 & 0 & 0 \\ 0 & 0 & b_2 & 0 \\ 0 & 0 & 0 & b_2 \\ b_3 & 0 & 0 & 0 \\ 0 & b_3 & 0 & 0 \end{bmatrix} \tag{10}$$

$$\mathbf{C} = \begin{bmatrix} 1 & 0 & 0 & 0 & 0 & 0 \\ 0 & 1 & 0 & 0 & 0 & 0 \\ 0 & 0 & 1 & 0 & 0 & 0 \\ 0 & 0 & 0 & 1 & 0 & 0 \end{bmatrix} \tag{11}$$

where:

$$\begin{array}{lll} a_{11} = a_{22} = 1 - T_s\, c_2\, R_s & a_{12} = -a_{21} = T_s\, c_4 L_m\, \omega_{r(k)} & a_{15} = a_{26} = T_s\, c_4\, R_r \\ a_{16} = -a_{25} = T_s\, c_4 L_r\, \omega_{r(k)} & a_{33} = a_{44} = 1 - T_s\, c_3\, R_s & a_{51} = a_{62} = T_s\, c_4\, R_s \\ a_{52} = -a_{61} = -T_s\, c_5\, L_m\, \omega_{r(k)} & a_{55} = a_{66} = 1 - T_s\, c_5\, R_r & a_{56} = -a_{65} = -c_5\, \omega_{r(k)}\, T_s\, L_r \\ b_1 = T_s\, c_2 & b_2 = T_s\, c_3 & b_3 = -T_s\, c_4 \end{array}$$

with T_s the sampling time and c_1 to c_5 are defined as: $c_1 = L_s L_r - L_m^2$, $c_2 = \frac{L_r}{c_1}$, $c_3 = \frac{1}{L_{ls}}$, $c_4 = \frac{L_m}{c_1}$, $c_5 = \frac{L_s}{c_1}$. The electrical parameters of the systems are R_s, R_r, $L_r = L_{lr} + L_m$, $L_s = L_{ls} + L_m$, L_r and L_m. The rotor electrical speed ω_r is related to the load torque T_l and the generated torque T_e as follows:

$$J_m\, \dot{\omega}_r + B_m\, \omega_r = P\left(T_e - T_l\right) \tag{12}$$

$$\omega_r = P\omega_m \tag{13}$$

where J_m denotes the inertia coefficient, B_m denotes the friction coefficient, P denotes the number of pole pairs and the generated torque T_e is defined by:

$$T_e = 3\,P\left(\psi_{s\alpha}\, i_{s\beta} - \psi_{s\beta}\, i_{s\alpha}\right) \tag{14}$$

where $\psi_{s\alpha}$ and $\psi_{s\beta}$ are the stator fluxes.

3. Controller Design and Stability Analysis

3.1. Outer Speed Control Loop

A two-degree PI controller with a saturation stage, introduced in [37], is used as the outer speed control loop, based on the IRFOC method. In this loop, the output of the PI regulator is used to get the dynamic current reference $i_{sq}^*(k)$. In addition, the slip frequency $\omega_{sl}(k)$ calculation is obtained from the current references $i_{sd}^*(k), i_{sq}^*(k)$ in the dynamic reference frame and the electrical parameters of the six-phase IM, as shown in Figure 2.

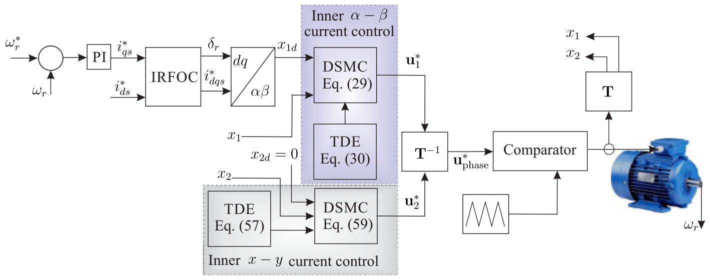

Figure 2. Block diagram of the closed-loop system based on IRFOC and the DSMC with TDE method.

3.2. Inner Current Control Loop

The inner loop aims to control the stator currents. For this purpose, the DSMC with TDE method will be derived to ensure the finite-time convergence of the stator currents in the $\alpha-\beta$ and the $x-y$ planes to their desired references with high accuracy even if some states are not measurable (i.e., rotor currents) and in the presence of uncertainties. First of all, let us decompose the discrete system described in (2) into three sub-systems as follows:

$$\mathbf{x}_1(k+1) = \mathbf{A}_1\,\mathbf{x}_1(k) + \overline{\mathbf{A}}_1\,\mathbf{x}_3(k) + \mathbf{B}_1\,\mathbf{u}_1(k) + \eta_1(k) \tag{15}$$

$$\mathbf{x}_2(k+1) = \mathbf{A}_2\,\mathbf{x}_2(k) + \mathbf{B}_2\,\mathbf{u}_2(k) + \eta_2(k) \tag{16}$$

$$\mathbf{x}_3(k+1) = \mathbf{A}_3\,\mathbf{x}_1(k) + \overline{\mathbf{A}}_3\,\mathbf{x}_3(k) + \mathbf{B}_3\,\mathbf{u}_1(k) + \eta_3(k) \tag{17}$$

where the stator and rotor current state vectors:

$$\mathbf{x}_1(k) = \left[i_{s\alpha}(k),\, i_{s\beta}(k)\right]^T \tag{18}$$

$$\mathbf{x}_2(k) = \left[i_{sx}(k),\, i_{sy}(k)\right]^T \tag{19}$$

$$\mathbf{x}_3(k) = \left[i_{r\alpha}(k),\, i_{r\beta}(k)\right]^T \tag{20}$$

while the stator voltages represent the input vectors:

$$\mathbf{u}_1(k) = \left[u_{s\alpha}(k),\, u_{s\beta}(k)\right]^T \tag{21}$$

$$\mathbf{u}_2(k) = \left[u_{sx}(k),\, u_{sy}(k)\right]^T \tag{22}$$

and $\eta_1(k) = [n_1(k),\, n_2(k)]^T$, $\eta_2(k) = [n_3(k),\, n_4(k)]^T$ and $\eta_3(k) = [n_5(k),\, n_6(k)]^T$ denote the uncertain vectors. The matrices $\mathbf{A}_1$, $\overline{\mathbf{A}}_1$, $\mathbf{A}_2$, $\mathbf{A}_3$, $\overline{\mathbf{A}}_3$, $\mathbf{B}_1$, $\mathbf{B}_2$ and $\mathbf{B}_3$ are defined as follows:

$$\mathbf{A}_1 = \begin{bmatrix} a_{11} & a_{12} \\ a_{21} & a_{22} \end{bmatrix},\ \mathbf{A}_2 = \begin{bmatrix} a_{33} & 0 \\ 0 & a_{44} \end{bmatrix},\ \mathbf{A}_3 = \begin{bmatrix} a_{51} & a_{52} \\ a_{61} & a_{62} \end{bmatrix},\ \overline{\mathbf{A}}_1 = \begin{bmatrix} a_{15} & a_{16} \\ a_{25} & a_{26} \end{bmatrix}$$

$$\overline{\mathbf{A}}_3 = \begin{bmatrix} a_{55} & a_{56} \\ a_{65} & a_{66} \end{bmatrix}, \mathbf{B}_1 = \begin{bmatrix} b_1 & 0 \\ 0 & b_1 \end{bmatrix}, \mathbf{B}_2 = \begin{bmatrix} b_2 & 0 \\ 0 & b_2 \end{bmatrix}, \mathbf{B}_3 = \begin{bmatrix} b_3 & 0 \\ 0 & b_3 \end{bmatrix}$$

3.2.1. Control of Stator Current in the $\alpha - \beta$ Sub-Space

To achieve our control objective, let $\mathbf{x}_1^*(k) = i_{s\phi}^*(k) = \left[i_{s\alpha}^*(k), i_{s\beta}^*(k)\right]^T$ be the vector of desired references with $\phi \in \{\alpha, \beta\}$ and $\mathbf{e}_\phi(k) = \mathbf{x}_1(k) - \mathbf{x}_1^*(k) = i_{s\phi}(k) - i_{s\phi}^*(k)$ be the vector of tracking error. As the relative degree of the stator current in $\alpha - \beta$ sub-space is equal to one, then, the sliding surface [24] is selected to be the error variable as follows:

$$\sigma(k) = \mathbf{e}_\phi(k) \tag{23}$$

In the DSMC design, the following conditions must be satisfied to achieve an ideal sliding motion:

$$\sigma(k) = 0, \qquad \sigma(k+1) = 0 \tag{24}$$

where $\sigma(k+1)$ is computed as:

$$\begin{aligned} \sigma(k+1) &= \mathbf{e}_\phi(k+1) = \mathbf{x}_1(k+1) - \mathbf{x}_1^*(k+1) \\ &= \mathbf{A}_1\,\mathbf{x}_1(k) + \overline{\mathbf{A}}_1\,\mathbf{x}_3(k) + \mathbf{B}_1\,\mathbf{u}_1(k) + \eta_1(k) - \mathbf{x}_1^*(k+1) \end{aligned} \tag{25}$$

The control obtained by setting $\sigma(k+1) = 0$ does not ensure robustness and finite-time convergence. For these reasons, the following reaching law is selected:

$$\sigma(k+1) = \Lambda\,\sigma(k) - T_s\,\rho\,\mathrm{sign}(\sigma(k)) \tag{26}$$

where $\Lambda = \mathrm{diag}(\lambda_1, \lambda_2)$ with $0 < \lambda_i < 1$ for $i = 1, 2$, $\rho \in R^{2\times 2}$ is a diagonal positive matrix and $\mathrm{sign}(\sigma(k)) = [\mathrm{sign}(\sigma_1(k)), \mathrm{sign}(\sigma_2(k))]^T$ with:

$$\mathrm{sign}(\sigma_i(k)) = \begin{cases} 1, & \text{if } \sigma_i(k) > 0 \\ 0, & \text{if } \sigma_i(k) = 0 \\ -1, & \text{if } \sigma_i(k) < 0 \end{cases} \tag{27}$$

Then, using (25) and (26), the DSMC law for the stator current in the $\alpha - \beta$ sub-space is obtained as:

$$\mathbf{u}_1(k) = -\mathbf{B}_1^{-1}\left[\mathbf{A}_1\,\mathbf{x}_1(k) + \overline{\mathbf{A}}_1\,\mathbf{x}_3(k) + \eta_1(k) - \mathbf{x}_1^*(k+1) - \Lambda\,\sigma(k) + T_s\,\rho\,\mathrm{sign}(\sigma(k))\right] \tag{28}$$

The control performance might not be satisfactory since the above equation is in terms of the rotor currents $\mathbf{x}_3(k)$ that are not measurable and the uncertain vector $\eta_1(k)$. Assuming that $\mathbf{x}_3(k)$ and $\eta_1(k)$ do not fluctuate widely between two consecutive sampling times, the TDE method [31,38] can be used to obtain an approximation as:

$$\begin{aligned} \overline{\mathbf{A}}_1\,\hat{\mathbf{x}}_3(k) + \hat{\eta}_1(k) &\cong \overline{\mathbf{A}}_1\,\mathbf{x}_3(k-1) + \eta_1(k-1) \\ &= \mathbf{x}_1(k) - \mathbf{A}_1\,\mathbf{x}_1(k-1) - \mathbf{B}_1\,\mathbf{u}_1(k-1) \end{aligned} \tag{29}$$

Definition 1. *For a discrete-time system, a quasi-sliding mode is said to be a trajectory in the vicinity of the sliding surface, such that* $|\sigma(k)| < \varepsilon$ *and where* $\varepsilon > 0$ *is the quasi-sliding mode bandwidth. In order to ensure a* *convergent quasi-sliding mode, the conditions given in [31,39] that are necessary and sufficient must be verified for each sliding surface, i.e.:*

$$\begin{cases} \sigma_i(k) > \varepsilon & \Rightarrow -\varepsilon \le \sigma_i(k+1) < \sigma_i(k) \\ \sigma_i(k) < -\varepsilon & \Rightarrow \sigma_i(k) < \sigma_i(k+1) \le \varepsilon \\ |\sigma_i(k)| \le \varepsilon & \Rightarrow |\sigma_i(k+1)| \le \varepsilon \end{cases} \tag{30}$$

Theorem 1. *If the following condition is satisfied for i= 1, 2:*

$$\rho_i > \frac{1}{T_s}\delta_i, \tag{31}$$

then, the DSMC with TDE method for the stator currents in the $\alpha - \beta$ *sub-space (15) given by:*

$$\mathbf{u}_1(k) = -\mathbf{B}_1^{-1}\left[\mathbf{A}_1\,\mathbf{x}_1(k) + \overline{\mathbf{A}}_1\,\hat{\mathbf{x}}_3(k) + \hat{\eta}_1(k) - \mathbf{x}_1^*(k+1) - \Lambda\,\sigma(k) - T_s\,\rho\,\mathrm{sign}(\sigma(k))\right] \tag{32}$$

ensures a quasi sliding mode. Moreover, each system trajectory will reach its corresponding sliding surface (23) within at most $k_i^{'}$ *+ 1 steps, where for i= 1, 2:*

$$k_i^{'} = \frac{|\sigma_i(0)|}{T_s\,\rho_i - \delta_i} \tag{33}$$

Proof of Theorem 1. Substituting the obtained discrete time controller (32) into Equation (25) leads to:

$$\sigma(k+1) = \Lambda\,\sigma(k) + \mathbf{E}(k) - T_s\,\rho\,\mathrm{sign}(\sigma(k)) \tag{34}$$

where $\mathbf{E}(k) = \overline{\mathbf{A}}_1\,(x_3(k) - \hat{x}_3(k)) + (\eta_1(k) - \hat{\eta}_1(k))$ is the bounded TDE error such as for $i = 1, 2$:

$$|E_i(k)| < \delta_i \tag{35}$$

Now, choose $\varepsilon = T_s\,\rho_i + \delta_i$. Hence, Equation (30) can be rewritten as:

$$\begin{aligned} &\sigma_i(k) > T_s\,\rho_i + \delta_i \Rightarrow -T_s\,\rho_i - \delta_i \le \sigma_i(k+1) < \sigma_i(k) \\ &\sigma_i(k) < -T_s\,\rho_i - \delta_i \Rightarrow \sigma_i(k) < \sigma_i(k+1) \le T_s\,\rho_i + \delta_i \\ &|\sigma_i(k)| \le T_s\,\rho_i + \delta_i \Rightarrow |\sigma_i(k+1)| \le T_s\,\rho_i + \delta_i. \end{aligned} \tag{36}$$

1. Consider the first case where $\sigma_i(k) > T_s\,\rho_i + \delta_i$, then $\sigma_i(k) > 0$, $\mathrm{sign}(\sigma_i(k)) = 1$ and:

$$\begin{aligned} &\sigma_i(k+1) = \lambda_i\,\sigma_i(k) + E_i(k) - T_s\,\rho_i \\ &\sigma_i(k+1) - \sigma_i(k) = E_i(k) + (\lambda_i - 1)\,\sigma_i(k) - T_s\,\rho_i. \end{aligned} \tag{37}$$

If the condition in (31) is satisfied, then $\sigma_i(k+1) - \sigma_i(k) < 0 \Rightarrow \sigma_i(k+1) < \sigma_i(k)$.

Moreover, $-T_s\,\rho_i - \delta_i \le \sigma_i(k+1)$ can be written as:

$$\lambda_i\,\sigma_i(k) + E_i(k) - T_s\,\rho_i \ge -T_s\,\rho_i - \delta_i. \tag{38}$$

Hence:

$$\sigma_i(k) \ge \frac{1}{\lambda_i}\left(E_i(k) - \delta_i\right), \tag{39}$$

since $\sigma_i(k) > 0$ and $(E_i(k) - \delta_i) < 0$, then the above inequality is always true.

2. Consider the second case where $\sigma_i(k) < -T_s\,\rho_i - \delta_i$. This implies $\sigma_i(k) < 0$ and $\mathrm{sign}(\sigma_i(k)) = -1$. Then, let us rewrite $\sigma_i(k) < \sigma_i(k+1)$ as follows:

$$\begin{aligned} \sigma_i(k) &< \lambda_i\,\sigma_i(k) + E_i(k) + T_s\,\rho_i \\ (1-\lambda_i)\,\sigma_i(k) &< E_i(k) + T_s\,\rho_i \end{aligned} \tag{40}$$

   which is always true since $\rho_i > \dfrac{1}{T_s}\delta_i$.

   Moreover, $\sigma_i(k+1) < T_s\,\rho_i + \delta_i$ can be rewritten as:

$$\lambda_i\,\sigma_i(k) + E_i(k) + T_s\,\rho_i < T_s\,\rho_i + \delta_i. \tag{41}$$

   Since $\sigma_i(k) < 0$ and $\delta_i > E_i(k)$, then, it is obvious that the inequality in (15) is always true.

3. Consider the third case where $|\sigma_i(k)| \leq \varepsilon$, then:

   a. if $\sigma_i(k) > 0$, then $|\sigma_i(k)| \leq \varepsilon$ becomes:

$$0 < \sigma_i(k) < \varepsilon. \tag{42}$$

   Multiplying (42) by λ_i and adding $E_i(k) - T_s\,\rho_i$ to all the part leads to:

$$\begin{aligned} E_i(k) - T_s\,\rho_i < \sigma_i(k+1) &< E_i(k) - T_s\,\rho_i + \lambda_i\,\varepsilon \\ -\varepsilon < \sigma_i(k+1) &< \varepsilon \\ |\sigma_i(k+1)| &\leq \varepsilon \end{aligned} \tag{43}$$

   b. if $\sigma_i(k) < 0$, then $|\sigma_i(k)| \leq \varepsilon$ becomes:

$$-\,\varepsilon < \sigma_i(k) < 0. \tag{44}$$

   Once again, multiplying (44) by λ_i and adding $E_i(k) + T_s\,\rho_i$ to all the parts gives:

$$\begin{aligned} E_i(k) + T_s\,\rho_i - \lambda_i\,\varepsilon < \sigma_i(k+1) &< E_i(k) + T_s\,\rho_i \\ -\varepsilon < \sigma_i(k+1) &< \varepsilon \\ |\sigma_i(k+1)| &\leq \varepsilon \end{aligned} \tag{45}$$

   Hence:

$$|\sigma_i(k+1)| < \varepsilon = T_s\,\rho_i + \delta_i. \tag{46}$$

Since the conditions in (36) are met, the existence of a convergent quasi sliding mode has been established. Consequently, the proposed DSMC with TDE method in (32) is stable.

Now, let us demonstrate by contradiction according to (34) that Equation (33) is true. For this part, let us assume that $\sigma_i(0) \neq 0$ and $\mathrm{sign}(\sigma_i(0)) = \mathrm{sign}(\sigma_i(1)) = \cdots = \mathrm{sign}(\sigma_i(k^{'}+1))$.

1. Consider the first case where $\sigma_i(0) > 0$ and $\sigma_i(m) > 0$ for all $m \leq (k_i^{'} + 1)$. Then:

$$\begin{aligned} \sigma_i(1) &= \lambda_i\, \sigma_i(0) + E_i(0) - T_s\, \rho_i \\ &\leq \sigma_i(0) + E_i(0) - T_s\, \rho_i \\ \sigma_i(2) &\leq \sigma_i(1) + E_i(1) - T_s\, \rho_i \\ &\leq \sigma_i(0) + E_i(0) + E_i(1) - 2\, T_s\, \rho_i \\ &\vdots \\ \sigma_i(m) &\leq \sigma_i(m-1) + E_i(m-1) - T_s \rho_i \\ &\leq \sigma_i(0) + \sum_{j=0}^{m-1} E_i(j) - m\, T_s\, \rho_i \\ &\leq |\sigma_i(0)| + m\, [\delta_i - T_s\, \rho_i]\,. \end{aligned} \tag{47}$$

Hence, it is obvious that $k_i^{'}$ ensures that:

$$|\sigma_i(0)| + k_i^{'}\, [\delta_i - T_s\, \rho_i] = 0. \tag{48}$$

It follows that:

$$\begin{aligned} \sigma_i(k_i^{'} + 1) &\leq |\sigma_i(0)| + (k_i^{'} + 1)\, [\delta_i - T_s\, \rho_i] \\ &< |\sigma_i(0)| + k_i^{'}\, [\delta_i - T_s\, \rho_i] = 0 \end{aligned} \tag{49}$$

which is contradictory to the fact that $\sigma_i(m) > 0$, $\forall\, m \leq (k_i^{'} + 1)$.

2. Consider the second case where $\sigma_i(0) < 0$ and $\sigma_i(m) < 0$ for all $m \leq (k_i^{'} + 1)$. Then:

$$\begin{aligned} \sigma_i(1) &= \lambda_i\, \sigma_i(0) + E_i(0) + T_s\, \rho_i \\ &\geq \sigma_i(0) + E_i(0) + T_s\, \rho_i \\ \sigma_i(2) &\geq \sigma_i(1) + E_i(1) + T_s\, \rho_i \\ &\geq \sigma_i(0) + E_i(0) + E_i(1) + 2\, T_s\, \rho_i \\ &\vdots \\ \sigma_i(m) &\geq \sigma_i(m-1) + E_i(m-1) + T_s\, \rho_i \\ &\geq \sigma_i(0) + \sum_{j=0}^{m-1} E_i(j) + m\, T_s\, \rho_i \\ &\geq -|\sigma_i(0)| + m\, [T_s\, \rho_i - \delta_i] \end{aligned} \tag{50}$$

Once again, it is obvious that $k_i^{'}$ verifies:

$$-\, |\sigma_i(0)| + k_i^{'}\, [T_s\, \rho_i - \delta_i] = 0. \tag{51}$$

It follows that:

$$\begin{aligned} \sigma_i(k_i^{'} + 1) &\geq -|\sigma_i(0)| + (k_i^{'} + 1)\, [T_s\, \rho_i - \delta_i] \\ &> -|\sigma_i(0)| + k_i^{'}\, [T_s\, \rho_i - \delta_i] = 0 \end{aligned} \tag{52}$$

which is contradictory to the fact that $\sigma_i(m) < 0$, $\forall\, m \leq (k_i^{'} + 1)$.

This concludes the proof of Theorem 1. □

3.2.2. Control of Stator Current in the $x-y$ Sub-Space

In this section, the same methodology used previously for the stator current $\mathbf{x}_1(k)$ will be adopted to control the stator current in the $x-y$ sub-space. In this case, the sliding surface is selected as follows:

$$\sigma''(k) = \mathbf{e}_{s_{xy}}(k) = \mathbf{x}_2(k) - \mathbf{x}_2^*(k) \tag{53}$$

where $\mathbf{x}_2^*(k) = [i_{sx}^*(k),\ i_{sy}^*(k)]^T$ is the desired $x-y$ current and $\mathbf{e}_{s_{xy}}(k)$ denotes the tracking error variable. Hence, $\sigma''(k+1)$ is computed as follows:

$$\begin{aligned} \sigma''(k+1) &= \mathbf{e}_{s_{xy}}(k+1) = \mathbf{x}_2(k+1) - \mathbf{x}_2^*(k+1) \\ &= \mathbf{A}_2\,\mathbf{x}_2(k) + \mathbf{B}_2\,\mathbf{u}_2(k) + \eta_2(k) - \mathbf{x}_2^*(k+1). \end{aligned} \tag{54}$$

The discrete-time controller is obtained by solving:

$$\sigma''(k+1) = \Gamma\,\sigma''(k) - T_s\,\varrho\,\mathrm{sign}(\sigma''(k)) \tag{55}$$

where $\Gamma = \mathrm{diag}(\Gamma_1, \Gamma_2)$ with $0 < \Gamma_i < 1$ for $i = 1, 2$, $\varrho \in R^{2\times 2}$ is a diagonal positive matrix and $\mathrm{sign}(\sigma''(k)) = \left[\mathrm{sign}(\sigma_1''(k)), \mathrm{sign}(\sigma_2''(k))\right]^T$, and by substituting the uncertain vector $\eta_2(k)$ by its estimate using TDE method:

$$\begin{aligned} \hat{\eta}_2(k) &\cong \eta_2(k-1) \\ &= \mathbf{x}_2(k) - \mathbf{A}_2\,\mathbf{x}_2(k-1) - \mathbf{B}_2\,\mathbf{u}_2(k-1). \end{aligned} \tag{56}$$

Theorem 2. *If the controller gains are chosen for i = 1, 2 as follows:*

$$\varrho_i > \frac{1}{T_s}\delta_i'' \tag{57}$$

with $\delta_i'' > 0$ *the upper-bound of the TDE error* $E''(k) = \eta_2(k) - \hat{\eta}_2(k)$*, then, the following DSMC with TDE method for the stator current in the* $x-y$ *sub-space* (16) *ensures a quasi sliding motion:*

$$\mathbf{u}_2(k) = -\mathbf{B}_2^{-1}\left[\mathbf{A}_2\,\mathbf{x}_2(k) + \hat{\eta}_2(k) - \mathbf{x}_2^*(k+1) - \Gamma\,\sigma''(k) + T_s\,\varrho\,\mathrm{sign}(\sigma''(k))\right]. \tag{58}$$

Proof of Theorem 2. The stability analysis is similar to the one described for the stator currents in the $\alpha-\beta$ sub-space. □

4. Experimental Results

The proposed DSMC technique was tested in order to validate its performance with experimental results obtained in the test bench, and this consisted of a six-phase IM powered by two conventional three-phase VSI, being equivalent to a six-leg VSI, using a constant DC-bus voltage from a DC power supply system. The six-leg VSI was controlled by a dSPACE MABXII DS1401 real-time rapid prototyping platform, with Simulink version 8.2. The results obtained were captured and processed using MATLAB R2013b script. The parameters of the asymmetrical six-phase IM were obtained using conventional methods of the AC time domain and stand-still with VSI supply tests [40,41]. The results are listed in Table 1. The experimental tests were performed with current sensors LA 55-P s, which had a frequency bandwidth from DC up to 200 kHz. The current measurements were then converted to digital form using a 16-bit A/D converter. The six-phase IM position was obtained with a 1024-ppr incremental encoder, and the rotor speed was estimated from it. Finally, a 5 HP eddy current brake was used to introduce a variable mechanical load on the IM. A block diagram of the experimental bench is shown in Figure 3, including some photos of the equipment.

Table 1. Parameters of the six-phase IM.

Parameter	Value	Parameter	Value	Parameter	Value
R_r (Ω)	6.9	L_r (mH)	626.8	P_w (kW)	2
R_s (Ω)	6.7	ω_{m-nom} (rpm)	3000	J_i (kg·m^2)	0.07
L_{ls} (mH)	5.3	L_s (mH)	654.4	B_i (kg·m^2/s)	0.0004
L_m (mH)	614	P	1	V_{dc} (V)	400

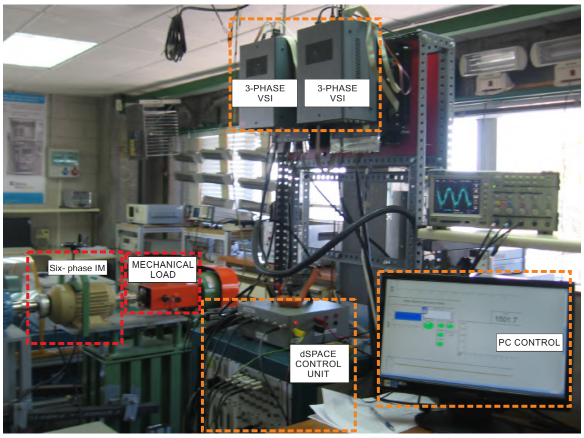

Figure 3. Block diagram of the test bench including the six-phase IM, the six-leg VSI, the dSPACE and the mechanical load.

The performance of the proposed DSMC was analysed in transient and steady-state conditions. The experimental results analysed the controller performance in terms of Mean Squared Error (MSE) between the reference and measured stator currents in the $\alpha-\beta$, $x-y$ and $d-q$ planes. The Root Mean Square (RMS) of the currents in the $d-q$ plane was used to calculate their corresponding Form Factor (FF) and Total Harmonic Distortion (THD) obtained in the $\alpha-\beta$ plane, as well as MSE for rotor speed. The MSE is defined as:

$$\text{MSE}(i_{s\Phi}) = \sqrt{\frac{1}{N}\sum_{k=1}^{N}(i_{s\Phi}(k) - i^*_{s\Phi}(k))^2} \tag{59}$$

where N is the number of analysed samples, $i^*_{s\Phi}$ the stator current reference, $i_{s\Phi}$ the measured stator currents and $\Phi \in \{\alpha, \beta, x, y, d, q\}$. On the other hand, the THD is calculated as:

$$\text{THD}(i_s) = \sqrt{\frac{1}{i^2_{s1}}\sum_{j=2}^{N}(i_{sj})^2} \tag{60}$$

where i_{s1} is the fundamental stator currents and i_{sj} is the harmonic stator currents. At last, the FF is computed as:

$$\text{FF}(i_{dqs}) = \frac{i_{dqs-RMS}}{i_{dqs-mean}}. \tag{61}$$

A fixed d current ($i^*_{ds} = 1$ A) was used. To perform a mechanical load for the six-phase IM, the eddy current brake was fixed at 1.65 A. Moreover, the chosen gains of the DSMC with TDE for stator current tracking are:

$$\lambda = \mathrm{diag}(0.5, 0.5), \qquad \rho_1 = \rho_2 = 100,$$

$$\Gamma = \mathrm{diag}(0.9, 0.9), \qquad \varrho_1 = \varrho_2 = 100.$$

The stator current reference in the $x-y$ sub-space was set to zero ($i^*_{xs} = i^*_{ys} = 0$ A) in order to reduce the copper losses. The sampling frequencies used in the tests were 8 kHz and 16 kHz. Three operation points were set for the rotor speed: 500 rpm, 1000 rpm and 1500 rpm for steady-state analysis. For a transient response, a step change in rotor speed was considered from 500 to -500 rpm (i.e., a reversal condition).

The proposed technique DSMC was tested under different operating points in steady state and under transient conditions. Table 2 shows the experimental results obtained for different rotor mechanical speeds and sampling frequencies, regarding the MSE of stator currents in the $\alpha-\beta$, $x-y$ and $d-q$planes. The results showed good performance of DSMC applied to the six-phase IM in terms of current tracking, in their corresponding planes, especially in $\alpha-\beta$ current tracking. Table 3 shows the results of THD in $\alpha-\beta$ stator currents, RMS ripple and FF in $d-q$ currents and the MSE of the measured and referenced rotor speed. The results presented a reduction on the THD stator currents with the higher sampling frequency and higher rotor speed. In terms of RMS ripple and FF, there was a significant reduction with higher sampling frequency in all the rotor speed tests. However, for rotor speed MSE, better performance was obtained at lower rotor speed and sampling frequency, but this was not significant.

Figure 4 presents the polar trajectories of stator currents in the $x-y$ and $\alpha-\beta$ sub-spaces at different rotor speeds. The tests were developed with the same mechanical load; thus, the amplitude of $\alpha-\beta$ currents was proportional to the rotor speed. The figures show that $x-y$ currents were reduced to almost the same ratio in every case and $\alpha-\beta$ current tracking was good. On the other hand, Figures 5 and 6 report a dynamic test, which consisted of the transient performance of DSMC for a step response in the q axis current reference (i^*_{qs}). The dynamic response was generated through a reversal condition of the rotor mechanical speed (ω_m) from 500 to -500 rpm. Figures 5a and 6a show an overshoot of 42% and 70%, respectively, and a settling time of 1.3 ms and 1.4 ms. respectively, presenting in both cases very fast responses.

Table 2. Performance analysis of stator currents $\alpha-\beta$, $x-y$, $d-q$ and MSE (A) for three different rotor speeds (rpm).

		Sampling	**Frequency**	**8 kHz**		
ω^*_m	**MSE**$_\alpha$	**MSE**$_\beta$	**MSE**$_x$	**MSE**$_y$	**MSE**$_d$	**MSE**$_q$
500	0.2502	0.2602	0.1875	0.1729	0.2494	0.2609
1000	0.2937	0.3021	0.2326	0.2280	0.3039	0.2919
1500	0.3000	0.3050	0.2491	0.2456	0.3327	0.2689
		Sampling	**Frequency**	**16 kHz**		
ω^*_m	**MSE**$_\alpha$	**MSE**$_\beta$	**MSE**$_x$	**MSE**$_y$	**MSE**$_d$	**MSE**$_q$
500	0.1867	0.1883	0.1931	0.1851	0.1830	0.1919
1000	0.1797	0.1779	0.2078	0.1975	0.1795	0.1780
1500	0.1731	0.1786	0.2342	0.2291	0.1767	0.1750

Table 3. Performance analysis of stator current $\alpha - \beta$, THD (%), $d - q$, RMS ripple (A), FF, rotor speed (ω_m) and MSE (rpm) at different rotor speeds (rpm).

		Sampling	**Frequency**	**8 kHz**			
ω_m^*	**THD$_\alpha$**	**THD$_\beta$**	**RMS ripple$_q$**	**RMS ripple$_d$**	**FF$_q$**	**FF$_d$**	**MSE$_{\omega_m}$**
500	29.6198	30.7074	0.2598	0.2492	1.0811	1.0300	1.3432
1000	17.8543	18.0026	0.2890	0.3005	1.0203	1.0405	2.2250
1500	17.8761	18.0059	0.2593	0.3194	1.0084	1.1389	2.4146
		Sampling	**Frequency**	**16 kHz**			
ω_m^*	**THD$_\alpha$**	**THD$_\beta$**	**RMS ripple$_q$**	**RMS ripple$_d$**	**FF$_q$**	**FF$_d$**	**MSE$_{\omega_m}$**
500	21.6914	22.6592	0.1895	0.1829	1.0466	1.0164	1.6508
1000	15.3291	14.8507	0.1751	0.1783	1.0087	1.0151	2.8814
1500	11.1020	11.2140	0.1707	0.1712	1.0040	1.0134	3.1855

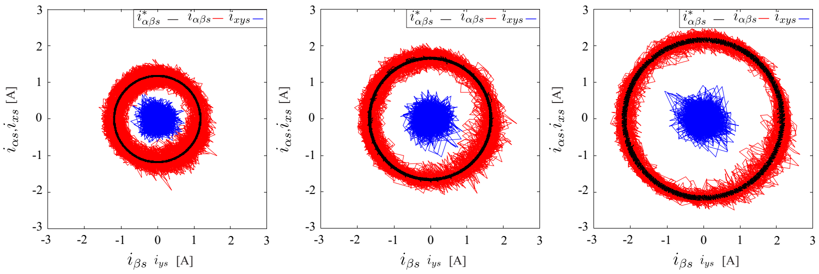

(a) (b) (c)

Figure 4. Stator currents in the $\alpha - \beta$ and $x - y$ planes for a rotor speed ω_m of: (**a**) 500 rpm; (**b**) 1 000 rpm; (**c**) 1 500 rpm.

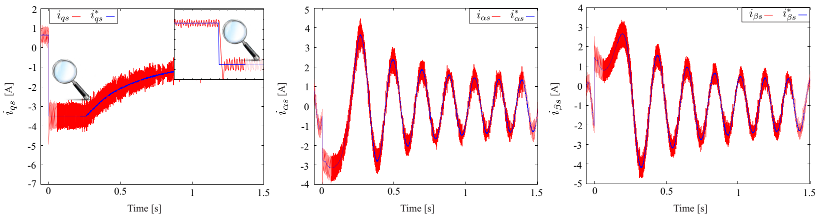

(a) (b) (c)

Figure 5. Transient response of stator currents from a step response of 500 rpm to −500 rpm from ω_m at a frequency sample of 8 kHz: (**a**) i_{qs}; (**b**) $i_{\alpha s}$; (**c**) $i_{\beta s}$.

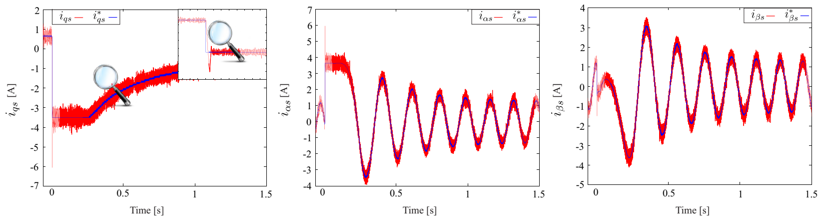

(a) (b) (c)

Figure 6. Transient response of stator currents from a step response of 500 rpm to −500 rpm from ω_m at a frequency sample of 16 kHz: (**a**) i_{qs}; (**b**) $i_{\alpha s}$; (**c**) $i_{\beta s}$.

5. Conclusions

In this work, a speed control based on the IRFOC strategy with an inner robust DSMC with the TDE method for stator currents in the $\alpha - \beta$ and $x - y$ sub-spaces has been proposed. On the one hand, the TDE method allows in a simple way highly accurate estimation of the uncertainties, perturbations and unmeasurable rotor current. On the other hand, discrete-time sliding mode cancels the effect of the TDE error, ensures robustness and delivers high precision and fast convergence. The efficiency of the proposed discrete control scheme has been confirmed by a real-time implementation on a six-phase induction motor drive. The proposed approach provides very good performances in dynamic processes, as well as in steady state. Moreover, the average switching frequency of the designed DSMC is low. Further research will be initiated to benefit from the advantages offered by multiphase machines. To that end, an extension of the proposed controller will be developed in the case of an open circuit fault in one or more phases occurring, since this fault is common for induction machines. The work will focus on the ability of ensuring good performances without good knowledge of the new mathematical model of the machine under fault condition.

Author Contributions: Conceptualization, Y.K., J.R. and M.S.; methodology, Y.K., M.A. and J.R.; software, Y.K., M.A. and J.R.; validation, M.A. and J.D.-G.; formal analysis, Y.K., J.R., M.S. and K.B.; investigation, Y.K. and J.R.; resources, J.D.-G.; data curation, J.D.-G. and M.A.; writing, original draft preparation, Y.K., M.A. and J.R.; writing, review and editing, Y.K., M.A., J.R., M.S., J.D.-G. and R.G.; visualization, J.D.G., M.A. and J.R.; project administration, J.R., M.S. and J.D.-G.; funding acquisition, R.G. and J.R.

Funding: This research and APC were funded by the Consejo Nacional de Ciencia y Tecnología (CONACYT)-Paraguay, Grant Numbers 14-INV-101 and POSG16-05.

Acknowledgments: The authors would like to thank Graham Goodwin (University of Newcastle-Australia) for his valuable comments on this research work.

Conflicts of Interest: The authors declare no conflict of interest.

Abbreviations

The following abbreviations are used in this manuscript:

DSMC	Discrete-Time Siding Mode Control
FF	Form Factor
IM	Induction Machine
IRFOC	Indirect Rotor Field-Oriented Control
MSE	Mean Squared Error
RMS	Root Mean Square
PI	Proportional-Integral

SMC	Sliding Mode Control
TDE	Time Delay Estimation
THD	Total Harmonic Distortion
VSD	Vector Space Decomposition
VSI	Voltage Source Inverter

References

1. Barrero, F.; Duran, M.J. Recent Advances in the Design, Modeling, and Control of Multiphase Machines: Part I. *IEEE Trans. Ind. Electron.* **2016**, *63*, 449–458, doi:10.1109/TIE.2015.2447733.
2. Duran, M.J.; Barrero, F. Recent Advances in the Design, Modeling, and Control of Multiphase Machines: Part II. *IEEE Trans. Ind. Electron.* **2016**, *63*, 459–468, doi:10.1109/TIE.2015.2448211.
3. Levi, E. Advances in Converter Control and Innovative Exploitation of Additional Degrees of Freedom for Multiphase Machines. *IEEE Trans. Ind. Electron.* **2016**, *63*, 433–448, doi:10.1109/TIE.2015.2434999.
4. Zoric, I.; Jones, M.; Levi, E. Arbitrary Power Sharing Among Three-Phase Winding Sets of Multiphase Machines. *IEEE Trans. Ind. Electron.* **2018**, *65*, 1128–1139, doi:10.1109/TIE.2017.2733468.
5. Yepes, A.G.; Malvar, J.; Vidal, A.; López, O.; Doval-Gandoy, J. Current harmonics compensation based on multiresonant control in synchronous frames for symmetrical n-phase machines. *IEEE Trans. Ind. Electron.* **2015**, *62*, 2708–2720, doi:10.1109/TIE.2014.2365155.
6. Lim, C.; Levi, E.; Jones, M.; Rahim, N.; Hew, W.P. FCS-MPC based current control of a five-phase induction motor and its comparison with PI-PWM control. *IEEE Trans. Ind. Electron.* **2014**, *61*, 149–163, doi:10.1109/TIE.2013.2248334.
7. Taheri, A.; Rahmati, A.; Kaboli, S. Efficiency improvement in DTC of six-phase induction machine by adaptive gradient descent of flux. *IEEE Trans. Power Electron.* **2012**, *27*, 1552–1562, doi:10.1109/TPEL.2011.2163420.
8. Riveros, J.A.; Barrero, F.; Levi, E.; Duran, M.J.; Toral, S.; Jones, M. Variable-speed five-phase induction motor drive based on predictive torque control. *IEEE Trans. Ind. Electron.* **2013**, *60*, 2957–2968, doi:10.1109/TIE.2012.2198034.
9. Gregor, R.; Rodas, J. Speed sensorless control of dual three-phase induction machine based on a Luenberger observer for rotor current estimation. In Proceedings of the 38th Annual Conference on IEEE Industrial Electronics Society (IECON), Montreal, QC, Canada, 25–28 Octorber 2012; pp. 3653–3658, doi:10.1109/IECON.2012.6389311.
10. Ayala, M.; Gonzalez, O.; Rodas, J.; Gregor, R.; Doval-Gandoy, J. A speed-sensorless predictive current control of multiphase induction machines using a Kalman filter for rotor current estimator. In Proceedings of the 2016 International Conference on Electrical Systems for Aircraft, Railway, Ship Propulsion and Road Vehicles & International Transportation Electrification Conference (ESARS-ITEC), Toulouse, France, 2–4 November 2016; pp. 1–6, doi:10.1109/ESARS-ITEC.2016.7841385.
11. Rodas, J.; Barrero, F.; Arahal, M.R.; Martín, C.; Gregor, R. Online estimation of rotor variables in predictive current controllers: a case study using five-phase induction machines. *IEEE Trans. Ind. Electron.* **2016**, *63*, 5348–5356, doi:10.1109/TIE.2016.2559420.
12. Rodas, J.; Martín, C.; Arahal, M.R.; Barrero, F.; Gregor, R. Influence of Covariance-Based ALS Methods in the Performance of Predictive Controllers with Rotor Current Estimation. *IEEE Trans. Ind. Electron.* **2017**, *64*, 2602–2607, doi:10.1109/TIE.2016.2636205.
13. Guzman, H.; Duran, M.J.; Barrero, F.; Zarri, L.; Bogado, B.; Prieto, I.G.; Arahal, M.R. Comparative study of predictive and resonant controllers in fault-tolerant five-phase induction motor drives. *IEEE Trans. Ind. Electron.* **2016**, *63*, 606–617, doi:10.1109/TIE.2015.2418732.
14. Bermudez, M.; Gonzalez-Prieto, I.; Barrero, F.; Guzman, H.; Duran, M.J.; Kestelyn, X. Open-Phase Fault-Tolerant Direct Torque Control Technique for Five-Phase Induction Motor Drives. *IEEE Trans. Ind. Electron.* **2017**, *64*, 902–911, doi:10.1109/TIE.2016.2610941.
15. Baneira, F.; Doval-Gandoy, J.; Yepes, A.G.; López, O.; Pérez-Estévez, D. Control Strategy for Multiphase Drives With Minimum Losses in the Full Torque Operation Range Under Single Open-Phase Fault. *IEEE Trans. Power Electron.* **2017**, *32*, 6275–6285, doi:10.1109/TPEL.2016.2620426.

16. Rodas, J.; Guzman, H.; Gregor, R.; Barrero, B. Model predictive current controller using Kalman filter for fault-tolerant five-phase wind energy conversion systems. In Proceedings of the 7th International Symposium on Power Electronics for Distributed Generation Systems (PEDG), Vancouver, BC, Canada, 27–30 June 2016; pp. 1–6, doi:10.1109/PEDG.2016.7526999.
17. Echeikh, H.; Trabelsi, R.; Mimouni, M.F.; Iqbal, A.; Alammari, R. High performance backstepping control of a fivephase induction motor drive. In Proceedings of the 2014 IEEE 23rd International Symposium on Industrial Electronics (ISIE), Istanbul, Turkey, 1–4 June 2014; pp. 812–817, doi:10.1109/ISIE.2014.6864716.
18. Echeikh, H.; Trabelsi, R.; Iqbal, A.; Bianchi, N.; Mimouni, M.F. Comparative study between the rotor flux oriented control and non-linear backstepping control of a five-phase induction motor drive—An experimental validation. *IET Power Electron.* **2016**, *9*, 2510–2521, doi:10.1049/iet-pel.2015.0726.
19. Kali, Y.; Rodas, J.; Saad, M.; Gregor, R.; Bejelloun, K.; Doval-Gandoy, J. Current Control based on Super-Twisting Algorithm with Time Delay Estimation for a Five-Phase Induction Motor Drive. In Proceedings of the 2017 International Electric Machines and Drives Conference (IEMDC), Miami, FL, USA, 21–24 May 2017; pp. 1–8, doi:10.1109/IEMDC.2017.8002122.
20. Kali, Y.; Rodas, J.; Saad, M.; Gregor, R.; Bejelloun, K.; Doval-Gandoy, J.; Goodwin, G. Speed Control of a Five-Phase Induction Motor Drive using Modified Super-Twisting Algorithm. In Proceedings of the 2018 International Symposium on Power Electronics, Electrical Drives, Automation and Motion (SPEEDAM), Amalfi, Italy, 20–22 June 2018; pp. 938–943, doi:10.1109/SPEEDAM.2018.8445404.
21. Ayala, M.; Gonzalez, O.; Rodas, J.; Gregor, R.; Kali, Y.; Wheeler, P. Comparative Study of Non-linear Controllers Applied to a Six-Phase Induction Machine. In Proceedings of the 2018 International Conference on Electrical Systems for Aircraft, Railway, Ship Propulsion and Road Vehicles & International Transportation Electrification Conference (ESARS-ITEC), Nottingham, UK, 7–9 November 2018; pp. 1–6,
22. Fnaiech, M.A.; Betin, F.; Capolino, G.A.; Fnaiech, F. Fuzzy logic and sliding-mode controls applied to six-phase induction machine with open phases. *IEEE Trans. Ind. Electron.* **2010**, *57*, 354–364, doi:10.1109/TIE.2009.2034285.
23. Utkin, V. *Sliding Mode in Control and Optimization*; Springer-Verlag: Berlin, German, 1992.
24. Utkin, V.; Guldner, J.; Shi, J. *Sliding Mode Control in Electromechanical Systems*; Taylor-Francis: Abingdon, UK, 1999.
25. Fridman, L. An averaging approach to chattering. *IEEE Trans. Autom. Control* **2001**, *46*, 1260–1265, doi:10.1109/9.940930.
26. Boiko, I.; Fridman, L. Analysis of Chattering in Continuous Sliding-mode Controllers. *IEEE Trans. Autom. Control* **2005**, *50*, 1442–1446, doi:10.1109/ACC.2005.1470332.
27. Young, K.D.; Utkin, V.I.; Ozguner, U. A control engineer's guide to sliding mode control. *IEEE Trans. Control Syst. Technol.* **1999**, *7*, 328–342, doi:10.1109/87.761053.
28. Drakunov, S.; Utkin, V. Sliding mode observers. Tutorial. In Proceedings of the 34th IEEE Conference on Decision and Control, New Orleans, LA, USA, 13–15 December 1995; pp. 3376–3378, doi:10.1109/CDC.1995.479009.
29. Yan, X.G.; Edwards, C. Nonlinear robust fault reconstruction and estimation using a sliding mode observer. *Automatica* **2007**, *43*, 1605–1614, doi:10.1016/j.automatica.2007.02.008.
30. Levant, A. Higher-order sliding modes, differentiation and output-feedback control. *Int. J. Control* **2003**, *76*, 924–941, doi:10.1080/0020717031000099029.
31. Kali, Y.; Saad, M.; Benjelloun, K.; Fatemi, A. Discrete-time second order sliding mode with time delay control for uncertain robot manipulators. *Robot. Auton. Syst.* **2017**, *94*, 53–60, doi:10.1016/j.robot.2017.04.010.
32. Kali, Y.; Saad, M.; Benjelloun, K.; Khairallah, C. Super-twisting algorithm with time delay estimation for uncertain robot manipulators. *Nonlinear Dyn.* **2018**, *93*, 557–569, doi:10.1007/s11071-018-4209-y.
33. Kali, Y.; Saad, M.; Benjelloun, K.; Benbrahim, M. Sliding Mode with Time Delay Control for MIMO Nonlinear Systems with Unknown Dynamics. In Proceedings of the 2015 International Workshop on Recent Advances in Sliding Modes (RASM), Istanbul, Turkey, 9–11 April 2015; pp. 1–6, doi:10.1109/RASM.2015.7154587.
34. Kali, Y.; Rodas, J.; Gregor, R.; Saad, M.; Benjelloun, K. Attitude Tracking of a Tri-Rotor UAV based on Robust Sliding Mode with Time Delay Estimation. In Proceedings of the 2018 International Conference on Unmanned Aircraft Systems (ICUAS), Dallas, TX, USA, 12–15 June 2018; pp. 346–351, doi:10.1109/ICUAS.2018.8453472.

35. Bandal, V.; Bandyopadhyay, B.; Kulkarni, A.M. Design of power system stabilizer using power rate reaching law based sliding mode control technique. In Proceedings of the 2005 International Power Engineering Conference, Singapore, 29 November–2 December 2005; pp. 923–928, doi:10.1109/IPEC.2005.207040.
36. Gonzalez, O.; Ayala, M.; Rodas, J.; Gregor, R.; Rivas, G.; Doval-Gandoy, J. Variable-Speed Control of a Six-Phase Induction Machine using Predictive-Fixed Switching Frequency Current Control Techniques. In Proceedings of the 9th IEEE International Symposium on Power Electronics for Distributed Generation Systems (PEDG), Charlotte, NC, USA, 25–28 June 2018; pp. 1–6, doi:10.1109/PEDG.2018.8447837.
37. Harnefors, L.; Saarakkala, S.E.; Hinkkanen, M. Speed Control of Electrical Drives Using Classical Control Methods. *IEEE Trans. Ind. Appl.* **2013**, *49*, 889–898, doi:10.1109/TIA.2013.2244194.
38. Jung, J.H.; Chang, P.; Kang, S.H. Stability Analysis of Discrete Time Delay Control for Nonlinear Systems. In Proceedings of the 2007 American Control Conference, New York City, NY, USA, July 11–13 2007; pp. 5995–6002, doi:10.1109/ACC.2007.4282317.
39. Qu, S.; Xia, X.; Zhang, J. Dynamics of Discrete-Time Sliding-Mode-Control Uncertain Systems With a Disturbance Compensator. *IEEE Trans. Ind. Electron.* **2014**, *61*, 3502–3510, doi:10.1109/TIE.2013.2279369.
40. Yepes, A.G.; Riveros, J.A.; Doval-Gandoy, J.; Barrero, F.; López, O.; Bogado, B.; Jones, M.; Levi, E. Parameter identification of multiphase induction machines with distributed windings Part 1: Sinusoidal excitation methods. *IEEE Trans. Energy Convers.* **2012**, *27*, 1056–1066, doi:10.1109/TEC.2012.2220967.
41. Riveros, J.A.; Yepes, A.G.; Barrero, F.; Doval-Gandoy, J.; Bogado, B.; Lopez, O.; Jones, M.; Levi, E. Parameter identification of multiphase induction machines with distributed windings Part 2: Time-domain techniques. *IEEE Trans. Energy Convers.* **2012**, *27*, 1067–1077, doi:10.1109/TEC.2012.2219862.

ARTÍCULO 2

TIME DELAY ESTIMATION BASED DISCRETE-TIME SUPER-TWISTING CURRENT CONTROL FOR A SIX-PHASE INDUCTION MOTOR

- Yassine Kali, **Magno Ayala**, Jorge Rodas, Maarouf Saad, Jesus Doval-Gandoy, Raul Gregor and Khalid Benjelloun, ”Time Delay Estimation based Discrete-Time Super-Twisting Current Control for a Six-Phase Induction Motor”, IEEE Transactions on Power Electronics, pp. 1-8, 2020. (R2)

Time Delay Estimation based Discrete-Time Super-Twisting Current Control for a Six-Phase Induction Motor

***Abstract*—In this paper, the problem of high-accuracy stator currents tracking of a six-phase induction motor in the presence of uncertainties, disturbances and unmeasurable rotor currents is tackled. Since the good features offered by sliding mode theory motivate the community of researchers on control, a time delay estimation based discrete-time super-twisting controller is proposed. First of all, an outer loop is performed to regulate the speed and to construct the desired stator currents. Then, the inner loop, based on an indirect rotor field-oriented control, is performed based on the proposed method. The proposed structure allows an accurate and simple estimation of uncertainties and rotor currents, a high tracking precision, a fast convergence of the currents tracking error to a neighbour of zero. The design procedure and the stability analysis are detailed for the current closed-loop system. Experimental work was carried out on an asymmetrical six-phase induction motor to give a demonstration of the effectiveness of the developed discrete approach. In addition, the performances obtained are compared to the ones obtained using the discrete-time sliding mode controller with time delay estimation. The results obtained highlighted the satisfactory stator currents tracking performance in steady-state and transient conditions and under different sampling times, parameters mismatch and with load and no-load conditions.**

***Index Terms*—Multiphase motor drive, sliding model control, stator currents control, super twisting algorithm, time delay estimation.**

NOMENCLATURE

List of Symbols

L_m	Magnetizing inductance.
L_{lr}	Leakage inductance of the rotor.
L_r	Inductance of the rotor.
L_{ls}	Leakage inductance of the stator.
L_s	Inductance of the stator.
R_r	Resistance of the rotor.
R_s	Resistance of the stator.
ω_r	Electrical speed.
ω_m	Mechanical speed.
ψ_s	Stator fluxes.
v_s	Stator input voltages.
i_s	Stator currents.
i_r	Rotor currents.
P	Number of pole pairs.
T_e	Electromagnetic torque.
T_L	Load torque.
F_m	Friction coefficient.
I_m	Inertia coefficient.
T_s	Sampling time.

I. INTRODUCTION

INDUSTRIAL applications of multiphase motor drives are becoming more common during the last decade. The 12-phase Gamesa wind turbine, the 9-phase Hyundai traction system for ultrahigh-speed elevators and the 15-phase General Electric motor for ship propulsion system are good examples of multiphase machines commercial applications [1], [2]. The possibility of split the power among more phases as well as the post-fault operation without extra hardware makes multiphase machines an excellent choice for high-power applications. However, the control of multiphase machines is more complicated than the three-phase machines due to the new degrees of freedom [3]. This challenge has been tackled by the research community by the extension of well-known control techniques such as Indirect Rotor Field Oriented Control (IRFOC) with multiple Proportional Integral (PI) pulse width modulator current controllers or the direct torque control [4]. Thanks to the advance of the digital platforms, the real-time implementation of nonlinear controllers such as fuzzy logic control [5], [6], model predictive control [7]–[10] and Sliding Mode Control (SMC) [6], [11] have also been successfully implemented for multiphase machines.

SMC is a well-known nonlinear robust technique for uncertain dynamical systems [12]. Many works have proposed the use of this variable structure controller because of its good features; among them, invariance to matched uncertainties and perturbations, reduction of the system order, convergence in finite-time, simplicity of design... The aim of SMC is to guarantee the occurrence of a sliding mode on a designed manifold known as sliding surface by adding to the controller a switching action (discontinuous action) that forces the trajectories of the controlled systems to remain on the surface [12]. Nonetheless, attempts to implement this method in real-time applications were stopped by its major disadvantage, the famous chattering phenomenon. The origin of this serious problem that can easily damage the controlled system comes from the fact that the time of calculation in practice doesn't allow the required infinite switching frequency [13]. In order to fix this problem, sampled-data systems have been used. However, the obtained performances are not always satisfactory because the inherent properties are no longer maintained. Thus, based on the discrete-time dynamics, the Discrete-time Sliding Mode Control (DSMC) has been derived. Most of the existing works that tackle the DSMC derive the control law by discretizing the different proposed continuous reaching laws [14]–[17]. It has been noticed through different case studies that the DSMC ensures that the states converge in predefined-time to the sliding surface but don't slide along it. These works proved that after the states reach the sliding surface, they evolve inside a band in the vicinity of the switching function known as quasi sliding mode and finally, the error converges to a final ultimate bound even in the presence of uncertainties.

Despite the huge popularity of the conventional SMC, many works tried to improve its drawbacks mentioned above [18]–[21]. The most attractive one is the High Order Sliding Mode (HOSM) that owes his success to two major improvements [22]. Indeed, the performances obtained with HOSM are better compared to the conventional SMC because HOSM allows a higher precision since it ensures not only the convergence of the sliding function to zero but also its derivatives. Moreover, HOSM is a very effective method that reduces and/or eliminates the chattering phenomenon since the switching action is acting on the control input's higher derivatives which make the signal that fed into the system continuous. However, few works treated the discrete-time HOSM in the literature [23], [24] especially the most popular algorithm, the so-called Super-Twisting Algorithm (STA) that was used in discrete form only as an observer to reconstitute the systems states [25]–[27].

In this work, an attempt is made to develop and to implement experimentally in real-time a robust stator currents controller based on the combination of Time Delay Estimation (TDE) and Discrete-time Super-Twisting Control (DSTC) algorithm on an asymmetrical six-phase Induction Motor (IM) drive. TDE will be used not only to approximate the uncertainties, perturbations and unmeasurable rotor currents but also to circumvent the fact that upper bound of the unknown parts is obligatory when designing the STA controller. Hence, the estimation obtained will be added to the control action and will allow the choice of smaller DSTC algorithm gains to reduce the chattering and the control effort. Finally, the presented discrete method is implemented in real-time to demonstrate our theoretical findings and to show its suitability for the current control of multiphase machines. The results obtained are compared with those obtained with the DSMC with TDE [11] to verify that the proposed one is more suited.

The rest of the manuscript has been organized as follows: in Section II, the discrete-time dynamical model of the considered IM is developed by using the Euler approximation method and the control objective is enunciated. Section III details the development of the proposed DSTC algorithm supported by TDE. Moreover, the stability analysis has been established based on a quadratic Lyapunov function. In Section IV, the results of the real-time application of the proposed DSTC algorithm with TDE on a six-phase IM under different conditions are presented to illustrate its efficiency and its superiority in comparison with the DSMC with TDE. Lastly, some conclusions are given in Section V.

II. PRELIMINARIES

A. Dynamic Model of Asymmetrical Six-Phase IM

The dynamic model of an asymmetrical six-phase IM powered by two 3-phase 2-Level Voltage Source Converter (2L-VSC) (see Fig. 1) is described by [28]:

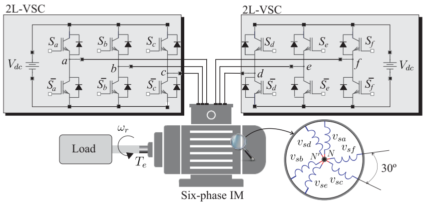

Fig. 1. Structure of the considered machine.

$$
\begin{aligned}
\frac{di_{r\alpha}}{dt} &= R_s l_1 i_{s\alpha} - l_2\left(R_r i_{r\alpha} + L_m\omega_r i_{s\beta} + L_r\omega_r i_{r\beta}\right) - l_1 v_{s\alpha}\\
\frac{di_{r\beta}}{dt} &= R_s l_1 i_{s\beta} + l_2\left(L_m\omega_r i_{s\alpha} + L_r\omega_r i_{r\alpha} - R_r i_{r\beta}\right) - l_1 v_{s\beta}\\
\frac{di_{s\alpha}}{dt} &= -R_s l_3 i_{s\alpha} + l_1\left(L_m\omega_r i_{s\beta} + R_r i_{r\alpha} + L_r\omega_r i_{r\beta}\right) + l_3 v_{s\alpha}\\
\frac{di_{s\beta}}{dt} &= -R_s l_3 i_{s\beta} + l_1\left(R_r i_{r\beta} - L_m\omega_r i_{s\alpha} - L_r\omega_r i_{r\alpha}\right) + l_3 v_{s\beta}\\
\frac{di_{sx}}{dt} &= -R_s l_4 i_{sx} + l_4 v_{sx}\\
\frac{di_{sy}}{dt} &= -R_s l_4 i_{sy} + l_4 v_{sy}
\end{aligned}
\tag{1}
$$

where the coefficients l_1 to l_4 are defined by: $l_1 = \frac{L_m}{L_r L_s - L_m^2}$, $l_2 = \frac{L_s}{L_m} l_1$, $l_3 = \frac{L_r}{L_m} l_1$ and $l_4 = \frac{1}{L_{ls}}$.

The mechanical equations of the system are described as follows:

$$
\begin{aligned}
\dot{\omega}_r &= -\frac{F_m}{I_m}\,\omega_r + \frac{P}{I_m}\left(T_e - T_L\right)\\
T_e &= 3\,P\left(\psi_{s\alpha}\, i_{s\beta} - \psi_{s\beta}\, i_{s\alpha}\right).
\end{aligned}
\tag{2}
$$

Assuming that it exists a sufficiently small T_s. Then, the discrete model of the considered machine can be derived using the Euler approximation method as [29]:

$$
\chi(k+1) = \mathbf{A}\,\chi(k) + \mathbf{B}\,\mathbf{v}(k) + \mathbf{p}(k) \tag{3}
$$

$$
\mathbf{y}(k) = \mathbf{C}\,\chi(k) \tag{4}
$$

where $\chi(k) = [i_{r\alpha}(k),\, i_{r\beta}(k),\, i_{s\alpha}(k),\, i_{s\beta}(k),\, i_{sx}(k),\, i_{sy}(k)]^T$ is the state vector, $\mathbf{v}(k) = [v_{s\alpha}(k),\, v_{s\beta}(k),\, v_{sx}(k),\, v_{sy}(k)]^T$ is the input vector, $\mathbf{y}(k) = [i_{s\alpha}(k),\, i_{s\beta}(k),\, i_{sx}(k),\, i_{sy}(k)]^T$ is the output vector, $\mathbf{p}(k) \in R^6$ is the vector of uncertainties caused by uncertain dynamics, parameters and disturbances. Moreover, $\mathbf{A}$, $\mathbf{B}$ and $\mathbf{C}$ are defined by:

$$
\mathbf{A} = \begin{bmatrix}
A_{11} & A_{12} & A_{13} & A_{14} & 0 & 0\\
A_{21} & A_{22} & A_{23} & A_{24} & 0 & 0\\
A_{31} & A_{32} & A_{33} & A_{34} & 0 & 0\\
A_{41} & A_{42} & A_{43} & A_{44} & 0 & 0\\
0 & 0 & 0 & 0 & A_{55} & 0\\
0 & 0 & 0 & 0 & 0 & A_{66}
\end{bmatrix} \tag{5}
$$

$$
\mathbf{B} = \begin{bmatrix}
-T_s l_1 & 0 & 0 & 0\\
0 & -T_s l_1 & 0 & 0\\
T_s l_3 & 0 & 0 & 0\\
0 & T_s l_3 & 0 & 0\\
0 & 0 & T_s l_4 & 0\\
0 & 0 & 0 & T_s l_4
\end{bmatrix} \tag{6}
$$

$$\mathbf{C} = \begin{bmatrix} 0 & 0 & 1 & 0 & 0 & 0 \\ 0 & 0 & 0 & 1 & 0 & 0 \\ 0 & 0 & 0 & 0 & 1 & 0 \\ 0 & 0 & 0 & 0 & 0 & 1 \end{bmatrix} \tag{7}$$

with:

$A_{11} = A_{22} = 1 - T_s l_2 R_r,\ A_{12} = -A_{21} = -T_s l_2 L_r \omega_r(k),$

$A_{13} = A_{24} = T_s l_1 R_s,\ A_{14} = -A_{23} = -T_s l_2 L_m \omega_r(k),$

$A_{31} = A_{42} = T_s l_1 R_r,\ A_{32} = -A_{41} = T_s l_1 L_r \omega_r(k),$

$A_{33} = A_{44} = 1 - T_s l_3 R_s,\ A_{34} = -A_{43} = T_s l_1 L_m \omega_r(k),$

$A_{55} = A_{66} = 1 - T_s l_4 R_s$

B. Problem formulation

The principal objective in controlling multiphase IM is to ensure that the stator currents track with high precision the known desired references even in the presence of unmodelled dynamics, disturbances and unmeasurable rotor currents. Hence, the above-mentioned objective can be resumed as follows:

Let $\mathbf{y}^*(k) = \left[i^*_{s\alpha}(k),\, i^*_{s\beta}(k),\, i^*_{sx}(k),\, i^*_{sy}(k)\right]^T$ be the desired stator currents in $\alpha - \beta$ and $x - y$ planes and $\mathbf{e}(k) = \mathbf{y}(k) - \mathbf{y}^*(k)$ is the vector of currents tracking error, the objective is to derive a nonlinear discrete-time controller $\mathbf{v}(k)$ and to test it in real-time to ensure the robustness and the fast convergence of the error to zero (i.e., $\mathbf{e}(k) \to 0$).

III. PROPOSED CONTROLLER

A. Outer Speed Control Loop

The mechanical speed is regulated in this outer loop. Thus, a 2 Degree-Of-Freedom (DOF) PI controller with saturator, designed in [30], is used due to its robustness. The 2 DOF PI speed regulator is responsible for generating the dynamic current reference $i^*_{sq}(k)$. Thereupon, the slip frequency (ω_{sl}) estimation is carried out in an equivalent process as IRFOC technique, through the stator current references in the $d - q$ plane ($i^*_{sd}(k), i^*_{sq}(k)$) and the rotor parameters R_r, L_r of the asymmetrical six-phase IM. Fig. 2 shows the global structure of the stator currents controller.

B. Inner Stator Currents Control Loop

For this inner loop, a TDE-based DSTC algorithm will be developed to ensure that each stator current $(i_{s\alpha}(k), i_{s\beta}(k))$ in the $\alpha - \beta$ sub-space track with high accuracy his respective desired references even if the rotor currents are unmeasurable and to force the stator current $(i_{sx}(k), i_{sy}(k))$in the $x - y$ sub-space to remain at 0 A in order to minimize the energy losses. First of all, let us select the switching surface as follows:

$$\mathbf{S}(k) = \mathbf{e}(k). \tag{8}$$

Now, let us compute $\mathbf{S}(k+1)$ as follows:

$$\begin{aligned} \mathbf{S}(k+1) &= \mathbf{e}(k+1) \\ &= \mathbf{y}(k+1) - \mathbf{y}^*(k+1) \\ &= \mathbf{C}\chi(k+1) - \mathbf{y}^*(k+1) \\ &= \mathbf{C}\mathbf{A}\chi(k) + \mathbf{C}\mathbf{B}\mathbf{v}(k) + \mathbf{C}\mathbf{p}(k) - \mathbf{y}^*(k+1) \\ &= \overline{\mathbf{A}}\mathbf{y}(k) + \overline{\mathbf{B}}\mathbf{v}(k) + \mathbf{P}(k) - \mathbf{y}^*(k+1) \end{aligned} \tag{9}$$

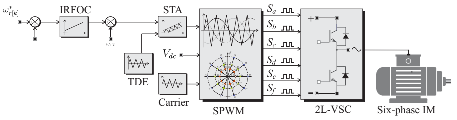

Fig. 2. Overall structure of the designed TDE-based DSTC algorithm for a six-phase IM.

where:

$$\overline{\mathbf{A}} = \begin{bmatrix} A_{33} & A_{34} & 0 & 0 \\ A_{43} & A_{44} & 0 & 0 \\ 0 & 0 & A_{55} & 0 \\ 0 & 0 & 0 & A_{66} \end{bmatrix} \tag{10}$$

$$\overline{\mathbf{B}} = \begin{bmatrix} T_s l_3 & 0 & 0 & 0 \\ 0 & T_s l_3 & 0 & 0 \\ 0 & 0 & T_s l_4 & 0 \\ 0 & 0 & 0 & T_s l_4 \end{bmatrix} \tag{11}$$

$$\mathbf{P}(k) = \begin{bmatrix} p_3(k) + A_{31}\, i_{r\alpha}(k) + A_{32}\, i_{r\beta}(k) \\ p_4(k) + A_{41}\, i_{r\alpha}(k) + A_{42}\, i_{r\beta}(k) \\ p_5(k) \\ p_6(k) \end{bmatrix} \tag{12}$$

Otherwise, the discrete-time form of the modified DSTC algorithm is as follows:

$$\begin{aligned} \mathbf{S}(k+1) &= \mathbf{Q}_1\mathbf{S}(k) - T_s\boldsymbol{\Gamma}_1 \mathrm{sig}^{0.5}(\mathbf{S}(k)) + T_s\mathbf{W}(k) \\ \mathbf{W}(k+1) &= \mathbf{Q}_2\mathbf{W}(k) - T_s\boldsymbol{\Gamma}_2\, \mathrm{sign}(\mathbf{S}(k)) \end{aligned} \tag{13}$$

where $\mathbf{Q}_1 = \mathrm{diag}(Q_{11}, \cdots, Q_{14})$ and $\mathbf{Q}_2 = \mathrm{diag}(Q_{21}, \cdots, Q_{24})$ are diagonal matrices where the elements are chosen such as $Q_{ji} \in R^+$ and $Q_{ji} < 1$ for $j = 1, 2$ and $i = 1, \cdots, 4$, $\boldsymbol{\Gamma}_1 = \mathrm{diag}(\Gamma_{11}, \cdots, \Gamma_{14})$ and $\boldsymbol{\Gamma}_2 = \mathrm{diag}(\Gamma_{21}, \cdots, \Gamma_{24})$ are diagonal positive matrices, $\mathrm{sig}^{0.5}(\mathbf{S}(k)) = \left[|S_1(k)|^{0.5}\mathrm{sign}(S_1(k)), \cdots, |S_4(k)|^{0.5}\mathrm{sign}(S_4(k))\right]^T$, and $\mathrm{sign}(\mathbf{S}(k)) = [\mathrm{sign}(S_1(k)), \cdots, \mathrm{sign}(S_4(k))]^T$ with:

$$\mathrm{sign}(S_i(k)) = \begin{cases} 0, & \text{if } S_i(k) = 0 \\ -1, & \text{if } S_i(k) < 0 \\ 1, & \text{if } S_i(k) > 0 \end{cases} \tag{14}$$

Combining (9) using (13) yields to the following control law:

$$\begin{aligned} \mathbf{v}(k) = -\overline{\mathbf{B}}^{-1} \big[& \overline{\mathbf{A}}\mathbf{y}(k) - \mathbf{y}^*(k+1) + \mathbf{P}(k) - \mathbf{Q}_1\mathbf{S}(k) \cdots \\ & \cdots + T_s\boldsymbol{\Gamma}_1 \mathrm{sig}^{0.5}(\mathbf{S}(k)) - T_s\mathbf{W}(k) \big] \end{aligned} \tag{15}$$

The control performance might not be satisfactory since the vector $\mathbf{P}(k)$ of perturbations and the unavailable rotor currents for measurements is unknown. Then, assuming that during two consecutive sampling times, the variations of the elements of $\mathbf{P}(k)$ are not large such as:

$$|P_i(k) - P_i(k-1)| \leq T_s\rho_i < \infty \tag{16}$$

Hence, TDE method [11] can be used to approximate it as follows:

$$\hat{\mathbf{P}}(k) \cong \mathbf{P}(k-1) = \mathbf{y}(k) - \overline{\mathbf{A}}\mathbf{y}(k-1) - \overline{\mathbf{B}}\mathbf{v}(k-1) \tag{17}$$

Theorem III.1. *Consider the six-phase machine described in* (3) *and* (4)*. Then, the proposed TDE-based DSTC for the stator currents is given by:*

$$\begin{aligned}\mathbf{v}(k) &= \overline{\mathbf{B}}^{-1}\Big[\mathbf{y}^*(k+1) - \overline{\mathbf{A}}\mathbf{y}(k) - \hat{\mathbf{P}}(k)\cdots \\ &\quad \cdots + \mathbf{Q}_1\mathbf{S}(k) - T_s\mathbf{\Gamma}_1\mathrm{sig}^{0.5}(\mathbf{S}(k)) + T_s\mathbf{W}(k)\Big] \\ \mathbf{W}(k+1) &= \mathbf{Q}_2\mathbf{W}(k) - T_s\mathbf{\Gamma}_2\,\mathrm{sign}(\mathbf{S}(k))\end{aligned} \tag{18}$$

ensures the convergence of the error to a ball b that has a radius r_b smaller than:

$$r_b \leq \frac{\left(\left(\frac{\bar{\phi}_1}{2}\right)^2 \|\overline{\Theta}^{-1}\|^2 + \bar{\phi}_2\right)}{r} \tag{19}$$

if the following conditions are met for $i = 1:4$:

$$\Gamma_{1i} > 0,\ \ \Gamma_{2i} > \frac{(1+Q_{2i})}{T_s}\rho_i. \tag{20}$$

Proof. First of all, let us substitute the proposed discrete-time controller (18) into (9):

$$\begin{aligned}\mathbf{S}(k+1) &= \mathbf{Q}_1\mathbf{S}(k) - T_s\mathbf{\Gamma}_1\mathrm{sig}^{0.5}(\mathbf{S}(k)) + T_s\mathbf{W}(k) + \mathbf{\Delta P}(k) \\ \mathbf{W}(k+1) &= \mathbf{Q}_2\mathbf{W}(k) - T_s\mathbf{\Gamma}_2\,\mathrm{sign}(\mathbf{S}(k))\end{aligned} \tag{21}$$

where $\mathbf{\Delta P}(k) = \mathbf{P}(k) - \mathbf{P}(k-1)$ is the TDE error. The above closed-loop error dynamics can be rewritten for $i = 1, \cdots, 4$ as follows:

$$\begin{aligned}S_i(k+1) =& Q_{1i}S_i(k) - T_s\Gamma_{1i}|S_i(k)|^{0.5}\mathrm{sign}(S_i(k)) \\ &+ \Delta P_i(k) + T_sW_i(k) \\ W_i(k+1) =& Q_{2i}W_i(k) - T_s\Gamma_{2i}\mathrm{sign}(S_i(k))\end{aligned} \tag{22}$$

For the convenience of this demonstration, let us introduce a new variable defined by $Z_i(k) = W_i(k) + T_s^{-1}\Delta P_i(k)$ such as (22) can be rewritten as:

$$\begin{aligned}S_i(k+1) =& Q_{1i}S_i(k) - T_s\Gamma_{1i}|S_i(k)|^{0.5}\mathrm{sign}(S_i(k)) + T_sZ_i(k) \\ Z_i(k+1) =& Q_{2i}Z_i(k) - T_s\Gamma_{2i}\mathrm{sign}(S_i(k)) + \zeta_i(k)\end{aligned} \tag{23}$$

where

$$\zeta_i(k) = T_s^{-1}(\Delta P_i(k+1) - Q_{2i}\Delta P_i(k)) \tag{24}$$

Now, let us define $\eta_i(k) = [S_i(k), Z_i(k)]^T$, then, equation (22) can be written in the following matrix form:

$$\eta_i(k+1) = \Psi\eta_i(k) + \Phi(k)\mathrm{sign}(S_i(k)) \tag{25}$$

where Ψ and $\Phi(k)$ are defined as:

$$\begin{aligned}\Psi &= \begin{bmatrix} Q_{1i} & T_s \\ 0 & Q_{2i} \end{bmatrix} \\ \Phi(k) &= \begin{bmatrix} -T_s\Gamma_{1i}|S_i(k)|^{0.5} \\ -T_s\Gamma_{2i} + \zeta_i(k)\mathrm{sign}(S_i(k)) \end{bmatrix}\end{aligned} \tag{26}$$

Now, consider the following discrete Lyapunov function candidate:

$$V(k) = \eta_i^T(k)L\eta_i(k) \tag{27}$$

where $L = L^T \in R^{2\times 2}$ is symmetric definite positive matrix. Then, one can imply:

$$\begin{aligned}\Delta V(k) &= V(k+1) - V(k) \\ &= \eta_i^T(k+1)L\eta_i(k+1) - \eta_i^T(k)L\eta_i(k)\end{aligned} \tag{28}$$

Combining (25) with (28) and using the Λ-matrix inequality [31] $A^TB + B^TA \leq A^T\Lambda A + B^T\Lambda^{-1}B$ yields to:

$$\begin{aligned}\Delta V(k) =& \eta_i^T(k)(\Psi^TL\Psi - L)\eta_i(k) + \Phi^T(k)L\Phi(k) \\ &+ 2\eta_i^T(k)\Psi^TL\Phi(k)\mathrm{sign}(S_i(k)) \\ \leq& \eta_i^T(k)(\Psi^TL\Psi - L)\eta_i(k) + \Phi^T(k)L\Phi(k) \\ &+ \eta_i^T(k)(\Psi^TL\Lambda L\Psi)\eta_i(k) + \Phi^T(k)\Lambda^{-1}\Phi(k) \\ \leq& \eta_i^T(k)(\Psi^T(L + L\Lambda L)\Psi - (1-r)L)\eta_i(k) \\ &+ \Phi^T(k)(L + \Lambda^{-1})\Phi(k) - rV(k) \\ \leq& -\eta_i^T(k)\Theta\eta_i(k) + \Phi^T(k)R\Phi(k) - rV(k)\end{aligned} \tag{29}$$

where $0 < r < 1$, $R = L + \Lambda^{-1}$ and Θ is a (2×2) symmetric definite-positive matrix that solves the matrix inequality [25] such as: $\Psi^T(L + L\Lambda L)\Psi - (1-r)L = -\Theta$. Now, let us expand the term $\Phi^T(k)R\Phi(k)$ as follows:

$$\Phi^T(k)R\Phi(k) = \phi_1|S_i(k)| + \phi_2|S_i(k)|^{0.5} + \phi_3 \tag{30}$$

where ϕ_1, ϕ_2 and ϕ_3 are computed as follows:

$$\begin{aligned}\phi_1 =& T_s^2\Gamma_{1i}^2R_{11} \\ \phi_2 =& 2T_s\Gamma_{1i}R_{21}(T_s\Gamma_{2i} - \zeta_i(k)sign(S_i(k))) \\ \phi_3 =& R_{22}(T_s\Gamma_{2i} - \zeta_i(k)sign(S_i(k)))^2\end{aligned} \tag{31}$$

Otherwise $\zeta_i(k)$ is bounded by:

$$\begin{aligned}\zeta_i(k) &= T_s^{-1}(\Delta P_i(k+1) - Q_{2i}\Delta P_i(k)) \\ &\leq T_s^{-1}|\Delta P_i(k+1) - Q_{2i}\Delta P_i(k)| \\ &\leq T_s^{-1}\left(|\Delta P_i(k+1)| + |Q_{2i}\Delta P_i(k)|\right) \\ &\leq T_s^{-1}\left(T_s\rho_i + Q_{2i}T_s\rho_i\right) \\ &\leq (1 + Q_{2i})\rho_i\end{aligned} \tag{32}$$

Hence, if Γ_{2i} is chosen as in (20), the term ϕ_2 will be always positive such as $\phi_2|S_i(k)|^{0.5} \leq \phi_2(1 + |S_i(k)|)$ and the following inequality can be established:

$$\begin{aligned}\Phi^T(k)R\Phi(k) \leq& \phi_1|S_i(k)| + \phi_2(1 + |S_i(k)|) + \phi_3 \\ \leq& (\phi_1 + \phi_2)|S_i(k)| + \phi_2 + \phi_3 \\ \leq& \bar{\phi}_1|S_i(k)| + \bar{\phi}_2\end{aligned} \tag{33}$$

where $\bar{\phi}_1$ and $\bar{\phi}_2$ are computed as follows:

$$\begin{aligned}\bar{\phi}_1 =& T_s^2\Gamma_{1i}^2R_{11} + 2T_s\Gamma_{1i}R_{21}(T_s\Gamma_{2i} + (1 + Q_{2i})\rho_i) \\ \bar{\phi}_2 =& 2T_s\Gamma_{1i}R_{21}(T_s\Gamma_{2i} + (1 + Q_{2i})\rho_i) \\ &+ R_{22}\big(T_s\Gamma_{2i} + (1 + Q_{2i})\rho_i\big)^2\end{aligned} \tag{34}$$

Substituting (33) into (29) and using the Choleskii decomposition, $\Delta V(k)$ becomes:

$$\begin{aligned}\Delta V(k) \leq& -\eta_i^T(k)\Theta\eta_i(k) + \bar{\phi}_1|S_i(k)| + \bar{\phi}_2 - rV(k) \\ \leq& -\|\overline{\Theta}\eta_i(k)\|^2 + \bar{\phi}_1\|\overline{\Theta}\overline{\Theta}^{-1}\eta_i(k)\| + \bar{\phi}_2 - rV(k) \\ \leq& -\star^T\star + \left(\frac{\bar{\phi}_1}{2}\right)^2\|\overline{\Theta}^{-1}\|^2 + \bar{\phi}_2 - rV(k) \\ \leq& \left(\frac{\bar{\phi}_1}{2}\right)^2\|\overline{\Theta}^{-1}\|^2 + \bar{\phi}_2 - rV(k) \\ V(k+1) \leq& \left(\left(\frac{\bar{\phi}_1}{2}\right)^2\|\overline{\Theta}^{-1}\|^2 + \bar{\phi}_2\right) + (1-r)V(k)\end{aligned} \tag{35}$$

where $\overline{\Theta}^2 = \Theta$ and $\star = \left(\|\overline{\Theta}\eta_i(k)\| - \frac{\bar{\phi}_1}{2}\|\overline{\Theta}^{-1}\|\right)$. The solution of the above discrete linear inequality is given by:

$$V(k+1) \leq \left(\left(\frac{\bar{\phi}_1}{2}\right)^2\|\overline{\Theta}^{-1}\|^2 + \bar{\phi}_2\right)\sum_{i=1}^{k+1}(1-r)^{i-1} + (1-r)^{k+1}V(0) \tag{36}$$

Consider the case where k goes to ∞, then it can be concluded that:

$$\lim_{k \to +\infty} V(k) \leq \frac{\left(\left(\frac{\bar{\phi}_1}{2} \right)^2 \|\bar{\Theta}^{-1}\|^2 + \bar{\phi}_2 \right)}{r} \tag{37}$$

Hence, the DSTC ensures the convergence of the trajectories into a ball b that has a radius r_b smaller than:

$$r_b \leq \frac{\left(\left(\frac{\bar{\phi}_1}{2} \right)^2 \|\bar{\Theta}^{-1}\|^2 + \bar{\phi}_2 \right)}{r} \tag{38}$$

This concludes the proof.

IV. EXPERIMENTAL RESULTS

In this section, exhaustive experimental results are provided to evaluate the performance of the proposed controller. In all tests a pre-defined d current set point ($i^*_{sd} = 1$ A) has been used and stator currents set points in $x-y$ sub-space are defined to zero ($i^*_{sx} = i^*_{sy} = 0$ A) in order to diminish the stator losses. The controller was also tested under load and no-load situation, steady-state, reversal, with parameter mismatch and with two different sampling frequencies. Moreover, the selected parameters of the DSTC algorithm with TDE for the six-phase IM are:

$$\begin{aligned}
\mathbf{\Gamma}_1 &= \frac{1}{T_s} \mathrm{diag}\,(0.5, 0.5, 0.5, 0.5)\,, \\
\mathbf{Q}_1 &= \mathbf{Q}_2 = \mathrm{diag}\,(0.7, 0.7, 0.7, 0.7)\,, \\
\mathbf{\Gamma}_2 &= \frac{1}{T_s} \mathrm{diag}\,(0.3, 0.3, 0.3, 0.3)\,, \\
\mathbf{W}(0) &= [0, 0, 0, 0]^T.
\end{aligned}$$

A. Experimental test bench description

A custom test bench has been used to validate the proposed controller, which consists of an asymmetrical six-phase IM energized by a six-phase Voltage Source Inverter (VSI), composed of two three-leg VSI, powered by a DC voltage source. The two three-leg VSI is activated by a dSPACE MABXII DS1401 controller, which is a real-time rapid prototyping platform with MATLAB/Simulink version 8.2. Through the dSPACE, the experimental results are captured and then processed by a script from MATLAB R2014b. The electrical parameters of the six-phase IM have been estimated using typical approaches based on stand-still with VSC supply tests and AC time domain [32], [33]. These parameters are listed in Table I.

The tests were developed with current Hall effect transducers LA 55-P s, which can perform on a frequency bandwidth between DC and 200 kHz. Then a 16-bit A/D converter, converts the measured currents to digital data. A 1024 ppr incremental encoder is used to measure the asymmetrical six-phase IM position, and the rotor mechanical speed is calculated from it. A mechanical load on the machine is performed with a 5 HP Foucault current brake. Fig. 3 presents a block diagram of the test bench, with some photos of the selected equipments.

TABLE I

SIX-PHASE IM'S PARAMETERS

PARAMETER	VALUE	PARAMETER	VALUE
R_r (Ω)	6.9	L_r (mH)	626.8
P_w (kW)	2	V_{dc} (V)	400
R_s (Ω)	6.7	ω_{m-nom} (rpm)	2880
L_{ls} (mH)	5.3	L_s (mH)	654.4
J_m (kg.m^2)	0.07	B_m (kg.m^2/s)	0.0004
L_m (mH)	614	P	1

B. Figures of merit

The proposed controller performance is evaluated through the Mean Squared Error (MSE) between the set point and the measured stator currents in all the sub-spaces measured by the Hall transducers, as well as MSE for the rotor mechanical speed are selected as figures of merit. Moreover, the Root Mean Squared (RMS) of the $d-q$ currents are considered in order to obtain their corresponding RMS ripple and Total Harmonic Distortion (THD) in $\alpha-\beta$ sub-space is also evaluated. The MSE is calculated by the following equation:

$$\mathrm{MSE}(i_{s\gamma}) = \sqrt{\frac{1}{N} \sum_{k=1}^{N} (i_{s\gamma}(k) - i^*_{s\gamma}(k))^2} \tag{39}$$

where $i^*_{s\gamma}$ the stator currents set point, $i_{s\gamma}$ the real stator currents such as $\gamma \in \{d,\, q,\, \alpha,\, \beta,\, x,\, y\}$ and N denotes the total number of used samples. At the same time, the RMS ripple of $d-q$ sub-space is calculated as shown:

$$\mathrm{RMS}(ripple_\theta) = \sqrt{RMS(i_{s\theta})^2 - Mean(i_{s\theta})^2} \tag{40}$$

where $i_{s\theta}$ are the stator currents in $d-q$ sub-space and $Mean$ is the mean value of currents in $d-q$. At last, the THD is calculated as:

$$\mathrm{THD}(i_s) = \sqrt{\frac{1}{i^2_{s1}} \sum_{j=2}^{N} (i_{sj})^2} \tag{41}$$

where i_{s1} are the fundamental stator currents and i_{sj} are the harmonic stator currents.

C. Steady-state analysis

The selected sampling frequencies are 8 kHz and 16 kHz. The eddy current brake is tuned to obtain a q current at 1.4 A for the asymmetrical six-phase IM. For the steady state analysis, three mechanical speeds are set for the mechanical speed: 500 rpm, 1 000 rpm and 1 500 rpm. Table II shows the obtained results for different sampling frequencies and mechanical speeds, presented as MSE of stator currents in all the sub-spaces. The data shows good performance of TDE-based DSTC algorithm applied to our machine regarding the current control, in all the sub-spaces, especially in $\alpha-\beta$ currents control tracking. Table III presents the obtained RMS ripple in $d-q$ currents, THD in $\alpha-\beta$ currents and MSE of the mechanical speed. The results show low THD with a lower sampling frequency and low mechanical speed, as higher sampling frequency amplifies perturbations. For RMS ripple results, there is a significant improvement with lower sampling frequency in the three mechanical speed tests. At last for the mechanical speed, a better performance is obtained at lower sampling frequency and mechanical speed, but it is not significant to the other performed tests.

Moreover, Fig. 4 shows the polar representation of stator currents for three mechanical speeds. The analysis was performed with a fixed q current reference, thus the amplitudes of $\alpha-\beta$ stator currents maintain with different mechanical speeds. The figures present also the $x-y$ currents where it can be noticed that they are reduced

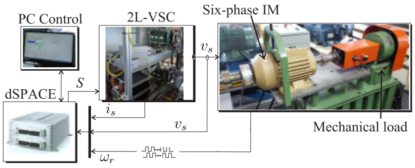

Fig. 3. Experimental test bench.

TABLE II

STEADY STATE TEST OF STATOR CURRENTS $d-q$, $\alpha-\beta$, $x-y$, MSE (A) FOR THREE DIFFERENT MECHANICAL SPEEDS (RPM).

		Sampling	frequency	8 kHz		
ω_m^*	MSE$_d$	MSE$_q$	MSE$_\alpha$	MSE$_\beta$	MSE$_x$	MSE$_y$
500	0.0416	0.0621	0.0537	0.0520	0.0383	0.0383
1000	0.0649	0.0791	0.0670	0.0773	0.0474	0.0443
1500	0.1145	0.1395	0.1262	0.1290	0.1109	0.0995
		Sampling	frequency	16 kHz		
ω_m^*	MSE$_d$	MSE$_q$	MSE$_\alpha$	MSE$_\beta$	MSE$_x$	MSE$_y$
500	0.1343	0.1377	0.1341	0.1379	0.1598	0.1456
1000	0.1300	0.1393	0.1341	0.1353	0.1805	0.1591
1500	0.1274	0.1358	0.1320	0.1313	0.1785	0.1766

TABLE III

STEADY STATE TEST OF STATOR CURRENTS: THD (%) IN $\alpha-\beta$, RMS RIPPLE (A) IN $d-q$, MSE (RPM) OF ROTOR SPEED (ω_m), AT THREE DIFFERENT DESIRED MECHANICAL SPEEDS (RPM).

		Sampling	frequency	8 kHz	
ω_m^*	THD$_\alpha$	THD$_\beta$	RMSripple$_d$	RMSripple$_q$	MSE$_{\omega_m}$
500	4.3418	4.0378	0.0322	0.0514	1.7722
1000	3.8585	5.5634	0.0452	0.0491	2.1242
1500	9.5917	9.9925	0.0957	0.1016	3.8799
		Sampling	frequency	16 kHz	
ω_m^*	THD$_\alpha$	THD$_\beta$	RMSripple$_d$	RMSripple$_q$	MSE$_{\omega_m}$
500	12.8828	13.6806	0.1336	0.1332	1.8619
1000	13.1770	13.3089	0.1276	0.1323	2.5163
1500	12.6697	12.9736	0.1227	0.1269	3.6441

to a very low value in every case, highlighting the tests at low sampling frequency. On the other hand, $\alpha-\beta$ currents tracking is good, presenting more ripple at high sampling frequency, showing a direct relation between the disturbances and the switching frequency.

D. Dynamic analysis

Then, a transient test, which consists of a step change in the q stator current reference (i_{sq}^*) produced by a reversal condition (500 to -500 rpm) has been performed. Fig. 5 reports the test. Fig. 5(a) and Fig. 5(b) present a settling time of approximately 1.9 ms and 1.8 ms respectively and an overshoot of 42.1 % and 68 % respectively, presenting a very fast dynamic response in both cases.

At the same time, other transient tests were performed to observe the controller's performance with a step change from -500 rpm to 1000 rpm and then a second step change from 1000 rpm to -500 rpm. The only notable effect in the $\alpha-\beta$ currents change is the amplitude change of 4.25 A to 1.2 A as shown in Fig. 6. From the same figure, the fast dynamic response of the controller and the good tracking which are one of the main advantages of the TDE-based DSTC algorithm can be appreciated.

In addition, the values of MSE are MSE$_\alpha = 0.1539$ A, MSE$_\beta = 0.1655$ A, MSE$_x = 0.1192$ A and MSE$_y = 0.1145$ A for the first step profile and MSE$_\alpha = 0.0779$ A, MSE$_\beta = 0.0734$ A, MSE$_x = 0.0654$ A and MSE$_y = 0.0651$ A for the second step profile.

E. Disturbance response

Secondly, to show the robustness of the proposed method, it is tested under a steady-state condition for a rotor mechanical speed of 1000 rpm by introducing a load torque step from no-load to nominal-load and then for a load torque step from nominal-load to no-load. The results of these tests are depicted in Fig. 7. It can be noticed the high accuracy tracking of the stator current in the $\alpha-\beta$ sub-space. The obtained results are quite similar for 1000 rpm in the previous tests such as the obtained MSE values for the first case are: MSE$_\alpha = 0.0555$ A, MSE$_\beta = 0.0684$ A, MSE$_x = 0.0398$ A and MSE$_y = 0.0419$ A, while the values for the second case are: MSE$_\alpha = 0.0647$ A, MSE$_\beta = 0.0776$ A, MSE$_x = 0.0424$ A and MSE$_y = 0.0513$ A.

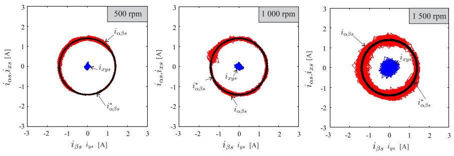

Fig. 4. Stator currents in $\alpha-\beta$ and $x-y$ sub-spaces for a different mechanical speed at a sampling frequency of 8 kHz.

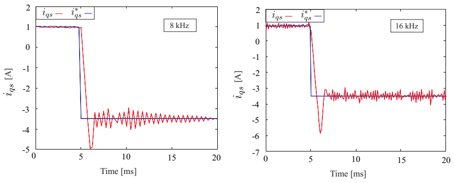

Fig. 5. Dynamic behaviour of q current from a speed reversal condition of 500 rpm to -500 rpm from ω_m at a sampling frequency of 8 kHz and 16 kHz.

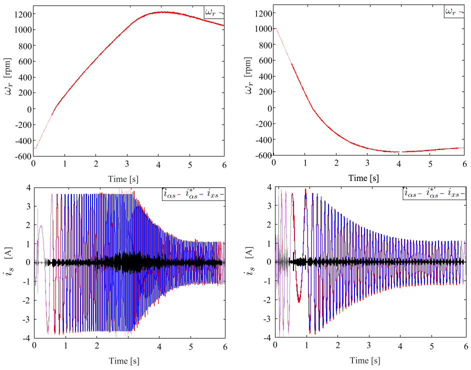

Fig. 6. Transient response of stator currents for different step rotor speed reference ω_r^*: first results from -500 to 1000 rpm, then from 1000 to -500.

F. Parameter Sensitivity

On the other hand, Fig. 8 presents the control performance with a L_m change of 25% of the determined value to verify the control robustness to uncertainties. The results show that at low speed, the control performance is practically the same, showing a good

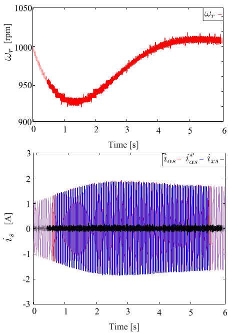

Fig. 7. Steady state response of stator currents for a desired rotor speed $\omega_r^* = 1000$ rpm for a load torque step from no-load to nominal-load then for a load torque step from nominal-load to no-load

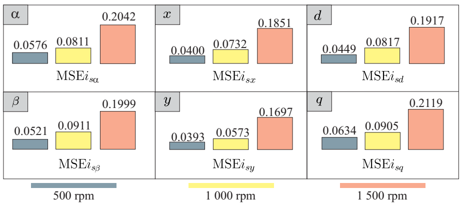

Fig. 8. Performance Analysis of Stator Currents MSE (A) under 25 % of variation of the nominal L_m.

robustness to this particular change. At higher rotor speed the results present a deteriorated tracking of approximately 21% and 60%, compared to the unchanged L_m value, for 1000 and 1500 rpm respectively, showing an increased sensibility in these operation points.

The analyzed transient tests are conducted while considering a variation of 25% on the machine L_m to prove the ability of the developed method to reject the uncertainties and the unknown dynamics. The obtained results are shown in Fig. 9. It is shown that similar good performances are obtained. This is confirmed by the obtained MSE values. The latter for the first case are: MSE$_\alpha$ = 0.1916 A, MSE$_\beta$ = 0.2016 A, MSE$_x$ = 0.1665 A and MSE$_y$ = 0.1525 A while the values for the second case are: MSE$_\alpha$ = 0.0835 A, MSE$_\beta$ = 0.0769 A, MSE$_x$ = 0.0712 A and MSE$_y$ = 0.0683 A. These values are almost equal to the first transient tests, showing a good robustness of the proposed controller on a transient state based of a reversal condition for the six-phase IM at a sampling frequency of 8 kHz.

G. Comparative analysis with classic DSMC

At last, Table IV presents a comparative analysis of the performance of TDE-based DSTC algorithm compared to TDE-based DSMC, proposed in [11], in terms of %, where positive (+) and negative (−) values mean improvement and deterioration respectively,

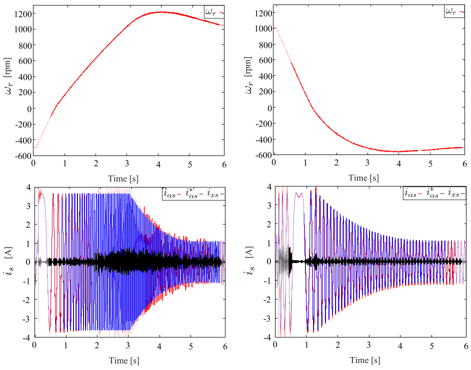

Fig. 9. Transient response of stator currents for different step rotor speed reference ω_r^* with a variation of a 25% on L_m: from -500 to 1000 rpm, and then from 1000 to -500 rpm.

calculated as follows:

$$\text{Imp}\ (\%) = 100\frac{\text{DSMC}_{\text{value}} - \text{DSTC}_{\text{value}}}{\text{DSMC}_{\text{value}}} \tag{42}$$

where "value" can be MSE of stator currents in $\alpha - \beta$ and $x - y$ sub-spaces, THD of $\alpha - \beta$ stator currents or RMS ripple of stator currents in $d - q$ sub-space. Fig. 10 summarizes the comparison between TDE-based DSMC and TDE-based DSTC algorithm by using the average value of MSE in every subspace for different rotor speeds at a sampling time of 8 kHz.

TABLE IV
COMPARATIVE ANALYSIS (%) OF DSTC AND DSMC AT DIFFERENT SPEEDS (RPM).

ω_m^*	MSE$_{\alpha\beta}$	MSE$_{xy}$	RMSripple$_d$	RMSripple$_q$	THD$_{\alpha\beta}$
	Sampling	frequency	8 kHz	(DSTC)	
500	79.29	78.75	87.08	80.22	86.11
1000	75.90	80.09	84.96	83.01	73.72
1500	57.82	57.47	70.04	60.82	45.42
	Sampling	frequency	16 kHz	(DSTC)	
500	27.47	19.25	26.95	29.71	40.11
1000	24.66	16.21	28.44	24.44	12.24
1500	25.14	23.35	28.33	25.66	-14.91

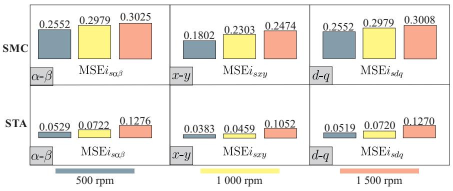

Fig. 10. Comparative performance (MSE (A)) of Stator Currents in $\alpha-\beta$, $x-y$ and $d-q$ subspaces for a sampling frequency of 8 kHz.

V. Conclusion

This paper has presented an inner robust TDE-based DSTC for the problem controlling the stator currents in the $\alpha - \beta$ and $x - y$ sub-spaces of an uncertain six-phase IM with an outer speed control loop. As presented in the results, TDE-based DSTC presents an optimal behaviour on current tracking with low harmonic distortion values, ensures robustness and delivers fast dynamics, in terms of settling time and overshoot, and fast convergence in all the operation points. In summary, TDE-based DSTC is an optimal option, at low sampling frequency, for low speeds and a good alternative for high speeds industrial applications.

References

[1] M. J. Duran, E. Levi, and F. Barrero, "Multiphase electric drives: Introduction," *Wiley encyclopedia of electrical and electronics engineering*, pp. 1–26, 2017.

[2] M. J. Duran and F. Barrero, "Recent advances in the design, modeling, and control of multiphase machines: Part II," *IEEE Trans. Ind. Electron.*, vol. 63, no. 1, pp. 459–468, Jan. 2016.

[3] E. Levi, "Advances in converter control and innovative exploitation of additional degrees of freedom for multiphase machines," *IEEE Trans. Ind. Electron.*, vol. 63, no. 1, pp. 433–448, Jan. 2016.

[4] F. Barrero and M. J. Duran, "Recent advances in the design, modeling, and control of multiphase machines: Part I," *IEEE Trans. Ind. Electron.*, vol. 63, no. 1, pp. 449–458, Jan. 2016.

[5] Z. Liu, Z. Zheng, and Y. Li, "Enhancing fault-tolerant ability of a nine-phase induction motor drive system using fuzzy logic current controllers," *IEEE Trans. Energy Convers.*, vol. 32, no. 2, pp. 759–769, Jun. 2017.

[6] M. A. Fnaiech, F. Betin, G. Capolino, and F. Fnaiech, "Fuzzy logic and sliding-mode controls applied to six-phase induction machine with open phases," *IEEE Trans. Ind. Electron.*, vol. 57, no. 1, pp. 354–364, Jan. 2010.

[7] F. Barrero, M. R. Arahal, R. Gregor, S. Toral, and M. J. Duran, "A proof of concept study of predictive current control for VSI-driven asymmetrical dual three-phase AC machines," *IEEE Trans. Ind. Electron.*, vol. 56, no. 6, pp. 1937–1954, Jun. 2009.

[8] J. Rodas, F. Barrero, M. R. Arahal, C. Martin, and R. Gregor, "On-line estimation of rotor variables in predictive current controllers: A case study using five-phase induction machines," *IEEE Trans. Ind. Electron.*, vol. 63, no. 9, pp. 5348–5356, Sept. 2016.

[9] J. Rodas, C. Martin, M. R. Arahal, F. Barrero, and R. Gregor, "Influence of covariance-based ALS methods in the performance of predictive controllers with rotor current estimation," *IEEE Trans. Ind. Electron.*, vol. 64, no. 4, pp. 2602–2607, Apr. 2017.

[10] M. Ayala, J. Doval-Gandoy, J. Rodas, O. Gonzalez, and R. Gregor, "Current control designed with model based predictive control for six-phase motor drives," *ISA Trans.*, Sep. 2019.

[11] Y. Kali, M. Ayala, J. Rodas, M. Saad, J. Doval-Gandoy, R. Gregor, and K. Benjelloun, "Current control of a six-phase induction machine drive based on discrete-time sliding mode with time delay estimation," *Energies*, vol. 12, no. 1, Jan. 2019.

[12] V. Utkin, J. Guldner, and J. Shi, *Sliding mode control in electromechanical systems*. Taylor-Francis, 1999.

[13] I. Boiko and L. Fridman, "Analysis of chattering in continuous sliding-mode controllers," *IEEE Trans. Autom. Control.*, vol. 50, no. 9, pp. 1442–1446, Sept. 2005.

[14] O. Kaynak and A. Denker, "Discrete-time sliding mode control in the presence of system uncertainty," *Int. J. Control*, vol. 57, no. 5, pp. 1177–1189, 1993.

[15] H. Ma, J. Wu, and Z. Xiong, "A novel exponential reaching law of discrete-time sliding-mode control," *IEEE Trans. Ind. Electron.*, vol. 64, no. 5, pp. 3840–3850, May 2017.

[16] H. Ma, Y. Li, and Z. Xiong, "Discrete-time sliding-mode control with enhanced power reaching law," *IEEE Trans. Ind. Electron.*, vol. 66, no. 6, pp. 4629–4638, Jun. 2019.

[17] J. Zhang, P. Shi, Y. Xia, and H. Yang, "Discrete-time sliding mode control with disturbance rejection," *IEEE Trans. Ind. Electron.*, vol. 66, no. 10, pp. 7967–7975, Oct. 2019.

[18] C. J. Fallaha, M. Saad, H. Y. Kanaan, and K. Al-Haddad, "Sliding-mode robot control with exponential reaching law," *IEEE Trans. Ind. Electron.*, vol. 58, no. 2, pp. 600–610, Feb. 2011.

[19] Y. Kali, M. Saad, K. Benjelloun, and M. Benbrahim, "Sliding mode with time delay control for MIMO nonlinear systems with unknown dynamics," in *2015 International Workshop on Recent Advances in Sliding Modes (RASM)*, April 2015, pp. 1–6.

[20] J. Yu, J. Liu, Z. Wu, and H. Fang, "Depth control of a bioinspired robotic dolphin based on sliding-mode fuzzy control method," *IEEE Trans. Ind. Electron.*, vol. 65, no. 3, pp. 2429–2438, Mar. 2018.

[21] Y. Kali, M. Saad, and K. Benjelloun, *Control of Robot Manipulators Using Modified Backstepping Sliding Mode*. Singapore: Springer Singapore, 2019, pp. 107–136.

[22] A. Levant, "Sliding order and sliding accuracy in sliding mode control," *Int. J. Control*, vol. 58, no. 6, pp. 1247–1263, 1993.

[23] G. Bartolini, A. Pisano, and E. Usai, "Digital second-order sliding mode control for uncertain nonlinear systems," *Automatica*, vol. 37, no. 9, pp. 1371 – 1377, Sep. 2001.

[24] Y. Kali, M. Saad, K. Benjelloun, and A. Fatemi, "Discrete-time second order sliding mode with time delay control for uncertain robot manipulators," *Robot. Auton. Syst.*, vol. 94, pp. 53 – 60, Aug. 2017.

[25] I. Salgado, I. Chairez, B. Bandyopadhyay, L. Fridman, and O. Camacho, "Discrete-time non-linear state observer based on a super twisting-like algorithm," *IET Control Theory Appl.*, vol. 8, no. 10, pp. 803–812, Jul. 2014.

[26] R. Meena, B. Pratap, and V. P. Singh, "Discrete-time super-twisting observer based control design for magnetically levitated system," in *2017 IEEE International Conference on Power, Control, Signals and Instrumentation Engineering (ICPCSI)*, Sep. 2017, pp. 470–474.

[27] B. Brogliato, A. Polyakov, and D. Efimov, "The implicit discretization of the super-twisting sliding-mode control algorithm," in *2018 15th International Workshop on Variable Structure Systems (VSS)*, Jul. 2018, pp. 349–353.

[28] E. Levi, "Multiphase AC machines," in *The Industrial Electronics Handbook: Power Electronics and Motor Drives*. CRC Press, 2011.

[29] Levi, E, "FOC - field oriented control," in *The Industrial Electronics Handbook: Power Electronics and Motor Drives*. CRC Press, 2011.

[30] L. Harnefors, S. E. Saarakkala, and M. Hinkkanen, "Speed control of electrical drives using classical control methods," *IEEE Trans. Ind. Appl.*, vol. 49, no. 2, pp. 889–898, Feb. 2013.

[31] A. S. Poznyak, "Chapter 12 - miscellaneous," in *Advanced Mathematical Tools for Automatic Control Engineers: Deterministic Techniques*, A. S. Poznyak, Ed. Oxford: Elsevier, 2008, pp. 213 – 227.

[32] A. G. Yepes, J. A. Riveros, J. Doval-Gandoy, F. Barrero, O. López, B. Bogado, M. Jones, and E. Levi, "Parameter identification of multiphase induction machines with distributed windings Part 1: Sinusoidal excitation methods," *IEEE Trans. Energy Conv.*, vol. 27, no. 4, pp. 1056–1066, Oct. 2012.

[33] J. A. Riveros, A. G. Yepes, F. Barrero, J. Doval-Gandoy, B. Bogado, O. Lopez, M. Jones, and E. Levi, "Parameter identification of multiphase induction machines with distributed windings Part 2: Time-domain techniques," *IEEE Trans. Energy Conv.*, vol. 27, no. 4, pp. 1067–1077, Oct. 2012.

ARTÍCULO 3

CURRENT CONTROL DESIGNED WITH MODEL BASED PREDICTIVE CONTROL FOR SIX-PHASE MOTOR DRIVES

- **Magno Ayala**, Jesus Doval-Gandoy, Jorge Rodas, Osvaldo González and Raul Gregor, ”Current control designed with model based predictive control for six-phase motor drives”, ISA Transactions, pp. 1-9, DOI: 10.1016/j.isatra.2019.08.052, 2019.

ISA Transactions 98 (2020) 496–504

Contents lists available at ScienceDirect

ISA Transactions

journal homepage: www.elsevier.com/locate/isatrans

Practice article

Current control designed with model based predictive control for six-phase motor drives

Magno Ayala [a,*], Jesus Doval-Gandoy [b], Jorge Rodas [a], Osvaldo Gonzalez [a], Raul Gregor [a]

[a] *Laboratory of Power and Control Systems, Facultad de Ingeniería, Universidad Nacional de Asunción, Paraguay*
[b] *Applied Power Electronics Technology Research Group, Universidad de Vigo, Spain*

ARTICLE INFO

Article history:
Received 6 May 2018
Received in revised form 27 February 2019
Accepted 28 August 2019
Available online 6 September 2019

Keywords:
Model-based predictive control
Multiphase induction machine
Power electronics
Six-phase drives

ABSTRACT

Finite control set model-based predictive control techniques are distinguished by being an interesting alternative to traditional field oriented control techniques for multiphase drives due to their fast dynamic response and flexibility in the introduction of constraints. However, those predictive control techniques have some drawbacks regulating the $(x-y)$ current components which can cause machine losses as well as a high computational burden. This paper presents a comparative study of an enhanced predictive current control technique with a conventional predictive control technique and two hybrid predictive control techniques applied to an asymmetrical six-phase induction motor drive in terms of current tracking, total harmonic distortion of stator currents and computational burden. Experimental results are reported to demonstrate the benefits of the different current control techniques by using the mean squared error and total harmonic distortion of stator currents as quality figures of merit and the number of floating point operations to measure the computational burden of each predictive control, thus concluding the advantages and limitations of each technique at transient and steady regimes.

1. Introduction

Model-based predictive control (MPC) has gained attention in the last years as an alternative to conventional linear control techniques [1–3]. MPC strategies are identified by the requirement of a defined system model in order to predict the next values for the system state variables. Once the future state variables are estimated, the MPC uses an optimization criterion by minimizing a cost function that describes the desired system behavior in every sample time. MPC has a fast dynamic response and can be applied to different systems, such as AC–DC converters [4], controlled grid-connected converters [5,6], permanent magnet synchronous machines [7,8] and induction motors (IMs) [9,10]. MPC is classified in a continuous control set MPC and finite-control-set MPC (FCS–MPC) which is mainly applied, due to its discrete nature, to three-phase and multiphase systems with different voltage source inverters (VSIs) topologies, being the two-level VSI the most studied [7–10].

At the same time, the research in the field of multiphase IM has been growing in the last decade [11–13]. Comparing to the conventional three-phase IM, multiphase IMs have some intrinsic advantages such as major power splitting, lower torque ripple and better fault tolerance [14]. By considering these advantages over three-phase IMs, the applications for multiphase IMs have been increasing in areas such as electric and hybrid vehicles [15] and wind energy conversion systems [11,16]. It is considered that any multiphase IM can be analyzed by the vector space decomposition (VSD) technique, obtaining multiple orthogonal planes, $(\alpha-\beta)$, $(x-y)$ and (z_1-z_2), which represent the electromagnetic energy conversion excluding some higher harmonics of the order $12n \pm 1$ $(n = 1, 2, 3\ldots)$, the machine energy losses and the homopolar plane, respectively [17]. For two isolated neutrals configuration, (z_1-z_2) currents cannot flow, therefore the components of the (z_1-z_2) sub-space can be ignored [18].

FCS–MPC, applied to multiphase IM drives, has been developed for the first time in 2009 in [19,20], verifying its performance as an alternative to conventional control techniques. However, FCS–MPC techniques are known for their high computational cost [20,21]. In addition, some state observers were considered to perform a speed-sensorless control in multiphase machines in [22–24] and also to improve the prediction of the FCS–MPC applied to multiphase induction machines [25–28]. Some restrained vectors techniques were presented in [29,30], which consist in reducing the selection of some space vector voltages as the control output based on a constraint such as avoiding the voltage vectors that generate more harmonics or generate more $(x-y)$ currents, to reduce the computational cost in FCS–MPC and some modulation techniques were described in [31–33], such as pulse width modulation (PWM), based on space vector modulation,

---

* Corresponding author.
E-mail addresses: mayala@ing.una.py (M. Ayala), jdoval@uvigo.es (J. Doval-Gandoy), jrodas@ing.una.py (J. Rodas), ogonzalez@ing.una.py (O. Gonzalez), rgregor@ing.una.py (R. Gregor).

https://doi.org/10.1016/j.isatra.2019.08.052
0019-0578/

added to FCS–MPC to reduce $(x-y)$ currents. It can be noticed that in these cited works there is not an exhaustive comparison between different predictive current control techniques in order to analyze their advantages and limitations for implementation of predictive control techniques applied to multiphase motor drives.

The main contribution of this paper is a comparative study of four FCS–MPC applied as a predictive current control (PCC) technique, with a Kalman filter (KF) as a state observer to operate an asymmetrical six-phase induction motor drive (ASIMD) in terms of current tracking, THD of stator currents and computational burden. The four PCC techniques, which differ each other by the method to select the optimal vector and the modulation technique applied in some of them, are compared by using the mean square error (MSE), THD and the number of floating point operations (FPOs), to measure the computational burden of each PCC, as figures of merit. These techniques are tested for different operating conditions, in steady-state and transient conditions.

This paper is organized as follows: the ASIMD state-space model is presented in Section 2. In Section 3, the PCC design is shown, where it describes the traditional PCC which will be used as a reference for the comparative study. Sections 4–6 describe the three PCC techniques to be compared. The experimental results show the transient and steady-state behavior, for the four PCC where the figures of merit are compared, in Section 7. Section 8 summarizes the conclusion.

2. Asymmetrical six-phase IM model

The system is composed of an ASIMD connected to a six-phase VSI and a DC voltage source (V_{dc}). An electrical scheme of the VSI drive is shown in Fig. 1. The ASIMD is a continuous system which can be described by a group of differential equations. By applying the VSD approach, the six-dimensional space of the ASIMD, defined by its six-phases (a, b, c, d, e, f), is transformed into three two-dimensional orthogonal planes in the stationary reference frame, represented as $(\alpha-\beta)$, $(x-y)$ and (z_1-z_2), by using the transformation matrix $\mathbf{T}$ [32]. The studied ASIMD has isolated neutrals configuration, thus (z_1-z_2) currents are not considered, simplifying the mathematical model used by only considering $(\alpha-\beta)$ and $(x-y)$ planes.

$$\mathbf{T}=\frac{1}{3}\begin{array}{cc} \begin{matrix} a & d & b & e & c & f \end{matrix} & \\ \begin{bmatrix} 1 & \frac{\sqrt{3}}{2} & -\frac{1}{2} & -\frac{\sqrt{3}}{2} & -\frac{1}{2} & 0 \\ 0 & \frac{1}{2} & \frac{\sqrt{3}}{2} & \frac{1}{2} & -\frac{\sqrt{3}}{2} & -1 \\ 1 & -\frac{\sqrt{3}}{2} & -\frac{1}{2} & \frac{\sqrt{3}}{2} & -\frac{1}{2} & 0 \\ 0 & \frac{1}{2} & -\frac{\sqrt{3}}{2} & \frac{1}{2} & \frac{\sqrt{3}}{2} & -1 \\ 1 & 0 & 1 & 0 & 1 & 0 \\ 0 & 1 & 0 & 1 & 0 & 1 \end{bmatrix} & \begin{matrix} \alpha \\ \beta \\ x \\ y \\ z_1 \\ z_2 \end{matrix} \end{array} \tag{1}$$

where an invariant amplitude criterion was selected.

The six-phase VSI has a discrete behavior and a total number of $2^6 = 64$ switching states defined by the six VSI legs $\mathbf{S} = [S_a, S_b, S_c, S_d, S_e, S_f]$, where $S_i \in \{0, 1\}$. The different switching states and V_{dc} determine the phase voltages, which can be represented into the $(\alpha-\beta)$ and $(x-y)$ planes according to the VSD approach [17]. Fig. 2 shows the 64 possibilities which lead only to 49 different vectors (48 vectors + 1 null vector) in the $(\alpha-\beta)$ and $(x-y)$ planes. The state-space model of the ASIMD is defined by:

$$\dot{\mathbf{X}}_{(t)} = \mathbf{A}_{(t)}\,\mathbf{X}_{(t)} + \mathbf{B}_{(t)}\,\mathbf{U}_{(t)} + \mathbf{H}\,\varpi_{(t)} \tag{2}$$

where $\mathbf{U}_{(t)}$ is the input vector of the state-space model, $\mathbf{X}_{(t)}$ the state vector and $\mathbf{A}_{(t)}$ and $\mathbf{B}_{(t)}$ are matrices determined by the electrical parameters of the ASIMD. The process noise is defined as $\varpi_{(t)}$ and $\mathbf{H}$ is the noise weight matrix. The state-space model described by (2) and $\mathbf{X}_{(t)} = [x_1, x_2, x_3, x_4, x_5, x_6]^T$, define the following equation:

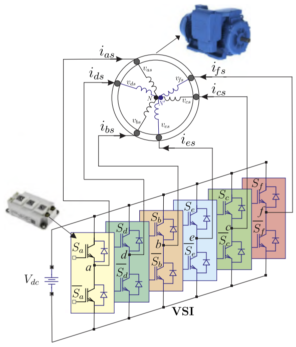

Fig. 1. Scheme of an ASIMD connected to a six-phase VSI.

$$\begin{bmatrix} \dot{x}_1 \\ \dot{x}_2 \\ \dot{x}_3 \\ \dot{x}_4 \\ \dot{x}_5 \\ \dot{x}_6 \end{bmatrix} = \begin{bmatrix} A_{11} & A_{12} & 0 & 0 & A_{15} & A_{16} \\ A_{21} & A_{22} & 0 & 0 & A_{25} & A_{26} \\ 0 & 0 & A_{33} & 0 & 0 & 0 \\ 0 & 0 & 0 & A_{44} & 0 & 0 \\ A_{51} & A_{52} & 0 & 0 & A_{55} & A_{56} \\ A_{61} & A_{62} & 0 & 0 & A_{65} & A_{66} \end{bmatrix} \begin{bmatrix} x_1 \\ x_2 \\ x_3 \\ x_4 \\ x_5 \\ x_6 \end{bmatrix} + \begin{bmatrix} B_{11} & 0 & 0 & 0 & 0 & 0 \\ 0 & B_{22} & 0 & 0 & 0 & 0 \\ 0 & 0 & B_{33} & 0 & 0 & 0 \\ 0 & 0 & 0 & B_{44} & 0 & 0 \\ B_{55} & 0 & 0 & 0 & 0 & 0 \\ 0 & B_{66} & 0 & 0 & 0 & 0 \end{bmatrix} \begin{bmatrix} u_1 \\ u_2 \\ u_3 \\ u_4 \\ 0 \\ 0 \end{bmatrix} \tag{3}$$

being

$A_{11} = A_{22} = -R_s c_2$ $\quad A_{12} = -A_{21} = c_4 L_m \omega_r$

$A_{15} = A_{26} = c_4 R_r$ $\quad A_{16} = -A_{25} = c_4 L_r \omega_r$

$A_{33} = A_{44} = -R_s c_3$ $\quad A_{51} = A_{62} = R_s c_4$

$A_{52} = -A_{61} = -c_5 L_m \omega_r$ $\quad A_{55} = A_{66} = -c_5 R_r$

$A_{56} = -A_{65} = -c_5 L_r \omega_r$ $\quad B_{11} = B_{22} = c_2$

$B_{33} = B_{44} = c_3$ $\quad B_{55} = B_{66} = -c_4$

where R_s, R_r, L_m, $L_r = L_{lr} + L_m$ and $L_s = L_{ls} + L_m$ are the electrical parameters of the ASIMD. The coefficients are determined as $c_1 = L_s L_r - L_m^2$, $c_2 = \frac{L_r}{c_1}$, $c_3 = \frac{1}{L_{ls}}$, $c_4 = \frac{L_m}{c_1}$ and $c_5 = \frac{L_s}{c_1}$. The input vector is composed of the applied voltages to the stator $u_1 = v_{\alpha s}$, $u_2 = v_{\beta s}$, $u_3 = v_{xs}$, $u_4 = v_{ys}$ and the state vector corresponds to the ASIMD stator and rotor currents $x_1 = i_{\alpha s}$, $x_2 = i_{\beta s}$, $x_3 = i_{xs}$, $x_4 = i_{ys}$, $x_5 = i_{\alpha r}$ and $x_6 = i_{\beta r}$. Stator voltages are dependent on the input control signals $\mathbf{S}$. In this particular case, the simplest VSI model has been considered to obtain a good optimization process. The stator voltages can be calculated from the ideal six-phase VSI model $\mathbf{M}_{[\mathbf{S}]}$ [32].

$$\mathbf{M}_{[\mathbf{S}]} = \frac{1}{3}\begin{bmatrix} 2 & 0 & -1 & 0 & -1 & 0 \\ 0 & 2 & 0 & -1 & 0 & -1 \\ -1 & 0 & 2 & 0 & -1 & 0 \\ 0 & -1 & 0 & 2 & 0 & -1 \\ -1 & 0 & -1 & 0 & 2 & 0 \\ 0 & -1 & 0 & -1 & 0 & 2 \end{bmatrix} \mathbf{S}^T \tag{4}$$

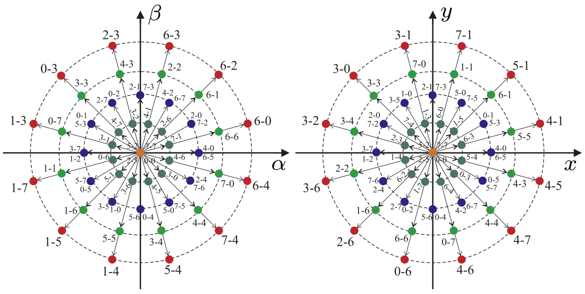

Fig. 2. Voltage space vectors and switching states in $(\alpha-\beta)$ and $(x-y)$ planes for an ASIMD.

An ideal six-phase VSI transforms gating signals into stator voltages which can be projected to $(\alpha-\beta)$ and $(x-y)$ planes and defined in $\mathbf{U}_{(t)} = [u_1,\ u_2,\ u_3,\ u_4]^T$, determined with the following equation:

$$\mathbf{U}_{(t)} = V_{dc}\, \mathbf{T}\, \mathbf{M}_{[\mathbf{S}]} \tag{5}$$

The output vector, $\mathbf{Y}$, is:

$$\mathbf{Y}_{(t)} = \mathbf{C}\mathbf{X}_{(t)} + \nu_{(t)} \tag{6}$$

being $\nu_{(t)}$ is the measurement noise and

$$\mathbf{C} = \begin{bmatrix} 1 & 0 & 0 & 0 & 0 & 0 \\ 0 & 1 & 0 & 0 & 0 & 0 \\ 0 & 0 & 1 & 0 & 0 & 0 \\ 0 & 0 & 0 & 1 & 0 & 0 \end{bmatrix}$$

The mechanical equations of the ASIMD are given by:

$$T_e = 3\,P\left(\psi_{\alpha s} i_{\beta s} - \psi_{\beta s} i_{\alpha s}\right) \tag{7}$$

$$J_i\,\dot{\omega}_m + B_i\,\omega_m = (T_e - T_L) \tag{8}$$

$$\omega_r = P\omega_m \tag{9}$$

where B_i is the friction coefficient, J_i the inertia coefficient, T_e defines the produced torque, T_L is the load torque, ω_r is the rotor electrical speed, ω_m is the rotor mechanical speed, $\psi_{\alpha s}$ and $\psi_{\beta s}$ are the stator fluxes and P is the number of pole pairs.

3. FCS–MPC method for an asymmetrical six-phase IM model (PC1)

This section presents the conventional PCC technique equipped with KF for rotor current estimator proposed in [25] (PC1 in what follows). The equations of the ASIMD (3) and (6) have to be discretized so it can be adapted for the PC1. A forward-Euler discretization method is selected to maintain a low computational cost. The resulting equations will be in a digital control form with predicted variables only dependent on the variables past values. Hence, a prediction of the future next-sample state $\hat{\mathbf{X}}_{[k+1|k]}$ is:

$$\hat{\mathbf{X}}_{[k+1|k]} = \mathbf{X}_{[k]} + \mathrm{f}\left(\mathbf{X}_{[k]},\ \mathbf{U}_{[k]},\ T_s,\ \boldsymbol{\omega}_{r[k]}\right) \tag{10}$$

being $[k]$ the current sample and T_s is the sampling time.

3.1. Reduced order observer

The state-space representation in (3) has six state variables, where only stator currents can be measured. Stator voltages are easily calculated from (5), where the switching commands cause the output voltage from the VSI. On the other hand, rotor currents cannot be directly measured. This can be overcome by a reduced order observer to estimate the rotor currents. The reduced order observers estimate a calculation for only the unmeasured part of the state vector. This is the main issue which has been recently covered by the application of the Luenberger observer (LO) and KF techniques, where the KF shows better results due to the observer gains are computed online by considering the measurement and process noises of the ASIMD. However, LO has gains which are not so optimized and it has a deterministic setting [25,28]. Therefore, a reduced order KF is implemented in this work for rotor currents estimation. By considering a zero-mean Gaussian measurement and uncorrelated process noises, the system's equations can be:

$$\hat{\mathbf{X}}_{[k+1|k]} = \mathbf{A}_{[k]}\mathbf{X}_{[k]} + \mathbf{B}_{[k]}\mathbf{U}_{[k]} + \mathbf{H}\varpi_{[k]} \tag{11}$$

$$\mathbf{Y}_{[k+1|k]} = \mathbf{C}\mathbf{X}_{[k+1]} + \nu_{[k+1]} \tag{12}$$

where $\mathbf{A}_{[k]}$ and $\mathbf{B}_{[k]}$ are discretized matrices from (3). $\mathbf{A}_{[k]}$ is also dependable on the present value of $\omega_{r[k]}$ and must be considered at every sampling period. The error dynamics of the reduced order observer is presented as:

$$e_{[k+1]} = \boldsymbol{\lambda}_{[k]} e_{[k]} = \left\{ \begin{bmatrix} 1 + A_{55}T_s & A_{56}T_s \\ A_{65}T_s & 1 + A_{66}T_s \end{bmatrix} - \mathbf{K}_{[k]} \begin{bmatrix} A_{15}T_s & A_{16}T_s \\ A_{25}T_s & A_{26}T_s \end{bmatrix} \right\} e_{[k]} \tag{13}$$

where $e_{[k]}$ is the error between the estimated rotor currents and the real rotor currents while $\mathbf{K}_{[k]}$ is the KF gain. For a fast error convergence to zero, the real parts of the eigenvalues of $\boldsymbol{\lambda}_{[k]}$ should be as negative as possible. It can also be considered that rotor currents have a very low dynamic facilitating the KF speed convergence. A detailed description of the convergence and dynamics of the reduced order KF (and LO) can be found in [25,26] and it was not included for the sake of conciseness.

3.2. Cost function

The cost function design can grant the optimization of many important variables such as machine torque ripple minimization, VSI switching losses and harmonic content reduction [2]. As consequence, by including more terms in the cost function the controller can easily include other variables or constraints. In PC1 the parameter is the tracking error in the predicted stator currents for the next sample. Therefore, the cost function is determined as:

$$J_{[k+2|k]} = \|i^*_{\alpha s[k+2]} - \hat{i}_{\alpha s[k+2|k]}\|^2 + \|i^*_{\beta s[k+2]} - \hat{i}_{\beta s[k+2|k]}\|^2 + \lambda_{xy}\left(\|i^*_{xs[k+2]} - \hat{i}_{xs[k+2|k]}\|^2 + \|i^*_{ys[k+2]} - \hat{i}_{ys[k+2|k]}\|^2\right) \tag{14}$$

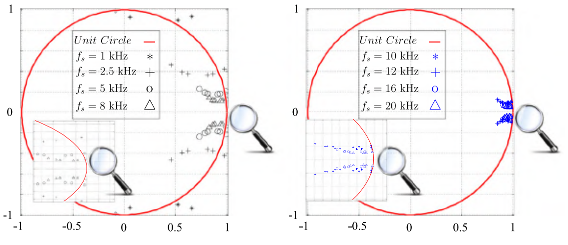

(a) (b)

Fig. 3. Eigenvalues of $(\mathbf{A}_{[k]} - \mathbf{B}_{[k]}\mathbf{L}_{[k]})$ matrix at different sampling frequencies: (a) lower than 10 kHz; (b) higher than 10 kHz.

A second-step ahead prediction of the stator current $\hat{i}_{s[k+2|k]}$ is required for the delay compensation of the computational burden and $i^{*}_{s[k+2]}$ exhibits the reference trajectory of the stator currents. The tuning parameter λ_{xy} is related to the ASIMD losses [25,32]. As a result, through an iterative algorithm PC1 obtains the optimal output control vector $\mathbf{S}^{opt}$, which is the one that minimizes (14). Then, this optimal switching state is used in (5) and it is applied during the next sampling period. Taking into account the computational cost, it is considered the 49 no redundant voltage vectors to be selected for PC1 which is the number of iterations performed in every sample time. In every iteration there are 48 FPOs related to the prediction calculation, the cost function minimization and the second step prediction process, giving a total amount of 2352 FPOs, while the KF has 450 FPOs.

3.3. Stability analysis

There are many MPC techniques presented in the literature, which have some common properties which formalize the stability field [34]. The main common property is a defined cost function to forecast the future behavior of the system. Hence, one of the most used methods to prove the stability of FCS–MPC is by considering the defined cost function as a candidate-Lyapunov function [35,36], another approach, presented in [35,37] consists in produce a determined gain $\mathbf{L}_{[k]}$ to obtain a stable matrix $(\mathbf{A}_{[k]} - \mathbf{B}_{[k]}\mathbf{L}_{[k]})$ whose eigenvalues are less than 1. The second method is used due to its simplicity and by considering that FCS–MPC has a limited control effort, i.e. 49 voltage vectors in the particular case of the six-phase VSI. For a limited current reference (due to security issues), there is a finite number of $\mathbf{L}_{[k]}$ values through the cost function minimization and it shows guaranteed asymptotic stability with a high sampling frequency (f_s), above 10 kHz, as it shows in Fig. 3(a) and Fig. 3(b).

4. FCS–MPC technique with PWM (PC2)

PC1 technique selects an optimal vector $\mathbf{S}^{opt}$ by minimizing the cost function in (14). Instead of applying the optimal vector to the ASIMD during the entire switching period, PC2 method, presented in [38], uses an optimal vector combining it with the VSD theory to obtain the duty cycles as follows:

$$\boldsymbol{\tau} = \frac{1}{2} + \frac{3}{4}\mathbf{M}_{[\mathbf{S}^{opt}]} \tag{15}$$

where $\boldsymbol{\tau} = \left[\tau_a,\ \tau_b,\ \tau_c,\ \tau_d,\ \tau_e,\ \tau_f\right]^T$ and $\mathbf{M}_{[\mathbf{S}^{opt}]}$ is the ideal VSI model from (4) with the optimal vector selected. The duty cycles, defined as $\boldsymbol{\tau}$, are related with the VSI phases and are normalized between 0 and 1. $\mathbf{S}^{opt}$ produces a certain level of voltage for each phase and this technique, through the duty cycles calculation, allows the VSI to generate a similar level of voltage (75% of the optimal vector value) with a combination of space vectors. This technique can be considered as the application of several vectors in order to reduce the voltage vector amplitude in order to minimize the stator currents in $(x - y)$ plane in one sampling period as shown (with an example for optimal vector $6 - 4$) in Fig. 4. As for the computational cost, it is slightly higher than PC1, since the modulation stage has 90 FPOs.

5. FCS–MPC with computation load reduction method (PC3)

PC3 technique is based on the conventional PC1, which selects an optimal vector through the cost function minimization in (14) for a sample time, and a restrained vector technique which will be applied in the next sample time. The main target of this technique is to reduce the $(x - y)$ stator currents by limiting the selected vectors to a determined region depending on the previously selected vector, in order to give priority to an optimal vector which will generate an opposite voltage vector in the $(x - y)$ plane. However, this technique will limit the $(\alpha - \beta)$ stator currents regulation due to the fact that PC3 uses restrained vectors prioritizing the $(x - y)$ stator currents reduction.

As shown in Fig. 5, the $(x{-}y)$ plane can be subdivided into four regions, where each region contains 12 not redundant voltage vectors. PC3 will operate as the conventional PC1, where an optimal vector will be selected from the minimization of the cost function. Then the algorithm will reduce the possible vectors for the next sample time, being the selected region, the opposite of the previously selected vector.

This PCC technique is a restrained voltage vector technique, thus it gets a computational load reduction due to the limited iterations executed to process comparing to PC1, being a total of 61 iterations comparing to 98 from PC1 in two sample times. This restrained technique reduces the computational cost by approximately 888 FPOs in every sampling time.

6. FCS–MPC with computation load reduction and PWM (PC4)

PC4 is a combination between PC2 and PC3, where there is a restriction in the voltage vectors selection and a PWM modulation applied in the final stage of the control, as shown in Fig. 6. The main objective of this technique is to improve the $(x - y)$ stator currents reduction by combining the two techniques and still managing to get a PCC with a reduced computational cost due to the limited executed iterations, just adding 90 FPOs for the modulation stage comparing to PC3.

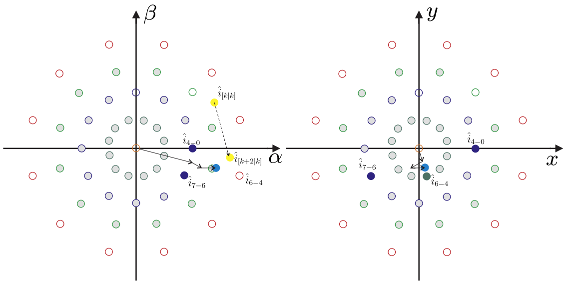

Fig. 4. Stator currents predictions projected by PC2 in the $(\alpha - \beta)$ and $(x - y)$ planes.

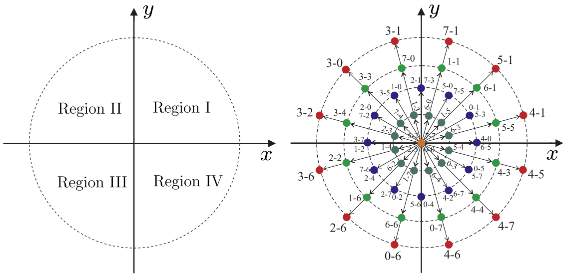

Fig. 5. Voltage space vectors regions in the $(x - y)$ plane determined by PC3 for an ASIMD.

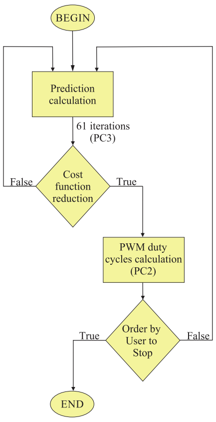

Fig. 6. Block diagram of the PC4 algorithm.

7. Experimental results

7.1. Experimental setup description

The previously described PCC techniques are tested in order to compare the experimental results obtained in the same test bench. The parameters of the ASIMD used in these tests have been obtained using conventional, AC-time domain and stand-still with VSI supply tests [39,40], and the obtained values are described in Table 1. The ASIMD is powered by two conventional three-phase VSI, using a constant DC voltage of 400 V from a DC power supply system. The VSIs are finally controlled by a dSPACE MABXII DS1401 real-time rapid prototyping platform. This platform is designed to perform controllers of the electric motor for automotive applications. As a consequence, this platform is comparable, in robustness and immunity to electromagnetic noise, to any industrial ones. The experimental results included are captured and then processed using MATLAB R2013b. In the experimental tests, the phase currents are measured with the current sensors LA 55-P s, which have a frequency bandwidth from DC up to 200 kHz. The analog measurements are converted to digital with 16-bit A/D converters. The motor position is measured with a 1024-pulses-per-revolution incremental encoder, and then, the speed is calculated from it. Finally, a 5 HP eddy current brake, based on Foucault currents, is used to introduce a variable mechanic load in the system. This brake is able to emulate typical loads attached to the ASIMD, from positive or negative loading steps to linear or quadratic load variations. It is important to mention that the brake control is made externally to the converter's control. A block diagram of the test bench is shown in Fig. 7, including some photos of the equipment.

7.2. Performance parameters

The performance of the three enhanced PCC techniques and the conventional PCC are compared in transient and steady-state conditions. The experimental results show a comparison of the

Table 1
Electrical and mechanical parameters of the ASIMD.

PARAMETER	VALUE	PARAMETER	VALUE
R_r (Ω)	6.9	L_s (mH)	654.4
R_s (Ω)	6.7	P	1
L_{ls} (mH)	5.3	P_w (kW)	2
L_m (mH)	614	J_i (kg m^2)	0.07
L_r (mH)	626.8	B_i (kg m^2/s)	0.0004
ω_{r-nom} (rpm)	3000	V_{dc} (V)	400

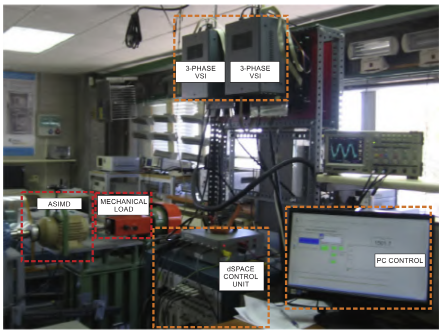

Fig. 7. Block diagram of the test bench including the ASIMD, the VSI, the dSPACE and the mechanical load.

MSE and THD obtained in stator currents in the $(\alpha-\beta)$ and $(x-y)$ planes for all PCC techniques. The MSE is computed as:

$$\mathrm{MSE}(i_{\phi s}) = \sqrt{\frac{1}{N}\sum_{j=1}^{N}(i_{\phi s} - i_{\phi s}^{*})^2} \tag{16}$$

being N the number of analyzed samples, $i_{\phi s}^{*}$ the stator current reference, $i_{\phi s}$ the measured stator current and $\phi \in \{\alpha,\ \beta,\ x,\ y\}$. On the other hand, the THD is computed as:

$$\mathrm{THD}(i_s) = \sqrt{\frac{1}{i_{s1}^2}\sum_{j=2}^{N}(i_{sj})^2} \tag{17}$$

being i_{s1} the fundamental stator current and i_{sj} is the harmonic stator current. The defined cost function in (14) with λ_{xy} = 0.01, was selected to evaluate the dynamic performance of the proposed PCC techniques, prioritizing the $(\alpha-\beta)$ stator current tracking over the $(x-y)$ currents reduction [32]. The process noise and the measurement noise values can be estimated by using the method proposed in [26], as $\hat{Q}_w$ = 0.0022 and $\hat{R}_v$ = 0.0022. In every case, the $(x-y)$ current references are set to zero ($i_{xs}^{*} = i_{ys}^{*} = 0$) and the sampling frequency used in the tests are 12, 16 and 20 kHz.

7.3. Analysis of experimental results

The comparison among the three proposed PCC techniques, defined as PC2, PC3 and PC4, and the conventional PCC, described as PC1, is first analyzed under a steady-state condition, a mechanical load condition based on Foucault currents brake of 5 CV and different rotor speeds (ω_m). Table 2 reports the experimental results obtained for PC1, at different rotor speeds and sampling frequencies, regarding the MSE and THD of stator currents in the $(\alpha-\beta)$ and $(x-y)$ planes. The results demonstrate a good tracking of the current references in the $(\alpha-\beta)$ plane, but a low reduction of the stator currents in the $(x-y)$ plane. Table 3 exposes the results for PC2, considering the MSE and THD of stator currents. For PC2, there is an improvement in the $(x-y)$ stator currents reduction over PC1 of 24 % in average, but there is a decrease of the $(\alpha-\beta)$ current tracking of approximately 21 %.

Table 2
Performance Analysis of Stator Currents $(\alpha-\beta)$, $(x-y)$, MSE (A), THD (%) for PC1 at different rotor speeds (rpm).

ω_m^*	MSE$_\alpha$	MSE$_\beta$	MSE$_x$	MSE$_y$	THD$_\alpha$	THD$_\beta$
		Sampling	frequency	12 kHz		
500	0.0856	0.0874	0.6008	0.5859	8.3101	8.6441
1000	0.0975	0.0952	0.7127	0.7293	6.8383	6.8663
1500	0.0988	0.1006	0.7344	0.7140	5.8643	6.0550
		Sampling	frequency	16 kHz		
500	0.0717	0.0730	0.4707	0.4747	8.9044	8.9615
1000	0.0853	0.0855	0.5505	0.5538	6.1956	6.1703
1500	0.0783	0.0790	0.5736	0.5710	4.4041	4.4777
		Sampling	frequency	20 kHz		
500	0.0641	0.0661	0.4137	0.4103	6.4833	7.1390
1000	0.0745	0.0791	0.4764	0.4813	5.4602	5.8339
1500	0.0726	0.0737	0.4701	0.4649	4.0989	4.3228

Table 3
Performance Analysis of Stator Currents $(\alpha-\beta)$, $(x-y)$, MSE (A), THD (%) for PC2 at different rotor speeds (rpm).

ω_m^*	MSE$_\alpha$	MSE$_\beta$	MSE$_x$	MSE$_y$	THD$_\alpha$	THD$_\beta$
		Sampling	frequency	12 kHz		
500	0.1259	0.1095	0.4862	0.4796	13.2002	11.5178
1000	0.1100	0.1010	0.5360	0.5380	7.6581	7.0963
1500	0.1539	0.1465	0.5092	0.5547	10.1893	9.6681
		Sampling	frequency	16 kHz		
500	0.0827	0.0807	0.3801	0.3652	9.8252	9.3829
1000	0.0927	0.0886	0.4086	0.4058	6.7514	6.5256
1500	0.1102	0.1075	0.4685	0.4627	5.2311	5.3378
		Sampling	frequency	20 kHz		
500	0.0944	0.0877	0.3262	0.3139	10.7465	10.2255
1000	0.1072	0.1025	0.3566	0.3677	7.5919	7.0918
1500	0.1114	0.1096	0.4202	0.4271	5.7400	5.6312

Table 4 shows the results of the system performance with PC3. From the comparison between PC3 and PC1, there is an improvement of 13 % in average regarding the $(x-y)$ stator currents reduction, however it shows a decrease in the $(\alpha-\beta)$ current tracking of 41 %. At last it is presented in Table 5 the results for PC4 at different rotor speeds and sampling frequencies.

If the results are compared to PC1, it can be seen an improvement of 30 % in average for the $(x-y)$ stator currents reduction and a decrease of the $(\alpha-\beta)$ current tracking of approximately 52 %.

Fig. 8 exposes the polar trajectories of the stator currents in the $(\alpha-\beta)$ and $(x-y)$ planes. The obtained results with PC1, PC2, PC3 and PC4 techniques are shown in Fig. 8(a), 8(b), 8(c) and 8(d) respectively. Fig. 9(a), 9(b), 9(c) and 9(d) report the stator phase currents in time domain for PC1, PC2, PC3 and PC4 respectively. By considering the MSE and root mean square (RMS) of the stator currents ripple in the $(\alpha-\beta)$ and $(x-y)$ planes for the four PCC techniques, it can be defined that PC1 has the lowest MSE and RMS current ripple in the $(\alpha-\beta)$ plane, where PC2 has 83 % of RMS ripple and 56 % of MSE greater than PC1, but PC2 has lesser RMS current ripple and MSE in the $(x-y)$ plane comparing to PC1 of approximately 23 % and 44 % respectively. On the other hand, by comparing with PC1, PC3 and PC4 present a lower RMS ripple (12 % and 19 % approximately) and MSE (10 % and 19 % approximately) regarding the currents in the $(x-y)$ plane.

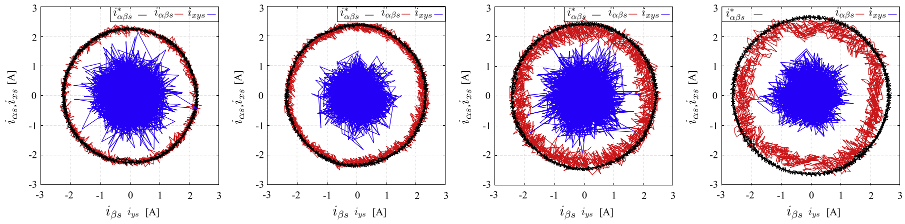

(a) (b) (c) (d)

Fig. 8. Stator currents in $(\alpha - \beta)$ and $(x - y)$ planes for a frequency of 25 Hz and ω_m being 1500 rpm: (a) for PC1; (b) for PC2; (c) for PC3; (d) for PC4.

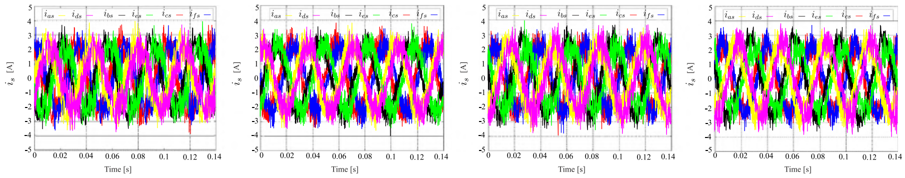

(a) (b) (c) (d)

Fig. 9. Stator phase currents in time domain for a frequency of 25 Hz and ω_m being 1500 rpm.: (a) for PC1; (b) for PC2; (c) for PC3; (d) for PC4.

Table 4
Performance Analysis of Stator Currents $(\alpha - \beta)$, $(x - y)$, MSE (A), THD (%) for PC3 at different rotor speeds (rpm).

ω^*_m	MSE_α	MSE_β	MSE_x	MSE_y	THD_α	THD_β
		Sampling	frequency	12 kHz		
500	0.1699	0.1749	0.4996	0.5063	16.2516	16.8039
1000	0.2162	0.2203	0.5759	0.5867	12.9967	13.0654
1500	0.2734	0.2722	0.6339	0.6288	11.4490	11.8897
		Sampling	frequency	16 kHz		
500	0.1419	0.1386	0.3983	0.4023	14.5515	15.0068
1000	0.1798	0.1826	0.4800	0.4792	11.2449	11.1217
1500	0.2133	0.2195	0.5225	0.5345	9.9848	9.9575
		Sampling	frequency	20 kHz		
500	0.1101	0.1223	0.3525	0.3547	11.3357	12.7361
1000	0.1444	0.1557	0.4051	0.4197	9.3282	10.1117
1500	0.1935	0.1827	0.4504	0.4648	8.3290	8.5807

Table 5
Performance Analysis of Stator Currents $(\alpha - \beta)$, $(x - y)$, MSE (A), THD (%) for PC4 at different rotor speeds (rpm).

ω^*_m	MSE_α	MSE_β	MSE_x	MSE_y	THD_α	THD_β
		Sampling	frequency	12 kHz		
500	0.2544	0.2125	0.3685	0.3844	22.3211	17.6980
1000	0.2627	0.2528	0.4467	0.4587	13.7984	13.3634
1500	0.3440	0.3262	0.4961	0.4908	17.4150	16.7115
		Sampling	frequency	16 kHz		
500	0.1716	0.1605	0.3057	0.2980	14.2297	13.3001
1000	0.2113	0.1934	0.3909	0.3742	10.6151	9.8541
1500	0.2882	0.2846	0.4814	0.4773	9.8225	9.5776
		Sampling	frequency	20 kHz		
500	0.1641	0.1463	0.2856	0.2695	15.2786	13.5077
1000	0.1937	0.1817	0.3376	0.3545	11.2976	10.4904
1500	0.2895	0.2719	0.4689	0.4668	10.3093	9.6217

Table 6
Computational cost of the four PCC in terms of FPOs.

PCC	FPOs	PCC	FPOs
PC1	2 802	PC3	1 914
PC2	2 892	PC4	2 004

A dynamic comparison test is carried out as shown in Fig. 10 which consists in the transient behavior of the different PCC techniques for a step response in the q axis current reference (i^*_{qs}). The step response is obtained through a modification of the rotor mechanical speed (ω_m) from 500 to −500 rpm, making a reversal condition. In all the figures [Fig. 10(a) to Fig. 10(d)] it is observed the transient performance of PC1 is approximately 2.8 ms, for PC2 is approximately 4.2 ms, PC3 is 10 ms and PC4 is 18 ms for a 5% criterion, showing that PC1 has the highest response speed to reach the new reference (i^*_{qs}). PC2, PC3 and PC4 present a better efficiency regarding the $(x-y)$ currents reduction showing a good performance in terms of energy losses in the ASIMD. However, they present an increased steady-state error in the $(d-q)$ currents tracking of 7%, 12% and 14% respectively, compromising the torque/flux regulation. In this particular subject, PC1 presents the best performance in the $(d-q)$ currents tracking but it has the least efficient current reduction in the $(x-y)$ plane. On the other hand, Table 6 shows the computational cost of the four studied PCC techniques in terms of FPOs, where PC2 has the highest computational cost of all the techniques, while PC3 has the lowest computational cost.

8. Conclusion

A comparative study of four PCC techniques (PC1, PC2, PC3, PC4) is presented. By comparing the currents performance in terms of MSE (with the reference), THD with different operating conditions and the computational burden, it can be determined

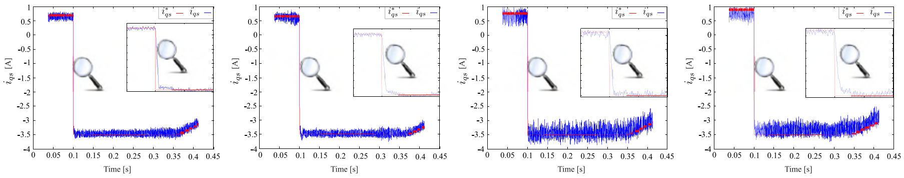

(a) (b) (c) (d)

Fig. 10. Transient step response of i_{qs} from a step response of 500 to −500 rpm from ω_m at a frequency sample of 16 kHz: (a) for PC1; (b) for PC2; (c) for PC3; (d) for PC4.

the advantages and limitations of each proposed technique compared to traditional PCC technique (PC1). PC1 presents a better performance regarding the $(\alpha - \beta)$ currents tracking, comparing to the other PCC techniques, however, it has a decreased capacity in the $(x - y)$ currents reduction. On the other hand, PC2 has an improved performance in terms of $(x - y)$ currents reduction comparing to PC1, and the $(\alpha - \beta)$ currents tracking is a little inferior to PC1. For PC3 and PC4, there is a notorious improvement on the $(x-y)$ currents reduction comparing to PC1, however the performance on the $(\alpha - \beta)$ currents tracking is vastly decreased, consequently worsening the steady-state error eclipsing their $(x - y)$ currents reduction performance. Still, PC3 and PC4 are viable options if considered the lower computational cost compared to PC1 and PC2 in terms of lesser FPOs executed.

Declaration of competing interest

The authors declare that they have no known competing financial interests or personal relationships that could have appeared to influence the work reported in this paper.

Acknowledgments

This research has been funded through the Consejo Nacional de Ciencia y Tecnología (CONACYT)-Paraguay, Grant Numbers 14-INV-101 and POSG16-05.

References

[1] Barrero F, Duran MJ. Recent advances in the design, modeling, and control of multiphase machines: Part I. IEEE Trans Ind Electron 2016;63(1):449–58. http://dx.doi.org/10.1109/TIE.2015.2447733.

[2] Vazquez S, Rodriguez J, Rivera M, Franquelo LG, Norambuena M. Model predictive control for power converters and drives: Advances and trends. IEEE Trans Ind Electron 2017;64(2):935–47. http://dx.doi.org/10.1109/TIE.2016.2625238.

[3] Arahal M, Barrero F, Toral S, Duran M, Gregor R. Multi-phase current control using finite-state model-predictive control. Control Eng Pract 2009;17(5):579–87. http://dx.doi.org/10.1016/j.conengprac.2008.10.005.

[4] Kim S-K, Choi D-K, Lee K-B, Lee YI. Offset-free model predictive control for the power control of three-phase AC/DC converters. IEEE Trans Ind Electron 2015;62(11):7114–26. http://dx.doi.org/10.1109/TIE.2015.2436353.

[5] Rohten JA, Espinoza JR, Muñoz JA, Pérez MA, Melin PE, Silva JJ, Espinosa EE, Rivera M. Model predictive control for power converters in a distorted three-phase power supply. IEEE Trans Ind Electron 2016;63(9):5838–48. http://dx.doi.org/10.1109/TIE.2016.2527732.

[6] Mirzaeva G, Goodwin GC, McGrath BP, Teixeira C, Rivera M. A generalized MPC framework for the design and comparison of VSI current controllers. IEEE Trans Ind Electron 2016;63(9):5816–26. http://dx.doi.org/10.1109/TIE.2016.2578283.

[7] Fuentes E, Silva CA, Kennel RM. MPC implementation of a quasi-time-optimal speed control for a PMSM drive, with inner modulated- FS-MPC torque control. IEEE Trans Ind Electron 2016;63(6):3897–905. http://dx.doi.org/10.1109/TIE.2016.2519326.

[8] Preindl M. Robust control invariant sets and Lyapunov-based MPC for IPM synchronous motor drives. IEEE Trans Ind Electron 2016;63(6):3925–33. http://dx.doi.org/10.1109/TIE.2016.2527722.

[9] Karamanakos P, Stolze P, Kennel RM, Manias S, du Toit Mouton H. Variable switching point predictive torque control of induction machines. IEEE Trans Emerg Sel Topics Power Electron 2014;2(2):285–95. http://dx.doi.org/10.1109/JESTPE.2013.2296794.

[10] Zbede YB, Gadoue SM, Atkinson DJ. Model predictive MRAS estimator for sensorless induction motor drives. IEEE Trans Ind Electron 2016;63(6):3511–21. http://dx.doi.org/10.1109/TIE.2016.2521721.

[11] Duran MJ, Barrero F. Recent advances in the design, modeling, and control of multiphase machines: Part II. IEEE Trans Ind Electron 2016;63(1):459–68. http://dx.doi.org/10.1109/TIE.2015.2448211.

[12] Levi E. Advances in converter control and innovative exploitation of additional degrees of freedom for multiphase machines. IEEE Trans Ind Electron 2016;63(1):433–48. http://dx.doi.org/10.1109/TIE.2015.2434999.

[13] Martín C, Bermúdez M, Barrero F, Arahal MR, Kestelyn X, Durán MJ. Sensitivity of predictive controllers to parameter variation in five-phase induction motor drives. Control Eng Pract 2017;68:23–31. http://dx.doi.org/10.1016/j.conengprac.2017.08.001.

[14] Che HS, Duran MJ, Levi E, Jones M, Hew W-P, Rahim NA. Postfault operation of an asymmetrical six-phase induction machine with single and two isolated neutral points. IEEE Trans Power Electron 2014;29(10):5406–16. http://dx.doi.org/10.1109/TPEL.2013.2293195.

[15] Yeoh SS, Yang T, Tarisciotti L, Hill CI, Bozhko S, Zanchetta P. More electric aircraft starter-generator system with utilization of hybrid modulated model predictive control. In: Proc. ESARS/ITEC; 2016, p. 1–6, http://dx.doi.org/10.1109/ESARS-ITEC.2016.7841399.

[16] Gonzalez-Prieto I, Duran MJ, Che H, Levi E, Bermúdez M, Barrero F. Fault-tolerant operation of six-phase energy conversion systems with parallel machine-side converters. IEEE Trans Power Electron 2016;31(4):3068–79. http://dx.doi.org/10.1109/TPEL.2015.2455595.

[17] Zhao Y, Lipo T. Space vector PWM control of dual three-phase induction machine using vector space decomposition. IEEE Trans Ind Electron 1995;31(5):1100–9. http://dx.doi.org/10.1109/28.464525.

[18] Che HS, Hew WP. Dual three-phase operation of single neutral symmetrical six-phase machine for improved performance. In: Proc. IECON; 2015, p. 1176–81, http://dx.doi.org/10.1109/IECON.2015.7392259.

[19] Arahal M, Barrero F, Toral S, Duran M, Gregor R. Multi-phase current control using finite-state model-predictive control. Control Eng Pract 2009;17(5):579–87. http://dx.doi.org/10.1016/j.conengprac.2008.10.005.

[20] Barrero F, Arahal MR, Gregor R, Toral S, Duran MJ. A proof of concept study of predictive current control for VSI-driven asymmetrical dual three-phase AC machines. IEEE Trans Ind Electron 2009;56(6):1937–54. http://dx.doi.org/10.1109/TIE.2008.2011604.

[21] Rodriguez J, Kazmierkowski MP, Espinoza JR, Zanchetta P, Abu-Rub H, Young HA, Rojas CA. State of the art of finite control set model predictive control in power electronics. IEEE Trans Ind Inf 2013;9(2):1003–16. http://dx.doi.org/10.1109/TII.2012.2221469.

[22] Hosseyni A, Trabelsi R, Mimouni MF, Iqbal A, Alammari R. Sensorless sliding mode observer for a five-phase permanent magnet synchronous motor drive. ISA Trans 2015;58:462–73. http://dx.doi.org/10.1016/j.isatra.2015.05.007.

[23] Ayala M, Gonzalez O, Rodas J, Gregor R, Doval-Gandoy J. A speed-sensorless predictive current control of multiphase induction machines using a Kalman filter for rotor current estimator, In: Proc. ESARS/ITEC; 2016. http://dx.doi.org/10.1109/ESARS-ITEC.2016.7841385.

[24] Mengoni M, Zarri L, Tani A, Serra G, Casadei D. Sensorless speed observer based on third-order spatial field harmonic for multiphase induction motor drives. In: Proc SLED; 2016, p. 1–6. http://dx.doi.org/10.1109/SLED.2016.7518792.

[25] Rodas J, Barrero F, Arahal MR, Martin C, Gregor R. On-line estimation of rotor variables in predictive current controllers: A case study using five-phase induction machines. IEEE Trans Ind Electron 2016;63(9):5348–56. http://dx.doi.org/10.1109/TIE.2016.2559420.

[26] Rodas J, Martin C, Arahal MR, Barrero F, Gregor R. Influence of covariance-based ALS methods in the performance of predictive controllers with rotor current estimation. IEEE Trans Ind Electron 2017;64(4):2602–7. http://dx.doi.org/10.1109/TIE.2016.2636205.

[27] Martin C, Arahal M, Barrero F, Duran M. Five-phase induction motor rotor current observer for finite control set model predictive control of stator current. IEEE Trans Ind Electron 2016;63(7):4527–38. http://dx.doi.org/10.1109/TIE.2016.2536578.

[28] Martín C, Arahal MR, Barrero F, Duran MJ. Multiphase rotor current observers for current predictive control: A five-phase case study. Control Eng Pract 2016;49:101–11. http://dx.doi.org/10.1016/j.conengprac.2016.01.011.

[29] Duran MJ, Prieto J, Barrero F, Toral S. Predictive current control of dual three-phase drives using restrained search techniques. IEEE Trans Ind Electron 2011;58(8):3253–63. http://dx.doi.org/10.1109/TIE.2010.2087297.

[30] Gonzalez-Prieto I, Duran MJ, Aciego JJ, Martin C, Barrero F. Model predictive control of six-phase induction motor drives using virtual voltage vectors. IEEE Trans Ind Electron 2017. http://dx.doi.org/10.1109/TIE.2017.2714126.

[31] Gregor R, Barrero F, Toral S, Duran M, Arahal M, Prieto J, Mora J. Predictive-space vector PWM current control method for asymmetrical dual three-phase induction motor drives. IET Electr Power App 2010;4(1):26–34. http://dx.doi.org/10.1049/iet-epa.2008.0274.

[32] Ayala M, Rodas J, Gregor R, Doval-Gandoy J, Gonzalez O, Saad M, Rivera M. Comparative study of predictive control strategies at fixed switching frequency for an asymmetrical six-phase induction motor drive. In: Proc. IEMDC; 2017, p. 1–8. http://dx.doi.org/10.1109/IEMDC.2017.8002121.

[33] Lu H, Li J, Qu R, Ye D. Fault-tolerant predictive current control with two-vector modulation for six-phase PMSM drives. IET Electr Power App 2018;12(2):169–78. http://dx.doi.org/10.1049/iet-epa.2017.0331.

[34] Mayne DQ, Rawlings JB, Rao CV, Scokaert PO. Constrained model predictive control: Stability and optimality. Automatica 2000;36(6):789–814. http://dx.doi.org/10.1016/S0005-1098(99)00214-9.

[35] Aguilera RP, Quevedo DE. On stability and performance of finite control set MPC for power converters. In: 2011 workshop on predictive control of electrical drives and power electronics. IEEE; 2011, p. 55–62. http://dx.doi.org/10.1109/PRECEDE.2011.6078688.

[36] Aguilera RP, Quevedo DE. On the stability of MPC with a finite input alphabet. IFAC Proc Vol 2011;44(1):7975–80. http://dx.doi.org/10.3182/20110828-6-IT-1002.02705.

[37] Aguilera RP, Quevedo DE. Stability analysis of quadratic MPC with a discrete input alphabet. IEEE Trans Automat Control 2013;58(12):3190–6. http://dx.doi.org/10.1109/TAC.2013.2264551.

[38] Gregor R, Rodas J, Muñoz J, Ayala M, Gonzalez O, Gregor D. Predictive-fixed switching frequency technique for 5-phase induction motor drives. In: Proc. SPEEDAM; 2016, p. 761–7. http://dx.doi.org/10.1109/SPEEDAM.2016.7525849.

[39] Yepes AG, Riveros JA, Doval-Gandoy J, Barrero F, López O, Bogado B, Jones M, Levi E. Parameter identification of multiphase induction machines with distributed windings Part 1: Sinusoidal excitation methods. IEEE Trans Energy Convers 2012;27(4):1056–66. http://dx.doi.org/10.1109/TEC.2012.2220967.

[40] Riveros JA, Yepes AG, Barrero F, Doval-Gandoy J, Bogado B, Lopez O, Jones M, Levi E. Parameter identification of multiphase induction machines with distributed windings part 2: Time-domain techniques. IEEE Trans Energy Convers 2012;27(4):1067–77. http://dx.doi.org/10.1109/TEC.2012.2219862.

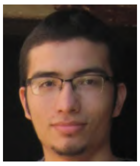

Magno Ayala received the B.Eng. degree in electronic engineering from the Universidad Nacional de Asunción (UNA), Paraguay, in 2014 and his M.Sc. in 2017. He joined the Laboratory of Power and Control System at the UNA, in 2015, working as a Research Assistant. Mr. Ayala is a recipient of the training program for university lecturers from the CONACYT of Paraguay for his Ph.D. studies.

Jesús Doval-Gandoy (M99) received the M.Sc. degree from Polytechnic University of Madrid, Madrid, Spain, in 1991 and the Ph.D. degree from the University of Vigo, Vigo, Spain in 1999. From 1991 till 1994 he worked at industry. He is currently an Associate Professor at the University of Vigo. His research interests are in the areas of ac power conversion.

Jorge Rodas (S'08–M'12) was born in Asunción, Paraguay in 1984. He received his B.Eng. degree in Electronic Engineering from the Universidad Nacional de Asunción (UNA), Paraguay, in 2009. He received his M.Sc. degrees from the Universidad de Vigo, Spain, in 2012 and from the Universidad de Sevilla, Spain, in 2013, and his joint-university Ph.D. degree between the Universidad Nacional de Asunción and the Universidad de Sevilla in 2016.

In 2011, he joined the Laboratory of Power and Control System at the UNA, where he is currently an Associate Professor. His main research areas are predictive control, multiphase drives, matrix converters and control of power converters for renewable energy applications.

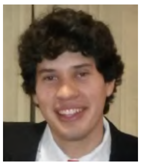

Osvaldo Gonzalez was born in Paraguay in 1987. B.Eng. degree in electronic engineering from the Universidad Nacional de Asunción (UNA), in 2014 and the M.Sc. degree in Power Electronics in 2017. His research interests include the area of control of multiphase motors. Mr. Gonzalez is a recipient of the training program for university lecturers from the CONACYT of Paraguay for his Ph.D. studies.

Raúl Gregor was born in Asunción, Paraguay, in 1979. He received the Bachelor Degree in Electronic Engineering from the Catholic University of Asunción, Paraguay, in 2005. He received the M.Sc. and Ph.D. degrees in Electronic, Signal Processing and Communications from the Higher Technical School of Engineering (ETSI), University of Seville, Spain, in 2008 and 2010, respectively. Since March 2010, Prof. Gregor is Head of the Laboratory of Power and Control System (LSPyC) of the Engineering Faculty in the National University of Asunción, Paraguay.

Prof. Gregor has authored or coauthored about 40 technical papers in the field of power electronics and control systems, six of which have been published in high impact factor journals. He obtained the Best Paper Award from the IEEE TRANSACTIONS ON INDUSTRIAL ELECTRONICS, Industrial Electronics Society, in 2010, and the Best Paper Award from the IET ELECTRIC POWER APPLICATIONS, in 2012. His research interests include; Multiphase Drives, Advanced Control of Power Converters Topologies, Quality of Electrical Power, Renewable Energy, Modeling, Simulation, Optimization and Control of Power Systems, Smart Metering & Smart Grids and Predictive Control.

ARTÍCULO 4

A NOVEL MODULATED MODEL PREDICTIVE CONTROL APPLIED TO SIX-PHASE INDUCTION MOTOR DRIVES

- **Magno Ayala**, Jesus Doval-Gandoy, Jorge Rodas, Osvaldo González, Raul Gregor and Marco Rivera, ”A Novel Modulated Model Predictive Control Applied to Six-Phase Induction Motor Drives”, IEEE Transactions on Industrial Electronics, pp. 1-10, 2020, DOI: 10.1109/TIE.2020.2984425.

A Novel Modulated Model Predictive Control Applied to Six-Phase Induction Motor Drives

***Abstract*—Model-based predictive control techniques, with finite set control, are considered an interesting option to control multiphase drives due to their control flexibility and fast dynamic response. However, those techniques have some drawbacks such as a high computational cost, poor $(x-y)$ currents reduction and steady-state error, especially at high speeds. To improve some of these drawbacks, modulation stages have been presented as an alternative. However, some of those drawbacks have not been improved. This paper proposes a novel approach to the classic predictive current control applied to an asymmetrical six-phase induction machine where a space vector modulation with specific vectors is used in order to improve the $(x-y)$ currents, the steady-state error and total harmonic distortion at high operation speeds. Experimental results are presented to demonstrate the characteristics of the proposed control technique in terms of current tracking, $(x-y)$ currents reduction and total harmonic distortion of stator currents compared to the classic predictive current control.**

***Index Terms*—Model-based predictive control, multiphase induction machine, space vector modulation.**

I. INTRODUCTION

MULTIPHASE machines have received great attention from the power electronics community due to their good features such as lower current per phase, availability, lower torque ripple and fault tolerant capabilities in comparison with traditional three-phase machines [1]. In the last few years, they were extensively applied especially in high-power applications such as electric vehicles and wind energy conversion systems [1], [2]. The majority of the control approaches applied to multiphase drives are commonly an extension of the control techniques applied to three-phase drives such as field oriented control (FOC) based on proportional-integral (PI) current control, direct torque control, among others [3], [4].

Lately, some new nonlinear control methods were developed to be applied in multiphase machines such as finite control set model predictive control (FCS-MPC), which presents fast transient response in comparison to linear controllers, addressed in [5]–[7], which has some variants already presented in the literature [8]–[10], i.e. MPC with virtual vectors (VV) which nullify the $(x-y)$ currents but with a limited voltage range proposed in [11]–[13]. Another example of these variants is the modulated model predictive control (M2PC) [14], [15]. In the remainder of the paper MPC will be used instead of the cumbersome FCS-MPC as the context makes the notation clear. M2PC is designed as a conventional MPC and a modulation stage, which is based on space vector modulation (SVM). This method was presented for different power converters [16]–[18]. This technique is applied by selecting two optimal active vectors and two zero vectors, where the duty cycles are calculated through their respective cost functions. These vectors are applied by a predetermined switching pattern in order to obtain an efficient performance for the system [18]. Recently, this technique was applied to an asymmetrical six-phase induction machine (ASIMD) in [19] and it showed some improvements over classic MPC, by obtaining a fixed switching frequency and a major reduction of $(x-y)$ stator currents. Still, the main drawback of classic MPC, which is the steady-state error [20], [21], was not improved with M2PC especially at high mechanical speeds.

This paper proposes a novel modulated MPC (N-M2PC) that improves the steady-state error, compared to M2PC, and reduces effectively the $(x-y)$ stator currents in an ASIMD. Experimental results are presented to show the advantages of this method in terms of current tracking by considering the mean squared error (MSE), mean value and total harmonic distortion (THD) of the stator currents. This method is tested under different operation points, considering transient and steady-state conditions.

The rest of this document is organized as follows: the ASIMD mathematical model is shown in Section II. In Section III, the classic MPC design is presented as a predictive current control (PCC), where it describes the traditional PCC which will be used as a reference to the obtained results. Section IV describes the M2PC design and Section V presents the proposed N-M2PC. The experimental results show the transient and steady-state performance, for the classic PCC, PCC-VV, M2PC and N-M2PC, where the figures of merit are analyzed, in Section VI. Finally, conclusions and special remarks are presented in the last section.

II. ASIMD MATHEMATICAL MODEL

The selected system is composed of an ASIMD connected to a six-leg voltage source inverter (VSI) and a DC voltage source. An electrical scheme of the six-phase VSI drive, based on isolated gate bipolar transistor (IGBT), is presented in Fig. 1. The ASIMD has a continuous model which can be analyzed by differential equations. By considering the six-dimensional space of the ASIMD defined by the six-phases (a, b, c, d, e, f) and the vector space decomposition (VSD) technique, the model can be represented into three two-dimensional orthogonal planes in the stationary reference frame, $(\alpha-\beta)$, $(x-y)$ and (z_1-z_2), by using (1), where the invariant amplitude criterion has been applied [15]. The ASIMD has a phase shift of 30° between the three phases and has an isolated neutral configuration, thus (z_1-z_2) currents are assumed to be null.

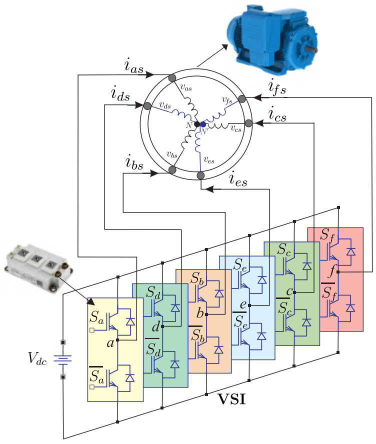

Fig. 1. Scheme of an ASIMD controlled by a six-leg VSI.

$$\mathbf{T} = \frac{1}{3}\begin{array}{c}\begin{array}{cccccc} a & d & b & e & c & f \end{array} \\ \begin{bmatrix} 1 & \frac{\sqrt{3}}{2} & -\frac{1}{2} & -\frac{\sqrt{3}}{2} & -\frac{1}{2} & 0 \\ 0 & \frac{1}{2} & \frac{\sqrt{3}}{2} & \frac{1}{2} & -\frac{\sqrt{3}}{2} & -1 \\ 1 & -\frac{\sqrt{3}}{2} & -\frac{1}{2} & \frac{\sqrt{3}}{2} & -\frac{1}{2} & 0 \\ 0 & \frac{1}{2} & -\frac{\sqrt{3}}{2} & \frac{1}{2} & \frac{\sqrt{3}}{2} & -1 \\ 1 & 0 & 1 & 0 & 1 & 0 \\ 0 & 1 & 0 & 1 & 0 & 1 \end{bmatrix}\end{array}\begin{array}{c} \\ \alpha \\ \beta \\ x \\ y \\ z_1 \\ z_2 \end{array} \tag{1}$$

The six-phase VSI has a discrete output and a total number of $2^6 = 64$ switching possible states defined by the six-legs. The different switching states and the DC voltage source determine the phase voltages, which can be represented into $(\alpha-\beta)$ and $(x-y)$ planes according to the VSD approach [22]. Fig. 2 denotes the 64 possibilities which only 49 different vectors (48 vectors + 1 null vector) are considered different in the $(\alpha-\beta)$ and $(x-y)$ planes. The state-space mathematical model of the ASIMD is modeled by:

$$\dot{\mathbf{X}}_{(t)} = \mathbf{A}_{(t)}\,\mathbf{X}_{(t)} + \mathbf{B}_{(t)}\,\mathbf{U}_{(t)} + \mathbf{H}\,\varpi_{(t)} \tag{2}$$

where $\mathbf{X}_{(t)} = [x_1,\, x_2,\, x_3,\, x_4, x_5,\, x_6]^T$ is the state vector that represents the stator and rotor currents $x_1 = i_{\alpha s}$, $x_2 = i_{\beta s}$, $x_3 = i_{xs}$, $x_4 = i_{ys}$, $x_5 = i_{\alpha r}$ and $x_6 = i_{\beta r}$, $\mathbf{U}_{(t)} = [u_1,\, u_2,\, u_3,\, u_4]^T = [v_{\alpha s},\, v_{\beta s},\, v_{xs},\, v_{ys}]^T$ is the input vector applied to the stator coils, the process noise is represented as $\varpi_{(t)}$, $\mathbf{H}$ is considered the noise weight matrix and $\mathbf{A}_{(t)}$ and $\mathbf{B}_{(t)}$ are matrices defined by the physical parameters of the ASIMD as follows:

$$\mathbf{A}_{(t)} = \begin{bmatrix} -R_s c_2 & c_4 L_m \omega_r & 0 & 0 & c_4 R_r & c_4 L_r \omega_r \\ c_4 L_m \omega_r & -R_s c_2 & 0 & 0 & c_4 L_r \omega_r & c_4 R_r \\ 0 & 0 & -R_s c_3 & 0 & 0 & 0 \\ 0 & 0 & 0 & -R_s c_3 & 0 & 0 \\ R_s c_4 & -c_5 L_m \omega_r & 0 & 0 & -c_5 R_r & -c_5 L_r \\ -c_5 L_m \omega_r & R_s c_4 & 0 & 0 & -c_5 L_r & -c_5 R_r \end{bmatrix}$$

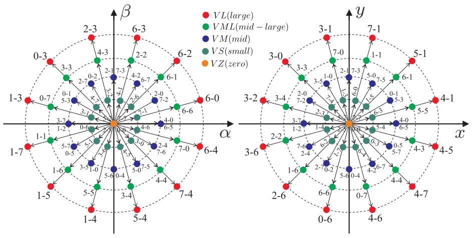

Fig. 2. Voltage space vectors and 64 switching states in $(\alpha-\beta)$ and $(x-y)$ planes for an ASIMD.

$$\mathbf{B}_{(t)} = \begin{bmatrix} c_2 & 0 & 0 & 0 \\ 0 & c_2 & 0 & 0 \\ 0 & 0 & c_3 & 0 \\ 0 & 0 & 0 & c_3 \\ -c_4 & 0 & 0 & 0 \\ 0 & -c_4 & 0 & 0 \end{bmatrix}$$

being R_s, R_r, L_m, $L_r = L_{lr} + L_m$ and $L_s = L_{ls} + L_m$ are the electrical parameters of the ASIMD. The coefficients are defined as $c_1 = L_s L_r - L_m^2$, $c_2 = \frac{L_r}{c_1}$, $c_3 = \frac{1}{L_{ls}}$, $c_4 = \frac{L_m}{c_1}$ and $c_5 = \frac{L_s}{c_1}$. Stator voltages depend on the input control signals $\mathbf{S}$, which is considered the switching state. The ideal VSI model has been considered to obtain a good optimization process. Stator voltages can be estimated from the ideal six-leg VSI model $\mathbf{M}_{[\mathbf{S}]}$ [15].

$$\mathbf{M}_{[\mathbf{S}]} = \frac{1}{3}\begin{bmatrix} 2 & 0 & -1 & 0 & -1 & 0 \\ 0 & 2 & 0 & -1 & 0 & -1 \\ -1 & 0 & 2 & 0 & -1 & 0 \\ 0 & -1 & 0 & 2 & 0 & -1 \\ -1 & 0 & -1 & 0 & 2 & 0 \\ 0 & -1 & 0 & -1 & 0 & 2 \end{bmatrix}\mathbf{S}^T. \tag{3}$$

where $\mathbf{S} = [S_a,\, S_b,\, S_c,\, S_d,\, S_e,\, S_f]$, where $\mathbf{S}_i \in \{0,1\}$. The ideal six-leg VSI converts the switching gating signals into stator voltages which are converted to $(\alpha-\beta)$ and $(x-y)$ planes and they are determined in $\mathbf{U}_{(t)}$, defined by:

$$\mathbf{U}_{(t)} = V_{dc}\,\mathbf{T}\,\mathbf{M}_{[\mathbf{S}]}. \tag{4}$$

where V_{dc} is the DC voltage source. The output vector, $\mathbf{Y}$, is:

$$\mathbf{Y}_{(t)} = \mathbf{C}\,\mathbf{X}_{(t)} + \nu_{(t)} \tag{5}$$

where $\nu_{(t)}$ is considered the measurement noise and

$$\mathbf{C} = \begin{bmatrix} 1 & 0 & 0 & 0 & 0 & 0 \\ 0 & 1 & 0 & 0 & 0 & 0 \\ 0 & 0 & 1 & 0 & 0 & 0 \\ 0 & 0 & 0 & 1 & 0 & 0 \end{bmatrix}.$$

The mechanical variables of the ASIMD are related by:

$$T_e = 3\,P\,(\psi_{\alpha s} i_{\beta s} - \psi_{\beta s} i_{\alpha s}) \tag{6}$$

$$J_i\,\dot{\omega}_m + B_i\,\omega_m = (T_e - T_L) \tag{7}$$

$$\omega_r = P\omega_m \tag{8}$$

where J_i is the inertia coefficient, B_i is considered the friction coefficient, T_e represents the electromagnetic torque, T_L is the load torque, ω_r is the rotor electrical angular speed, ω_m the rotor mechanical speed, $\psi_{\alpha s}$ and $\psi_{\beta s}$ are considered the stator fluxes and P the number of pole pairs.

III. CLASSIC PCC

The mathematical model of the ASIMD (2) and (5) must be in discrete form so it can be applied for the PCC. A forward-Euler method is considered to maintain a low computational cost for the controller. The equations will be in digital form with predicted variables only depending on past values of the variables and not on present values. Thus, a prediction of the next sample state $\hat{\mathbf{X}}_{[k+1|k]}$ is defined as:

$$\hat{\mathbf{X}}_{[k+1|k]} = \mathbf{X}_{[k]} + \mathrm{f}\left(\mathbf{X}_{[k]},\, \mathbf{U}_{[k]},\, T_s,\, \omega_{r[k]}\right) \tag{9}$$

being $[k]$ the current sample, f the function nomenclature and T_s is the sampling time.

A. Reduced Order Observers

In the state-space modeling (2), only the stator currents and mechanical rotor speed are measured. The stator voltages are easily estimated from the switching commands sent to the six-phase VSI. However, the rotor currents are rarely measured in real system and they have to be estimated. This issue can be solved by the estimation of the rotor currents through the concept of reduced order observers. The reduced order observers only estimate the value of the unmeasured parts of the state vector. This is an important topic which has been recently solved by the use of Luenberger Observer (LO) [23] and Kalman Filter (KF) [9], [24] techniques, where the KF is considered a better selection due to the fact that the observer gains are optimized taking into account the noise input to the sensors. In LO-based estimator, the gains are not so optimized and the setting is deterministic [9]. Therefore, KF is designed and implemented in this paper to improve the control performance of PCC, by increasing the accuracy of the predictions. By considering zero-mean Gaussian measurement noises and uncorrelated process, the equations of the system state-space mathematical model can be defined as:

$$\hat{\mathbf{X}}_{[k+1|k]} = \mathbf{A}_{[k]}\mathbf{X}_{[k]} + \mathbf{B}_{[k]}\mathbf{U}_{[k]} + \mathbf{H}\varpi_{[k]} \tag{10}$$

$$\mathbf{Y}_{[k+1|k]} = \mathbf{C}\,\mathbf{X}_{[k+1]} + \nu_{[k+1]} \tag{11}$$

where $\mathbf{A}_{[k]}$ and $\mathbf{B}_{[k]}$ are defined by (12)-(14). It can be noted that $\mathbf{A}_{[k]}$ is also dependable on the present value of $\omega_{r[k]}$ and consequently must be considered at every sampling period. A detailed explanation of the dynamics and error convergence of the KF can be found in [9], [24] and it was not included in this work for the sake of conciseness. The aforementioned matrices are defined as:

$$\mathbf{A}_{[k]} = \begin{bmatrix} A_{11} & A_{12} & 0 & 0 & A_{15} & A_{16} \\ A_{21} & A_{22} & 0 & 0 & A_{25} & A_{26} \\ 0 & 0 & A_{33} & 0 & 0 & 0 \\ 0 & 0 & 0 & A_{44} & 0 & 0 \\ A_{51} & A_{52} & 0 & 0 & A_{55} & A_{56} \\ A_{61} & A_{62} & 0 & 0 & A_{65} & A_{66} \end{bmatrix} \tag{12}$$

where $\mathbf{A}_{[k]}$ parameters are defined as follows:

$$\begin{aligned} &A_{11} = A_{22} = 1 - T_s c_2 R_s \\ &A_{12} = -A_{21} = T_s c_4 L_m \omega_{r[k]} \\ &A_{15} = A_{26} = T_s c_4 R_r \\ &A_{16} = -A_{25} = T_s c_4 L_r \omega_{r[k]} \\ &A_{33} = A_{44} = 1 - T_s c_3 R_s \\ &A_{51} = A_{62} = -T_s c_4 R_s \\ &A_{52} = -A_{61} = -T_s c_5 L_m \omega_{r[k]} \\ &A_{55} = A_{66} = 1 - T_s c_5 R_r \\ &A_{56} = -A_{65} = -c_5 \omega_{r[k]} T_s L_r \end{aligned} \tag{13}$$

$$\mathbf{B}_{[k]} = \begin{bmatrix} B_{11} & 0 & 0 & 0 & 0 & 0 \\ 0 & B_{22} & 0 & 0 & 0 & 0 \\ 0 & 0 & B_{33} & 0 & 0 & 0 \\ 0 & 0 & 0 & B_{44} & 0 & 0 \\ 0 & 0 & 0 & 0 & B_{55} & 0 \\ 0 & 0 & 0 & 0 & 0 & B_{66} \end{bmatrix} \tag{14}$$

being $\mathbf{B}_{[k]}$ parameters the following: $B_{11} = B_{22} = T_s c_2$, $B_{33} = B_{44} = T_s c_3$ and $B_{55} = B_{66} = -T_s c_4$

B. Cost Function

The cost function problem can allow the optimization of several important variables such as machine torque ripple minimization, VSI switching losses and harmonic content minimization [20]. However in current control, the most important figure of merit is the tracking error in the predicted stator currents in $(\alpha - \beta)$ and $(x - y)$ planes. PCC analyses the cost function for 49 iterations with the following:

$$\begin{aligned} J_{[k+2|k]} = \Bigg[&(i^*_{\alpha s[k+2]} - \hat{i}_{\alpha s[k+2|k]})^2 + (i^*_{\beta s[k+2]} - \hat{i}_{\beta s[k+2|k]})^2 \\ &+ \lambda_{xy} \left((i^*_{xs[k+2]} - \hat{i}_{xs[k+2|k]})^2 + (i^*_{ys[k+2]} - \hat{i}_{ys[k+2|k]})^2 \right) \Bigg]^{\frac{1}{2}} \end{aligned} \tag{15}$$

By using (16), a second-step ahead prediction of the stator currents $\hat{i}_{s[k+2|k]}$ is computed for delay compensation [25]. The desired reference trajectory of the stator currents is represented by $i^*_{s[k+2]}$. The weighting factor optimization is a hot research topic and some recent works tackled this issue [7], [26], [27]. Typically, for multiphase machines, λ_{xy} allows to prioritize the stator currents in $(\alpha - \beta)$ plane [9], [28].

$$\hat{\mathbf{X}}_{[k+2|k]} = \mathbf{A}_{[k]}\mathbf{X}_{[k+1]} + \mathbf{B}_{[k]}\mathbf{U}_{[k+1]} + \mathbf{H}\varpi_{[k]} \tag{16}$$

IV. M2PC

This technique consists in the determination of each available sector for the six-leg VSI in the $(\alpha - \beta)$ plane, being 48 sectors in total, which are composed of two adjacent active vectors and a null vector (VZ), as shown in Fig. 3. This technique, which is based on SVM, estimates the prediction of two active vectors that conform the 12 outside sectors at every sampling time and analyses their respective cost functions (J_0, J_1 and J_2) separately. Each prediction is evaluated based on (15) and the only difference is in the calculation of the input voltage vector $\mathbf{U}_{[k]}$ [15], [19]. The main goal of this modulation technique is to obtain any voltage vector in the $(\alpha - \beta)$ plane by using the large vectors (VL) and the VZ, covering the entire space vector, and at the same time, note that the outside vectors are the smallest voltage vectors in $(x - y)$ plane, managing a reduction of $(x - y)$ currents [19].

The duty cycles, for the two active vectors d_1 and d_2, are obtained by solving the following equations, related to their respective cost functions (24 for every sample time):

$$d_0 = \frac{\sigma}{J_0} \qquad d_1 = \frac{\sigma}{J_1} \qquad d_2 = \frac{\sigma}{J_2} \tag{17}$$

$$d_0 + d_1 + d_2 = 1 \tag{18}$$

where d_0 is the duty cycle of a null vector. Then, it is possible to calculate the expression for σ and the duty cycles for each vector given as:

$$J_T = J_1 J_2 + J_0 J_1 + J_0 J_2 \tag{19}$$

$$d_0 = \frac{J_1 J_2}{J_T} \tag{20}$$

$$d_1 = \frac{J_0 J_2}{J_T} \tag{21}$$

$$d_2 = \frac{J_0 J_1}{J_T} \tag{22}$$

Considering these expressions, the final cost function, which is calculated for 12 iterations during T_s, is considered as:

$$G_{[k+2|k]} = d_1 J_1 + d_2 J_2 \tag{23}$$

The two vectors, which reduce $G_{[k+2|k]}$, are selected and applied to the six-phase VSI at the next sampling time. After calculating the duty cycles for the two vectors to be applied, it is necessary to propose an equation relating the duty cycles and the selected voltage vectors, in order to implement a symmetric pulse width modulation (PWM):

$$\tau_i = \frac{d_0}{2} + d_1 v_{1(i)} + d_2 v_{2(i)} \tag{24}$$

where $i = [a, b, c, d, e, f]$ and τ_i is the duty cycle per phase. This variable is compared to a triangular waveform to obtain the respective symmetric PWM, accomplishing a fixed switching frequency fixing the sampling frequency.

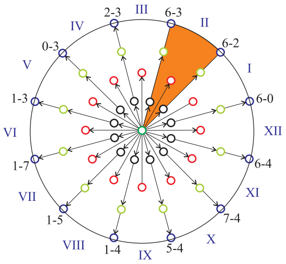

Fig. 3. Available sectors for the six-leg VSI.

V. N-M2PC

As well as M2PC, N-M2PC is also based on SVM. The main difference is that M2PC only uses 2 VL per sector and N-M2PC uses 4 which include 2 mid vectors (VM) and 2 VL. The main goal of this modulation is to improve further the steady-state error of the stator currents tracking in $(d - q)$ plane by including these adjacent VM per sector in order to avoid the application of VZ which limits the range. This is due to the fact that the desired optimal vector is within the corresponding sector and a certain combination of vector can represent that particular optimal vector. However, VZ reduces the range of the combination of vectors with its corresponding duty cycle, reducing the controller's capacity of tracking the desired stator current in $(\alpha - \beta)$ plane, due to the fact that the duty cycle of VZ increases when the $(x - y)$ currents are being reduced in M2PC. In summary, N-M2PC does not have the same limitation as M2PC, due to the fact that it does not apply VZ and the used vectors add any point in the upper area of the $(\alpha - \beta)$ plane.

The duty cycles, for the four active vectors d_1, d_2, d_3 and d_4, are obtained by solving the following equations:

$$d_1 = \frac{\sigma}{J_1} \quad d_2 = \frac{\sigma}{J_2} \quad d_3 = \frac{\sigma}{J_3} \quad d_4 = \frac{\sigma}{J_4} \tag{25}$$

$$d_1 + d_2 + d_3 + d_4 = 1 \tag{26}$$

where J_1, J_2, J_3 and J_4 are the corresponding cost function (15) for the vectors in the selected sector. As M2PC, it is possible to calculate the expression for σ and the duty cycles for each vector given as:

$$J_{T1} = J_1 J_3 J_4 + J_2 J_3 J_4 \tag{27}$$

$$J_{T2} = J_1 J_2 J_4 + J_1 J_2 J_3 \tag{28}$$

$$d_1 = \frac{J_2 J_3 J_4}{J_{T1} + J_{T2}} \tag{29}$$

$$d_2 = \frac{J_1 J_3 J_4}{J_{T1} + J_{T2}} \tag{30}$$

$$d_3 = \frac{J_1 J_2 J_4}{J_{T1} + J_{T2}} \tag{31}$$

$$d_4 = \frac{J_1 J_2 J_3}{J_{T1} + J_{T2}} \tag{32}$$

N-M2PC evaluates all the 12 sectors, as shown in Fig. 4, by calculating the corresponding cost function for each vector (48 in total), then the duty cycles of each vector is calculated as in M2PC, at last, the final cost function is computed as:

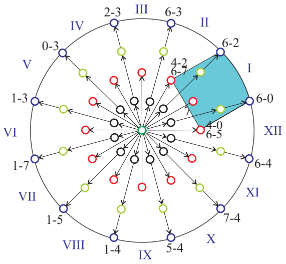

Fig. 4. Available sectors of N-M2PC for the six-leg VSI.

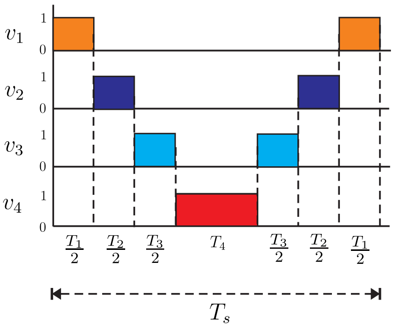

Fig. 5. Switching pattern for the selected optimal vectors.

$$G_{[k+2|k]} = d_1 J_1 + d_2 J_2 + d_3 J_3 + d_4 J_4 \tag{33}$$

It can be noticed that the VM used to obtain the 12 sectors are the redundant ones, giving the possibility to select each of those vectors in order to apply a certain switching pattern, as the one shown in Fig. 5. This allows the use of a simple equation to calculate the duty cycles $\tau_{(i)}$ for the switching devices of each leg of the VSI, as follows:

$$\tau_{(i)} = d_1 v_{1(i)} + d_2 v_{2(i)} + d_3 v_{3(i)} + d_4 v_{4(i)} \tag{34}$$

where $\tau_{(i)}$ is normalized between 0 and 1, for the switching devices for the six-phase legs VSI. At last, a triangular carrier waveform is used to apply the value of $\tau_{(i)}$ in the corresponding switching devices.

VI. EXPERIMENTAL RESULTS

The proposed N-M2PC technique is validated in order to compare its performance with M2PC and classic PCC through experimental results obtained in the test bench.

A. Test bench composition

The test bench is composed of an ASIMD connected to two conventional three-phase VSI, using a constant DC-bus voltage from a DC power supply. The six-phase VSI is controlled by a dSPACE MABXII DS1401 real-time rapid prototyping platform, with MATLAB/Simulink. The results are processed using MATLAB R2013b script. Table I shows the electrical and mechanical parameters of the ASIMD obtained using stand-still with VSI tests and conventional methods of AC time domain [29], [30]. The experimental measurements were obtained with current sensors LA 55-P s, with several turns to improve precision at low current measurement, which have a frequency bandwidth from DC up to 200 kHz. Those values are then converted to digital through 16-bit A/D converter. The ASIMD rotor angle is measured with a 1024 ppr incremental encoder and the mechanical speed is calculated from it. Finally, a 5 HP eddy current brake is used as a variable mechanical load on the ASIMD which is fixed at 1 A. A block diagram of the test bench is shown in Fig. 6. The defined cost function in (15) with λ_{xy} = 0.05 was selected to evaluate the performance of classic PCC, which its influence in the performance is minimal, and M2PC giving more priority to $(\alpha - \beta)$ stator currents tracking over the $(x - y)$ currents reduction. As for N-M2PC, λ_{xy} = 0.1 is selected, due to the fact that it does not use the null vector and the $(x - y)$ currents reduction is obtained through the active vectors combination. It is worth mentioning that these values of λ_{xy} are selected through heuristic method by focusing on obtaining a sub-optimal system. The process and measurement noise values can be

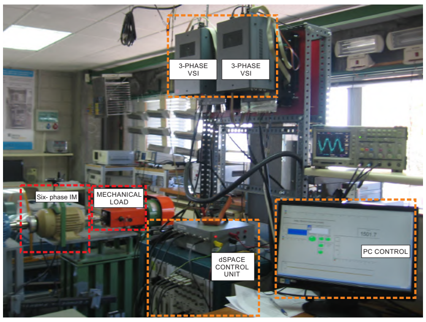

Fig. 6. Block diagram of the test bench including the ASIMD, the dSPACE platform, the eddy current brake and the six-phase VSI.

TABLE I
PARAMETERS OF THE ASIMD.

PARAMETER	VALUE	PARAMETER	VALUE
R_r (Ω)	6.9	R_s (Ω)	6.7
L_s (mH)	654.4	L_r (mH)	626.8
L_m (mH)	614	L_{ls} (mH)	5.3
ω_{m-nom} (rpm)	3 000	P_w (kW)	2
J_i (kg.m^2)	0.07	B_i (kg.m^2/s)	0.0004
P	1	V_{dc} (V)	400

calculated by using the autocovariance-least-squared (ALS) method since provides unbiased estimates with the lowest covariance, guaranteeing optimal KF tuning. By collecting data from a closed-loop operation of the system and then using the method proposed in [24]. The obtained values are $\hat{Q}_w = 0.0022$ and $\hat{R}_v = 0.0022$.

B. Figures of merit

The performance of the proposed N-M2PC is analyzed and compared to classic PCC and M2PC in transient and steady-state conditions. The experimental results analyze the controller performance in terms of MSE between the reference and measured stator currents in $(\alpha - \beta)$ and $(x - y)$ planes. At the same time, the mean value error of $(d - q)$ currents are analyzed to obtain the steady-state error in current tracking for the three techniques. At last, THD is calculated in $(\alpha - \beta)$ plane to complete the analysis. The MSE is defined as:

$$\mathrm{MSE}(i_{s\Phi}) = \sqrt{\frac{1}{N}\sum_{k=1}^{N}(i_{s\Phi}[k] - i^*_{s\Phi}[k])^2} \qquad (35)$$

where N is the number of analyzed samples, $i^*_{s\Phi}$ the stator current reference, $i_{s\Phi}$ the measured stator currents and $\Phi \in \{\alpha,\ \beta,\ x,\ y\}$. On the other hand, the mean value is calculated as:

$$\mathrm{Error}(\%)(i_{s\theta}) = |\frac{100}{N}\sum_{k=1}^{N} i_{s\theta}[k] - i^*_{s\theta}[k]| \qquad (36)$$

where $i^*_{s\theta}$ is $(d - q)$ stator currents reference and $i_{s\theta}$ the measured $(d - q)$ stator currents. At last, THD is defined as:

$$\mathrm{THD}(i_s) = \sqrt{\frac{1}{i_{s1}^2}\sum_{j=2}^{N}(i_{sj})^2} \qquad (37)$$

where i_{s1} is the fundamental stator currents and i_{sj} is the harmonic stator currents.

C. Steady state analysis

For all cases, $(x - y)$ current references are set to zero ($i^*_{xs} = i^*_{ys} = 0$). A fixed d current ($i^*_{ds} = 1$ A) has been used. The sampling frequencies used in the tests are 8 kHz and 16 kHz. Four steady-state operations are set for mechanical speed: 500 rpm, 1 000 rpm, 1 500 rpm and 2 000 rpm.

TABLE II
PERFORMANCE ANALYSIS OF STATOR CURRENTS, MSE (A), MEAN ERROR (%) FOR CLASSIC PCC AT DIFFERENT ROTOR SPEEDS (RPM).

		Sampling	frequency	8 kHz		
ω^*_m	MSE$_\alpha$	MSE$_\beta$	MSE$_x$	MSE$_y$	Error$_d$	Error$_q$
500	0.1437	0.1282	0.8228	0.8158	1.48	9.41
1000	0.1443	0.1372	0.9605	0.9570	0.54	7.02
1500	Uns	Uns	Uns	Uns	Uns	Uns
2000	Uns	Uns	Uns	Uns	Uns	Uns
		Sampling	frequency	16 kHz		
ω^*_m	MSE$_\alpha$	MSE$_\beta$	MSE$_x$	MSE$_y$	Error$_d$	Error$_q$
500	0.0831	0.0755	0.4676	0.4763	0.70	3.70
1000	0.0974	0.0858	0.5087	0.5072	0.24	3.79
1500	0.0812	0.0771	0.5185	0.5057	1.48	3.45
2000	Uns	Uns	Uns	Uns	Uns	Uns

TABLE III
PERFORMANCE ANALYSIS OF STATOR CURRENTS, MSE (A), MEAN ERROR (%) FOR PCC-VV AT DIFFERENT ROTOR SPEEDS (RPM).

		Sampling	frequency	8 kHz		
ω^*_m	MSE$_\alpha$	MSE$_\beta$	MSE$_x$	MSE$_y$	Error$_d$	Error$_q$
500	0.1623	0.1620	0.0856	0.0784	0.94	6.23
1000	0.1682	0.1691	0.0905	0.0904	1.02	6.52
1500	Uns	Uns	Uns	Uns	Uns	Uns
2000	Uns	Uns	Uns	Uns	Uns	Uns
		Sampling	frequency	16 kHz		
ω^*_m	MSE$_\alpha$	MSE$_\beta$	MSE$_x$	MSE$_y$	Error$_d$	Error$_q$
500	0.1256	0.1182	0.0640	0.0600	0.86	4.11
1000	0.1299	0.1231	0.0810	0.0638	0.89	4.46
1500	0.1445	0.1231	0.0760	0.0714	6.26	5.89
2000	0.1455	0.1309	0.0860	0.0838	6.50	8.95

TABLE IV
PERFORMANCE ANALYSIS OF STATOR CURRENTS, MSE (A), MEAN ERROR (%) FOR M2PC AT DIFFERENT ROTOR SPEEDS (RPM).

		Sampling	frequency	8 kHz		
ω^*_m	MSE$_\alpha$	MSE$_\beta$	MSE$_x$	MSE$_y$	Error$_d$	Error$_q$
500	0.0562	0.0592	0.1241	0.1130	1.34	2.69
1000	0.0861	0.0903	0.1485	0.1545	1.9	7.03
1500	0.1039	0.0958	0.1960	0.1944	2.2	7.33
2000	Uns	Uns	Uns	Uns	Uns	Uns
		Sampling	frequency	16 kHz		
ω^*_m	MSE$_\alpha$	MSE$_\beta$	MSE$_x$	MSE$_y$	Error$_d$	Error$_q$
500	0.1046	0.1094	0.1332	0.1334	0.51	3.04
1000	0.1037	0.1059	0.1401	0.1417	0.14	4.59
1500	0.0972	0.0986	0.1038	0.1069	0.4	5.93
2000	0.0976	0.0989	0.1150	0.1182	0.26	9.04

Table II shows the experimental results obtained for different mechanical speeds and sampling frequencies for classic PCC, regarding the MSE of stator currents in $(\alpha - \beta)$ and $(x - y)$ planes and Mean Error (%) in $(d - q)$ planes. The results show good performance of classic PCC in terms of $(\alpha - \beta)$ current tracking and steady-state error for $(d - q)$ currents at a higher sampling frequency compared to lower sampling frequency. However, the $(x - y)$ reduction is insufficient,

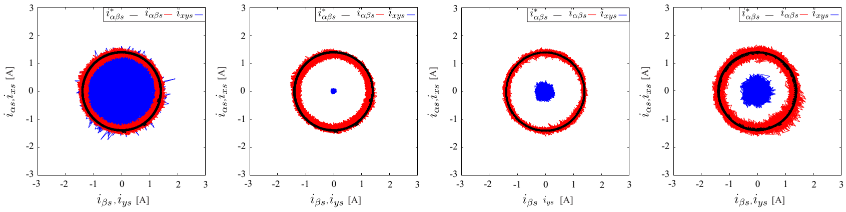

(a) (b) (c) (d)

Fig. 7. Stator currents in $(\alpha-\beta)$ and $(x-y)$ planes at 500 rpm for: (a)classic PCC; (b)PCC-VV; (c)M2PC; (d)N-M2PC.

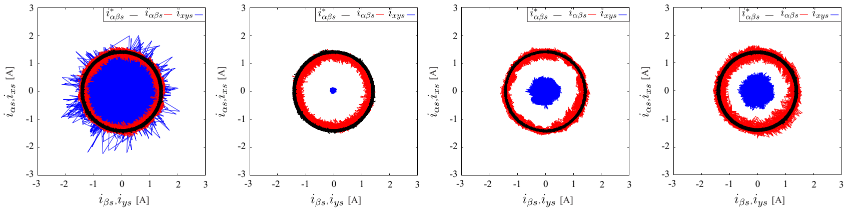

(a) (b) (c) (d)

Fig. 8. Stator currents in $(\alpha-\beta)$ and $(x-y)$ planes at 1500 rpm for: (a)classic PCC; (b)PCC-VV; (c)M2PC; (d)N-M2PC.

TABLE V
PERFORMANCE ANALYSIS OF STATOR CURRENTS, MSE (A), MEAN ERROR (%) FOR N-M2PC AT DIFFERENT ROTOR SPEEDS (RPM).

		Sampling	frequency	8 kHz		
ω_m^*	MSE$_\alpha$	MSE$_\beta$	MSE$_x$	MSE$_y$	Error$_d$	Error$_q$
500	0.1977	0.1998	0.2490	0.2553	1.8	2.6
1000	0.2135	0.2159	0.2659	0.2684	3.3	6.9
1500	0.1983	0.1924	0.3012	0.2956	2.25	13.8
2000	0.2033	0.2062	0.3020	0.3020	5.32	18.2
		Sampling	frequency	16 kHz		
ω_m^*	MSE$_\alpha$	MSE$_\beta$	MSE$_x$	MSE$_y$	Error$_d$	Error$_q$
500	0.1004	0.1003	0.2009	0.2130	0.81	2.52
1000	0.1051	0.1049	0.2091	0.2064	1.04	4.84
1500	0.1030	0.1097	0.2172	0.2125	1.97	5.72
2000	0.1084	0.1081	0.2325	0.2287	1.99	8.71

TABLE VI
PERFORMANCE ANALYSIS OF STATOR CURRENTS, THD (%) FOR CLASSIC PCC, PCC-VV, M2PC AND N-M2PC AT DIFFERENT SPEEDS (RPM).

Sampling frequency of 8 kHz				
	PCC	PCC-VV	M2PC	N-M2PC
ω_m^*	THD$_{\alpha\beta}$	THD$_{\alpha\beta}$	THD$_{\alpha\beta}$	THD$_{\alpha\beta}$
500	12.84	13.78	5.39	15.78
1000	14.27	14.85	7.38	14.42
1500	Uns	Uns	8.16	17.98
2000	Uns	Uns	Uns	17.65
Sampling frequency of 16 kHz				
	PCC	PCC-VV	M2PC	N-M2PC
ω_m^*	THD$_{\alpha\beta}$	THD$_{\alpha\beta}$	THD$_{\alpha\beta}$	THD$_{\alpha\beta}$
500	7.55	12.57	10.61	9.95
1000	8.41	12.49	10.17	9.73
1500	7.27	12.70	8.10	9.78
2000	Uns	13.23	7.65	9.54

and the performance is worse at higher mechanical speed to the point of becoming unstable (Uns) at low sampling frequency, where the error system is tending towards infinity due to the fact that parameters such as sampling time, rotor speed, electrical parameters have a direct impact on the poles placement of the ASIMD [31].

Table III presents the performance of PCC-VV which improves the reduction of $(x-y)$ currents compared to classic PCC. On the other hand, Table IV shows the results of M2PC which show a far better performance at lower sampling frequency and lower mechanical speed in all the figures of merit, compared to classic PCC. However, the performance also worsens at higher sampling frequency and mechanical speed, specially in steady-state error for $(d-q)$ currents. Table V exposes the N-M2PC performance in terms of the current tracking and steady-state error in $(d-q)$ currents. It can be seen that N-M2PC improves the steady-state error in $(d-q)$ currents and $(x-y)$ currents reduction compared to classic PCC, but M2PC is better in every aspect, except at high mechanical speeds where N-M2PC is the only stable controller. At higher sampling frequency, N-M2PC is better in every figure of merit in comparison lower sampling frequency and is comparable to M2PC in every figure of merit.

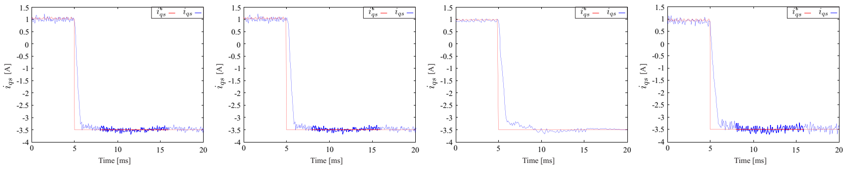

(a) (b) (c) (d)

Fig. 9. Transient response of stator current (q) from a step response of 1 A to -3.5 A for different techniques: (a)classic PCC; (b)PCC-VV; (c)M2PC; (d)N-M2PC.

TABLE VII
IMPROVEMENT ANALYSIS (%) OF M2PC AND N-M2PC OVER CLASSIC PCC AT DIFFERENT SPEEDS (RPM).

ω_m^*	MSE$_{\alpha\beta}$	MSE$_{xy}$	Error$_d$	Error$_q$	THD$_{\alpha\beta}$
	Sampling	frequency	8 kHz	(M2PC)	
500	57.36	85.53	9.46	71.41	57.73
1000	37.26	84.20	-251.85	-0.14	46.86
1500	100	100	100	100	100
2000	–	–	–	–	–
	Sampling	frequency	8 kHz	(N-M2PC)	
500	-46.71	69.22	-21.62	72.37	-23.38
1000	-52.66	72.14	-511.11	1.71	-1.12
1500	100	100	100	100	100
2000	100	100	100	100	100
	Sampling	frequency	16 kHz	(M2PC)	
500	-35.39	71.75	27.14	17.84	-41.25
1000	-14.95	72.94	41.67	-21.11	-21.76
1500	-23.80	79.42	72.97	-71.88	-11.74
2000	100	100	100	100	100
	Sampling	frequency	16 kHz	(N-M2PC)	
500	-26.83	56.16	-15.71	31.89	-32.59
1000	-15.08	59.10	-333.33	-27.70	-16.50
1500	-34.57	58.04	-33.11	-65.80	-35.21
2000	100	100	100	100	100

Table VI shows the THD in $(\alpha - \beta)$ stator currents for Classic PCC, M2PC and N-M2PC for different mechanical speeds. The results present a reduction on the THD stator currents with higher sampling frequency and higher mechanical speed for classic PCC. For M2PC, the currents THD are better at lower mechanical speed at low sampling frequency, M2PC changes its tendency at high sampling frequency. As for N-M2PC, the THD improves at high sampling frequency and is consistent for every operation.

Fig. 7 and Fig. 8 present the stator currents performance with a polar representation in $(\alpha - \beta)$ and $(x - y)$ planes for classic PCC, PCC-VV, M2PC and N-M2PC. The operations were tested with the same eddy current (mechanical load), thus the value of $(\alpha - \beta)$ amplitude is proportional to the mechanical speed. The figures show that $(x - y)$ currents are lower for N-M2PC and especially for M2PC and PCC-VV compared to classic PCC. At last, Table VII presents the performance of M2PC and N-M2PC compared to classic PCC in terms of %, where positive $(+)$ and negative $(-)$ values mean improvement and deterioration respectively.

D. Transient analysis

For a transient condition, a step modification in mechanical speed is considered from 500 to -500 rpm (reversal operation). Fig. 9 exposes a dynamic test (performance of q axis current), which consists of the transient behavior of classic PCC, PCC-VV, M2PC and N-M2PC for a step response in the q axis current (i_{qs}^*). The dynamic response is generated through a reversal operation of the mechanical speed (ω_m) from 500 to -500 rpm. Fig. 9(a) and Fig. 9(b) show a transient test for classic PCC and PCC-VV where the time to reach the new reference is approximately 1 ms. Fig. 9(c) and Fig. 9(d) show the dynamic response of M2PC and N-M2PC, which they present a reaching time of 4 and 3 ms respectively.

E. Robustness analysis

The robustness analysis consists in the performance comparison of the controller at a nominal L_m value and with a variation of 25% of its nominal value, being L_m the most sensitive parameter in induction machines [32], [33]. This is analyzed by taking in consideration the effect of magnetic saturation of the ASIMD, where L_m value typically changes in approximately that ratio. Table VIII presents the control performance with a L_m change of 25% of the nominal value to analyze the control robustness to uncertainties. The results show that at low speed, the control performance presents a good tracking of stator currents with a variation of approximately 12% and 11%, compared to the unmodified L_m value, for 500 and 1000 rpm respectively, showing an low sensibility in these operation points. On the other hand, at higher speed, the control performance also shows a good current tracking with a variation of approximately 14% and 8%, showing a good robustness at 1500 and 2000 rpm. However, the steady state error in $(d - q)$ currents is severely affected in all the mechanical speeds at 8 kHz, being approximately 5 and 2 times higher, but minimal change in steady state error is obtained, at 16 kHz, of approximately 16%, presenting a good performance at that sampling frequency.

F. Comparative analysis

A comparative analysis regarding computational cost for classic PCC, M2PC and N-M2PC. It is considered the number of floating point operations (FPOs) per technique and then

TABLE VIII
Performance Analysis of Stator Currents for N-M2PC under 25% of variation of the nominal L_m.

		Sampling	frequency	8 kHz		
ω_m^*	MSE$_\alpha$	MSE$_\beta$	MSE$_x$	MSE$_y$	Error$_d$	Error$_q$
500	0.2175	0.2270	0.2706	0.2721	1.48	11.07
1000	0.2332	0.2389	0.3061	0.3009	6.43	13.82
1500	0.2006	0.2027	0.3019	0.3000	1.87	16.2
2000	0.2094	0.2065	0.3120	0.3096	4.70	19.66
		Sampling	frequency	16 kHz		
ω_m^*	MSE$_\alpha$	MSE$_\beta$	MSE$_x$	MSE$_y$	Error$_d$	Error$_q$
500	0.1145	0.1057	0.2056	0.2130	0.21	3.23
1000	0.1168	0.1157	0.2027	0.2014	0.21	5.30
1500	0.1199	0.1195	0.2042	0.2118	0.95	6.77
2000	0.1219	0.1181	0.2125	0.2200	2.26	8.09

TABLE IX
Comparative analysis of computational cost of classic PCC, PCC-VV, M2PC and N-M2PC in terms of FPOs.

	PCC	PCC-VV	M2PC	N-M2PC
FPOs	2352	1452	1968	2736

summarized on Table IX. For classic PCC, it is considered 49 iterations to perform correctly, and every iteration has 48 FPOs related to the prediction estimation, the cost function reduction and the second step prediction process. For PCC-VV, it is considered 13 iterations with 121 FPOs and for M2PC and N-M2PC, it is considered 12 iterations with 164 and 228 FPOs respectively.

At last, Table X shows a comparative analysis of the average switching frequency for classic PCC, PCC-VV, M2PC and N-M2PC at different rotor speeds, where the results show a lower switching frequency for lower sampling frequency and higher speeds, due to the fact that the larger voltage vectors are more used in those operation points. As presented in [34], M2PC is a fixed switching frequency technique which maintains the amount of the sampling frequency, due to the fact that it uses null vector, generating less harmonic content, but limiting the sampling range according to the transistor type. As for N-M2PC, the switching frequency is lower, due to the fact it only uses the large and mid vectors, diminishing the semiconductor stress and losses.

TABLE X
Comparative analysis of average switching frequency (kHz) of classic PCC, PCC-VV, M2PC and N-M2PC at different speeds (rpm) and sampling frequencies (kHz).

ω_m^*	PCC	PCC-VV	M2PC	N-M2PC
Sampling frequency of 8 kHz				
500	2.8	3.7	8	1.35
1000	2.7	3.5	8	1.32
1500	–	3.2	8	1.3
2000	–	–	–	1.28
Sampling frequency of 16 kHz				
500	5.3	6.9	16	2.63
1000	5.15	6.5	16	2.6
1500	4.75	6.2	16	2.5
2000	–	5.8	16	2.37

VII. Conclusion

This paper proposed a novel modulated MPC technique applied to an ASIMD. This technique has been designed to improve the steady-state error in the $(d-q)$ stator currents and effectively reducing the $(x-y)$ sub-space using VL and VM of the $(\alpha-\beta)$ sub-space. The experimental results showed the performance of the proposed technique compared to another modulated technique presented as M2PC, PCC-VV and to classic PCC, where the tests have been done under different operation points (steady and transient conditions) including low and high mechanical speeds, sampling frequencies and tuning parameters for $(x-y)$ stator currents, respectively. As shown in the results, M2PC and PCC-VV are excellent alternatives to classic PCC for low mechanical speeds, specially M2PC which performs excellent in the $(\alpha-\beta)$ sub-space, where all the figures of merit prove a better performance than classic PCC and N-M2PC. However, there is a limitation in terms of high mechanical speeds and higher sampling frequencies, where M2PC worsens its performance, due to the fact that it fixes the switching frequency from the sampling frequency, aggravating the switching losses. On the other hand, N-M2PC is proven to be a great alternative to classic PCC, PCC-VV and M2PC in high mechanical speeds, specially at higher sampling frequencies, where the performance in terms of steady-state error and $(x-y)$ currents minimization are good proving that at lower sampling frequency, it can still perform with stability, unlike classic PCC and M2PC. In transient condition, the results demonstrated a good transient current behavior in terms of response time, where classic PCC is the fastest, followed by N-M2PC. In summary, M2PC presents an excellent performance to be a good alternative in low mechanical speeds up to 1500 rpm (25 Hz, 1 pole pair) and N-M2PC is proven to be a great alternative for high speeds, above 1500 rpm, for industrial applications.

References

[1] E. Levi, "Advances in converter control and innovative exploitation of additional degrees of freedom for multiphase machines," *IEEE Trans. Ind. Electron.*, vol. 63, DOI 10.1109/TIE.2015.2434999, no. 1, pp. 433–448, 2016.

[2] I. Subotic, N. Bodo, E. Levi, B. Dumnic, D. Milicevic, and V. Katic, "Overview of fast on-board integrated battery chargers for electric vehicles based on multiphase machines and power electronics," *Elect. Power Appl.*, vol. 10, DOI 10.1049/iet-epa.2015.0292, no. 3, pp. 217–229, 2016.

[3] E. Levi, R. Bojoi, F. Profumo, H. Toliyat, and S. Williamson, "Multiphase induction motor drives–a technology status review," *Elect. Power Appl.*, vol. 1, DOI 10.1049/iet-epa:20060342, no. 4, pp. 489–516, 2007.

[4] A. G. Yepes, A. Vidal, J. Malvar, O. López, and J. Doval-Gandoy, "Tuning method aimed at optimized settling time and overshoot for synchronous proportional-integral current control in electric machines," *IEEE Trans. Power Electron.*, vol. 29, DOI 10.1109/TPEL.2013.2276059, no. 6, pp. 3041–3054, 2014.

[5] F. Barrero, J. Prieto, E. Levi, R. Gregor, S. Toral, M. J. Durán, and M. Jones, “An enhanced predictive current control method for asymmetrical six-phase motor drives,” *IEEE Trans. Ind. Electron.*, vol. 58, DOI 10.1109/TIE.2010.2089943, no. 8, pp. 3242–3252, 2010.

[6] F. Barrero, M. R. Arahal, R. Gregor, S. Toral, and M. J. Durán, “A proof of concept study of predictive current control for VSI-driven asymmetrical dual three-phase AC machines,” *IEEE Trans. Ind. Electron.*, vol. 56, DOI 10.1109/TIE.2008.2011604, no. 6, pp. 1937–1954, 2009.

[7] C. S. Lim, E. Levi, M. Jones, N. A. Rahim, and W. P. Hew, “FCS-MPC-based current control of a five-phase induction motor and its comparison with PI-PWM control,” *IEEE Trans. Ind. Electron.*, vol. 61, DOI 10.1109/TIE.2013.2248334, no. 1, pp. 149–163, 2013.

[8] E. Fuentes, C. A. Silva, and R. M. Kennel, “MPC implementation of a quasi-time-optimal speed control for a PMSM drive, with inner modulated-fs-mpc torque control,” *IEEE Trans. Ind. Electron.*, vol. 63, DOI 10.1109/TIE.2016.2519326, no. 6, pp. 3897–3905, 2016.

[9] J. Rodas, F. Barrero, M. R. Arahal, C. Martín, and R. Gregor, “Online estimation of rotor variables in predictive current controllers: a case study using five-phase induction machines,” *IEEE Trans. Ind. Electron.*, vol. 63, DOI 10.1109/TIE.2016.2559420, no. 9, pp. 5348–5356, 2016.

[10] I. Gonzalez-Prieto, M. J. Duran, J. J. Aciego, C. Martin, and F. Barrero, “Model predictive control of six-phase induction motor drives using virtual voltage vectors,” *IEEE Trans. Ind. Electron.*, vol. 65, DOI 10.1109/TIE.2017.2714126, no. 1, pp. 27–37, 2018.

[11] I. Gonzalez-Prieto, M. J. Duran, J. J. Aciego, C. Martin, and F. Barrero, “Model predictive control of six-phase induction motor drives using virtual voltage vectors,” *IEEE Trans. Ind. Electron.*, vol. 65, DOI 10.1109/TIE.2017.2714126, no. 1, pp. 27–37, 2017.

[12] J. J. Aciego, I. G. Prieto, and M. J. Duran, “Model predictive control of six-phase induction motor drives using two virtual voltage vectors,” *IEEE Journal of Emerging and Selected Topics in Power Electronics*, vol. 7, DOI 10.1109/JESTPE.2018.2883359, no. 1, pp. 321–330, 2018.

[13] I. González-Prieto, M. Durán, M. Bermúdez, F. Barrero, and C. Martín, “Assessment of Virtual-Voltage-based Model Predictive Controllers in Six-phase Drives under Open-Phase Faults,” *IEEE Journal of Emerging and Selected Topics in Power Electronics*, DOI 10.1109/JESTPE.2019.2915666, 2019.

[14] S. Toledo, M. Rivera, J. Muñoz, R. Peña, J. Riveros, and R. Gregor, “Fixed switching frequency predictive control for a multi-drive indirect matrix converter system,” in *Proc. SPEC*, DOI 10.1109/SPEC.2017.8333672, 2017, pp. 1–6.

[15] M. Ayala, J. Rodas, R. Gregor, J. Doval-Gandoy, O. Gonzalez, M. Saad, and M. Rivera, “Comparative study of predictive control strategies at fixed switching frequency for an asymmetrical six-phase induction motor drive,” in *Proc. IEMDC*, DOI 10.1109/IEMDC.2017.8002121, 2017, pp. 1–8.

[16] F. Gavilan, D. Caballero, S. Toledo, E. Maqueda, R. Gregor, J. Rodas, M. Rivera, and I. Araujo-Vargas, “Predictive power control strategy for a grid-connected 2l-vsi with fixed switching frequency,” in *Proc. ROPEC*, DOI 10.1109/ROPEC.2016.7830631, 2016, pp. 1–6.

[17] L. Comparatore, R. Gregor, J. Rodas, J. Pacher, A. Renault, and M. Rivera, “Model based predictive current control for a three-phase cascade H-bridge multilevel statcom operating at fixed switching frequency,” in *Proc. PEDG*, DOI 10.1109/PEDG.2017.7972540, 2017, pp. 1–6.

[18] M. Rivera, S. Toledo, C. Baier, L. Tarisciotti, P. Wheeler, and S. Verne, “Indirect predictive control techniques for a matrix converter operating at fixed switching frequency,” in *Proc. PRECEDE*, DOI 10.1109/PRECEDE.2017.8071101, 2017, pp. 13–18.

[19] O. Gonzalez, M. Ayala, J. Rodas, R. Gregor, G. Rivas, and J. Doval-Gandoy, “Variable-speed control of a six-phase induction machine using predictive-fixed switching frequency current control techniques,” in *Proc. PEDG*, DOI 10.1109/PEDG.2018.8447837, 2018, pp. 1–6.

[20] J. Rodriguez, M. P. Kazmierkowski, J. R. Espinoza, P. Zanchetta, H. Abu-Rub, H. A. Young, and C. A. Rojas, “State of the art of finite control set model predictive control in power electronics,” *IEEE Trans. Ind. Inform.*, vol. 9, DOI 10.1109/TII.2012.2221469, no. 2, pp. 1003–1016, 2013.

[21] S. Vazquez, J. Rodriguez, M. Rivera, L. G. Franquelo, and M. Norambuena, “Model predictive control for power converters and drives: Advances and trends,” *IEEE Trans. Ind. Electron.*, vol. 64, DOI 10.1109/TIE.2016.2625238, no. 2, pp. 935–947, 2017.

[22] Y. Zhao and T. Lipo, “Space vector PWM control of dual three-phase induction machine using vector space decomposition,” *IEEE Trans. Ind. Electron.*, vol. 31, DOI 10.1109/28.464525, no. 5, pp. 1100–1109, 1995.

[23] C. Martín, M. R. Arahal, F. Barrero, and M. J. Durán, “Multiphase rotor current observers for current predictive control: A five-phase case study,” *Control Eng. Prac.*, vol. 49, DOI 10.1016/j.conengprac.2016.01.011, pp. 101–111, 2016.

[24] J. Rodas, C. Martin, M. R. Arahal, F. Barrero, and R. Gregor, “Influence of covariance-based ALS methods in the performance of predictive controllers with rotor current estimation,” *IEEE Trans. Ind. Electron.*, vol. 64, DOI 10.1109/TIE.2016.2636205, no. 4, pp. 2602–2607, 2017.

[25] J. Rodriguez and P. Cortes, *Predictive control of power converters and electrical drives*. John Wiley & Sons, 2012, DOI 10.1002/9781119941446, vol. 40.

[26] M. Novak, T. Dragicevic, and F. Blaabjerg, “Weighting factor design based on Artificial Neural Network for Finite Set MPC operated 3L-NPC converter,” in *Proc. APEC)*, DOI 10.1109/APEC.2019.8722062. IEEE, 2019, pp. 77–82.

[27] B. Majmunović, T. Dragičević, and F. Blaabjerg, “Multi Objective Modulated Model Predictive Control of Stand-Alone Voltage Source Converters,” *IEEE Journal of Emerging and Selected Topics in Power Electronics*, DOI 10.1109/JESTPE.2019.2925603, 2019.

[28] C. Martin, M. Arahal, F. Barrero, and M. Duran, “Five-phase induction motor rotor current observer for finite control set model predictive control of stator current,” *IEEE Trans. Ind. Electron.*, vol. 63, DOI 10.1109/TIE.2016.2536578, no. 7, pp. 4527–4538, 2016.

[29] A. G. Yepes, J. A. Riveros, J. Doval-Gandoy, F. Barrero, O. López, B. Bogado, M. Jones, and E. Levi, “Parameter identification of multiphase induction machines with distributed windings Part 1: Sinusoidal excitation methods,” *IEEE Trans. Energy Conv.*, vol. 27, DOI 10.1109/TEC.2012.2220967, no. 4, pp. 1056–1066, 2012.

[30] J. A. Riveros, A. G. Yepes, F. Barrero, J. Doval-Gandoy, B. Bogado, O. Lopez, M. Jones, and E. Levi, “Parameter identification of multiphase induction machines with distributed windings Part 2: Time-domain techniques,” *IEEE Trans. Energy Conv.*, vol. 27, DOI 10.1109/TEC.2012.2219862, no. 4, pp. 1067–1077, 2012.

[31] M. Ayala, J. Doval-Gandoy, J. Rodas, O. Gonzalez, and R. Gregor, “Current control designed with model based predictive control for six-phase motor drives,” *ISA transactions*, DOI 10.1016/j.isatra.2019.08.052, 2019.

[32] B. Bogado, F. Barrero, M. Arahal, S. Toral, and E. Levi, “Sensitivity to electrical parameter variations of predictive current control in multiphase drives,” in *Proc. IECON*, DOI 10.1109/IECON.2013.6699982. IEEE, 2013, pp. 5215–5220.

[33] F. Wang, Z. Zhang, X. Mei, J. Rodríguez, and R. Kennel, “Advanced control strategies of induction machine: Field oriented control, direct torque control and model predictive control,” *Energies*, vol. 11, DOI 10.3390/en11010120, no. 1, p. 120, 2018.

[34] O. Gonzalez, M. Ayala, J. Doval-Gandoy, J. Rodas, R. Gregor, and M. Rivera, “Predictive-Fixed Switching Current Control Strategy Applied to Six-Phase Induction Machine,” *Energies*, vol. 12, DOI 10.3390/en12122294, no. 12, p. 2294, 2019.

ARTÍCULO 5

STABILITY ANALYSIS OF MODULATED MODEL PREDICTIVE CONTROLLERS APPLIED TO SIX-PHASE INDUCTION MOTOR DRIVES

- **Magno Ayala**, Jesus Doval-Gandoy, Osvaldo González, Jorge Rodas, Raul Gregor and Marco Rivera, ”Stability Analysis of Modulated Model Predictive Controllers Applied to Six-Phase Induction Motor Drives”, IEEE Transactions on Industrial Electronics, pp. 1-10, 2020. (R1)

Stability Analysis of Modulated Model Predictive Controllers Applied to Six-Phase Induction Motor Drives

***Abstract*—Model-based predictive control techniques, with finite set control, are considered an interesting option to control multiphase drives due to their control flexibility and fast dynamic response. However, a practical stability analysis of those techniques is still missing. This paper presents a practical stability analysis to traditional and modulated predictive current controllers applied to an asymmetrical six-phase induction machine. Experimental results are presented to verify the results of the theoretical analysis in terms of stability ranges regarding sampling frequency and rotor speed.**

***Index Terms*—Model-based predictive control, multiphase induction machine, practical stability, space vector modulation.**

I. INTRODUCTION

MULTIPHASE machines have received great attention due to their good features in comparison to three phase machines such as lower torque ripple, lower current per phase, availability and fault tolerant capabilities [1]. In the last few years, they were extensively applied especially in high-power applications such as renewable energies and electric vehicles [1], [2]. The majority of the control approaches applied to multiphase drives are commonly an extension of the control techniques applied to three-phase drives such as field oriented control (FOC) based on proportional-integral (PI) current control, direct torque control, among others [3]–[6].

Lately, some new nonlinear control methods were developed to apply to multiphase machines such as sliding mode control [7], [8] and finite control set model predictive control (FCS-MPC), which behaves with a fast transient response in comparison to linear controllers, addressed in [9]–[11]. FCS-MPC has already some variants published in the literature [12]–[17]. An example of these variants are the modulated model predictive control (M2PC) [18]–[21] and a novel variation named N-M2PC [22]. MPC will be used instead of FCS-MPC in the rest of the document to make the notation more clear. MPC and their newest variants were presented in [23].

On the other hand, MPC stability analysis applied to different systems were approached in previous works [24], such as Buck converters and three phase inverters [25] and synchronous machines [26]. The main common property is a defined cost function to optimize the behaviour in the future of the system. Hence, one of the most popular methods to prove the stability of MPC is the consideration of the optimized cost function as a candidate-Lyapunov function [27]–[29]. However, this method presents many complications as to find a candidate-Lyapunov function requires a heavy mathematical proof. Therefore, a practical stability analysis of traditional MPC and their variants applied to multiphase machines, has not been presented.

This paper presents a practical stability analysis for traditional MPC, M2PC and N-M2PC applied to an asymmetrical six-phase induction motor (SPIM) in terms of stability ranges regarding sampling frequency and rotor speed. Experimental results are presented to verify the results of the theoretical analysis. The rest of this paper is organized as follows: the SPIM mathematical model is shown in Section II. In Section III, the traditional MPC design is presented as a predictive current control (PCC), where it describes the traditional MPC and two variants named M2PC and N-M2PC. Section IV describes the theoretical stability analysis. Section VI present the experimental results of the system performance verifying the theoretical analysis in terms of stability ranges regarding sampling frequency and rotor speed. Finally, conclusions are summarized in the last section.

II. SPIM MATHEMATICAL MODEL

The studied system is made of a SPIM fed by a six-phase voltage source inverter (VSI) which is energized by a DC voltage source (V_{dc}). The electrical scheme of the six-phase VSI, based on isolated gate bipolar transistors (IGBT), is illustrated in Fig. 1. The SPIM is considered as a continuous model which can be represented by differential equations. The six-dimensional space of the SPIM, which is defined by its six-phases (a, b, c, d, e, f), and the vector space decomposition (VSD) technique are considered so the model can be represented into three different two-dimensional orthogonal planes in stationary reference planes, ($\alpha - \beta$), ($x - y$) and ($z_1 - z_2$), by using (1), where the invariant amplitude criteria has been considered [19]. The SPIM is asymmetrical, so it has a phase shift of 30° between the three phases and has an isolated neutral configuration, thus ($z_1 - z_2$) currents are considered null.

$$\mathbf{T} = \frac{1}{3}\begin{array}{c} \begin{array}{cccccc} a & d & b & e & c & f \end{array} \\ \left[\begin{array}{cccccc} 1 & \frac{\sqrt{3}}{2} & -\frac{1}{2} & -\frac{\sqrt{3}}{2} & -\frac{1}{2} & 0 \\ 0 & \frac{1}{2} & \frac{\sqrt{3}}{2} & \frac{1}{2} & -\frac{\sqrt{3}}{2} & -1 \\ 1 & -\frac{\sqrt{3}}{2} & -\frac{1}{2} & \frac{\sqrt{3}}{2} & -\frac{1}{2} & 0 \\ 0 & \frac{1}{2} & -\frac{\sqrt{3}}{2} & \frac{1}{2} & \frac{\sqrt{3}}{2} & -1 \\ 1 & 0 & 1 & 0 & 1 & 0 \\ 0 & 1 & 0 & 1 & 0 & 1 \end{array}\right] \end{array} \begin{array}{c} \alpha \\ \beta \\ x \\ y \\ z_1 \\ z_2 \end{array} \tag{1}$$

The six-leg VSI has a digital output which depends on the different $2^6 = 64$ switching possible states defined by the six-legs. The switching states and V_{dc} determine the phase

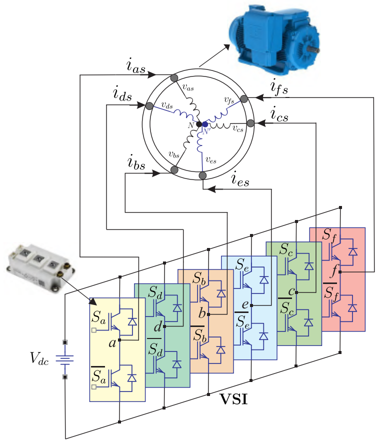

Fig. 1. Electrical scheme of a SPIM fed by a six-phase VSI.

voltages, which can be drawn into $(\alpha - \beta)$ and $(x - y)$ planes according to the VSD approach [30]. Fig. 2 shows the 64 possibilities with only 49 different vectors (48 vectors + 1 null vector) in the $(\alpha-\beta)$ and $(x-y)$ planes. The state-space mathematical model of the SPIM is modeled by:

$$\dot{\mathbf{X}}_{(t)} = \mathbf{A}_{(t)}\,\mathbf{X}_{(t)} + \mathbf{B}_{(t)}\,\mathbf{U}_{(t)} + \mathbf{H}\,\varpi_{(t)} \tag{2}$$

where $\mathbf{X}_{(t)} = [x_1,\, x_2,\, x_3,\, x_4, x_5,\, x_6]^T$ is the state vector which represents the stator and rotor currents $x_1 = i_{\alpha s}$, $x_2 = i_{\beta s}$, $x_3 = i_{xs}$, $x_4 = i_{ys}$, $x_5 = i_{\alpha r}$ and $x_6 = i_{\beta r}$, $\mathbf{U}_{(t)} = [u_1,\, u_2,\, u_3,\, u_4]^T = [v_{\alpha s},\, v_{\beta s},\, v_{xs},\, v_{ys}]^T$ is the input voltage vector applied to the stator windings, $\mathbf{H}$ represents the noise weight matrix, the process noise is considered as $\varpi_{(t)}$ and $\mathbf{A}_{(t)}$ and $\mathbf{B}_{(t)}$ are matrices defined by the electrical parameters of the SPIM as follows:

$$\mathbf{A}_{(t)} = \begin{bmatrix} -R_s c_2 & c_4 L_m \omega_r & 0 & 0 & c_4 R_r & c_4 L_r \omega_r \\ c_4 L_m \omega_r & -R_s c_2 & 0 & 0 & c_4 L_r \omega_r & c_4 R_r \\ 0 & 0 & -R_s c_3 & 0 & 0 & 0 \\ 0 & 0 & 0 & -R_s c_3 & 0 & 0 \\ R_s c_4 & -c_5 L_m \omega_r & 0 & 0 & -c_5 R_r & -c_5 L_r \\ -c_5 L_m \omega_r & R_s c_4 & 0 & 0 & -c_5 L_r & -c_5 R_r \end{bmatrix}$$

$$\mathbf{B}_{(t)} = \begin{bmatrix} c_2 & 0 & 0 & 0 \\ 0 & c_2 & 0 & 0 \\ 0 & 0 & c_3 & 0 \\ 0 & 0 & 0 & c_3 \\ -c_4 & 0 & 0 & 0 \\ 0 & -c_4 & 0 & 0 \end{bmatrix}$$

where R_s, R_r, L_m, $L_r = L_{lr} + L_m$ and $L_s = L_{ls} + L_m$ are the electrical parameters of the SPIM. The coefficients are considered as $c_1 = L_s L_r - L_m^2$, $c_2 = \frac{L_r}{c_1}$, $c_3 = \frac{1}{L_{ls}}$, $c_4 = \frac{L_m}{c_1}$ and $c_5 = \frac{L_s}{c_1}$. Stator voltages are dependant on the input control signals $\mathbf{S}$, which is considered the actual switching state. For this analysis, the ideal VSI has been modeled to obtain a good optimization process. The stator voltages can be calculated from the ideal six-leg VSI model $\mathbf{M}_{[\mathbf{S}]}$ [19].

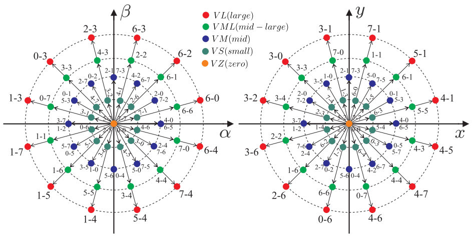

Fig. 2. Voltage space vectors of 64 switching states in $(\alpha-\beta)$ and $(x-y)$ planes for the SPIM.

$$\mathbf{M}_{[\mathbf{S}]} = \frac{1}{3} \begin{bmatrix} 2 & 0 & -1 & 0 & -1 & 0 \\ 0 & 2 & 0 & -1 & 0 & -1 \\ -1 & 0 & 2 & 0 & -1 & 0 \\ 0 & -1 & 0 & 2 & 0 & -1 \\ -1 & 0 & -1 & 0 & 2 & 0 \\ 0 & -1 & 0 & -1 & 0 & 2 \end{bmatrix} \mathbf{S}^T \tag{3}$$

where $\mathbf{S} = [S_a,\, S_d,\, S_b,\, S_e,\, S_c,\, S_f]$, and $\mathbf{S}_i \in \{0, 1\}$. The ideal six-phase VSI generates the stator voltages through the switching gating signals and V_{dc} and then they are transformed to $(\alpha - \beta)$ and $(x - y)$ planes, represented by $\mathbf{U}_{(t)}$, calculated in the following equation:

$$\mathbf{U}_{(t)} = V_{dc}\,\mathbf{T}\,\mathbf{M}_{[\mathbf{S}]}. \tag{4}$$

The output vector, $\mathbf{Y}$, is:

$$\mathbf{Y}_{(t)} = \mathbf{C}\,\mathbf{X}_{(t)} + \nu_{(t)} \tag{5}$$

where $\nu_{(t)}$ is the measurement noise and $\mathbf{C}$ is considered as follows:

$$\mathbf{C} = \begin{bmatrix} 1 & 0 & 0 & 0 & 0 & 0 \\ 0 & 1 & 0 & 0 & 0 & 0 \\ 0 & 0 & 1 & 0 & 0 & 0 \\ 0 & 0 & 0 & 1 & 0 & 0 \end{bmatrix}$$

The mechanical variables of the SPIM are considered in the following equations:

$$T_e = 3\,P\,(\psi_{\alpha s} i_{\beta s} - \psi_{\beta s} i_{\alpha s}) \tag{6}$$

$$J_i\,\dot{\omega}_m + B_i\,\omega_m = (T_e - T_L) \tag{7}$$

$$\omega_r = P \omega_m \tag{8}$$

where T_e represents the electromagnetic torque, P the number of pole pairs, $\psi_{\alpha s}$ and $\psi_{\beta s}$ are considered the stator fluxes, J_i is the inertia coefficient, B_i is considered the friction coefficient, T_L is the load torque, ω_r is the rotor electrical angular speed and ω_m is the rotor mechanical speed.

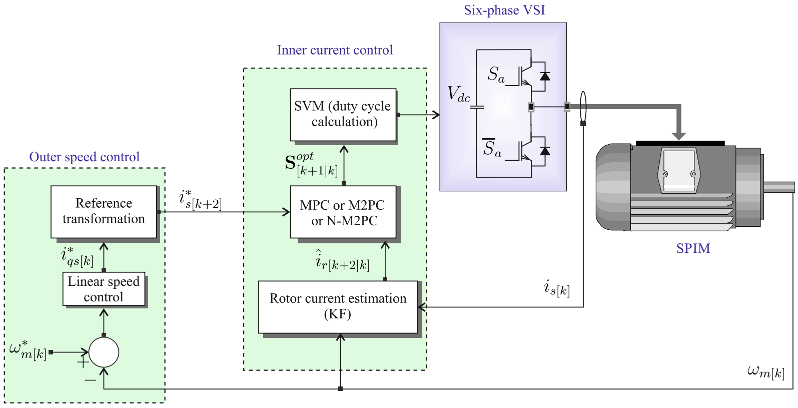

Fig. 3. Block diagram of the controlled system based on FOC and traditional MPC, M2PC and N-M2PC.

III. TRADITIONAL MPC AND ITS VARIANTS

The mathematical model of the SPIM (2) and (5) has to be discretized so it can be considered for the MPC. A forward-Euler method is computed to avoid a high computational cost for the digital controller. The equations will then be in discrete form with the future variables only depending on past values of the variables and not on present values. Thus, a prediction of the future (next sample state) $\hat{\mathbf{X}}_{[k+1|k]}$ is written as:

$$\hat{\mathbf{X}}_{[k+1|k]} = \mathbf{X}_{[k]} + \mathrm{f}\left(\mathbf{X}_{[k]},\, \mathbf{U}_{[k]},\, T_s,\, \omega_{r[k]}\right) \tag{9}$$

where $[k]$ is the current sample and T_s the sampling time. Fig. 3 presents the block diagram of the system with the SPIM and the analyzed controllers.

A. Reduced Order Observers

Stator currents and mechanical rotor speed are the only measured variables in the state-space modeling (2). On the other hand, stator voltages can be calculated from the switching states sent to the VSI. However, rotor currents cannot be measured easily in a real system and they have to be estimated. This topic can be solved by reduced order observers of rotor currents. The reduced order observers only estimate the value of the unmeasured parts of the state vector. This is an important issue which has been already solved by using Luenberger Observer (LO) [31] and Kalman Filter (KF) [13], [32], where KF is considered a superior option as this observer gains are estimated and optimized in every sampling time by taking into account the noise input in the system. For LO, gains are not so optimized and the setting is deterministic [13]. Therefore, KF is considered and implemented in this work to improve the control performance of MPC, by reducing the error of the predictions. Zero-mean Gaussian measurement noises and uncorrelated process are considered. The equations state-space mathematical model of the system are defined as:

$$\hat{\mathbf{X}}_{[k+1|k]} = \mathbf{A}_{[k]}\mathbf{X}_{[k]} + \mathbf{B}_{[k]}\mathbf{U}_{[k]} + \mathbf{H}\varpi_{[k]} \tag{10}$$

$$\mathbf{Y}_{[k+1|k]} = \mathbf{C}\,\mathbf{X}_{[k+1]} + \nu_{[k+1]} \tag{11}$$

where $\mathbf{A}_{[k]}$ and $\mathbf{B}_{[k]}$ are matrices defined by equations (12)-(15). $\mathbf{A}_{[k]}$ also depends on the actual value of $\omega_{r[k]}$ and has to be measured at every sampling time. A more detailed explanation of the error convergence of the KF and dynamics are described in [13], [32] and it was not included in this paper for the sake of conciseness. The system matrices are defined as:

$$\mathbf{A}_{[k]} = \begin{bmatrix} A_{11} & A_{12} & 0 & 0 & A_{15} & A_{16} \\ A_{21} & A_{22} & 0 & 0 & A_{25} & A_{26} \\ 0 & 0 & A_{33} & 0 & 0 & 0 \\ 0 & 0 & 0 & A_{44} & 0 & 0 \\ A_{51} & A_{52} & 0 & 0 & A_{55} & A_{56} \\ A_{61} & A_{62} & 0 & 0 & A_{65} & A_{66} \end{bmatrix} \tag{12}$$

where $\mathbf{A}_{[k]}$ parameters are:

$$\begin{aligned} A_{11} &= A_{22} = 1 - T_s c_2 R_s \\ A_{12} &= -A_{21} = T_s c_4 L_m \omega_{r[k]} \\ A_{15} &= A_{26} = T_s c_4 R_r \\ A_{16} &= -A_{25} = T_s c_4 L_r \omega_{r[k]} \\ A_{33} &= A_{44} = 1 - T_s c_3 R_s \\ A_{51} &= A_{62} = -T_s c_4 R_s \\ A_{52} &= -A_{61} = -T_s c_5 L_m \omega_{r[k]} \\ A_{55} &= A_{66} = 1 - T_s c_5 R_r \\ A_{56} &= -A_{65} = -c_5 \omega_{r[k]} T_s L_r \end{aligned} \tag{13}$$

$$\mathbf{B}_{[k]} = \begin{bmatrix} B_{11} & 0 & 0 & 0 & 0 & 0 \\ 0 & B_{22} & 0 & 0 & 0 & 0 \\ 0 & 0 & B_{33} & 0 & 0 & 0 \\ 0 & 0 & 0 & B_{44} & 0 & 0 \\ 0 & 0 & 0 & 0 & B_{55} & 0 \\ 0 & 0 & 0 & 0 & 0 & B_{66} \end{bmatrix} \tag{14}$$

being $\mathbf{B}_{[k]}$ parameters:

$$\begin{aligned} B_{11} &= B_{22} = T_s c_2 \\ B_{33} &= B_{44} = T_s c_3 \\ B_{55} &= B_{66} = -T_s c_4 \end{aligned} \tag{15}$$

B. Cost Function

The cost function is considered as an optimization process of different system variables such as the harmonic content minimization, machine torque ripple minimization, VSI switching losses and current tracking error [33]. This last variable is the most important figure of merit in MPC in $(\alpha-\beta)$ and $(x-y)$ planes. MPC analyses the cost function for 49 iterations regarding 49 different voltage vectors. Therefore, the selected cost function is:

$$J_{[k+2|k]} = \Bigg[(i^*_{\alpha s[k+2]} - \hat{i}_{\alpha s[k+2|k]})^2 + (i^*_{\beta s[k+2]} - \hat{i}_{\beta s[k+2|k]})^2 + \lambda_{xy} \left((i^*_{xs[k+2]} - \hat{i}_{xs[k+2|k]})^2 + (i^*_{ys[k+2]} - \hat{i}_{ys[k+2|k]})^2 \right) \Bigg]^{\frac{1}{2}} \tag{16}$$

A second-step ahead prediction of stator currents $\hat{i}_{s[k+2|k]}$ is computed for delay compensation, by considering equations (10) and (11). The desired reference trajectory of the stator currents is represented by $i^*_{s[k+2]}$. The weighting factor optimization is tackled in [11], [34], [35]. Typically, for SPIM, λ_{xy} gives more priority to stator currents in $(\alpha-\beta)$ plane than $(x-y)$ [13], [36].

C. M2PC

This modulation consists on determine each available sector for the six-leg VSI in the $(\alpha-\beta)$ plane, being 12 outside sectors in total, which are composed of two adjacent active vectors and the null vector (VZ), as shown in Fig. 4. Then, it calculates the future prediction of the three vectors at every sampling time and analyses their respective cost functions (J_0, J_1 and J_2) separately [21]. This technique can generate any voltage vector in the $(\alpha-\beta)$ plane by using the large vectors (VL) and VZ, covering the entire space vector area. It can be noted that VL are the smallest voltage vectors in $(x-y)$ plane, managing a natural reduction of $(x-y)$ currents [21], [37].

The duty cycles (d_0, d_1 and d_2) are obtained by solving the following equations:

$$d_0 = \frac{\gamma}{J_0} \qquad d_1 = \frac{\gamma}{J_1} \qquad d_2 = \frac{\gamma}{J_2} \tag{17}$$

$$d_0 + d_1 + d_2 = T_s \tag{18}$$

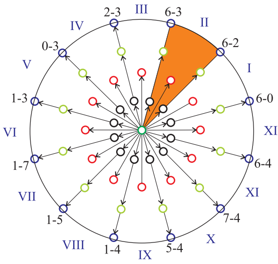

Fig. 4. Space voltage sectors for the six-phase VSI.

The duty cycles for each vector are given as:

$$J_T = J_1 J_2 + J_0 J_1 + J_0 J_2 \tag{19}$$

$$d_0 = \frac{T_s J_1 J_2}{J_T} \tag{20}$$

$$d_1 = \frac{T_s J_0 J_2}{J_T} \tag{21}$$

$$d_2 = \frac{T_s J_0 J_1}{J_T} \tag{22}$$

At last, the selected sector cost function is considered as:

$$G_{[k+2|k]} = d_1 J_1 + d_2 J_2 \tag{23}$$

The sector, which reduces $G_{[k+2|k]}$, is applied to the six-leg VSI at the next sampling time. It is necessary to synthesize the duty cycles, to be able to implement a symmetric pulse width modulation (PWM) as follows:

$$\tau_{(i)} = \frac{d_0}{2T_s} + \frac{d_1}{T_s} v_{1(i)} + \frac{d_2}{T_s} v_{2(i)} \tag{24}$$

where $i = [a, d, b, e, c, f]$ and τ_i is the PWM duty cycle per leg, obtaining a fixed switching frequency.

D. N-M2PC

The main difference of N-M2PC with M2PC is the shape of each voltage sector. M2PC uses 2 VL and VZ per sector and N-M2PC uses 4 which includes 2 mid vectors (VM) and 2 VL. The main goal of this modulation is to reduce the steady-state error of the stator currents tracking in $(d-q)$ plane by including these adjacent VM per sector avoiding the use of VZ which limits the voltage range, reducing the tracking capacity of the stator currents in $(\alpha-\beta)$ plane, due to the fact that VZ has an increased duty cycle when $(x-y)$ currents are being reduced [22].

The duty cycles, for VL and VM d_1, d_2, d_3 and d_4, are obtained as follows:

$$d_1 = \frac{\gamma}{J_1} \quad d_2 = \frac{\gamma}{J_2} \quad d_3 = \frac{\gamma}{J_3} \quad d_4 = \frac{\gamma}{J_4} \tag{25}$$

$$d_1 + d_2 + d_3 + d_4 = T_s \tag{26}$$

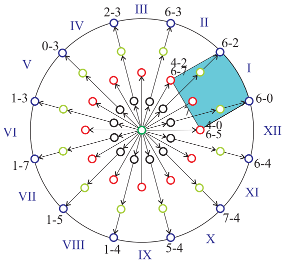

Fig. 5. Space voltage sectors of N-M2PC.

where J_1, J_2, J_3 and J_4 are the corresponding cost functions (16) for the four vectors. Then, the duty cycles for each vector are calculated as:

$$J_{T1} = J_1 J_3 J_4 + J_2 J_3 J_4 \tag{27}$$

$$J_{T2} = J_1 J_2 J_4 + J_1 J_2 J_3 \tag{28}$$

$$d_1 = \frac{T_s J_2 J_3 J_4}{J_{T1} + J_{T2}} \tag{29}$$

$$d_2 = \frac{T_s J_1 J_3 J_4}{J_{T1} + J_{T2}} \tag{30}$$

$$d_3 = \frac{T_s J_1 J_2 J_4}{J_{T1} + J_{T2}} \tag{31}$$

$$d_4 = \frac{T_s J_1 J_2 J_3}{J_{T1} + J_{T2}} \tag{32}$$

At last, the final cost function is computed as:

$$G_{[k+2|k]} = d_1 J_1 + d_2 J_2 + d_3 J_3 + d_4 J_4 \tag{33}$$

A simple equation is used to obtain the duty cycles $\tau_{(i)}$ for the switching devices of each phase of the six-leg VSI, as follows:

$$\tau_{(i)} = \frac{d_1}{T_s} v_{1(i)} + \frac{d_2}{T_s} v_{2(i)} + \frac{d_3}{T_s} v_{3(i)} + \frac{d_4}{T_s} v_{4(i)} \tag{34}$$

where $\tau_{(i)}$ is normalized between 0 and 1, for the switching devices for the six-leg VSI.

IV. PRACTICAL STABILITY ANALYSIS

Examples of MPC variants are vastly known in the literature, which present some common properties and allow to formalize the stability analysis [38]. A candidate-Lyapunov function is often considered as a popular method to prove stability of MPC. Another considered approach, presented in [16], [39], [40] consists in estimate a certain gain $\mathbf{L}_{[k]}$ in order to obtain a stable matrix $(\mathbf{A}_{[k]} - \mathbf{B}_{[k]}\mathbf{L}_{[k]})$ whose eigenvalues are less than 1. The second method is more practical due to its simplicity and by considering that MPC has a finite control effort, i.e. 49 voltage vectors in the particular case of the SPIM. For a limited current reference (due to security issues), there is a finite number of $\mathbf{L}_{[k]}$ through the cost function minimization and it shows the same behaviour in terms of local stability by analyzing different scenarios, such as typical values of rotor speed and sampling frequency (F_s).

$$\mathbf{U}_{[k]} = -\mathbf{L}_{[k]}\mathbf{X}_{[k]} \tag{35}$$

where $\mathbf{L}_{[k]}$ is selected as follows:

$$\mathbf{L}_{[k]} = \begin{bmatrix} L_1 & L_2 & 0 & 0 & L_3 & L_4 \\ -L_2 & L_1 & 0 & 0 & -L_4 & L_3 \\ 0 & 0 & L_5 & L_6 & 0 & 0 \\ 0 & 0 & -L_6 & L_5 & 0 & 0 \end{bmatrix}$$

It is considered a limited range of $[-3.5, 3.5]$ A for state variables ($\mathbf{X}_{[k]}$), by the separation theorem the closed loop eigenvalues are the union of those of the observer and state feedback assuming measured states, and finite values of the voltage vector ($\mathbf{U}_{[k]}$) i.e. 49 different values for traditional MPC, a finite number of $\mathbf{L}_{[k]}$ is found by means of an exhaustive search, as shown in Table I. At the same time, Table II presents the maximum stable rotor speed (eigenvalues inside the unit circle) at different sampling frequencies for traditional MPC, M2PC and N-M2PC. At last, eigenvalues of $(\mathbf{A}_{[k]} - \mathbf{B}_{[k]}\mathbf{L}_{[k]})$ matrix at 10 kHz of sampling frequency and rotor speed of 2500 rpm for the three techniques are shown in Fig. 6 where, at those conditions, N-M2PC is the only controller with eigenvalues inside the unit circle.

TABLE I
RANGE VALUES OF DIFFERENT GAINS ($\mathbf{L}_{[k]}$) OF TRADITIONAL MPC, M2PC AND N-M2PC.

Gains	Traditional MPC	M2PC	N-M2PC
L_1	$[-10, 10]$	$[-10, 10]$	$[-10, 10]$
L_2	$[-40, 40]$	$[-40, 40]$	$[-40, 40]$
L_3	$[-155, -150]; [-80, -70]$	$[-150, 10]$	$[-760, -300]$
L_4	$[-40, 40]$	$[-40, 40]$	$[-40, 40]$
L_5	$[-10, 10]$	$[-10, 10]$	$[-10, 10]$
L_6	$[-40, 40]$	$[-40, 40]$	$[-40, 40]$

TABLE II
STABILITY THEORETICAL ANALYSIS OF TRADITIONAL MPC, M2PC AND N-M2PC AND THEIR MAXIMUM STABLE SPEEDS (RPM).

F_s (kHz)	Traditional MPC	M2PC	N-M2PC
	Maximum Stable Speed		
2	700	850	250
2.5	850	1000	550
4	1100	1300	1250
5	1250	1400	1650
7.5	1600	1700	2800
8	1700	1850	2850
10	1900	2000	3000
12.5	2400	2300	3000
15	2600	2600	3000
16	2700	2700	3000
17.5	2800	2800	3000
20	3000	3000	3000

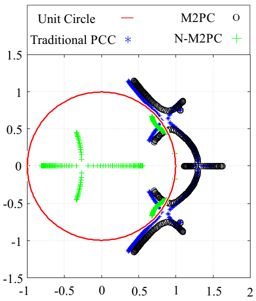

Fig. 6. Eigenvalues of $(\mathbf{A}_{[k]} - \mathbf{B}_{[k]}\mathbf{L}_{[k]})$ matrix at 10 kHz of sampling frequency and rotor speed of 2500 rpm for traditional MPC, M2PC and N-M2PC.

V. EXPERIMENTAL RESULTS

The stability analysis is validated trough experimental tests for traditional MPC, M2PC and N-M2PC in the experimental bench.

A. Experimental bench

The experimental bench is composed of a SPIM fed by to two conventional three-phase VSI, using a DC voltage source. The six-phase VSI is controlled by a real-time rapid prototyping platform defined as dSPACE MABXII DS1401, with MATLAB/Simulink incorporated. Table III presents the parameters of the SPIM obtained using stand-still VSI tests and typical methods of AC time domain [41], [42].

The measurements were made with current sensors LA 55-P s, with many turns to improve the precision at low current amplitude, they also have a frequency bandwidth from DC up to 200 kHz. The data then is converted to digital through a 16-bit A/D converter. The SPIM rotor angle is obtained by a 1024 ppr incremental encoder and the rotor speed is estimated from the angle. At last, a 5 HP eddy current brake is selected as a variable mechanical load on the SPIM which is considered at 1 A. A block diagram of the experimental bench is shown in Fig. 7. The cost function in (16) with λ_{xy} = 0.05 is considered to apply the traditional MPC and M2PC. This gives priority to $(\alpha - \beta)$ stator currents tracking over the $(x - y)$ currents reduction. As for N-M2PC, λ_{xy} = 0.1 is selected, due to the fact that the null vector is not used and the $(x - y)$ currents reduction is obtained through the active vectors combination. These values of λ_{xy} were obtained through heuristic method by focusing on obtaining a sub-optimal system. The process and measurement noise values can be estimated by using the proposed method in [32], as $\hat{Q}_w = 0.0022$ and $\hat{R}_v = 0.0022$.

TABLE III
PARAMETERS OF THE SPIM

PARAMETER	VALUE	PARAMETER	VALUE
R_r (Ω)	6.9	R_s (Ω)	6.7
L_s (mH)	654.4	L_r (mH)	626.8
L_m (mH)	614	L_{ls} (mH)	5.3
ω_{m-nom} (rpm)	2 880	P_w (kW)	2
J_i (kg.m^2)	0.07	B_i (kg.m^2/s)	0.0004
P	1	V_{dc} (V)	700

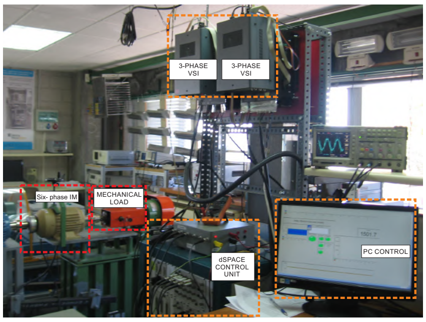

Fig. 7. Block diagram of the experimental bench including the dSPACE platform, the SPIM, the six-phase VSI and the eddy current brake.

B. Stability analysis

In every case, $(x-y)$ current references are considered zero ($i^*_{xs} = i^*_{ys} = 0$). Then, a fixed d stator current ($i^*_{ds} = 1$ A) has been set. The sampling frequencies, in the tests, are 2.5 kHz, 5 kHz, 7.5 kHz, 10 kHz, 12.5 kHz, 15 kHz, 17.5 kHz and 20 kHz. Table IV shows the experimental results obtained at different sampling frequencies for traditional MPC, M2PC and N-M2PC, regarding the maximum stable rotor speeds, presenting similar results to the theoretical analysis. At the same time, Table V presents the average switching frequency at different sampling frequencies for traditional MPC, M2PC and N-M2PC. At last, Fig. 8(a) and Fig. 8(b) show the trend charts of the maximum stable rotor speeds and average switching frequencies for traditional MPC, M2PC and N-M2PC at different sampling frequencies. The results show that N-M2PC has the best performance regarding local stability with the maximum rotor speed of the SPIM, where at low sampling frequency the performance is not much different to traditional MPC and M2PC but at higher sampling frequency, N-M2PC can operate in the entire speed range of the machine, as for traditional MPC and M2PC, they tend to improve linearly local stability at higher sampling frequency where traditional MPC has a steep slope compared to M2PC. As for average switching frequency, M2PC is a fixed switching frequency technique, so it matches the switching frequency and the sampling frequency. However, traditional MPC and N-M2PC are variable switching frequency techniques, therefore the average switching frequencies are lower where N-M2PC has almost half the switching frequency than traditional MPC, worsening the performance of stator currents total harmonic distortion (THD) but improving the switching losses in the six-phase VSI.

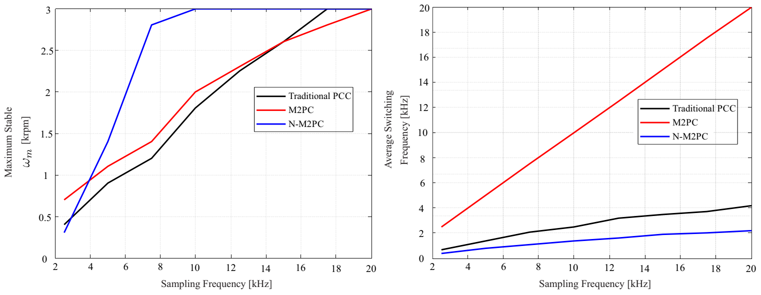

(a) (b)

Fig. 8. Trend chart of traditional MPC, M2PC and N-M2PC regarding different sampling frequencies and: (a)rotor mechanical speed; (b)average switching frequency.

TABLE IV
STABILITY ANALYSIS OF TRADITIONAL MPC, M2PC AND N-M2PC AND THEIR MAXIMUM STABLE SPEEDS (RPM).

F_s (kHz)	Traditional MPC	M2PC	N-M2PC
	Maximum Stable Speed		
2.5	400	700	300
5	900	1100	1400
7.5	1200	1400	2800
10	1800	2000	3000
12.5	2250	2300	3000
15	2600	2600	3000
17.5	3000	2800	3000
20	3000	3000	3000

TABLE V
AVERAGE SWITCHING FREQUENCY (KHZ) OF TRADITIONAL MPC, M2PC AND N-M2PC AT THEIR MAXIMUM STABLE SPEEDS (RPM) AND SAMPLING FREQUENCIES (KHZ).

F_s (kHz)	Traditional MPC	M2PC	N-M2PC
	Average Switching Frequency		
2.5	0.7	2.5	0.4
5	1.4	5	0.8
7.5	2.1	7.5	1.1
10	2.5	10	1.4
12.5	3.2	12.5	1.6
15	3.5	15	1.9
17.5	3.7	17.5	2
20	4.2	20	2.2

VI. CONCLUSION

This paper presented a practical stability analysis to traditional MPC, M2PC and N-M2PC applied to an asymmetrical SPIM. The experimental results validated the limits of stability regarding rotor speed and sampling frequencies for all the studied current controllers. It was shown an approximately linear relation between the maximum rotor speed and the sampling frequency and the theoretical analysis showed a very similar behaviour by considering a finite range of gains to represent the different current controllers, validating the proposed method which can be applied to other systems with predictive control.

REFERENCES

[1] E. Levi, “Advances in converter control and innovative exploitation of additional degrees of freedom for multiphase machines,” *IEEE Trans. Ind. Electron.*, vol. 63, DOI 10.1109/TIE.2015.2434999, no. 1, pp. 433–448, 2016.

[2] I. Subotic, N. Bodo, E. Levi, B. Dumnic, D. Milicevic, and V. Katic, “Overview of fast on-board integrated battery chargers for electric vehicles based on multiphase machines and power electronics,” *Elect. Power Appl.*, vol. 10, DOI 10.1049/iet-epa.2015.0292, no. 3, pp. 217–229, 2016.

[3] A. G. Yepes, A. Vidal, J. Malvar, O. López, and J. Doval-Gandoy, “Tuning method aimed at optimized settling time and overshoot for synchronous proportional-integral current control in electric machines,” *IEEE Trans. Power Electron.*, vol. 29, DOI 10.1109/TPEL.2013.2276059, no. 6, pp. 3041–3054, 2014.

[4] F. Baneira, J. Doval-Gandoy, A. G. Yepes, O. Lopez, and D. Pérez-Estévez, “Control strategy for multiphase drives with minimum losses in the full torque operation range under single open-phase fault,” *IEEE Trans. Power Electron.*, vol. 32, no. 8, pp. 6275–6285, 2016.

[5] A. G. Yepes, J. Doval-Gandoy, and H. Toliyat, “Multifrequency current control for multiphase machines with antiwindup, distortion-free saturation and full DC-link utilization,” in *Proc. ECCE*. IEEE, 2018, pp. 776–783.

[6] I. G. Prieto, M. Duran, P. Entrambasaguas, and M. Bermudez, “Field oriented control of multiphase drives with passive fault-tolerance,” *IEEE Trans. Ind. Electron.*, 2019.

[7] Y. Kali, M. Ayala, J. Rodas, M. Saad, J. Doval-Gandoy, R. Gregor, and K. Benjelloun, “Current control of a six-phase induction machine drive based on discrete-time sliding mode with time delay estimation,” *Energies*, vol. 12, no. 1, p. 170, 2019.

[8] Y. Kali, M. Saad, J. Doval-Gandoy, J. Rodas, and K. Benjelloun, “Discrete sliding mode control based on exponential reaching law and time delay estimation for an asymmetrical six-phase induction machine drive,” *IET Electric Power Appl.*, vol. 13, no. 11, pp. 1660–1671, 2019.

[9] F. Barrero, M. R. Arahal, R. Gregor, S. Toral, and M. J. Durán, “A proof of concept study of predictive current control for VSI-driven asymmetrical dual three-phase AC machines,” *IEEE Trans. Ind. Electron.*, vol. 56, DOI 10.1109/TIE.2008.2011604, no. 6, pp. 1937–1954, 2009.

[10] F. Barrero, J. Prieto, E. Levi, R. Gregor, S. Toral, M. J. Durán, and M. Jones, “An enhanced predictive current control method for asymmetrical six-phase motor drives,” *IEEE Trans. Ind. Electron.*, vol. 58, DOI 10.1109/TIE.2010.2089943, no. 8, pp. 3242–3252, 2010.

[11] C. S. Lim, E. Levi, M. Jones, N. A. Rahim, and W. P. Hew, “FCS-MPC-based current control of a five-phase induction motor and its comparison with PI-PWM control,” *IEEE Trans. Ind. Electron.*, vol. 61, DOI 10.1109/TIE.2013.2248334, no. 1, pp. 149–163, 2013.

[12] E. Fuentes, C. A. Silva, and R. M. Kennel, “MPC implementation of a quasi-time-optimal speed control for a PMSM drive, with inner modulated-fs-mpc torque control,” *IEEE Trans. Ind. Electron.*, vol. 63, DOI 10.1109/TIE.2016.2519326, no. 6, pp. 3897–3905, 2016.

[13] J. Rodas, F. Barrero, M. R. Arahal, C. Martín, and R. Gregor, “Online estimation of rotor variables in predictive current controllers: a case study using five-phase induction machines,” *IEEE Trans. Ind. Electron.*, vol. 63, DOI 10.1109/TIE.2016.2559420, no. 9, pp. 5348–5356, 2016.

[14] I. Gonzalez-Prieto, M. J. Duran, J. J. Aciego, C. Martin, and F. Barrero, “Model predictive control of six-phase induction motor drives using virtual voltage vectors,” *IEEE Trans. Ind. Electron.*, vol. 65, DOI 10.1109/TIE.2017.2714126, no. 1, pp. 27–37, 2017.

[15] J. J. Aciego, I. G. Prieto, and M. J. Duran, “Model predictive control of six-phase induction motor drives using two virtual voltage vectors,” *IEEE Journal of Emerging and Selected Topics in Power Electronics*, vol. 7, DOI 10.1109/JESTPE.2018.2883359, no. 1, pp. 321–330, 2018.

[16] M. Ayala, J. Doval-Gandoy, J. Rodas, O. Gonzalez, and R. Gregor, “Current control designed with model based predictive control for six-phase motor drives,” *ISA transactions*, 2019.

[17] I. González-Prieto, M. Durán, M. Bermúdez, F. Barrero, and C. Martín, “Assessment of Virtual-Voltage-based Model Predictive Controllers in Six-phase Drives under Open-Phase Faults,” *IEEE Journal of Emerging and Selected Topics in Power Electronics*, DOI 10.1109/JESTPE.2019.2915666, 2019.

[18] S. Toledo, M. Rivera, J. Muñoz, R. Peña, J. Riveros, and R. Gregor, “Fixed switching frequency predictive control for a multi-drive indirect matrix converter system,” in *Proc. SPEC*, DOI 10.1109/SPEC.2017.8333672, 2017, pp. 1–6.

[19] M. Ayala, J. Rodas, R. Gregor, J. Doval-Gandoy, O. Gonzalez, M. Saad, and M. Rivera, “Comparative study of predictive control strategies at fixed switching frequency for an asymmetrical six-phase induction motor drive,” in *Proc. IEMDC*, DOI 10.1109/IEMDC.2017.8002121, 2017, pp. 1–8.

[20] I. Gonzalez-Prieto, M. J. Duran, J. J. Aciego, C. Martin, and F. Barrero, “Model predictive control of six-phase induction motor drives using virtual voltage vectors,” *IEEE Trans. Ind. Electron.*, vol. 65, DOI 10.1109/TIE.2017.2714126, no. 1, pp. 27–37, 2018.

[21] O. Gonzalez, M. Ayala, J. Doval-Gandoy, J. Rodas, R. Gregor, and M. Rivera, “Predictive-fixed switching current control strategy applied to six-phase induction machine,” *Energies*, vol. 12, DOI 10.3390/en12122294, no. 12, p. 2294, 2019.

[22] M. Ayala, J. Doval-Gandoy, J. Rodas, O. Gonzalez, R. Gregor, and M. Rivera, “A novel modulated model predictive control applied to six-phase induction motor drives,” *IEEE Trans. Ind. Electron.*, 2020.

[23] P. Gonçalves, S. Cruz, and A. Mendes, “Finite control set model predictive control of six-phase asymmetrical machinesAn overview,” *Energies*, vol. 12, no. 24, p. 4693, 2019.

[24] M. Morari and J. H. Lee, “Model predictive control: past, present and future,” *Computers & Chemical Engineering*, vol. 23, DOI 10.1016/S0098-1354(98)00301-9, no. 4-5, pp. 667–682, 1999.

[25] R. P. Aguilera and D. E. Quevedo, “Predictive control of power converters: Designs with guaranteed performance,” *IEEE Trans. Ind. Informatics*, vol. 11, DOI 10.1109/TII.2014.2363933, no. 1, pp. 53–63, 2014.

[26] M. Preindl, “Robust control invariant sets and Lyapunov-based MPC for ipm synchronous motor drives,” *IEEE Trans. Ind. Electron.*, vol. 63, DOI 10.1109/TIE.2016.2527722, no. 6, pp. 3925–3933, 2016.

[27] R. P. Aguilera and D. E. Quevedo, “On the stability of MPC with a finite input alphabet,” *Proc. IFAC*, vol. 44, DOI 10.3182/20110828-6-IT-1002.02705, no. 1, pp. 7975–7980, 2011.

[28] M. N. Zeilinger, M. Morari, and C. N. Jones, “Soft constrained model predictive control with robust stability guarantees,” *IEEE Trans. Automatic Control*, vol. 59, DOI 10.1109/TAC.2014.2304371, no. 5, pp. 1190–1202, 2014.

[29] L. Zhang, S. Zhuang, and R. D. Braatz, “Switched model predictive control of switched linear systems: Feasibility, stability and robustness,” *Automatica*, vol. 67, DOI 10.1016/j.automatica.2016.01.010, pp. 8–21, 2016.

[30] Y. Zhao and T. Lipo, “Space vector PWM control of dual three-phase induction machine using vector space decomposition,” *IEEE Trans. Ind. Electron.*, vol. 31, DOI 10.1109/28.464525, no. 5, pp. 1100–1109, 1995.

[31] C. Martín, M. R. Arahal, F. Barrero, and M. J. Durán, “Multiphase rotor current observers for current predictive control: A five-phase case study,” *Control Eng. Prac.*, vol. 49, DOI 10.1016/j.conengprac.2016.01.011, pp. 101–111, 2016.

[32] J. Rodas, C. Martin, M. R. Arahal, F. Barrero, and R. Gregor, “Influence of covariance-based ALS methods in the performance of predictive controllers with rotor current estimation,” *IEEE Trans. Ind. Electron.*, vol. 64, DOI 10.1109/TIE.2016.2636205, no. 4, pp. 2602–2607, 2017.

[33] J. Rodriguez, M. P. Kazmierkowski, J. R. Espinoza, P. Zanchetta, H. Abu-Rub, H. A. Young, and C. A. Rojas, “State of the art of finite control set model predictive control in power electronics,” *IEEE Trans. Ind. Inform.*, vol. 9, DOI 10.1109/TII.2012.2221469, no. 2, pp. 1003–1016, 2013.

[34] M. Novak, T. Dragicevic, and F. Blaabjerg, “Weighting factor design based on Artificial Neural Network for Finite Set MPC operated 3L-NPC converter,” in *Proc. APEC)*, DOI 10.1109/APEC.2019.8722062. IEEE, 2019, pp. 77–82.

[35] B. Majmunović, T. Dragičević, and F. Blaabjerg, “Multi Objective Modulated Model Predictive Control of Stand-Alone Voltage Source Converters,” *IEEE Journal of Emerging and Selected Topics in Power Electronics*, DOI 10.1109/JESTPE.2019.2925603, 2019.

[36] C. Martin, M. Arahal, F. Barrero, and M. Duran, “Five-phase induction motor rotor current observer for finite control set model predictive control of stator current,” *IEEE Trans. Ind. Electron.*, vol. 63, DOI 10.1109/TIE.2016.2536578, no. 7, pp. 4527–4538, 2016.

[37] O. Gonzalez, M. Ayala, J. Rodas, R. Gregor, G. Rivas, and J. Doval-Gandoy, “Variable-speed control of a six-phase induction machine using predictive-fixed switching frequency current control techniques,” in *Proc. PEDG*, DOI 10.1109/PEDG.2018.8447837, 2018, pp. 1–6.

[38] D. Q. Mayne, J. B. Rawlings, C. V. Rao, and P. O. Scokaert, “Constrained model predictive control: Stability and optimality,” *Automatica*, vol. 36, DOI 10.1016/S0005-1098(99)00214-9, no. 6, pp. 789–814, 2000.

[39] R. P. Aguilera and D. E. Quevedo, “On stability and performance of finite control set MPC for power converters,” in *Proc. PRECEDE*, DOI 10.1109/PRECEDE.2011.6078688. IEEE, 2011, pp. 55–62.

[40] R. P. Aguilera and D. E. Quevedo, “Stability analysis of quadratic MPC with a discrete input alphabet,” *IEEE Trans. Automatic Control*, vol. 58, DOI 10.1109/TAC.2013.2264551, no. 12, pp. 3190–3196, 2013.

[41] A. G. Yepes, J. A. Riveros, J. Doval-Gandoy, F. Barrero, O. López, B. Bogado, M. Jones, and E. Levi, “Parameter identification of multiphase induction machines with distributed windings Part 1: Sinusoidal excitation methods,” *IEEE Trans. Energy Conv.*, vol. 27, DOI 10.1109/TEC.2012.2220967, no. 4, pp. 1056–1066, 2012.

[42] J. A. Riveros, A. G. Yepes, F. Barrero, J. Doval-Gandoy, B. Bogado, O. Lopez, M. Jones, and E. Levi, “Parameter identification of multiphase induction machines with distributed windings Part 2: Time-domain techniques,” *IEEE Trans. Energy Conv.*, vol. 27, DOI 10.1109/TEC.2012.2219862, no. 4, pp. 1067–1077, 2012.

ARTÍCULO 6

VARIABLE-SPEED CONTROL OF A SIX-PHASE INDUCTION MACHINE USING PREDICTIVE-FIXED SWITCHING FREQUENCY CURRENT CONTROL TECHNIQUES

- Osvaldo González, **Magno Ayala**, Jesus Doval-Gandoy, Raul Gregor and Gustavo Rivas, ”Variable-Speed Control of a Six-Phase Induction Machine using Predictive-Fixed Switching Frequency Current Control Techniques”, Proc. PEDG, Charlotte, US, pp. 1-6, DOI: 10.1109/PEDG.2018.8447837, 2018.

Variable-Speed Control of a Six-Phase Induction Machine using Predictive-Fixed Switching Frequency Current Control Techniques

Osvaldo Gonzalez[1], Magno Ayala[1], Jesus Doval-Gandoy[2], Jorge Rodas[1], Raul Gregor[1] and Gustavo Rivas[1]
[1]Laboratory of Power and Control Systems, Facultad de Ingeniería, Universidad Nacional de Asunción, Paraguay,
ogonzalez@ing.una.py, mayala@ing.una.py, jrodas@ing.una.py, rgregor@ing.una.py, gusyri@hotmail.com
[2]Applied Power Electronics Technology Research Group, Universidad de Vigo, Spain, jdoval@uvigo.es

***Abstract*—Model predictive control method has been recently introduced as an alternative to inner current controllers of multiphase drives using rotor field oriented control methods. Model predictive controllers are distinguished by a variable switching frequency which causes noise, large voltage and current ripples at low sampling frequency. Therefore, this paper proposes a variable-speed control for six-phase induction motor drives by using an inner loop of predictive-fixed switching frequency current control scheme. Experimental results are provided in order to prove the feasibility of the proposed control technique, considering mean squared error as well as the total harmonic distortion of the stator currents as figure of merit. The efficiency of the proposed control could be verified by applying the non-parametric Mann-Whitney statistical test on the experimentally obtained data.**

***Index Terms*—Fixed switching frequency, multiphase machines, predictive control.**

I. INTRODUCTION

Multiphase induction machine (IM) has gained higher attention compared to its three-phase counterparts due to its fault tolerance, lower torque pulsation and better power distribution per phase which are very attractive to the research community for industrial applications where a high-performance control is required [1]. In recent times, several applications of multiphase IMs are being studied, such as wind power generation system, electric vehicles (EV) and hybrid EV [2]. In all these applications, multiphase IM would be performed under variable-speed conditions, including speed sensorless operations [3]. The most common speed control structure for multiphase IM is the field-oriented control (FOC) technique, a cascaded scheme with an inner current control loop and an outer speed control loop [4]. Several new control strategies have been developed for the inner current control loop for multiphase IM such as: model predictive control (MPC), resonant and direct torque control and also its extension to post-fault operation [5]. The implemented solution of MPC shows excellent transient performance as well as the easy inclusion of nonlinearities in the model comparing with traditional proportional-integral (PI) controllers [6]. The main obstacle of the MPC methods is that the control can only select from a finite number of valid switching states because of the absence of a modulator. This generates distortion and also large voltage and current ripples at low sampling frequency. The variable switching frequency produces a spread spectrum, decreasing the performance of the system in terms of power quality [7]. To overcome this issue, an enhanced predictive controller with fixed switching frequency is presented in this paper. This method is based on a modulation scheme incorporated to the conventional MPC for different power converters [8]–[11]. This method is applied to a two-level voltage source inverter (VSI), where for a selected number of switching states the duty cycles are generated by using two active vectors and two zero vectors which are applied to the converter using a given switching pattern in order to obtain an efficient dynamic of the system. For the external speed control loop, a PI controller is designed by a technique detailed in [12].

The main contribution of this paper is the experimental validation of the aforementioned predictive-fixed switching frequency technique used as an inner current control applied to a variable-speed six-phase IM drive. The efficiency of the predictive-fixed current control technique is analyzed by using the mean square error (MSE) and the total harmonic distortion (THD) as indices of performance. The figures of merit used are not of constant magnitude. This is easily appreciated when a replication of the experiment is performed. In such cases, we have a probability distribution function for each variable considered (MSE and THD). When sample sizes are small it is more appropriate to make no assumption about the distribution of variables when comparisons are to be made. This results in the application of non-parametric statistical techniques [13]. Specifically, the Mann-Whitney test is used to compare the central tendencies of the values obtained through the experimental results for each scenario described in Section IV.

II. SIX-PHASE INDUCTION MACHINE DRIVE

A six-phase IM associated with a six-phase VSI and a DC voltage source (V_{dc}) is considered where the phase propagation angles of this IM are:

$$[\theta_p] = \begin{bmatrix} 0 & \frac{\pi}{6} & \frac{2\pi}{3} & \frac{5\pi}{6} & \frac{4\pi}{3} & \frac{3\pi}{2} \end{bmatrix} \quad (1)$$

The electrical scheme of the VSI drive is shown in Fig. 1. The six-phase IM is a continuous system which can be described by a group of differential equations. By applying the vector space decomposition (VSD) technique [14], the

978-1-5386-6705-7/18/$31.00

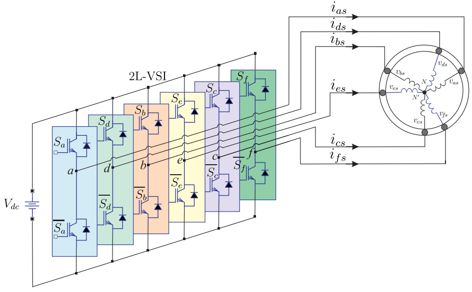

Fig. 1. Scheme of a six-phase IM connected to a six-phase VSI.

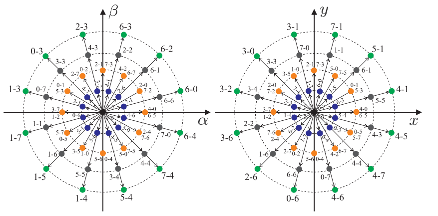

Fig. 2. Voltage space vectors and switching states in the (α-β) and (x-y) sub-spaces for a six-phase IM.

original six dimensional space of the six-phase IM, defined by its six phases (a, b, c, d, e, f), is converted into three two dimensional orthogonal sub-spaces in the stationary reference frame, represented as (α-β), (x-y) and (z_1-z_2), by using the transformation matrix $\mathbf{T}$ [15] and an invariant amplitude criterion was selected, where only (α-β) components contribute to the torque and flux production. The (z_1-z_2) components are not considered due to the isolated neutral points configuration.

$$\mathbf{T} = \frac{1}{3}\begin{array}{c} \left[\begin{array}{cccccc} \multicolumn{6}{c}{\cos\left([\theta_p]\right)} \\ \multicolumn{6}{c}{\sin\left([\theta_p]\right)} \\ \multicolumn{6}{c}{\cos\left(5\,[\theta_p]\right)} \\ \multicolumn{6}{c}{\sin\left(5\,[\theta_p]\right)} \\ 1 & 0 & 1 & 0 & 1 & 0 \\ 0 & 1 & 0 & 1 & 0 & 1 \end{array}\right] \end{array} \begin{array}{c} \alpha \\ \beta \\ x \\ y \\ z_1 \\ z_2 \end{array} \tag{2}$$

The VSI has a discrete nature with an amount of $64 = 2^6$ different switching states defined by six switching functions corresponding to the six inverter legs $[S_a, S_b, S_c, S_d, S_e, S_f]$, where $\mathbf{S}_i \in \{0, 1\}$. The different switching states and the voltage of the V_{dc} define the phase voltages which can be mapped to the (α-β)-(x-y) sub-spaces according to the VSD approach. Fig. 2 shows the 64 possibilities which lead only to 48 different active voltage vectors plus one null vector in the (α-β)-(x-y) sub-spaces. The six-phase IM can be written by using a state-space model, based on the VSD technique and the dynamic reference transformation which is defined by:

$$\frac{d\mathbf{X}_{(t)}}{dt} = \mathbf{A}_{(t)}\,\mathbf{X}_{(t)} + \mathbf{B}_{(t)}\,\mathbf{U}_{(t)} + \mathbf{H}\,\varpi_{(t)} \tag{3}$$

being $\mathbf{U}_{(t)}$ the input vector of the state-space model, $\mathbf{X}_{(t)}$ the state vector and $\mathbf{A}_{(t)}$ and $\mathbf{B}_{(t)}$ are matrices determined by the electrical parameters of the six-phase IM. The process noise is defined as $\varpi_{(t)}$ and $\mathbf{H}$ is the noise weight matrix.

The state-space model, expressed in (3), and $\mathbf{X}_{(t)} = [x_1,\, x_2,\, x_3,\, x_4, x_5,\, x_6]^T$ defines the following equations:

$$\begin{aligned}
\frac{dx_1}{dt} &= -R_s c_2 x_1 + c_4\left(L_m\omega_r x_2 + R_r x_5 + L_r\omega_r x_6\right) + c_2 u_1 \\
\frac{dx_2}{dt} &= -R_s c_2 x_2 + c_4\left(-L_m\omega_r x_1 - L_r\omega_r x_5 + R_r x_6\right) + c_2 u_2 \\
\frac{dx_3}{dt} &= -R_s c_3 x_3 + c_3 u_3 \\
\frac{dx_4}{dt} &= -R_s c_3 x_4 + c_3 u_4 \\
\frac{dx_5}{dt} &= R_s c_4 x_1 + c_5\left(-L_m\omega_r x_2 - R_r x_5 - L_r\omega_r x_6\right) - c_4 u_1 \\
\frac{dx_6}{dt} &= R_s c_4 x_2 + c_5\left(L_m\omega_r x_1 + L_r\omega_r x_5 - R_r x_6\right) - c_4 u_2
\end{aligned} \tag{4}$$

where ω_r is the rotor electrical speed, R_s, R_r, L_m, $L_r = L_{lr} + L_m$ and $L_s = L_{ls} + L_m$ are the electrical parameters of the six-phase IM. The coefficients are determined as $c_1 = L_s L_r - L_m^2$, $c_2 = \frac{L_r}{c_1}$, $c_3 = \frac{1}{L_{ls}}$, $c_4 = \frac{L_m}{c_1}$ and $c_5 = \frac{L_s}{c_1}$. The input vector is constituted of the applied voltages to the stator $u_1 = v_{\alpha s}$, $u_2 = v_{\beta s}$, $u_3 = v_{xs}$, $u_4 = v_{ys}$ and the state vector corresponds to the six-phase IM stator and rotor currents $x_1 = i_{\alpha s}$, $x_2 = i_{\beta s}$, $x_3 = i_{xs}$, $x_4 = i_{ys}$, $x_5 = i_{\alpha r}$ and $x_6 = i_{\beta r}$.

Stator voltages are dependant of the input control signals. In this particular case, the simplest VSI model has been considered to achieve a good optimization process. Through this model the stator voltages can be obtained from the ideal six-phase VSI model $\mathbf{M}_{[\mathbf{S}]}$ [15].

$$\mathbf{M}_{[\mathbf{S}]} = \frac{1}{3}\begin{bmatrix} 2 & 0 & -1 & 0 & -1 & 0 \\ 0 & 2 & 0 & -1 & 0 & -1 \\ -1 & 0 & 2 & 0 & -1 & 0 \\ 0 & -1 & 0 & 2 & 0 & -1 \\ -1 & 0 & -1 & 0 & 2 & 0 \\ 0 & -1 & 0 & -1 & 0 & 2 \end{bmatrix}\mathbf{S}^T \tag{5}$$

Taking into account the ideal six-phase VSI, is possible to transform the gating signals into stator voltages which can be mapped to (α-β) and (x-y) sub-spaces and defined in $\mathbf{U}_{(t)} = [u_1,\, u_2,\, u_3,\, u_4]^T$ which yields to the following equations:

$$\mathbf{U}_{(t)} = V_{dc}\,\mathbf{T}\,\mathbf{M}_{[\mathbf{S}]} \tag{6}$$

$$\mathbf{Y}_{(t)} = \mathbf{C}\,\mathbf{X}_{(t)} + \nu_{(t)} \tag{7}$$

being $\mathbf{Y}$ the output vector, $\nu_{(t)}$ the measurement noise and $\mathbf{C}$:

$$\mathbf{C} = \begin{bmatrix} 1 & 0 & 0 & 0 & 0 & 0 \\ 0 & 1 & 0 & 0 & 0 & 0 \\ 0 & 0 & 1 & 0 & 0 & 0 \\ 0 & 0 & 0 & 1 & 0 & 0 \end{bmatrix}$$

The mechanical equations of the six-phase IM are:

$$T_e = 3P\left(\psi_{\alpha s} i_{\beta s} - \psi_{\beta s} i_{\alpha s}\right) \tag{8}$$

$$J_i \frac{d\omega_m}{dt} + B_i \omega_m = (T_e - T_L) \tag{9}$$

where B_i is the friction coefficient, J_i the inertia coefficient, T_e defines the generated torque, T_L is the load torque, ω_m is the rotor mechanical speed, $\psi_{\alpha s}$ and $\psi_{\beta s}$ are the stator fluxes, and P is the number of pole pairs.

III. PROPOSED SPEED CONTROLLER

A two degree PI controller with saturator, proposed in [12], is utilized as the external speed control loop, based on FOC control technique due to its easiness. In the FOC scheme, PI speed controller is utilized to create the reference current in dynamic reference frame. The current reference utilized by the MPC are obtained from the calculation of the electric angle used to change the current reference, initially in dynamic reference frame (d-q), to static reference frame (α-β). The process of calculation of the slip frequency (ω_{sl}) is achieved in the same way as the FOC techniques, from the reference currents in dynamic reference frame (i^*_{ds}, i^*_{qs}) and the electrical parameters of the machine (R_r, L_r), and the mechanical speed is acquired by using an encoder. A detailed block diagram of the proposed speed control technique for the six-phase IM drive is presented in Fig. 3.

A. Classic MPC

MPC uses the mathematical model of the system, namely predictive model, to predict at time $[k]$ the future values $[k{+}1]$, by using measured variables such as the stator currents and the mechanical speed.

$$\hat{\mathbf{X}}_{[k+1|k]} = \mathbf{X}_{[k]} + T_s\, f\left(\mathbf{X}_{[k]},\, \mathbf{U}_{[k]},\, \omega_{r[k]}\right) \tag{10}$$

In the state-space representation (10) only the stator currents, voltages and mechanical speed are measured. The stator voltages are easily predicted from the switching commands issued to the VSI, however, the rotor currents cannot be directly measured. This fact can be solve by means of estimating the rotor current using a reduced order estimators where the reduced order estimators provide an estimate for only the unmeasured part of the state vector. Then, in this work, the rotor current is estimated by the method proposed in [16] by using a reduced order estimator based on a Kalman filter (KF). In that sense, considering a zero-mean Gaussian measurement and uncorrelated process noises, the system's equations can be written as:

$$\hat{\mathbf{X}}_{[k+1|k]} = \mathbf{A}_{[k]}\mathbf{X}_{[k]} + \mathbf{B}_{[k]}\mathbf{U}_{[k]} + \mathbf{H}\varpi_{[k]} \tag{11}$$

$$\mathbf{Y}_{[k+1|k]} = \mathbf{C}\,\mathbf{X}_{[k+1]} + \nu_{[k+1]} \tag{12}$$

where $\mathbf{A}_{[k]}$ and $\mathbf{B}_{[k]}$ are discretized matrices from (4). $\mathbf{A}_{[k]}$ depends on the present value of $\omega_{r[k]}$ and must be considered at every sampling time. A detailed description of the dynamics of the reduced order KF can be found in [16], [17] which has not been exhibit for the sake of conciseness.

B. Cost Function

Then, the MPC performs a optimization process at every sampling time. This process consists in the evaluation of a cost function (13) for all possible stator voltages in order to achieve its control objective. As the cost function can be represented in several ways, in this paper, it is selected the minimization of the current tracking error, defined as the following equation:

$$\begin{aligned} J_{[k+2|k]} =& \parallel i^*_{\alpha s[k+2]} - \hat{i}_{\alpha s[k+2|k]} \parallel^2 + \parallel i^*_{\beta s[k+2]} - \hat{i}_{\beta s[k+2|k]} \parallel^2 \\ &+ \lambda_{xy}\left(\parallel i^*_{xs[k+2]} - \hat{i}_{xs[k+2|k]} \parallel^2 + \parallel i^*_{ys[k+2]} - \hat{i}_{ys[k+2|k]} \parallel^2\right) \end{aligned} \tag{13}$$

being $i^*_{s[k+2]}$ the vector containing the reference for the stator currents and $\hat{i}_{s[k+2]}$ the vector containing the predictions based on the second-step ahead state. In order to put more emphasis on (α-β) or (x-y) sub-spaces a tuning parameter (λ_{xy}) is used [16], [17].

C. Modulated model predictive control (M2PC)

It is feasible to determine each available vector for the VSI in the (α-β) plane, which defines 64 sectors (48 different), which are given by two adjacent vectors. The proposed technique evaluates the prediction of the two active vectors that conform each sector at every sampling time and evaluates the cost function separately for each prediction. Each prediction is evaluated based on (10) and the only difference is in the calculation of the input vector $\mathbf{U}_{[k]}$ [15]. The duty cycles, for the two active vectors d_1 and d_2, are calculated by solving the following equations:

$$d_0 = \tfrac{\sigma}{J_0} \qquad d_1 = \tfrac{\sigma}{J_1} \qquad d_2 = \tfrac{\sigma}{J_2} \tag{14}$$

$$d_0 + d_1 + d_2 = T_s \tag{15}$$

where d_0 corresponds to the duty cycle of a zero vector. Then, it is possible to obtain the expression for σ and the duty cycles for each vector given as:

$$d_0 = \frac{T_s J_1 J_2}{J_0 J_1 + J_1 J_2 + J_0 J_2} \tag{16}$$

$$d_1 = \frac{T_s J_0 J_2}{J_0 J_1 + J_1 J_2 + J_0 J_2} \tag{17}$$

$$d_2 = \frac{T_s J_0 J_1}{J_0 J_1 + J_1 J_2 + J_0 J_2} \tag{18}$$

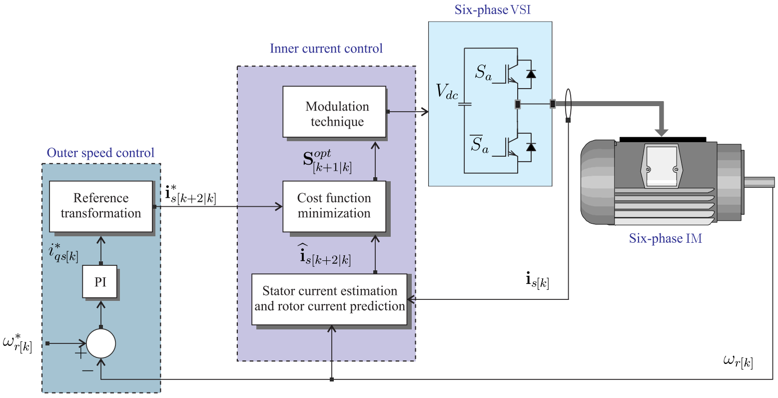

Fig. 3. Speed control with an inner current control based on predictive-fixed control and using KF for rotor current estimation.

Considering these expressions, the new cost function, which is evaluated at every T_s, is defined as:

$$G_{[k+2|k]} = d_1 J_1 + d_2 J_2 \tag{19}$$

The two vectors which minimize $G_{[k+2|k]}$ are selected and applied to the VSI at the next sampling time. After obtaining the duty cycles and selecting the optimal two vectors to be applied, a switching pattern procedure, shown in [15], is adopted with the goal of applying the two active vectors $(v_1 - v_2)$ and two zero vectors (v_0), considering the calculated duty cycles obtaining a fixed-switching frequency.

IV. EXPERIMENTAL RESULTS

A detailed block diagram of the MPC technique for the six-phase IM is provided in Fig. 3. The six-phase IM is powered by two typical three-phase VSI, using a constant DC voltage of 400 V from a DC power supply. The VSI are controlled by a dSPACE MABXII DS1401 real-time prototyping platform. The experimental results are captured and processed using MATLAB R2013b. The motor position is measured with a 1024-pulses-per-revolution incremental encoder, and then, the speed is estimated from it. A 5 HP eddy current brake is used to connect a variable mechanical load. Table I shows the electrical and mechanical parameters for the six-phase IM.

TABLE I
ELECTRICAL AND MECHANICAL PARAMETERS OF THE SIX-PHASE IM

R_r	6.9 Ω	L_s	654.4 mH
R_s	6.7 Ω	P	1
L_{ls}	5.3 mH	P_w	2 kW
L_{lr}	12.8 mH	J_i	0.07 kg.m^2
L_m	614 mH	B_i	0.0004 kg.m^2/s
L_r	626.8 mH	ω_{r-nom}	3000 rpm

In Table II and Table III, a steady state analysis for stator currents under different rotor speed references (ω^*_r), are shown with M2PC and classic MPC, respectively. A total of 7 samples are obtained to measure the MSE for (α-β), (x-y) stator currents and the mechanical rotor speed (ω_r) as well as the THD for (α-β) stator currents.

TABLE II
ANALYSIS OF N SAMPLES OF STATOR CURRENTS (α-β), (x-y), MSE [A], THD [%] FOR M2PC AT DIFFERENT ROTOR SPEEDS [RPM].

		Speed	ω^*_r =	500	[rpm]		
N	MSE$_\alpha$	MSE$_\beta$	MSE$_x$	MSE$_y$	THD$_\alpha$	THD$_\beta$	MSE$_{\omega_r}$
1	0.1140	0.1226	0.1662	0.2060	10.7	9.6	1.9233
2	0.1210	0.1199	0.1508	0.2037	10.5	9.5	1.6378
3	0.1151	0.1207	0.1653	0.2084	10.7	9.4	1.8141
4	0.1233	0.1183	0.1458	0.1981	11.0	9.7	1.8051
5	0.1171	0.1141	0.1529	0.1969	10.1	8.8	1.6634
6	0.1196	0.1158	0.1590	0.1958	10.3	9.0	1.8145
7	0.1111	0.1184	0.1691	0.2027	10.6	9.5	1.5835
		Speed	ω^*_r =	1000	[rpm]		
N	MSE$_\alpha$	MSE$_\beta$	MSE$_x$	MSE$_y$	THD$_\alpha$	THD$_\beta$	MSE$_{\omega_r}$
1	0.1546	0.1470	0.1644	0.2615	12.4	9.9	2.3932
2	0.1491	0.1432	0.1761	0.2599	12.3	9.7	2.6218
3	0.1583	0.1465	0.1677	0.2648	12.3	9.7	2.3217
4	0.1596	0.1480	0.1666	0.2630	12.5	9.9	2.3814
5	0.1594	0.1487	0.1797	0.2650	12.0	9.7	2.6432
6	0.1508	0.1487	0.1807	0.2685	12.0	10.0	2.7061
7	0.1487	0.1485	0.1771	0.2656	12.6	9.9	2.3885
		Speed	ω^*_r =	1500	[rpm]		
N	MSE$_\alpha$	MSE$_\beta$	MSE$_x$	MSE$_y$	THD$_\alpha$	THD$_\beta$	MSE$_{\omega_r}$
1	0.2044	0.1895	0.1875	0.3331	17.5	11.7	3.5112
2	0.2182	0.1908	0.1864	0.3199	18.0	12.1	2.9387
3	0.2193	0.1938	0.1820	0.3220	18.6	12.6	3.2329
4	0.2068	0.1921	0.1863	0.3204	17.8	12.0	2.9350
5	0.2197	0.1909	0.1920	0.3131	17.5	12.0	3.0535
6	0.2106	0.1926	0.1953	0.3277	17.1	12.0	3.2980
7	0.2094	0.1924	0.1907	0.3350	18.3	12.2	2.9544

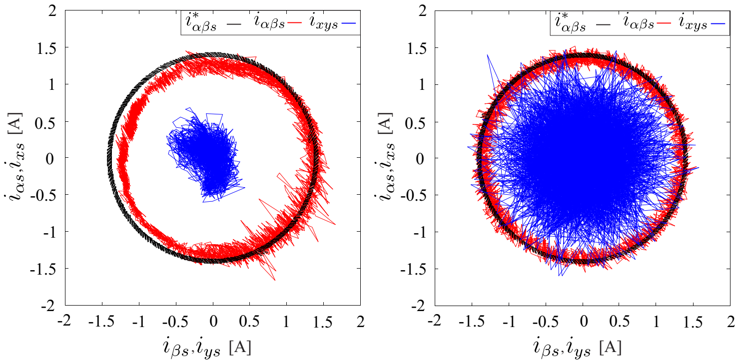

(a) (b)

Fig. 4. Stator currents in (α-β) and (x-y) sub-spaces for rotor speed of 500 [rpm] and a sampling frequency of 16 [kHz]: (a) Amplitude of 1.5 [A] for M2PC; (b) Amplitude of 1.5 [A] for classic MPC.

TABLE III
ANALYSIS OF N SAMPLES OF STATOR CURRENTS (α-β), (x-y), MSE [A], THD [%] FOR CLASSIC MPC AT DIFFERENT ROTOR SPEEDS [RPM].

		Speed	ω_r^* =	500	[rpm]		
N	MSE$_\alpha$	MSE$_\beta$	MSE$_x$	MSE$_y$	THD$_\alpha$	THD$_\beta$	MSE$_{\omega_r}$
1	0.0730	0.0719	0.4849	0.4929	8.3	8.3	1.7649
2	0.0713	0.0718	0.4825	0.4729	8.3	8.3	1.7851
3	0.0717	0.0713	0.4766	0.4771	8.5	8.2	1.9413
4	0.0726	0.0710	0.4868	0.4791	8.4	8.3	1.6323
5	0.0728	0.0713	0.4839	0.4800	8.5	8.3	1.9156
6	0.0731	0.0722	0.4835	0.4868	8.1	8.3	1.6481
7	0.0731	0.0726	0.4911	0.4839	8.2	8.0	1.6629
		Speed	ω_r^* =	1000	[rpm]		
N	MSE$_\alpha$	MSE$_\beta$	MSE$_x$	MSE$_y$	THD$_\alpha$	THD$_\beta$	MSE$_{\omega_r}$
1	0.0847	0.0837	0.5332	0.5322	7.4	7.3	2.1235
2	0.0851	0.0827	0.5298	0.5407	7.5	7.1	2.2418
3	0.0841	0.0808	0.5386	0.5408	7.4	7.1	2.2721
4	0.0848	0.0813	0.5405	0.5327	7.4	7.2	2.1209
5	0.0845	0.0833	0.5356	0.5326	7.4	7.4	1.9444
6	0.0830	0.0822	0.5434	0.5340	7.3	7.3	2.1001
7	0.0844	0.0827	0.5385	0.5347	7.5	7.3	2.1238
		Speed	ω_r^* =	1500	[rpm]		
N	MSE$_\alpha$	MSE$_\beta$	MSE$_x$	MSE$_y$	THD$_\alpha$	THD$_\beta$	MSE$_{\omega_r}$
1	0.0720	0.0706	0.5283	0.5144	7.0	6.9	3.0061
2	0.0726	0.0728	0.5190	0.5214	7.0	7.0	3.1270
3	0.0726	0.0703	0.5211	0.5101	7.6	6.9	2.9781
4	0.0706	0.0721	0.5238	0.5180	6.8	6.6	2.7550
5	0.0727	0.0727	0.5328	0.5241	7.0	6.8	3.1873
6	0.0720	0.0703	0.5239	0.5221	6.9	6.7	2.9386
7	0.0682	0.0698	0.5180	0.5134	6.8	6.7	2.5484

TABLE IV
EFFICIENCY ANALYSIS OF BOTH CONTROLLERS BASED ON STATISTICAL TEST.

AH1:	M2PC/Speed	AH2:	Classic MPC/Speed
Variables	p-value	Variables	p-value
MSE$_\alpha$	0.001	MSE$_\alpha$	0.001
MSE$_\beta$	0.001	MSE$_\beta$	0.001
MSE$_x$	0.001	MSE$_x$	0.001
MSE$_y$	0.001	MSE$_y$	0.001
THD$_\alpha$	0.001	THD$_\alpha$	0.001
THD$_\beta$	0.001	THD$_\beta$	0.001
MSE$_{\omega_r}$	0.001	MSE$_{\omega_r}$	0.001
AH3:	M2PC/Classic MPC 500 [rpm]	AH4:	M2PC/Classic MPC 1500 [rpm]
Variables	p-value	Variables	p-value
MSE$_\alpha$	0.002	MSE$_\alpha$	0.001
MSE$_\beta$	0.002	MSE$_\beta$	0.001
MSE$_x$	0.002	MSE$_x$	0.001
MSE$_y$	0.002	MSE$_y$	0.001
THD$_\alpha$	0.002	THD$_\alpha$	0.001
THD$_\beta$	0.001	THD$_\beta$	0.001
MSE$_{\omega_r}$	0.949	MSE$_{\omega_r}$	0.259

Fig. 4 exposes the (α-β) and (x-y) stator currents tracking, for M2PC and classic MPC, in steady state for the rotor speed. Fig. 5 shows the transient response for q stator current in a reversal test (speed reference changes from 500 [rpm] to -500 [rpm]) where the M2PC and classic MPC show similar response speed. The presented results in Table IV were obtained by the Mann-Whitney non-parametric statistical test using the software SPSS version 20.0. AH1 is a alternative hypothesis where the variables (MSE and THD) equality is verified for M2PC at different rotor speeds (500 [rpm] and 1000 [rpm]). By considering the obtained probability value (p-value) it can be deducted that the M2PC efficiency is better for a rotor speed of 500 [rpm] in comparison to 1000 [rpm]. After processing other data revolving different rotor speeds, it is obtained a similar result where M2PC has better performance with lower rotor speeds. AH2 is defined as the same analysis than AH1 for classic MPC, where the results are the same, a better performance at lower speed. AH3 and AH4

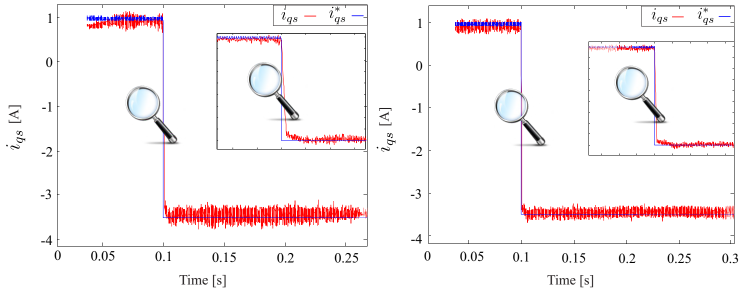

(a)

(b)

Fig. 5. Transient response in q-axis stator current for rotor speed of 500 [rpm] to -500 [rpm] and a sampling frequency of 16 [kHz]: (a) For M2PC; (b) For classic MPC.

are alternative hypothesis that compare the efficiency of both techniques (M2PC and classic MPC) at rotor speeds of 500 and 1500 [rpm], respectively. The registered p-values demonstrate a different efficiency, particularly better for classic MPC over M2PC in terms of MSE$_\alpha$, MSE$_\beta$, THD$_\alpha$ and THD$_\beta$. While M2PC efficiency is far superior for MSE$_x$ and MSE$_y$. On the other hand, for MSE$_{\omega_r}$ the p-value shows that there is not sufficient statistical evidence to reject the same efficiency for both techniques.

V. CONCLUSION

In this paper a variable-speed control with a modified predictive current control technique with fixed switching frequency (M2PC) applied to the six-phase IM is presented. The experimental and statistical results were compared between M2PC and the classic MPC and showed a better performance in the (x-y) currents reduction for M2PC. However, in the (α-β) currents tracking, M2PC had a worse performance compared to classic MPC due to a saturation effect in the measured currents. In terms of speed tracking both techniques had similar results and in the transient analysis, the response was almost the same for both techniques. It can be concluded that M2PC is a good alternative to classic MPC to improve the (x-y) currents reduction.

ACKNOWLEDGMENT

The authors wish to thank the financial support from the Paraguayan Science and Technology National Council (CONACYT) through project 14-INV-101.

REFERENCES

[1] E. Levi, “Advances in converter control and innovative exploitation of additional degrees of freedom for multiphase machines,” *IEEE Trans. Ind. Electron.*, vol. 63, no. 1, pp. 433–448, 2016.

[2] I. Subotic, N. Bodo, and E. Levi, “Integration of six-phase EV drivetrains into battery charging process with direct grid connection,” *IEEE Trans. Energy Convers.*, vol. 32, no. 3, pp. 1012–1022, 2017.

[3] M. Ayala, O. Gonzalez, J. Rodas, R. Gregor, and J. Doval-Gandoy, “A speed-sensorless predictive current control of multiphase induction machines using a Kalman filter for rotor current estimator,” in *Proc. ESARS-ITEC*, pp. 1–6, 2016.

[4] M. Jones, S. N. Vukosavic, D. Dujic, and E. Levi, “A synchronous current control scheme for multiphase induction motor drives,” *IEEE Trans. Energy Convers.*, vol. 24, no. 4, pp. 860–868, 2009.

[5] H. S. Che, M. J. Duran, E. Levi, M. Jones, W.-P. Hew, and N. A. Rahim, “Postfault operation of an asymmetrical six-phase induction machine with single and two isolated neutral points,” *IEEE Trans. Power Electron.*, vol. 29, no. 10, pp. 5406–5416, 2014.

[6] S. Vazquez, J. Rodriguez, M. Rivera, L. G. Franquelo, and M. Norambuena, “Model predictive control for power converters and drives: Advances and trends,” *IEEE Trans. on Ind. Electron.*, vol. 64, no. 2, pp. 935–947, 2016.

[7] M. Vijayagopal, P. Zanchetta, L. Empringham, L. De Lillo, L. Tarisciotti, and P. Wheeler, “Modulated model predictive current control for direct matrix converter with fixed switching frequency,” in *Proc. EPE*, 2015, pp. 1–10, 2015.

[8] F. Gavilan, D. Caballero, S. Toledo, E. Maqueda, R. Gregor, J. Rodas, M. Rivera, and I. Araujo-Vargas, “Predictive power control strategy for a grid-connected 2L-VSI with fixed switching frequency,” in *Proc. ROPEC*, pp. 1–6, 2016.

[9] S. Toledo, M. Rivera, J. Muñoz, R. Peña, J. Riveros, and R. Gregor, “Fixed switching frequency predictive control for a multi-drive indirect matrix converter system,” in *Proc. SPEC*, pp. 1–6, 2017.

[10] M. Rivera, S. Toledo, C. Baier, L. Tarisciotti, P. Wheeler, and S. Verne, “Indirect predictive control techniques for a matrix converter operating at fixed switching frequency,” in *Proc. PRECEDE*, pp. 13–18, 2017.

[11] L. Comparatore, R. Gregor, J. Rodas, J. Pacher, A. Renault, and M. Rivera, “Model based predictive current control for a three-phase cascade H-bridge multilevel STATCOM operating at fixed switching frequency,” in *Proc. PEDG*, pp. 1–6, 2017.

[12] L. Harnefors, S. Saarakkala, and M. Hinkkanen, “Speed control of electrical drives using classical control methods,” *IEEE Trans. Ind. Appl.*, vol. 49, no. 2, pp. 889–898, 2013.

[13] H. B. Mann and D. R. Whitney, “On a test of whether one of two random variables is stochastically larger than the other,” *The annals of mathematical statistics*, pp. 50–60, 1947.

[14] Y. Zhao and T. Lipo, “Space vector PWM control of dual three-phase induction machine using vector space decomposition,” *IEEE Trans. Ind. Electron.*, vol. 31, no. 5, pp. 1100–1109, 1995.

[15] M. Ayala, J. Rodas, R. Gregor, J. Doval-Gandoy, O. Gonzalez, M. Saad, and M. Rivera, “Comparative study of predictive control strategies at fixed switching frequency for an asymmetrical six-phase induction motor drive,” in *Proc. IEMDC*, pp. 1–8, 2017.

[16] J. Rodas, F. Barrero, M. R. Arahal, C. Martin, and R. Gregor, “On-line estimation of rotor variables in predictive current controllers: A case study using five-phase induction machines,” *IEEE Trans. Ind. Electron.*, vol. 63, no. 9, pp. 5348–5356, 2016.

[17] J. Rodas, C. Martin, M. R. Arahal, F. Barrero, and R. Gregor, “Influence of covariance-based ALS methods in the performance of predictive controllers with rotor current estimation,” *IEEE Trans. Ind. Electron.*, vol. 64, no. 4, pp. 2602–2607, 2017.

ARTÍCULO 7

PREDICTIVE-FIXED SWITCHING CURRENT CONTROL STRATEGY APPLIED TO SIX-PHASE INDUCTION MACHINE

- Osvaldo González, **Magno Ayala**, Jesus Doval-Gandoy, Jorge Rodas, Raul Gregor and Marco Rivera, ”Predictive-Fixed Switching Current Control Strategy Applied to Six-Phase Induction Machine”, Energies, pp. 1-14, DOI: 10.3390/en12122294, 2019.

energies

Article

Predictive-Fixed Switching Current Control Strategy Applied to Six-Phase Induction Machine

Osvaldo Gonzalez [1,*], **Magno Ayala** [1], **Jesus Doval-Gandoy** [2], **Jorge Rodas** [1], **Raul Gregor** [1] and **Marco Rivera** [3]

[1] Laboratory of Power and Control Systems (LSPyC), Facultad de Ingeniería, Universidad Nacional de Asunción, Luque 2060, Paraguay; mayala@ing.una.py (M.A.); jrodas@ing.una.py (J.R.); rgregor@ing.una.py (R.G.)
[2] Applied Power Electronics Technology Research Group (APET), Universidad de Vigo, 363310 Vigo, Spain; jdoval@uvigo.es
[3] Laboratory of Energy Conversion and Power Electronics, Universidad de Talca, 3340000 Curicó, Chile; marcoriv@utalca.cl
* Correspondence: ogonzalez@ing.una.py; Tel.: +59-598-370-1765

Received: 27 April 2019; Accepted: 30 May 2019; Published: 15 June 2019

Abstract: In applications such as multiphase motor drives, classical predictive control strategies are characterized by a variable switching frequency which adds high harmonic content and ripple in the stator currents. This paper proposes a model predictive current control adding a modulation stage based on a switching pattern with the aim of generating a fixed switching frequency. Hence, the proposed controller takes into account the prediction of the two adjacent active vectors and null vector in the (α-β) frame defined by space vector modulation in order to reduce the (x-y) currents according to a defined cost function at each sampling period. Both simulation and experimental tests for a six-phase induction motor drive are provided and compared to the classical predictive control to validate the feasibility of the proposed control strategy.

Keywords: multiphase induction machine; model predictive control; fixed switching frequency

1. Introduction

In recent years, multiphase induction machines (IMs) have been considered to be such a viable alternative in comparison to three-phase machines due to their fault tolerance capabilities with no extra hardware, lower torque ripple and better power splitter per phase which result very attractive to the research community for various industrial applications where a high-performance control strategy, as well as, reliability are required [1]. Presently, some applications of multiphase IMs that are being investigated include wind energy generation system [2], hybrid electric vehicles (EV) [3] and ship propulsion. In the applications mentioned above, multiphase IMs can be used under different conditions, such as healthy and post-fault operations [4,5]. From the point of view of control, the most common control strategy to regulate multiphase IMs is the field-oriented control (FOC), which is constituted by an inner current control loop, to obtain the references voltages, and an outer speed control loop for speed regulation [6]. However, several new control approaches have been carried out for the inner current control loop in multiphase IMs, some of them are: sliding mode control [7], resonant control [8] and model predictive control (MPC) [9]. Although there are other controllers such as the well-known proportional-integral (PI) controllers [10], the preferred choice is the MPC due to the fact that it shows a good transient behavior and facilitates the inclusion of nonlinearities in the system as described in [11,12], and in [13] where a comparative study between MPC and PI-PWM control has been addressed. In this context, the MPC strategy produces the reference voltage through the instantaneous discrete states of the power converter according to the minimization of a predefined cost function. However, the classic MPC strategy presents some limitations regarding to the application of only one vector in the whole sampling period. This results in current ripples as well as large voltages at low sampling frequency. Besides, the variable switching frequency develops a spread spectrum, decreasing the performance of the system in terms of useful power [14].

To overcome this subject, a predictive-fixed switching current control strategy, named (PFSCCS) from now on, applied to a two-level six-phase voltage source inverter (VSI) is presented in this paper. The strategy is based on a modulation concept employed with the MPC scheme, which has been studied for different power converters such as the mentioned two-level six-phase VSI described in [15,16] and also other topologies presented in [17,18]. In the proposed current strategy, three vectors have been considered at every sampling period, composed by two active vectors (taking only into account the largest vectors) and null vector, where their corresponding duty cycles are achieved according to the switching states and a switching pattern has also been used before being applied to VSI in order to generate a fixed switching frequency. Whereas, for the speed control loop, a PI controller has been developed by a technique shown in [19].

The main focus of this work is the implementation of the PFSCCS so as to reduce the (x-y) currents compared to the classic MPC strategy using a six-phase IM supplied through a two-level six-phase VSI. In that context, both simulation and experimental validations have been included to demonstrate the capability of the proposed technique. In addition, the effectiveness of the PFSCCS is tested under steady-state and transient requirements, respectively, incorporating the mean square error (MSE) and the total harmonic distortion (THD) analysis.

The paper is organized as follows: the model of the six-phase IM and VSI are presented in Section 2. In Section 3 are described the speed controller, classic MPC and the proposed current controller based on modulated model predictive control. Section 4 shows the performance of the proposed control through simulation and experimental results in steady-state and transient conditions. Finally, Section 5 summarizes the conclusion.

2. Six-Phase IM Drive Model

The six-phase IM, supplied by a two-level six-phase VSI with a DC-Link voltage source (V_{dc}), is taken into account in this work. The simplified topology is presented in Figure 1. The six-phase IM is a dependant of time system, for this reason it is possible to represent it through a group of equations in order to define a model of the real system.

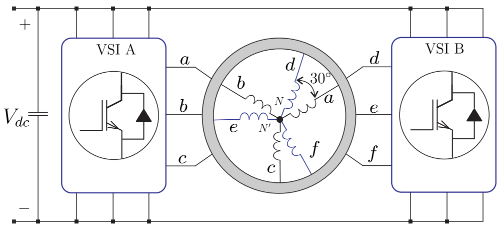

Figure 1. Six-phase IM topology supplied trough a two-level six-phase VSI.

In that sense, vector space decomposition (VSD) strategy [20] has been used to translate the actual six dimensional plane, formed through the six phases of the six-phase IM, into three two dimensional rectangular sub-spaces in the stationary reference frame, named as (α-β), (x-y) and (z_1-z_2) frame, by applying the amplitude invariant decoupling Clarke conversion matrix T [21]. The (α-β) frame contains the variables that provide the torque and flux regulation, unlike the (x-y) frame which is linked with the energy losses. The zero elements mapped in the (z_1-z_2) frame are not examined due to the adopted topology (isolated neutral points).

$$T = \frac{1}{3} \left(\begin{array}{cccccc} \cos(0) & \cos(\frac{\pi}{6}) & \cos(\frac{2\pi}{3}) & \cos(\frac{5\pi}{6}) & \cos(\frac{4\pi}{3}) & \cos(\frac{3\pi}{2}) \\ \sin(0) & \sin(\frac{\pi}{6}) & \sin(\frac{2\pi}{3}) & \sin(\frac{5\pi}{6}) & \sin(\frac{4\pi}{3}) & \sin(\frac{3\pi}{2}) \\ \cos(0) & \cos(\frac{5\pi}{6}) & \cos(\frac{10\pi}{3}) & \cos(\frac{25\pi}{6}) & \cos(\frac{20\pi}{3}) & \cos(\frac{15\pi}{2}) \\ \sin(0) & \sin(\frac{5\pi}{6}) & \sin(\frac{10\pi}{3}) & \sin(\frac{25\pi}{6}) & \sin(\frac{20\pi}{3}) & \sin(\frac{15\pi}{2}) \\ 1 & 0 & 1 & 0 & 1 & 0 \\ 0 & 1 & 0 & 1 & 0 & 1 \end{array} \right) \begin{array}{c} \alpha \\ \beta \\ x \\ y \\ z_1 \\ z_2 \end{array} \tag{1}$$

Moreover, the model of the VSI must be included in the system. Thus, due to the discrete nature of the VSI, it is necessary to define an amount of 2^6 different switching states which represent every state of each VSI leg specified as $S_m = (S_a, ..., S_f)$, where S_m is considered as binary number, i.e., $S_m = 0$ or $S_m = 1$. Therefore, the stator phase voltages can be projected into (α-β)-(x-y) frame by considering the vector S_m and the V_{dc} voltage employing the VSD strategy. In Figure 2, the 64 control alternatives (48 active and one null vectors) are depicted in the (α-β)-(x-y) frame.

By considering the mentioned analysis, the six-phase IM can be performed by employing the state-space representation as follows:

$$x'(t) = \underbrace{\begin{pmatrix} -R_s r_2 & r_4 L_m \omega_r & 0 & 0 & r_4 R_r & r_4(L_{lr} + L_m)\omega_r \\ r_4 L_m \omega_r & -R_s r_2 & 0 & 0 & r_4(L_{lr} + L_m)\omega_r & r_4\, R_r \\ 0 & 0 & -R_s r_3 & 0 & 0 & 0 \\ 0 & 0 & 0 & -R_s r_3 & 0 & 0 \\ R_s r_4 & -r_5 L_m \omega_r & 0 & 0 & -r_5 R_r & -c_5(L_{lr} + L_m) \\ -r_5 L_m \omega_r & R_s r_4 & 0 & 0 & -r_5(L_{lr} + L_m) & -r_5\, R_r \end{pmatrix}}_{M_1(t)} x(t) +$$

$$\underbrace{\begin{pmatrix} r_2 & 0 & 0 & 0 \\ 0 & r_2 & 0 & 0 \\ 0 & 0 & r_3 & 0 \\ 0 & 0 & 0 & r_3 \\ -r_4 & 0 & 0 & 0 \\ 0 & -r_4 & 0 & 0 \end{pmatrix}}_{M_2(t)} u(t) + K_n\, v(t) \tag{2}$$

being $x(t) = (x_1, ..., x_6)^T$ the state vector constituted by stator-rotor currents of the six-phase IM, shown in Equation (3), $u(t) = (u_1, ..., u_4)^T$ is the input vector constituted by the stator voltages, presented in Equation (4). While $M_1(t)$ and $M_2(t)$ are matrices obtained by the electrical parameters of the six-phase IM. The process noise is defined as $v(t)$ and K_n represents the noise weight matrix.

$$x_1 = i_{\alpha s}, \quad x_2 = i_{\beta s}, \quad x_3 = i_{xs}, \quad x_4 = i_{ys}, \quad x_5 = i_{\alpha r}, \quad x_6 = i_{\beta r}. \tag{3}$$

$$u_1 = u_{\alpha s}, \quad u_2 = u_{\beta s}, \quad u_3 = u_{xs}, \quad u_4 = u_{ys}. \tag{4}$$

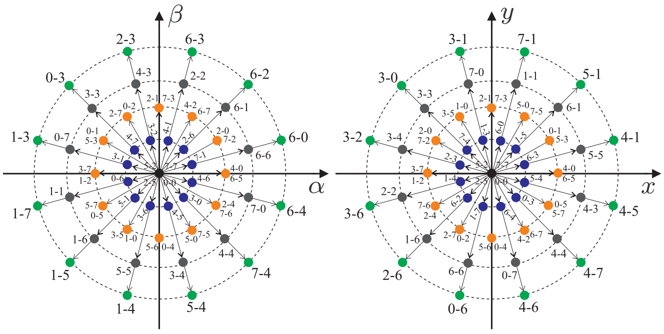

Figure 2. Mapping of the space vectors in the (α-β)-(x-y) frame for a two-level six-phase VSI.

Consequently, by taking into account the state-space representation in Equation (2) and the state vectors, it is feasible to establish the following equations:

$$\begin{aligned}
x_1' &= -R_s r_2 x_1 + r_4\left[L_m \omega_r x_2 + R_r x_5 + (L_{lr}+L_m)\omega_r x_6\right] + r_2 u_1\\
x_2' &= -R_s r_2 x_2 + r_4\left[-L_m \omega_r x_1 - (L_{lr}+L_m)\omega_r x_5 + R_r x_6\right] + r_2 u_2\\
x_3' &= -R_s r_3 x_3 + r_3 u_3\\
x_4' &= -R_s r_3 x_4 + r_3 u_4\\
x_5' &= R_s r_4 x_1 + r_5\left[-L_m \omega_r x_2 - R_r x_5 - (L_{lr}+L_m)\omega_r x_6\right] - r_4 u_1\\
x_6' &= R_s r_4 x_2 + r_5\left[L_m \omega_r x_1 + (L_{lr}+L_m)\omega_r x_5 - R_r x_6\right) - r_4 u_2
\end{aligned} \tag{5}$$

where the electrical variables of the six-phase IM are represented by R_s, R_r, L_m, L_{lr} and L_{ls}, ω_r represents the rotor electrical speed and the coefficients ($r_1, \dots, r_5$) are defined as:

$$r_1 = (L_{ls}+L_m)(L_{lr}+L_m) - L_m^2, \quad r_2 = \frac{L_{lr}+L_m}{r_1}, \quad r_3 = \frac{1}{L_{ls}}, \quad r_4 = \frac{L_m}{r_1}, \quad r_5 = \frac{L_{ls}+L_m}{r_1}. \tag{6}$$

Besides, in order to produce the stator phase voltages, which are dependant of the V_{dc} voltage and the vector S_m, an ideal six-phase VSI has been used [21] as it is defined in Equation (7).

$$M_{VSI} = \frac{1}{3}\begin{pmatrix} 2 & 0 & -1 & 0 & -1 & 0\\ 0 & 2 & 0 & -1 & 0 & -1\\ -1 & 0 & 2 & 0 & -1 & 0\\ 0 & -1 & 0 & 2 & 0 & -1\\ -1 & 0 & -1 & 0 & 2 & 0\\ 0 & -1 & 0 & -1 & 0 & 2 \end{pmatrix}\begin{pmatrix} S_a\\ S_b\\ S_c\\ S_d\\ S_e\\ S_f \end{pmatrix}. \tag{7}$$

In turn, the stator phase voltages can be mapped into (α-β)-(x-y) frames defined as follows:

$$\begin{pmatrix} u_{\alpha s}\\ u_{\beta s}\\ u_{xs}\\ u_{ys} \end{pmatrix} = V_{dc}\, T\, M_{VSI} \tag{8}$$

$$\begin{pmatrix} i_{\alpha s}\\ i_{\beta s}\\ i_{xs}\\ i_{ys} \end{pmatrix} = \begin{pmatrix} 1 & 0 & 0 & 0 & 0 & 0\\ 0 & 1 & 0 & 0 & 0 & 0\\ 0 & 0 & 1 & 0 & 0 & 0\\ 0 & 0 & 0 & 1 & 0 & 0 \end{pmatrix} x(t) + n(t) \tag{9}$$

where Equation (9) is considered the output vector, denoted by $y(t)$, and $n(t)$ is the measurement noise. Finally, the mechanical equations of the six-phase IM are specified as:

$$T_e = P\left(\psi_{\alpha s} i_{\beta s} - \psi_{\beta s} i_{\alpha s}\right) 3 \tag{10}$$

$$J_i \omega'_m + B_i \omega_m = (T_e - T_L) \tag{11}$$

where J_i defines the inertia coefficient, B_i is the friction coefficient, T_e represents the generated torque, T_L is the load torque, ω_m is the rotor mechanical speed, which is related to the rotor electrical speed as $\omega_r = P\omega_m$, $\psi_{\alpha s}$ and $\psi_{\beta s}$ are the stator fluxes, and P is the number of pole pairs.

3. Drive Control

A complete diagram of the PFSCCS for the six-phase IM drive is shown in Figure 3, where the outer speed control and the proposed inner current control will be detailed in the following sections.

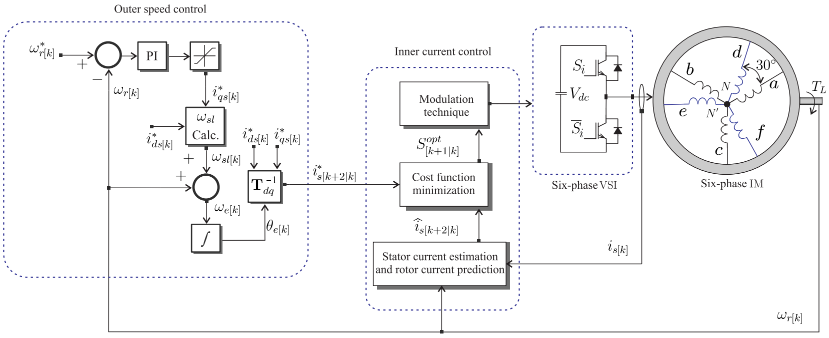

Figure 3. Complete diagram of the PFSCCS applied to six-phase IM.

3.1. Speed Control

For the external speed control loop a two degree PI controller has been incorporated, described in [19], which is based on the FOC strategy due to its easiness. Into the FOC strategy, the reference current is generated by the PI speed controller in the dynamic reference frame, known as *d*-*q* frame. Then, the reference currents are achieved by the calculation of the electric angle employed to convert the current reference, at the beginning in *d*-*q* frame, to the static reference frame (α-β), which are needed for the MPC. This method estimates the slip frequency (ω_{sl}) which is executed in the same manner as the FOC strategies, by using the reference currents in the dynamic reference frame (i^*_{ds}, i^*_{qs}) and the electrical parameters of the IM (R_r, L_r), while the rotor mechanical speed is acquired through an encoder.

3.2. Classic MPC

The MPC is related to the mathematical model of a given system, the six-phase IM in this case, commonly termed as predictive model, which consists of the prediction of the future action (at time k) of the system through measured variables, such as the rotor mechanical speed and the stator currents. Hence, for that purpose a forward Euler discretization strategy has been implemented.

$$x^p[k+1|k] = x[k] + T_s\, f(x[k],\, u[k],\, \omega_r[k]) \tag{12}$$

being k the actual sample and T_s the sampling period. Superscript p represents the predicted variables of the system.

According to the state-space representation (12), the stator currents and the rotor mechanical speed can be measured. Thus, the stator voltages are directly predicted through the switching states of the six-phase VSI. Nevertheless, the rotor currents are not easily measured. This issue can be faced through the estimation of the rotor currents by a reduced order estimator which determines the unmeasured fraction of the state vector. Then, in this work, the rotor currents are estimated by the proposed strategy in [22] which employs a reduced order estimator based on a Kalman Filter (KF). In that sense, uncorrelated process noises and a zero-mean Gaussian measurement have been considered. Finally, the the studied system equations are established as:

$$x^p[k+1|k] = M_1[k]x[k] + M_2[k]u[k] + K_n v[k] \tag{13}$$

$$y[k+1|k] = \begin{pmatrix} 1 & 0 & 0 & 0 & 0 & 0 \\ 0 & 1 & 0 & 0 & 0 & 0 \\ 0 & 0 & 1 & 0 & 0 & 0 \\ 0 & 0 & 0 & 1 & 0 & 0 \end{pmatrix} x[k+1] + n[k+1] \tag{14}$$

where $M_1[k]$ and $M_2[k]$ represent the discretized matrices since (5). $M_1[k]$ is related to the current value of $\omega_r[k]$ and must be included at every sampling period. A completed explanation of the aforementioned reduced order KF is presented in [22,23].

Cost Function

The optimization action is carried out at every sampling period by the MPC strategy. The action is based on the evaluation of a defined cost function, shown in (15), for every feasible stator voltages in order to obtain the control purpose. Since the cost function can be expressed in various manners, in this work, the minimization of the current tracking error has been taken into account specified by the following equation:

$$CF[k+2|k] = \sqrt{(e_{\alpha s})^2 + (e_{\beta s})^2} + \lambda_{xy}\sqrt{(e_{xs})^2 + (e_{ys})^2} \tag{15}$$

being the errors defined as follows:

$$\begin{aligned} e_{\alpha s} &= i^*_{\alpha s}[k+2] - i^p_{\alpha s}[k+2|k], \\ e_{\beta s} &= i^*_{\beta s}[k+2] - i^p_{\beta s}[k+2|k], \\ e_{xs} &= i^*_{xs}[k+2] - i^p_{xs}[k+2|k], \\ e_{ys} &= i^*_{ys}[k+2] - i^p_{ys}[k+2|k]. \end{aligned} \tag{16}$$

considering $i^*_s[k+2]$ as the reference vector for the stator currents and $i^p_s[k+2]$ as the predicted values based on the second-step forward state. At the same time, a tuning parameter is included in the cost function, described as λ_{xy}, in order to provide an extra weight on (α-β) or (x-y) frames [22,23].

3.3. *Proposed Current Controller (Pfsccs)*

According to the space vector modulation (SVM) strategy, it is feasible to find the available vectors for the six-phase VSI in the (α-β) frame, this produces 64 sectors (48 different ones), which are conformed by two active vectors and a null vector as depicted in Figure 4. The proposed strategy realizes the prediction of the vectors (null vector and two active vectors) that compose every sectors and calculates the cost function independently (G_0, G_1 and G_2) for each prediction at every sampling period. However, the proposed strategy only select the twelve largest vectors including the null vector in order to represent the optimal vector. This current control approach has been adopted in order to reduce the (x-y) currents [24,25].

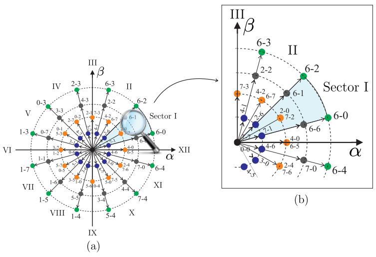

Figure 4. Considered sectors for the six-phase VSI in the (α-β) frame: (**a**) Available vectors; (**b**) A selected specific sector shown as zoom.

The prediction is obtained by Equation (13), but differs in the calculation of the input vector ($u[k]$) [21]. The duty cycles (d_c), considering the null vector and the two active vectors (d_{c-0}, d_{c-1} and d_{c-2}), respectively, are achieved through the following equations:

$$d_{c-0} = \frac{\mu}{G_0}, \qquad d_{c-1} = \frac{\mu}{G_1}, \qquad d_{c-2} = \frac{\mu}{G_2}, \tag{17}$$

$$d_{c-0} + d_{c-1} + d_{c-2} = 1, \tag{18}$$

Hence, it is possible to acquire the relation for μ and the duty cycles for the specified vectors as:

$$d_{c-0} = \frac{G_1G_2}{G_0G_1 + G_1G_2 + G_0G_2}, \tag{19}$$

$$d_{c-1} = \frac{G_0G_2}{G_0G_1 + G_1G_2 + G_0G_2}, \tag{20}$$

$$d_{c-2} = \frac{G_0G_1}{G_0G_1 + G_1G_2 + G_0J_2}. \tag{21}$$

Taking account these relations, the cost function is redefined, as shown in Equation (22), and calculated at each T_s.

$$CF_n[k+2|k] = d_{c-1}G_1 + d_{c-2}G_2. \tag{22}$$

In this way, the two vectors that reduce $CF_n[k+2|k]$ are chosen and then applied to the VSI at the following sampling period. Once the optimal vectors are obtained, the two active vectors (v_1-v_2) and null vector (v_0), their respective duty cycles to be applied and a switching pattern scheme, described in [21], are taken with the aim of producing a fixed switching frequency.

4. Simulation and Experimental Results

First, simulations have been performed in a MATLAB/Simulink R2014a environment so as to verify the feasibility of the PFSCCS using a six-phase IM shown in Figure 1. Numerical integration using first order Euler's algorithm has been applied to calculate the progress of the studied system. The simulation parameters of the six-phase IM are listed in Table 1.

Table 1. Characteristics of the six-phase IM.

R_r	6.9 Ω	L_s	654.4 mH
L_{lr}	12.8 mH	L_r	626.8 mH
L_{ls}	5.3 mH	P_w	2 kW
R_s	6.7 Ω	J_i	0.07 kg.m^2
L_m	614 mH	B_i	0.0004 kg.m^2/s
P	1	ω_{r-nom}	3000 rpm

The effectiveness of the presented control technique for the six-phase IM has been evaluated under a load condition ($T_L = 2$ Nm), the sampling frequency is 8 kHz, V_{dc} is 400 V and the d-axis current reference (i_{ds}^*) has been set in 1 A, while for the gains of the two degree PI controller with a saturation, can be found in [19]. Moreover, for the proposed control, $\lambda_{xy} = 0.1$, defined in (15), has been used in order to give more emphasis to the (α-β) stator current tracking.

The performance of the proposed technique is compared in transient and steady-state conditions. Both proofs, simulation and experimental results, are analyzed in terms of mean squared error (MSE) and total harmonic distortion (THD) obtained between the reference and the measured stator currents in the (α-β) and (x-y) sub-spaces for MSE test and the THD is obtained in the (α-β) sub-space. The MSE is computed as follows:

$$\text{MSE}(i_{\sigma s}) = \sqrt{\frac{1}{N}\sum_{j=1}^{N}(i_{\sigma s} - i_{\sigma s}^*)^2} \tag{23}$$

where the stator current reference is represented through the superscript $*$, the measured stator current is defined by $i_{\sigma s}$ taking into account that σ includes the (α-β)-(x-y) frame and N is the number of studied samples. While, the THD is obtained as follows:

$$\text{THD}(i_s) = \sqrt{\frac{1}{i_{s1}^2}\sum_{k=2}^{N}(i_{sk})^2} \tag{24}$$

where i_{s1} corresponds to the fundamental stator current whereas i_{sk} is the harmonic stator current (multiple of the fundamental stator current).

In Figure 5 the performance of the stator currents in the (α-β)-(x-y) frame can be seen in steady-state condition. According to the simulations results, shown in Table 2, the proposed technique has a good behavior considering the MSE and THD analysis of the stator currents at different rotor mechanical speeds. In addition, it can be noticed that at lower speeds, the stator currents ripple in the (α-β) frame is slightly smaller than at higher mechanical rotor speeds, in the same way that occurs for the (x-y) currents.

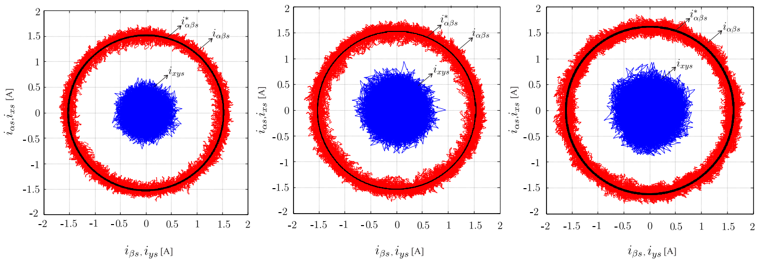

(**a**) (**b**) (**c**)

Figure 5. Simulation performance in steady-state condition of stator currents in (α-β) and (x-y) sub-spaces for a sampling frequency of 8 kHz at different speeds (ω_m): (**a**) 500 rpm; (**b**) 1000 rpm; (**c**) 1500 rpm.

Table 2. Simulation performance test of stator currents (α-β), (x-y), MSE (A), THD (%) at different rotor speeds (rpm).

f_s = 8 kHz						
ω_m^*	MSE$_\alpha$	MSE$_\beta$	MSE$_x$	MSE$_y$	THD$_\alpha$	THD$_\beta$
500	0.065	0.064	0.174	0.172	5.73	5.46
1000	0.076	0.075	0.211	0.203	5.43	5.34
1500	0.110	0.110	0.219	0.216	6.46	6.38

For the experimental proofs the PFSCCS, previously described, is examined in the test rig shown in Figure 6 in order to prove its effectiveness, employing a six-phase IM supplied through two tradictional three-phase VSI, being analogous to a six-phase VSI and the V_{dc} voltage is obtained by means of a DC power source. A dSPACE MABXII DS1401 real-time rapid prototyping bench including Simulink version 8.2 has been used to manage the two-level six VSI. Once the results are acquired, these have been analyzed through MATLAB/Simulink R2014a code. Employing stand-still with VSI proofs and AC time domain strategies, the electrical parameters have been acquired [26,27]. Table 1 summarizes these results. Current sensors LA 55-P s (frequency bandwidth since DC up to 200 kHz) have been used for the experimental measurements. The current measurements have been then turned to digital format by means of a 16-bit A/D converter. The six-phase IM angle has been measured with a 1024-pulses per revolution (ppr) incremental encoder in order to estimate the rotor speed and also a 5 HP eddy current brake has been used to insert a fixed mechanical load on the system.

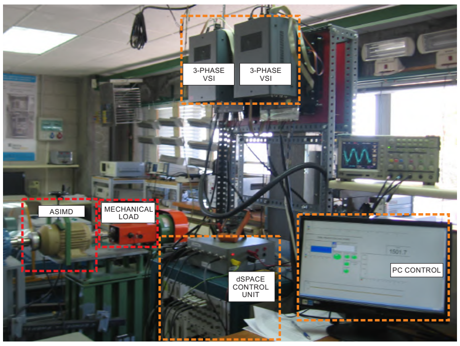

Figure 6. Experimental test rig.

Taking this into account, the experimental results have been analyzed with the same tests that simulations results as figures of merit. The stator currents reference in the (x-y) frame have been established to zero, i.e., $i_{xs}^* = i_{ys}^* = 0$ A so as to decrease the losses in the copper. The amounts for the process noise ($\hat{Q}_w = 0.0022$) and the measurement noise ($\hat{R}_v = 0.0022$) is estimated by means of the strategy proposed in [23]. The dynamic behavior of the proposed technique has been evaluated with two different values of λ_{xy}, defined in (15), giving more weight to (α-β) stator currents tracking. In the developed tests, the sampling frequencies have been fixed in 8 kHz for PFSCCS and 8 kHz and 16 kHz for classic MPC, respectively, due to the fact that the PFSCCS uses two active vectors and null vector twice in a sampling period and this procedure doubles the switching frequency compared to the sampling frequency. In that sense, tests have been included in order to expose a fair comparison between the classic MPC and PFSCCS at the mentioned sampling frequencies and also to show the performance of both techniques. For the rotor mechanical speeds, two operation points have been considered, 500 rpm and 1000 rpm, respectively, in steady-state condition. Furthermore, for a transient response, a reversal rotor mechanical speed test from 500 rpm to -500 rpm has been considered for PFSCCS and from 1500 rpm to 200 rpm for classic MPC and PFSCCS. The obtained results between classic MPC and PFSCCS are reported in Table 3, where the proposed current control technique has demonstrated a good tracking of the current references considering the MSE and THD in the (α-β)-(x-y) frame.

Table 3. Experimental performance test of stator currents (α-β), (x-y), MSE (A), THD (%) between classic MPC and the PFSCCS at different rotor speeds (rpm).

f_s = 8 kHz for Classic MPC						
ω_m^*	MSE$_\alpha$	MSE$_\beta$	MSE$_x$	MSE$_y$	THD$_\alpha$	THD$_\beta$
500	0.140	0.130	0.821	0.822	8.30	8.40
1000	0.147	0.138	0.953	0.934	7.40	7.30
f_s = 16 kHz for Classic MPC						
ω_m^*	MSE$_\alpha$	MSE$_\beta$	MSE$_x$	MSE$_y$	THD$_\alpha$	THD$_\beta$
500	0.073	0.072	0.491	0.483	8.40	8.30
1000	0.084	0.082	0.538	0.534	7.50	7.40
f_s = 8 kHz for PFSCCS						
ω_m^*	MSE$_\alpha$	MSE$_\beta$	MSE$_x$	MSE$_y$	THD$_\alpha$	THD$_\beta$
500	0.042	0.045	0.135	0.130	4.89	5.08
1000	0.069	0.068	0.197	0.204	4.69	4.78

Figure 7 presents the trajectories of the stator currents in the (α-β)-(x-y) frame of the PFSCCS applied to the six-phase IM. In this test two different values of the tuning parameter (λ_{xy}) have been considered, in Figure 7a, λ_{xy} = 0.05 has been considered and λ_{xy} = 0.1 in Figure 7b. The rotor mechanical speed has been set to 500 rpm at 8 kHz. The figure shows that (x-y) currents decrease when λ_{xy} increases, which imply that the selection of this parameter has a strong influence on the behavior of the system. Further, the (α-β) current tracking has a slightly better performance considering λ_{xy} = 0.1.

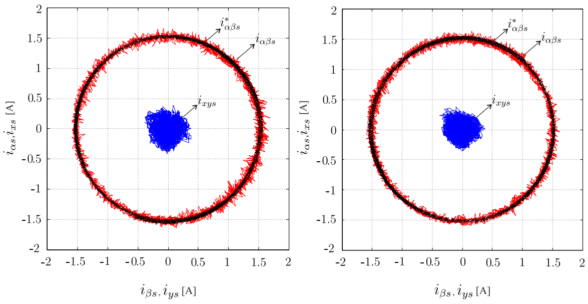

(**a**) (**b**)

Figure 7. Experimental results in the (α-β)-(x-y) frame for stator currents at 8 kHz of sampling frequency and 500 rpm rotor speed considering: (**a**) λ_{xy} = 0.05; (**b**) λ_{xy} = 0.1.

In addition, Figure 8a shows the harmonic content of the measured stator current ($i_{\alpha s}$) through THD analysis and also, in Figure 8b has been included the switching voltage in the six-phase VSI showing the pattern of the proposed modulation strategy.

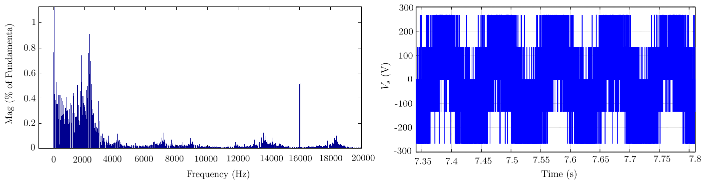

(**a**) (**b**)

Figure 8. Experimental performance for PFSCCS at 8 kHz of sampling frequency and 500 rpm: (**a**) Spectrum of the measured stator current; (**b**) Switching pattern in the VSI.

On the other hand, Figure 9 exposes the transient response of the proposed control for a step response in q axis. The transient response has been included through a reversal test from rotor mechanical speed (500 rpm to -500 rpm) at 8 kHz. Both cases report fast responses considering the overshoot and settling time, which were of 6.14% and 6 ms, respectively, for Figure 9a and 4.85% and 6.12 ms, respectively for Figure 9b. The criterion of the 5% has been selected. Finally, a experimental transient response from a step change of 1500 rpm to 200 rpm between classic MPC and PFSCCS has been depicted in Figure 10 in order to show the performance of the proposed strategy, which it has demonstrated that it can be used in industrial applications (e.g., regenerating braking).

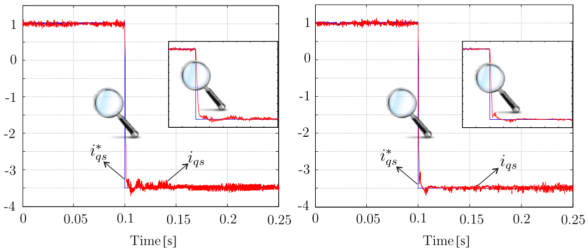

(**a**) (**b**)

Figure 9. Experimental transient test in q-axis of stator currents from a speed change of 500 rpm to -500 rpm at 8 kHz of sampling frequency considering: (**a**) λ_{xy} = 0.05; (**b**) λ_{xy} = 0.1.

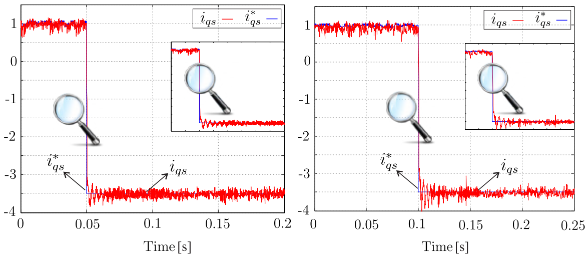

(**a**) (**b**)

Figure 10. Experimental transient test in q-axis of stator currents from a speed change of 1500 rpm to 200 rpm at 16 kHz and 8 kHz of sampling frequency, respectively: (**a**) Classic MPC; (**b**) PFSCCS.

5. Conclusions

In this paper, a predictive current control technique with a fixed switching frequency applied to a six-phase IM has been proposed. This technique has been developed to reduce the stator currents in the (x-y) frame using the largest vectors of the (α-β) frame with a stage of modulation based on a determined switching pattern in order to produce a fixed switching frequency. The simulation and experimental results have shown the performance of the proposed technique, where the system has been tested under different conditions (steady and transient conditions) including different rotor mechanical speeds, sampling frequency and tuning parameters for (x-y) stator currents, respectively. In terms of (α-β) currents tracking, the presented technique has a better behavior at lower speed and a remarkable reduction of (x-y) stator currents compared to classic MPC. The obtained results have also demonstrated a good transient current behavior in terms of overshoot and settling time. In summary, the proposed current control technique is a good alternative both in low and high speeds for industrial applications.

Author Contributions: Conceptualization, O.G., M.A. and J.R.; methodology, O.G., M.A.; software, M.A. and O.G.; validation, O.G., M.A. and J.D.-G.; formal analysis, O.G., M.A., J.D.-G., J.R., R.G. and M.R.; investigation, O.G. and M.A.; resources, J.D.-G.; data curation, J.D.-G., O.G. and M.A.; writing, original draft preparation, O.G., M.A. and J.R.; writing, review and editing, O.G., M.A., J.R., J.D.-G., R.G. and M.R.; visualization, J.D.-G., M.A., J.R., R.G. and M.R.; project administration, O.G., M.A., J.R., and J.D.-G.; funding acquisition, R.G. and J.R.

Funding: This research has been funded through the Consejo Nacional de Ciencia y Tecnología (CONACYT)-Paraguay, Grant Number POSG16-05 and FONDECYT Regular 1160690 Research Project.

Acknowledgments: The authors would like to thank members of the LSPyC, APET and LECPE for their significant comments on this work.

Conflicts of Interest: The authors declare no conflict of interest.

Abbreviations

The following abbreviations have been employed in this work:

FOC	Field Oriented Control
IM	Induction Machine
MPC	Model Predictive Control
PFSCCS	Predictive-Fixed Switching Current Control Strategy
MSE	Mean Squared Error
PI	Proportional-Integral
PWM	Pulse-Width Modulation
SVM	Space Vector Modulation
THD	Total Harmonic Distortion
VSI	Voltage Source Inverter
VSD	Vector Space Decomposition

References

1. Duran, M.J.; Levi, E.; Barrero, F. Multiphase Electric Drives: Introduction. In *Wiley Encyclopedia of Electrical and Electronics Engineering*. Available online: https://onlinelibrary.wiley.com/doi/abs/10.1002/047134608X.W8364 (accessed on 26 April 2019).
2. Precup, R.E.; Kamal, T.; Hassan, S.Z. *Advanced Control and Optimization Paradigms for Wind Energy Systems*; Springer: Berlin/Heidelberg, Germany, 2019.
3. Subotic, I.; Bodo, N.; Levi, E. Integration of six-phase EV drivetrains into battery charging process with direct grid connection. *IEEE Trans. Energy Conv.* **2017**, *32*, 1012–1022. [CrossRef]
4. Ayala, M.; Gonzalez, O.; Rodas, J.; Gregor, R.; Doval-Gandoy, J. A speed-sensorless predictive current control of multiphase induction machines using a Kalman filter for rotor current estimator. In Proceedings of the 2016 International Conference on Electrical Systems for Aircraft, Railway, Ship Propulsion and Road Vehicles & International Transportation Electrification Conference (ESARS-ITEC), Toulouse, France, 2–4 November 2016; pp. 1–6.

5. Munim, W.N.W.A.; Duran, M.J.; Che, H.S.; Bermúdez, M.; González-Prieto, I.; Rahim, N.A. A unified analysis of the fault tolerance capability in six-phase induction motor drives. *IEEE Trans. Power Electron.* **2017**, *32*, 7824–7836. [CrossRef]
6. Jones, M.; Vukosavic, S.N.; Dujic, D.; Levi, E. A synchronous current control scheme for multiphase induction motor drives. *IEEE Trans. Energy Conv.* **2009**, *24*, 860–868. [CrossRef]
7. Kali, Y.; Ayala, M.; Rodas, J.; Saad, M.; Doval-Gandoy, J.; Gregor, R.; Benjelloun, K. Current Control of a Six-Phase Induction Machine Drive based on Discrete-Time Sliding Mode with Time Delay Estimation. *Energies* **2019**, *12*, 170. [CrossRef]
8. Che, H.S.; Duran, M.J.; Levi, E.; Jones, M.; Hew, W.P.; Rahim, N.A. Postfault operation of an asymmetrical six-phase induction machine with single and two isolated neutral points. *IEEE Trans. Power Electron.* **2014**, *29*, 5406–5416. [CrossRef]
9. Mirzaeva, G.; Goodwin, G.C.; McGrath, B.P.; Teixeira, C.; Rivera, M. A generalized MPC framework for the design and comparison of VSI current controllers. *IEEE Trans. Ind. Electron.* **2016**, *63*, 5816–5826. [CrossRef]
10. Vazquez, S.; Rodriguez, J.; Rivera, M.; Franquelo, L.G.; Norambuena, M. Model Predictive Control for Power Converters and Drives: Advances and Trends. *IEEE Trans. Ind. Electron.* **2016**, *64*, 935–947. [CrossRef]
11. Barrero, F.; Arahal, M.R.; Gregor, R.; Toral, S.; Durán, M.J. A proof of concept study of predictive current control for VSI-driven asymmetrical dual three-phase AC machines. *IEEE Trans. Ind. Electron.* **2009**, *56*, 1937–1954. [CrossRef]
12. Barrero, F.; Prieto, J.; Levi, E.; Gregor, R.; Toral, S.; Durán, M.J.; Jones, M. An enhanced predictive current control method for asymmetrical six-phase motor drives. *IEEE Trans. Ind. Electron.* **2011**, *58*, 3242–3252. [CrossRef]
13. Lim, C.S.; Levi, E.; Jones, M.; Rahim, N.A.; Hew, W.P. FCS-MPC-based current control of a five-phase induction motor and its comparison with PI-PWM control. *IEEE Trans. Ind. Electron.* **2013**, *61*, 149–163. [CrossRef]
14. Vijayagopal, M.; Zanchetta, P.; Empringham, L.; De Lillo, L.; Tarisciotti, L.; Wheeler, P. Modulated model predictive current control for direct matrix converter with fixed switching frequency. In Proceedings of the 2015 17th European Conference on Power Electronics and Applications (EPE'15 ECCE-Europe), Geneva, Switzerland, 8–10 September 2015; pp. 1–10.
15. Gregor, R.; Rodas, J.; Munoz, J.; Ayala, M.; Gonzalez, O.; Gregor, D. Predictive-Fixed Switching Frequency Technique for 5-Phase Induction Motor Drives. In Proceedings of the 2016 International Symposium on Power Electronics, Electrical Drives, Automation and Motion (SPEEDAM), Anacapri, Italy, 22–24 June 2016.
16. Ayala, M.; Gonzalez, O.; Rodas, J.; Gregor, R.; Rivera, M. Predictive control at fixed switching frequency for a dual three-phase induction machine with Kalman filter-based rotor estimator. In Proceedings of the 2016 IEEE International Conference on Automatica (ICA-ACCA), Curico, Chile, 19–21 October 2016; pp. 1–6.
17. Rivera, M.; Toledo, S.; Baier, C.; Tarisciotti, L.; Wheeler, P.; Verne, S. Indirect predictive control techniques for a matrix converter operating at fixed switching frequency. In Proceedings of the 2017 IEEE International Symposium on Predictive Control of Electrical Drives and Power Electronics (PRECEDE), Pucón, Chile, 18–20 October 2017; pp. 13–18.
18. Comparatore, L.; Gregor, R.; Rodas, J.; Pacher, J.; Renault, A.; Rivera, M. Model based predictive current control for a three-phase cascade H-bridge multilevel STATCOM operating at fixed switching frequency. In Proceedings of the 2017 IEEE 8th International Symposium on Power Electronics for Distributed Generation Systems (PEDG), Florianopolis, Brazil, 17–20 April 2017; pp. 1–6.
19. Harnefors, L.; Saarakkala, S.; Hinkkanen, M. Speed Control of Electrical Drives Using Classical Control Methods. *IEEE Trans. Ind. Appl.* **2013**, *49*, 889–898. [CrossRef]
20. Zhao, Y.; Lipo, T. Space vector PWM control of dual three-phase induction machine using vector space decomposition. *IEEE Trans. Ind. Electron.* **1995**, *31*, 1100–1109.
21. Ayala, M.; Rodas, J.; Gregor, R.; Doval-Gandoy, J.; Gonzalez, O.; Saad, M.; Rivera, M. Comparative Study of Predictive Control Strategies at Fixed Switching Frequency for an Asymmetrical Six-Phase Induction Motor Drive. In Proceedings of the 2017 IEEE International Electric Machines and Drives Conference (IEMDC), Miami, FL, USA, 21–24 May 2017; pp. 1–8.
22. Rodas, J.; Barrero, F.; Arahal, M.R.; Martin, C.; Gregor, R. On-Line Estimation of Rotor Variables in Predictive Current Controllers: A Case Study Using Five-Phase Induction Machines. *IEEE Trans. Ind. Electron.* **2016**, *63*, 5348–5356. [CrossRef]

23. Rodas, J.; Martin, C.; Arahal, M.R.; Barrero, F.; Gregor, R. Influence of Covariance-Based ALS Methods in the Performance of Predictive Controllers with Rotor Current Estimation. *IEEE Trans. Ind. Electron.* **2017**, *64*, 2602–2607. [CrossRef]
24. Pandit, J.K.; Aware, M.V.; Nemade, R.V.; Levi, E. Direct torque control scheme for a six-phase induction motor with reduced torque ripple. *IEEE Trans. Power Electron.* **2017**, *32*, 7118–7129. [CrossRef]
25. Gonzalez, O.; Ayala, M.; Rodas, J.; Gregor, R.; Rivas, G.; Doval-Gandoy, J. Variable-Speed Control of a Six-Phase Induction Machine using Predictive-Fixed Switching Frequency Current Control Techniques. In Proceedings of the 2018 9th IEEE International Symposium on Power Electronics for Distributed Generation Systems (PEDG), Charlotte, NC, USA, 25–28 June 2018; pp. 1–6.
26. Yepes, A.G.; Riveros, J.A.; Doval-Gandoy, J.; Barrero, F.; López, O.; Bogado, B.; Jones, M.; Levi, E. Parameter identification of multiphase induction machines with distributed windings Part 1: Sinusoidal excitation methods. *IEEE Trans. Energy Conv.* **2012**, *27*, 1056–1066. [CrossRef]
27. Riveros, J.A.; Yepes, A.G.; Barrero, F.; Doval-Gandoy, J.; Bogado, B.; Lopez, O.; Jones, M.; Levi, E. Parameter identification of multiphase induction machines with distributed windings Part 2: Time-domain techniques. *IEEE Trans. Energy Conv.* **2012**, *27*, 1067–1077. [CrossRef]

ARTÍCULO 8

DISCRETE-TIME SLIDING MODE WITH TIME DELAY ESTIMATION OF A SIX-PHASE INDUCTION MOTOR DRIVE

- Yassine Kali, Jorge Rodas, **Magno Ayala**, Maarouf Saad, Raul Gregor, Khalid Benjelloun, Jesus Doval-Gandoy and Graham Goodwin, ”Discrete-Time Sliding Mode with Time Delay Estimation of a Six-Phase Induction Motor Drive”, Proc. IECON, Washington, US, pp. 1-6, DOI: 10.1109/IECON.2018.8591293, 2018.

Discrete-Time Sliding Mode with Time Delay Estimation of a Six-Phase Induction Motor Drive

Y. Kali[1], J. Rodas[2], M. Ayala[2], M. Saad[1], R. Gregor[2], K. Benjelloun[3], J. Doval-Gandoy[4] and G. Goodwin[5]
[1]École de Technologie Supérieure, Quebec University, Montreal, QC H3C 1K3, Canada (y.kali88@gmail.com)
[2]Laboratory of Power and Control Systems, Facultad de Ingeniería, Universidad Nacional de Asunción, Paraguay
[3]Engineering School, École Mohammadia d'Ingénieurs, University of Mohammed V, Rabat, Morocco
[4]Applied Power Electronics Technology Research Group, Universidad de Vigo, Spain
[5]School of Electrical Engineering and Computer Science, University of Newcastle, Australia

***Abstract*—This paper investigates the problem of stator current control in presence of uncertainties and unmeasurable rotor current for a six-phase induction motor drive. An inner control loop based on a robust discrete-time sliding mode with time delay estimation method is proposed to ensure the finite-time convergence of the stator currents to their desired references while the proportional-integral controller is used for the outer speed control. Sufficient conditions are established to ensure the stability of the closed-loop system. Simulation results were carried out to verify the performance of the proposed robust control strategy for a six-phase induction motor drive.**

***Index Terms*—Discrete-time sliding mode, time delay estimation, multiphase induction machine, speed control, current control, field oriented control.**

I. INTRODUCTION

Multiphase drives have received a great interests from power electronics community due to their good features in comparison with the traditional three-phase drives such as lower current/power per phase and lower torque ripple and fault tolerant capabilities without adding extra hardware [1]–[3]. Nowadays, they are extensively used for high-power and reliable applications such as wind energy generation systems and electric vehicles [3], [4]. Most of the control strategies applied for multiphase drives are an extension of the three-phase case such as proportional-integral pulse-width modulation, proportional-resonant finite-control-set model predictive control, predictive torque control, direct torque control, sensorless, among others [5]–[12]. Recent works also extends the above-mentioned techniques to the post-fault operation [13]–[16]. However, little attention has been paid to robust nonlinear controllers based on fuzzy logic and/or sliding mode control (SMC) strategies [17], [18].

Indeed, SMC is one of the robust proposed nonlinear control techniques in literature. The aim of this technique is to force the system trajectories to converge to a user-chosen switching surface [19] in finite-time even in presence of uncertainties and disturbances using discontinuous controller. However, to ensure high performances, the switching gains should be chosen as large as possible to reject the effect of the bounded uncertainties. Therefore, this choice causes the major drawback of SMC, the well-known chattering phenomenon [20], [21]. This phenomenon has a negative impact on the system actuators which can lead to the deterioration of the controlled system and/or the instability. To solve this problem, many developments have been published, we cite in this context:

- Sliding mode based on a boundary layer [22]. The idea consists on using continuous functions such as saturation instead the signum function. This proposition allows chattering reduction, but the finite-time convergence is not guaranteed anymore which is very desirable while critical convergence time is required.
- Observer-based sliding mode control [23], [24]. This method reduces the problem of designing a robust controller into the problem of designing a robust observer. It means that if the uncertainties estimation is not exact, the desired performances will be affected.
- Higher order sliding mode (HOSM) [25]–[27]. The basic idea is to make the discontinuous term acting on the first time derivative of the control input, then, by integrating the control input becomes continuous. This approach reduces the chattering phenomenon and allows higher precision. However, the required informations (first time derivative of the selected sliding surface) are increased which make the implementation difficult.

Recently, a promising idea that consists on combining sliding mode control with time delay estimation (TDE) method for uncertain nonlinear systems [28], [29]. The proposed method has been successfully tested on a redundant robot arm. The basic idea is to estimate matched uncertainties that are assumed to be Lipschitz using delayed states and inputs informations. Then, the estimated terms are added in the equivalent controller in order to allow a small choice of the switching gains of the discontinuous controller.

Nevertheless, the real time implementation is generally performed through discrete systems [30]. For this reason, the development of the controller should be done in discrete time. Therefore, it is suitable to use the six-phase IM model in discrete time representation during the design procedure because the inherent properties of the sliding mode method might not be maintained after discretization.

Therefore, in this paper, a discrete-time sliding mode (DTSM) controller with TDE method is proposed for the inner current control loop of a rotor field oriented control (RFOC) of a six-phase induction motor (IM) drive. The rest of the paper is organized as follows. Section II presents the mathematical model of the system while controller design is explained in Section III. Simulation results are provided in Section IV. Section V draws some conclusions.

II. SIX-PHASE IM AND VSI MODEL

The analyzed system consists of an asymmetrical six-phase IM fed by two 2-level (2L) VSI shown in Fig. 1. After using the vector space decomposition (VSD) approach, the decoupling transformation $\mathbf{T}$ gives $\alpha-\beta$ subspace which is related to flux/torque producing components and loss-producing $x-y$ subspace and a zero-sequence subspace. In the rest of this paper, matrices and vectors will be denoted by capital and small bold-face letters, respectively. Then, by using an amplitude invariant criterion, $\mathbf{T}$ is defined as follows:

$$\mathbf{T}=\frac{1}{3}\begin{bmatrix} 1 & \frac{\sqrt{3}}{2} & -\frac{1}{2} & -\frac{\sqrt{3}}{2} & -\frac{1}{2} & 0 \\ 0 & \frac{1}{2} & \frac{\sqrt{3}}{2} & \frac{1}{2} & -\frac{\sqrt{3}}{2} & -1 \\ 1 & -\frac{\sqrt{3}}{2} & -\frac{1}{2} & \frac{\sqrt{3}}{2} & -\frac{1}{2} & 0 \\ 0 & \frac{1}{2} & -\frac{\sqrt{3}}{2} & \frac{1}{2} & \frac{\sqrt{3}}{2} & -1 \\ 1 & 0 & 1 & 0 & 1 & 0 \\ 0 & 1 & 0 & 1 & 0 & 1 \end{bmatrix} \tag{1}$$

The discrete model of the system in state-space representation is represented by the following equations [7]:

$$\mathbf{x}_1(k+1)=\mathbf{A}_1\,\mathbf{x}_1(k)+\mathbf{H}_1\,\mathbf{x}_3(k)+\mathbf{B}_1\,\mathbf{u}_1(k)+\mathbf{n}_1(k) \tag{2}$$
$$\mathbf{x}_2(k+1)=\mathbf{A}_2\,\mathbf{x}_2(k)+\mathbf{B}_2\,\mathbf{u}_2(k)+\mathbf{n}_2(k) \tag{3}$$
$$\mathbf{x}_3(k+1)=\mathbf{A}_3\,\mathbf{x}_1(k)+\mathbf{H}_2\,\mathbf{x}_3(k)+\mathbf{B}_3\,\mathbf{u}_1(k)+\mathbf{n}_3(k) \tag{4}$$
$$\mathbf{y}(k)=\mathbf{C}\,\mathbf{x}(k) \tag{5}$$

being the stator and rotor currents state vector:

$$\mathbf{x}(k)=[\mathbf{x}_1(k),\,\mathbf{x}_2(k),\,\mathbf{x}_3(k)]^T \tag{6}$$

with:

$$\mathbf{x}_1(k)=[i_{s\alpha}(k),\,i_{s\beta}(k)]^T \tag{7}$$
$$\mathbf{x}_2(k)=[i_{sx}(k),\,i_{sy}(k)]^T \tag{8}$$
$$\mathbf{x}_3(k)=[i_{r\alpha}(k),\,i_{r\beta}(k)]^T \tag{9}$$

while the stator voltages represents the input vectors:

$$\mathbf{u}_1(k)=[u_{s\alpha}(k),\,u_{s\beta}(k)]^T \tag{10}$$
$$\mathbf{u}_2(k)=[u_{sx}(k),\,u_{sy}(k)]^T \tag{11}$$

and the stator currents the output vector:

$$\mathbf{y}(k)=[\mathbf{x}_1(k),\,\mathbf{x}_2(k)]^T \tag{12}$$
$$=[i_{s\alpha}(k),\,i_{s\beta}(k),\,i_{sx}(k),\,i_{sy}(k)]^T \tag{13}$$

and $\mathbf{n}_i(k)\in R^2$ for $i=1,2,3$ denote the uncertain vectors. The stator voltages have a discrete nature due to the VSI model and the relationship between them is represented as:

$$[u_{s\alpha}(k),\,u_{s\beta}(k),\,u_{sx}(k),\,u_{sy}(k)]^T=V_{\mathrm{dc}}\,\mathbf{T}\,\mathbf{M} \tag{14}$$

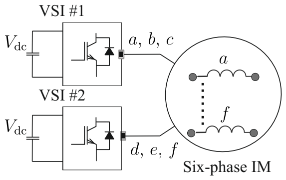

Fig. 1. Scheme of the six-phase IM drive.

where the gating signals are $\mathbf{S}=[S_a,\,S_b,\,S_c,\,S_d,\,S_e,\,S_f]$, being $S_i\in\{0,\,1\}$, V_{dc} is the DC-bus voltage and the VSI model is:

$$\mathbf{M}=\frac{1}{3}\begin{bmatrix} 2 & 0 & -1 & 0 & -1 & 0 \\ 0 & 2 & 0 & -1 & 0 & -1 \\ -1 & 0 & 2 & 0 & -1 & 0 \\ 0 & -1 & 0 & 2 & 0 & -1 \\ -1 & 0 & -1 & 0 & 2 & 0 \\ 0 & -1 & 0 & -1 & 0 & 2 \end{bmatrix}\mathbf{S}^T. \tag{15}$$

The matrices $\mathbf{A}_1$, $\mathbf{A}_2$, $\mathbf{A}_3$, $\mathbf{H}_1$, $\mathbf{H}_2$, $\mathbf{B}_1$, $\mathbf{B}_2$ and $\mathbf{B}_3$ are defined as follows:

$$\mathbf{A}_1=\begin{bmatrix} a_{11} & a_{12} \\ a_{21} & a_{22} \end{bmatrix},\,\mathbf{A}_2=\begin{bmatrix} a_{33} & 0 \\ 0 & a_{44} \end{bmatrix},\,\mathbf{A}_3=\begin{bmatrix} a_{51} & a_{52} \\ a_{61} & a_{62} \end{bmatrix}$$

$$\mathbf{H}_1=\begin{bmatrix} h_{11} & h_{12} \\ h_{21} & h_{22} \end{bmatrix},\,\mathbf{H}_2=\begin{bmatrix} h_{31} & h_{32} \\ h_{41} & h_{42} \end{bmatrix}$$

$$\mathbf{B}_1=\begin{bmatrix} b_1 & 0 \\ 0 & b_1 \end{bmatrix},\,\mathbf{B}_2=\begin{bmatrix} b_2 & 0 \\ 0 & b_2 \end{bmatrix},\,\mathbf{B}_3=\begin{bmatrix} b_3 & 0 \\ 0 & b_3 \end{bmatrix}$$

where:

$$\begin{array}{ll} a_{11}=a_{22}=1-T_s\,c_2\,R_s & a_{12}=-a_{21}=T_s\,c_4L_m\,\omega_{r(k)} \\ h_{11}=h_{22}=T_s\,c_4\,R_r & h_{12}=-h_{21}=T_s\,c_4L_r\,\omega_{r(k)} \\ a_{33}=a_{44}=1-T_s\,c_3\,R_s & a_{51}=a_{62}=-T_s\,c_4\,R_s \\ a_{52}=-a_{61}=-T_s\,c_5\,L_m\,\omega_{r(k)} & h_{31}=h_{42}=1-T_s\,c_5\,R_r \\ h_{32}=-h_{41}=-c_5\,\omega_{r(k)}\,T_s\,L_r & b_1=T_s\,c_2 \\ b_2=T_s\,c_3 & b_3=-T_s\,c_4 \end{array}$$

being T_s the sampling time and c_1 to c_5 are defined as: $c_1=L_sL_r-L_m^2$, $c_2=\frac{L_r}{c_1}$, $c_3=\frac{1}{L_{ls}}$ $c_4=\frac{L_m}{c_1}$ $c_5=\frac{L_s}{c_1}$. The electrical parameters of the systems are R_s, R_r, $L_r=L_{lr}+L_m$, $L_s=L_{ls}+L_m$, L_r and L_m. The rotor electrical speed (ω_r) has a relationship with load torque (T_l) and generated torque (T_e) as follows:

$$J_m\,\dot{\omega}_r+B_m\,\omega_r=P\,(T_e-T_l) \tag{16}$$

being B_m and J_m the friction and the inertia coefficient, respectively, P the number of pole pairs and T_e is:

$$T_e=3\,P\,M\,(i_{r\beta}\,i_{s\alpha}-i_{r\alpha}\,i_{s\beta}) \tag{17}$$

where M is the magnetizing inductance.

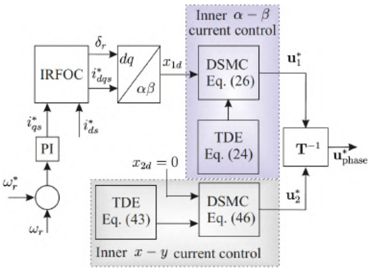

Fig. 2. Block diagram of the proposed speed control based on IRFOC technique and the DTSM with TDE method for the inner current control.

III. PROPOSED CONTROLLER

A. Outer Control Loop

The aim of the outer loop is to control the speed. To that end, a PI controller with a saturation is used due to its simplicity. For the outer loop, the PI speed controller is selected to obtain the dynamic reference current $i^*_{qs}(k)$. Then, the process of the slip frequency ($\omega_{sl}(k)$) estimation is executed in the same way as the indirect RFOC methods, from the reference currents ($i^*_{ds}(k), i^*_{qs}(k)$) in the dynamic reference frame and the electrical parameters of the six-phase IM.

B. Inner Control Loop

The aim of the inner loop is to control the stator currents. To that end, the discrete-time sliding mode control with time delay estimation method will be designed to force the stator current in the $\alpha-\beta$ and the $x-y$ sub-spaces to converge to their desired references in finite-time with high accuracy even in presence of unmeasurable states (i,e. rotor currents) and uncertainties.

1) Control of Stator Current in $\alpha-\beta$ Sub-Space: To quantify the control objective, let $\mathbf{x}^d_1(k) = i^*_{s\phi}(k) \in R^2$ to be the desired reference with $\phi \in \{\alpha, \beta\}$ and $e_\phi(k) = \mathbf{x}_1(k) - \mathbf{x}^d_1(k) = i_{s\phi}(k) - i^*_{s\phi}(k) \in R^2$ be the tracking error. Now, let us select the sliding surface [19] to be the error variable as:

$$\sigma(k) = e_\phi(k) \tag{18}$$

To ensure ideal sliding motion, the following conditions must be verified:

$$\sigma(k) = 0,\ \sigma(k+1) = 0 \tag{19}$$

where $\sigma(k+1)$ is obtained as:

$$\begin{aligned}\sigma(k+1) = e_\phi(k+1) &= \mathbf{x}_1(k+1) - \mathbf{x}^d_1(k+1)\\ &= \mathbf{A}_1\,\mathbf{x}_1(k) + \mathbf{H}_1\,\mathbf{x}_3(k) + \mathbf{B}_1\,\mathbf{u}_1(k)\\ &\quad + \mathbf{n}_1(k) - \mathbf{x}^d_1(k+1)\end{aligned} \tag{20}$$

As the classical sliding motion is not enough to ensure robustness, the following reaching law is chosen:

$$\sigma(k+1) = \lambda\,\sigma(k) - T_s\rho\,\text{sign}(\sigma(k)) \tag{21}$$

where $\lambda = \text{diag}(\lambda_1, \lambda_2)$ with $0 < \lambda_i < 1$ for $i = 1, 2$, $\rho \in R^{2\times 2}$ is a diagonal positive matrix and $\text{sign}(\sigma(k)) = [\text{sign}(\sigma_1(k)), \text{sign}(\sigma_2(k))]^T$ with:

$$\text{sign}(\sigma_i(k)) = \begin{cases} 1, & \text{if } \sigma_i(k) > 0\\ 0, & \text{if } \sigma_i(k) = 0\\ -1, & \text{if } \sigma_i(k) < 0\end{cases} \tag{22}$$

Hence, the discrete-time SMC law for the stator current in $\alpha-\beta$ sub-space described in (2) is obtained as:

$$\begin{aligned}\mathbf{u}_1(k) = -\mathbf{B}^{-1}_1 \left[\mathbf{A}_1\mathbf{x}_1(k) - \mathbf{x}^d_1(k+1) - \lambda\,\sigma(k) \cdots\right.\\ \left.\cdots + \mathbf{H}_1\mathbf{x}_3(k) + \mathbf{n}_1(k) + T_s\rho\,\text{sign}(\sigma(k))\right]\end{aligned} \tag{23}$$

As the rotor currents $\mathbf{x}_3(k)$ are not measurable and as $\mathbf{n}_1(k)$ is unknown, the control performance might not be satisfactory. Then, assuming that $\mathbf{x}_3(k)$ and $\mathbf{n}_1(k)$ do not vary largely between two consecutive sampling time and based on (2), they can be estimated using TDE [26], [31] method as:

$$\begin{aligned}\mathbf{H}_1\hat{\mathbf{x}}_3(k) + \hat{\mathbf{n}}_1(k) &\cong \mathbf{H}_1\mathbf{x}_3(k-1) + \mathbf{n}_1(k-1)\\ &= \mathbf{x}_1(k) - \mathbf{A}_1\mathbf{x}_1(k-1) - \mathbf{B}_1\mathbf{u}_1(k-1)\end{aligned} \tag{24}$$

Definition 3.1: For a discrete system, a quasi sliding mode is considered in the vicinity of the sliding surface, such that $|\sigma(k)| < \varepsilon$, with ε is a positive constant called the quasi-sliding-mode band width. To guarantee a convergent quasi sliding mode, the following sufficient and necessary conditions given in [26], [32] must be verified for $i = 1, 2$:

$$\begin{cases}\sigma_i(k) > \varepsilon \Rightarrow -\varepsilon \leq \sigma_i(k+1) < \sigma_i(k)\\ \sigma_i(k) < -\varepsilon \Rightarrow \sigma_i(k) < \sigma_i(k+1) \leq \varepsilon\\ |\sigma_i(k)| \leq \varepsilon \Rightarrow |\sigma_i(k+1)| \leq \varepsilon\end{cases} \tag{25}$$

Theorem 3.1: The discrete-time sliding mode control with time delay estimation method for the stator current in the $\alpha-\beta$ sub-space given in (2) is given by:

$$\begin{aligned}\mathbf{u}_1(k) = \mathbf{B}^{-1}_1 \left[\mathbf{x}_{1d}(k+1) - \mathbf{A}_1\mathbf{x}_1(k) - \mathbf{H}_1\hat{\mathbf{x}}_3(k) \cdots\right.\\ \left.\cdots - \hat{\mathbf{n}}_1(k) + \lambda\,\sigma(k) - T_s\rho\,\text{sign}(\sigma(k))\right]\end{aligned} \tag{26}$$

ensures a quasi sliding mode if the following condition is met:

$$\rho_i > \frac{1}{T_s}\delta_i \quad for\ i = 1, 2 \tag{27}$$

Proof. Substituting the calculated discrete-time controller (13) in equation (9) leads to:

$$\sigma(k+1) = E + \lambda\,\sigma(k) - T_s\rho\,\text{sign}(\sigma(k)) \tag{28}$$

where $E = \mathbf{H}_1\left(\mathbf{x}_3(k) - \hat{\mathbf{x}}_3(k)\right) + \left(\mathbf{n}_1(k) - \hat{\mathbf{n}}_1(k)\right)$ is the bounded time delay estimation error such as for $i = 1, 2$:

$$|E_i| < \delta_i \tag{29}$$

Now, let us choose $\varepsilon = T_s\rho_i + \delta_i$. Hence, equation (25) can be rewritten as:

$$\begin{aligned}\sigma_i(k) > T_s\rho_i + \delta_i &\Rightarrow -T_s\rho_i - \delta_i \leq \sigma_i(k+1) < \sigma_i(k)\\ \sigma_i(k) < -T_s\rho_i - \delta_i &\Rightarrow \sigma_i(k) < \sigma_i(k+1) \leq T_s\rho_i + \delta_i\\ |\sigma_i(k)| \leq T_s\rho_i + \delta_i &\Rightarrow |\sigma_i(k+1)| \leq T_s\rho_i + \delta_i\end{aligned} \tag{30}$$

1. Consider the first case where $\sigma_i(k) > T_s\rho_i + \delta_i$, then $\sigma_i(k) > 0$, $\mathrm{sign}(\sigma_i(k)) = 1$ and:

   $$\begin{aligned} \sigma_i(k+1) &= E_i + \lambda_i\,\sigma_i(k) - T_s\rho_i \\ \sigma_i(k+1) - \sigma_i(k) &= E_i + (\lambda_i - 1)\,\sigma_i(k) - T_s\rho_i \end{aligned} \tag{31}$$

   Since the condition in (27) is verified, then $\sigma_i(k+1) - \sigma_i(k) < 0 \Rightarrow \sigma_i(k+1) < \sigma_i(k)$.
   In addition, $-T_s\rho_i - \delta_i \leq \sigma_i(k+1)$ can be written as:

   $$E_i + \lambda_i\,\sigma_i(k) - T_s\rho_i \geq -T_s\rho_i - \delta_i \tag{32}$$

   Hence:

   $$\sigma_i(k) \geq \frac{1}{\lambda_i}(E_i - \delta_i) \tag{33}$$

   which is is always true since $\sigma_i(k) > 0$ and $(E_i - \delta_i) < 0$.
2. Consider the second case where $\sigma_i(k) < -T_s\rho_i - \delta_i$, which means that $\sigma_i(k) < 0$ and $\mathrm{sign}(\sigma_i(k)) = -1$. Then, $\sigma_i(k) < \sigma_i(k+1)$ can be rewritten as:

   $$\begin{aligned} \sigma_i(k) &< E_i + \lambda_i\,\sigma_i(k) + T_s\rho_i \\ (1 - \lambda_i)\,\sigma_i(k) &< E_i + T_s\rho_i \end{aligned} \tag{34}$$

   which is always true since the condition (27) is verified. Moreover, $\sigma_i(k+1) < T_s\rho_i + \delta_i$ can be rewritten as:

   $$E_i + \lambda_i\,\sigma_i(k) + T_s\rho_i < T_s\rho_i + \delta_i \tag{35}$$

   It is obvious that the above inequality is always true since $\sigma_i(k) < 0$ and $\delta_i > E_i$.
3. Consider the third case where $|\sigma_i(k)| \leq \varepsilon$, then:
   a. if $\sigma_i(k) > 0$, then $|\sigma_i(k)| \leq \varepsilon$ becomes:

      $$0 < \sigma_i(k) < \varepsilon \tag{36}$$

      Multiplying by λ_i and adding $E_i - T_s\rho_i$ to all the parts of the above equation leads to:

      $$\begin{gathered} E_i - T_s\rho_i < \sigma_i(k+1) < E_i - T_s\rho_i + \lambda_i\,\varepsilon \\ -\varepsilon < \sigma_i(k+1) < \varepsilon \\ |\sigma_i(k+1)| \leq \varepsilon \end{gathered} \tag{37}$$

   b. if $\sigma_i(k) < 0$, then $|\sigma_i(k)| \leq \varepsilon$ becomes:

      $$-\varepsilon < \sigma_i(k) < 0 \tag{38}$$

      Once again, multiplying by λ_i and adding $E_i + T_s\rho_i$ to all the parts of (38) gives:

      $$\begin{gathered} E_i + T_s\rho_i - \lambda_i\,\varepsilon < \sigma_i(k+1) < E_i + T_s\rho_i \\ -\varepsilon < \sigma_i(k+1) < \varepsilon \\ |\sigma_i(k+1)| \leq \varepsilon \end{gathered} \tag{39}$$

   Hence:

   $$|\sigma_i(k+1)| < \varepsilon = T_s\rho_i + \delta_i \tag{40}$$

   The conditions in (30) being verified, the existence of the convergent quasi sliding mode is proved. Therefore, the proposed discrete-time controller in (13) is stable.
   This concludes the proof.

2) Control of Stator Current in $x - y$ Sub-Space: The complete study of discrete-time sliding mode control with time delay estimation is described in the previous part. To control the stator current in the $x-y$ sub-space, the same methodology will be used. The sliding surface here is selected as:

$$\sigma^*(k) = e_{s_{xy}}(k) = \mathbf{x}_2(k) - \mathbf{x}_2^d(k) \tag{41}$$

where $\mathbf{x}_2^d(k) = [i_{sx}^*(k),\ i_{sy}^*(k)]^T$ denotes the desired currents and $e_{s_{xy}}(k)$ represents the tracking error variable. Therefore, $\sigma^*(k+1)$ is calculated as follows:

$$\begin{aligned} \sigma^*(k+1) = e_{s_{xy}}(k+1) &= \mathbf{x}_2(k+1) - \mathbf{x}_2^d(k+1) \\ &= \mathbf{A}_2\,\mathbf{x}_2(k) + \mathbf{B}_2\,\mathbf{u}_2(k) + \mathbf{n}_2(k) - \mathbf{x}_2^d(k+1) \end{aligned} \tag{42}$$

Finally, the discrete-time controller is obtained by substituting the uncertain vector $\mathbf{n}_2(k)$ by its estimate using TDE method:

$$\begin{aligned} \hat{\mathbf{n}}_2(k) &\cong \mathbf{n}_2(k-1) \\ &= \mathbf{x}_2(k) - \mathbf{A}_2\,\mathbf{x}_2(k-1) - \mathbf{B}_2\,\mathbf{u}_2(k-1) \end{aligned} \tag{43}$$

and by resolving:

$$\sigma^*(k+1) = \Gamma\,\sigma^*(k) - T_s\varrho\,\mathrm{sign}(\sigma^*(k)) \tag{44}$$

where $\Gamma = \mathrm{diag}(\Gamma_1, \Gamma_2)$ with $0 < \Gamma_i < 1$ for $i = 1, 2$, $\varrho \in R^{2\times 2}$ is a diagonal positive matrix and $\mathrm{sign}(\sigma^*(k)) = [\mathrm{sign}(\sigma_1^*(k)), \mathrm{sign}(\sigma_2^*(k))]^T$.

Theorem 3.2: If the controller gains are chosen for $i = 1, 2$ as follows:

$$\varrho_i > \frac{1}{T_s}\delta_i^* \tag{45}$$

with $\delta_i^* > 0$ is the upper-bound of the TDE error $E^* = \mathbf{n}_2(k) - \mathbf{n}_2(k-1)$. Then, the following discrete-time sliding mode control with time delay estimation method for the stator current in the $x - y$ sub-space (3) ensures a quasi sliding motion:

$$\begin{aligned} \mathbf{u}_2(k) = \mathbf{B}_2^{-1}\,[\mathbf{x}_{2d}(k+1) - \mathbf{A}_2\mathbf{x}_2(k) - \hat{\mathbf{n}}_2(k)\cdots \\ \cdots + \Gamma\,\sigma^*(k) - T_s\varrho\,\mathrm{sign}(\sigma^*(k))] \end{aligned} \tag{46}$$

Proof. The stability analysis is similar to the one described for the stator currents in $\alpha - \beta$ sub-space.

IV. NUMERICAL SIMULATION

A MATLAB/Simulink simulation program has been designed for a six-phase IM in order to prove the effectiveness of the proposed method. Numerical integration using first order Euler's discretization method has been applied to compute the evolution of the state space variables in the time domain. The electrical and mechanical parameters of the six-phase IM are detailed in Table I.

In this simulation, a sampling frequency of 10 kHz, a torque load of 2 Nm connected to the six-phase IM and a fixed d current ($i_{ds}^* = 1$ A) have been used. The PI gains are chosen to be $K_p = 9.17$ and $K_I = 0.027$.

In addition, the gains of the DSMC with TDE used for stator currents tracking in $\alpha - \beta$ sub-space are:

$$\lambda = \mathrm{diag}(0.5, 0.5),\ \rho_1 = \rho_2 = 30$$

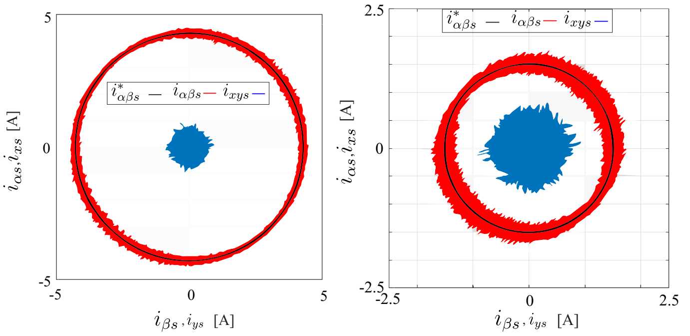

(a) (b)

Fig. 3. Stator currents in $\alpha-\beta$ and $x-y$ sub-spaces for a sampling frequency of 10 kHz: (a) Amplitude of 4.5 A; (b) Amplitude of 1.5 A.

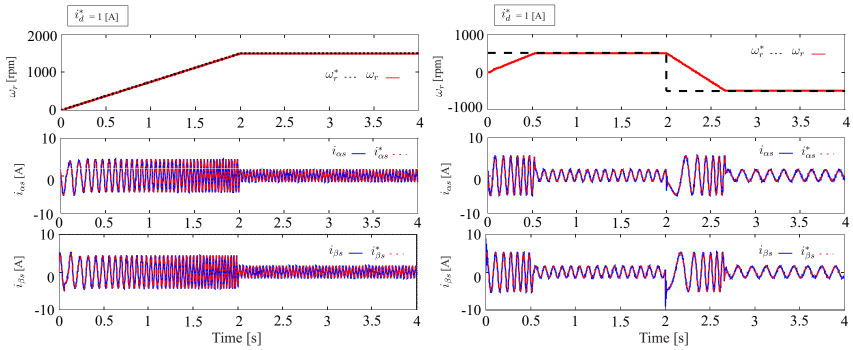

(a) (b)

Fig. 4. Stator currents in $\alpha-\beta$ sub-space for transient and steady-state rotor speed for a sampling frequency of 10 kHz: (a) 1500 rpm of steady state response; (b) Reversal condition of 500 to -500 rpm.

While the gains of the DSMC with TDE used for stator currents tracking in $x-y$ sub-space are:

$$\Gamma = \mathrm{diag}(0.9, 0.9), \;\; \varrho_1 = \varrho_2 = 30$$

The behavior of the stator currents in the $\alpha-\beta$ and $x-y$ sub-spaces are shown in Fig. 3(a) and Fig. 3(b) for different $i^d_{\alpha\beta s}$ amplitudes. Fig. 4(a) exposes the stator currents evolution in $\alpha-\beta$ sub-space for a transient and steady-state rotor speed reference and Fig. 4(b) demonstrates the stator currents behavior for a reversal condition where the rotor speed reference changes from 500 to -500 rpm. The proposed controllers ensure high accuracy tracking of the system currents to their desired references in a finite-time.

TABLE I
ELECTRICAL AND MECHANICAL PARAMETERS OF THE SIX-PHASE IM

R_r	6.9 Ω	L_s	654.4 mH
R_s	6.7 Ω	P	1
L_{ls}	5.3 mH	B_i	0.0004 kg.m^2/s
L_{lr}	12.8 mH	J_i	0.07 kg.m^2
L_r	626.8 mH	Nominal Power	2 kW
L_m	614 mH	Nominal Speed	3000 rpm

To quantify the speed and currents tracking, the mean square error (MSE) and total harmonic distortion (THD) are used as figures of merit. For a 500 rpm of speed rotor reference, the proposed controller obtains a MSE of 1.1460 rpm, 0.0550 A and 0.1640 A for the measured speed, $\alpha-\beta$ and $x-y$ currents respectively. For a 1500 rpm of speed rotor reference, the proposed controller shows a MSE of 1.1457 rpm, 0.0575 A and 0.1860 A for the measured speed, $\alpha-\beta$ and $x-y$ currents respectively. As for the THD analysis, for 500 and 1500 rpm of speed reference, it is obtained 5.3 % and 5.6 % for $\alpha-\beta$ currents respectively.

V. CONCLUSION

In this paper, a speed control based on RFOC strategy with an inner discrete-time sliding mode with time delay estimation stator currents control is proposed. The proposed method is based on TDE method that estimates effectively and simply the unmeasurable rotor currents, uncertainties and disturbances and on discrete-time sliding mode that provides robustness against TDE error, finite-time convergence and chattering reduction. The efficiency of the proposed DTSM controller with TDE is confirmed by numerical simulations on a six-phase induction machine drive. The proposed controller provides excellent performances in steady state as well as in dynamic process. Furthermore, the average switching frequency of the proposed method is even lower than the conventional SMC and other controllers. Further research will be initiated for real-time implementation.

ACKNOWLEDGMENT

The authors wish to thank the financial support from the Paraguayan Science and Technology National Council (CONACYT) through project 14-INV-101.

REFERENCES

[1] F. Barrero and M. J. Duran, "Recent advances in the design, modeling, and control of multiphase machines: Part I," *IEEE Trans. Ind. Electron.*, vol. 63, no. 1, pp. 449–458, 2016.

[2] M. J. Duran and F. Barrero, "Recent advances in the design, modeling, and control of multiphase machines: Part II," *IEEE Trans. Ind. Electron.*, vol. 63, no. 1, pp. 459–468, 2016.

[3] E. Levi, "Advances in converter control and innovative exploitation of additional degrees of freedom for multiphase machines," *IEEE Trans. Ind. Electron.*, vol. 63, no. 1, pp. 433–448, 2016.

[4] I. Zoric, M. Jones, and E. Levi, "Arbitrary power sharing among three-phase winding sets of multiphase machines," *IEEE Trans. Ind. Electron.*, vol. 65, no. 2, pp. 1128–1139, 2018.

[5] C. Lim, E. Levi, M. Jones, N. Rahim, and W. P. Hew, "FCS-MPC based current control of a five-phase induction motor and its comparison with PI-PWM control," *IEEE Trans. Ind. Electron.*, vol. 61, no. 1, pp. 149–163, 2014.

[6] J. A. Riveros, F. Barrero, E. Levi, M. J. Duran, S. Toral, and M. Jones, "Variable-speed five-phase induction motor drive based on predictive torque control," *IEEE Trans. Ind. Electron.*, vol. 60, no. 8, pp. 2957–2968, 2013.

[7] J. Rodas, F. Barrero, M. R. Arahal, C. Martín, and R. Gregor, "Online estimation of rotor variables in predictive current controllers: a case study using five-phase induction machines," *IEEE Trans. Ind. Electron.*, vol. 63, no. 9, pp. 5348–5356, 2016.

[8] J. Rodas, C. Martín, M. R. Arahal, F. Barrero, and R. Gregor, "Influence of covariance-based ALS methods in the performance of predictive controllers with rotor current estimation," *IEEE Trans. Ind. Electron.*, vol. 64, no. 4, pp. 2602–2607, 2017.

[9] A. Taheri, A. Rahmati, and S. Kaboli, "Efficiency improvement in DTC of six-phase induction machine by adaptive gradient descent of flux," *IEEE Trans. Power Electron.*, vol. 27, no. 3, pp. 1552–1562, 2012.

[10] A. G. Yepes, J. Malvar, A. Vidal, O. López, and J. Doval-Gandoy, "Current harmonics compensation based on multiresonant control in synchronous frames for symmetrical n-phase machines," *IEEE Trans. Ind. Electron.*, vol. 62, no. 5, pp. 2708–2720, 2015.

[11] R. Gregor and J. Rodas, "Speed sensorless control of dual three-phase induction machine based on a Luenberger observer for rotor current estimation," in *Proc. IECON*, pp. 3653–3658, 2012.

[12] M. Ayala, O. Gonzalez, J. Rodas, R. Gregor, and J. Doval-Gandoy, "A speed-sensorless predictive current control of multiphase induction machines using a Kalman filter for rotor current estimator," in *Proc. ESARS-ITEC*, pp. 1–6, 2016.

[13] H. Guzman, M. J. Duran, F. Barrero, L. Zarri, B. Bogado, I. G. Prieto, and M. R. Arahal, "Comparative study of predictive and resonant controllers in fault-tolerant five-phase induction motor drives," *IEEE Trans. Ind. Electron.*, vol. 63, no. 1, pp. 606–617, 2016.

[14] M. Bermudez, I. Gonzalez-Prieto, F. Barrero, H. Guzman, M. J. Duran, and X. Kestelyn, "Open-phase fault-tolerant direct torque control technique for five-phase induction motor drives," *IEEE Trans. Ind. Electron.*, vol. 64, no. 2, pp. 902–911, 2017.

[15] F. Baneira, J. Doval-Gandoy, A. G. Yepes, O. López, and D. Pérez-Estévez, "Control strategy for multiphase drives with minimum losses in the full torque operation range under single open-phase fault," *IEEE Trans. Power Electron.*, vol. 32, no. 8, pp. 6275–6285, 2017.

[16] J. Rodas, H. Guzman, R. Gregor, and B. Barrero, "Model predictive current controller using Kalman filter for fault-tolerant five-phase wind energy conversion systems," in *Proc. PEDG*, pp. 1–6, 2016.

[17] M. A. Fnaiech, F. Betin, G.-A. Capolino, and F. Fnaiech, "Fuzzy logic and sliding-mode controls applied to six-phase induction machine with open phases," *IEEE Trans. Ind. Electron.*, vol. 57, no. 1, pp. 354–364, 2010.

[18] Y. Kali, J. Rodas, M. Saad, R. Gregor, K. Bejelloun, and J. Doval-Gandoy, "Current control based on super-twisting algorithm with time delay estimation for a five-phase induction motor drive,," in *Proc. IEMDC*, pp. 1–8, 2017.

[19] V. Utkin, J. Guldner, and J. Shi, *Sliding mode control in electromechanical systems*. Taylor-Francis, 1999.

[20] L. Fridman, "An averaging approach to chattering," *IEEE Trans. Autom. Control*, vol. 46, pp. 1260–1265, 2001.

[21] I. Boiko and L. Fridman, "Analysis of chattering in continuous sliding-mode controllers," *IEEE Trans. Autom. Control*, vol. 50, pp. 1442–1446, 2005.

[22] K. D. Young, V. I. Utkin, and U. Ozguner, "A control engineer's guide to sliding mode control," *IEEE Transactions on Control Systems Technology*, vol. 7, pp. 328–342, May 1999.

[23] S. Drakunov and V. Utkin, "Sliding mode observers. tutorial," in *Proceedings of 1995 34th IEEE Conference on Decision and Control*, vol. 4, pp. 3376–3378, Dec 1995.

[24] X.-G. Yan and C. Edwards, "Nonlinear robust fault reconstruction and estimation using a sliding mode observer," *Automatica*, vol. 43, no. 9, pp. 1605 – 1614, 2007.

[25] A. Levant, "Higher-order sliding modes, differentiation and output-feedback control," *International Journal of Control*, vol. 76, no. 9-10, pp. 924–941, 2003.

[26] Y. Kali, M. Saad, K. Benjelloun, and A. Fatemi, "Discrete-time second order sliding mode with time delay control for uncertain robot manipulators," *Robotics and Autonomous Systems*, vol. 94, pp. 53 – 60, 2017.

[27] Y. Kali, M. Saad, K. Benjelloun, and C. Khairallah, "Super-twisting algorithm with time delay estimation for uncertain robot manipulators," *Nonlinear Dynamics*, Mar 2018.

[28] Y. Kali, M. Saad, K. Benjelloun, and M. Benbrahim, "Sliding mode with time delay control for MIMO nonlinear systems with unknown dynamics," in *Proc. RASM*, pp. 1–6, 2015.

[29] Y. Kali, M. Saad, K. Benjelloun, and M. Benbrahim, *Sliding Mode with Time Delay Control for Robot Manipulators*, pp. 135–156. Singapore: Springer Singapore, 2017.

[30] V. Bandal, B. Bandyopadhyay, and A. M. Kulkarni, "Design of power system stabilizer using power rate reaching law based sliding mode control technique," in *2005 International Power Engineering Conference*, pp. 923–928 Vol. 2, Nov 2005.

[31] J. H. Jung, P. H. Chang, and S. H. Kang, "Stability analysis of discrete time delay control for nonlinear systems," in *2007 American Control Conference*, pp. 5995–6002, July 2007.

[32] S. Qu, X. Xia, and J. Zhang, "Dynamics of discrete-time sliding-mode-control uncertain systems with a disturbance compensator," *IEEE Transactions on Industrial Electronics*, vol. 61, pp. 3502–3510, July 2014.

ARTÍCULO 9

COMPARATIVE STUDY OF NON-LINEAR CONTROLLERS APPLIED TO A SIX-PHASE INDUCTION MACHINE

- **Magno Ayala**, Osvaldo González, Jorge Rodas, Raul Gregor, Yassine Kali and Pat Wheeler, ”Comparative Study of Non-linear Controllers Applied to a Six-Phase Induction Machine”, Proc. ESARS-ITEC, Nottingham, England, United Kingdom, pp. 1-6, DOI: 10.1109/ESARS-ITEC.2018.8607288, 2018.

Comparative Study of Non-linear Controllers Applied to a Six-Phase Induction Machine

Magno Ayala[1], Osvaldo Gonzalez[1], Jorge Rodas[1], Raul Gregor[1], Yassine Kali[2] and Pat Wheeler[3]
[1]Laboratory of Power and Control Systems, Facultad de Ingeniería, Universidad Nacional de Asunción, Paraguay
mayala@ing.una.py, ogonzalez@ing.una.py, jrodas@ing.una.py, rgregor@ing.una.py
[2]École de Technologie Supérieure, Quebec University, Montreal, Canada, y.kali88@gmail.com
[3]Power Electronics, Machines and Control (PEMC) Group, University of Nottinham, UK, Pat.Wheeler@nottingham.ac.uk

***Abstract*—This paper presents a comparative study of two discrete nonlinear current controllers with fixed switching frequency, one based on the model predictive control and the other to robust discrete-time sliding mode, applied to a six-phase induction machine. The outer speed control is based on the proportional-integral controller. Simulation results are presented to demonstrate the performance of the two current control strategies using the mean squared error, root mean square and total harmonic distortion as figures of merit, thus concluding the advantages and limitations of each current controller at steady and transient states.**

***Index Terms*—Discrete time sliding mode, finite state model predictive control, fixed switching frequency, multiphase induction machine, pulse width modulation, space vector modulation.**

NOMENCLATURE

DTSM	Discrete time sliding mode.
FCS-MPC	Finite control set model predictive control.
IGBT	Isolated gate bipolar transistor.
IRFOC	Indirect rotor field oriented control.
KF	Kalman filter.
M2PC	Modulated model predictive control.
MPC	Model predictive control.
MSE	Mean squared error.
PCC	Predictive current control.
PI	Proportional integral.
PWM	Pulse width modulation.
RMS	Root mean square.
SIM	Six-phase induction machine.
SMC	Sliding mode control.
SVM	Space vector modulation.
TDE	Time delay estimation.
THD	Total harmonic distortion.
VSD	Vector space decomposition.
VSI	Voltage source inverter.

I. INTRODUCTION

Multiphase machines have received great interest from power electronics community due to their good features in comparison with traditional three-phase machines such as lower torque ripple, lower current per phase and fault tolerant capabilities [1]–[3]. Nowadays, they are extensively used for high-power and reliable applications such as wind energy conversion systems and electric vehicles [3], [4]. Most of the control strategies applied for multiphase drives in real applications are an extension of the three-phase case such as field oriented control based on proportional-integral current control, direct torque control, among others [5], [6].

In the last few years, some new nonlinear techniques were developed to apply to multiphase machines such as FCS-MPC [7], [8], predictive torque control [9], [10], fuzzy logic control [11] and SMC [11], [12]. Some of these techniques have variants already presented in the literature such as M2PC for FCS-MPC [13] and DTSM for SMC [14] which are considered improved versions on their original techniques. M2PC is based on a modulation scheme, based on SVM, incorporated to the conventional MPC for different power converters [15], [16]. This technique is applied to a two-level VSI, where the duty cycles are generated for two active vectors and two zero vectors which are selected for the converter using a given switching pattern in order to obtain an efficient performance for the SIM [17]. In the case of SMC, it is considered one of the robust proposed nonlinear control techniques in the literature. This technique forces the system trajectories to converge to a user-chosen switching surface [18] in finite-time using a discontinuous controller. However, to ensure high performances, the switching gains should be chosen as large as possible to reject the effect of bounded uncertainties. Therefore, this choice causes the major drawback of SMC, the well-known chattering phenomenon [19].

Recently, a promising idea that consists on combining sliding mode control with TDE method for uncertain nonlinear systems has been presented on [20]. The main contribution of this paper is a comparative study of M2PC, with a KF as an state observer and DTSM, with TDE as an state observer to operate a SIM in terms of current tracking, THD of stator currents and RMS of the current and torque ripple. The two fixed switching frequency techniques are compared by using the MSE, THD and RMS of the current and torque ripple, as figures of merit. These techniques are tested for different operation conditions, in steady state and transient conditions.

This paper is organized as follows: the SIM state-space mathematical model is presented in Section II. In Section III, the M2PC and DTSM designs are shown where, for M2PC it describes the traditional PCC and the modulation method, as for DTSM it explains the technique with TDE. The simulation results are shown in Section IV where the transient and steady state behavior, for the two methods are compared. Section V summarizes the conclusion.

II. MATHEMATICAL MODEL OF SIM

The studied system is composed of a SIM connected to a six-leg VSI and a DC voltage source (V_{dc}). An electrical scheme of the VSI drive, based on IGBT, is shown in Fig. 1. The SIM is a continuous system which can be analyzed by differential equations. By considering the VSD technique and the six-dimensional space of the SIM, defined by the six-phases (a, b, c, d, e, f), it can be transformed into three two-dimensional orthogonal planes in the stationary reference frame, represented as $(\alpha-\beta)$, $(x-y)$ and (z_1-z_2), by using the transformation matrix $\mathbf{T}$ [8]. The studied SIM is asymmetrical and has isolated neutrals configuration, thus (z_1-z_2) currents are not considered.

$$\mathbf{T} = \frac{1}{3}\begin{array}{c} \begin{array}{cccccc} a & d & b & e & c & f \end{array} \\ \left[\begin{array}{cccccc} 1 & \frac{\sqrt{3}}{2} & -\frac{1}{2} & -\frac{\sqrt{3}}{2} & -\frac{1}{2} & 0 \\ 0 & \frac{1}{2} & \frac{\sqrt{3}}{2} & \frac{1}{2} & -\frac{\sqrt{3}}{2} & -1 \\ 1 & -\frac{\sqrt{3}}{2} & -\frac{1}{2} & \frac{\sqrt{3}}{2} & -\frac{1}{2} & 0 \\ 0 & \frac{1}{2} & -\frac{\sqrt{3}}{2} & \frac{1}{2} & \frac{\sqrt{3}}{2} & -1 \\ 1 & 0 & 1 & 0 & 1 & 0 \\ 0 & 1 & 0 & 1 & 0 & 1 \end{array}\right] \end{array} \begin{array}{c} \\ \alpha \\ \beta \\ x \\ y \\ z_1 \\ z_2 \end{array} \tag{1}$$

where the invariant amplitude criterion has been selected.

The six-phase VSI has a discrete behavior and a total number of $2^6 = 64$ switching states defined by the six VSI legs $\mathbf{S} = [S_a,\, S_b,\, S_c,\, S_d,\, S_e,\, S_f]$, where $\mathbf{S}_i \in \{0,1\}$. The different switching states and V_{dc} determine the phase voltages, which can be represented into the $(\alpha-\beta)$ and $(x-y)$ planes according to the VSD approach [21]. Fig. 2 shows the 64 possibilities which lead only to 49 different vectors (48 vectors + 1 null vector) in the $(\alpha-\beta)$ and $(x-y)$ planes. The state-space model of the SIM is defined by:

$$\dot{\mathbf{X}}_{(t)} = \mathbf{A}_{(t)}\,\mathbf{X}_{(t)} + \mathbf{B}_{(t)}\,\mathbf{U}_{(t)} + \mathbf{H}\,\varpi_{(t)} \tag{2}$$

where $\mathbf{X}_{(t)} = [x_1,\, x_2,\, x_3,\, x_4, x_5,\, x_6]^T$ is the state vector that corresponds to the stator and rotor currents $x_1 = i_{\alpha s}$, $x_2 = i_{\beta s}$, $x_3 = i_{xs}$, $x_4 = i_{ys}$, $x_5 = i_{\alpha r}$ and $x_6 = i_{\beta r}$, $\mathbf{U}_{(t)} = [u_1,\, u_2,\, u_3,\, u_4]^T = [v_{\alpha s},\, v_{\beta s},\, v_{xs},\, v_{ys}]^T$ is the input vector applied to the stator, the process noise is defined as $\varpi_{(t)}$ and $\mathbf{H}$ is the noise weight matrix and $\mathbf{A}_{(t)}$ and $\mathbf{B}_{(t)}$ are matrices determined by the electrical parameters of the SIM as follows:

$$\begin{bmatrix} -R_s c_2 & c_4 L_m \omega_r & 0 & 0 & c_4 R_r & c_4 L_r \omega_r \\ c_4 L_m \omega_r & -R_s c_2 & 0 & 0 & c_4 L_r \omega_r & c_4 R_r \\ 0 & 0 & -R_s c_3 & 0 & 0 & 0 \\ 0 & 0 & 0 & -R_s c_3 & 0 & 0 \\ R_s c_4 & -c_5 L_m \omega_r & 0 & 0 & -c_5 R_r & -c_5 L_r \\ -c_5 L_m \omega_r & R_s c_4 & 0 & 0 & -c_5 L_r & -c_5 R_r \end{bmatrix}$$

$$\begin{bmatrix} c_2 & 0 & 0 & 0 \\ 0 & c_2 & 0 & 0 \\ 0 & 0 & c_3 & 0 \\ 0 & 0 & 0 & c_3 \\ -c_4 & 0 & 0 & 0 \\ 0 & -c_4 & 0 & 0 \end{bmatrix}$$

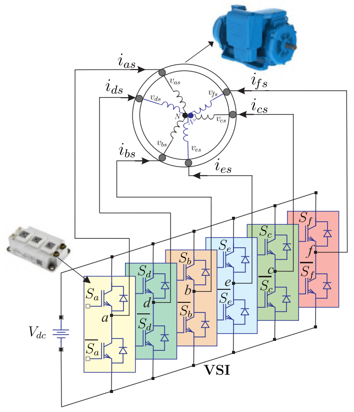

Fig. 1. Scheme of an SIM connected to a six-leg VSI.

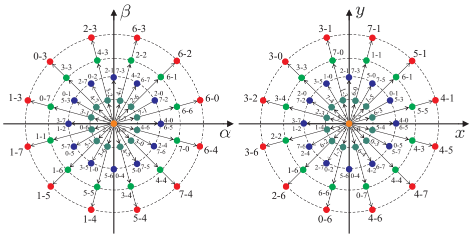

Fig. 2. Voltage space vectors and switching states in $(\alpha-\beta)$ and $(x-y)$ planes for a SIM.

where R_s, R_r, L_m, $L_r = L_{lr} + L_m$ and $L_s = L_{ls} + L_m$ are the electrical parameters of the SIM. The coefficients are determined as $c_1 = L_s L_r - L_m^2$, $c_2 = \frac{L_r}{c_1}$, $c_3 = \frac{1}{L_{ls}}$, $c_4 = \frac{L_m}{c_1}$ and $c_5 = \frac{L_s}{c_1}$. Stator voltages are dependent of the input control signals $\mathbf{S}$. In this particular case, the simplest VSI model has been considered to obtain a good optimization process. In this model the stator voltages can be calculated from the ideal six-leg VSI model $\mathbf{M}_{[\mathbf{S}]}$ [8].

$$\mathbf{M}_{[\mathbf{S}]} = \frac{1}{3}\begin{bmatrix} 2 & 0 & -1 & 0 & -1 & 0 \\ 0 & 2 & 0 & -1 & 0 & -1 \\ -1 & 0 & 2 & 0 & -1 & 0 \\ 0 & -1 & 0 & 2 & 0 & -1 \\ -1 & 0 & -1 & 0 & 2 & 0 \\ 0 & -1 & 0 & -1 & 0 & 2 \end{bmatrix}\mathbf{S}^T \tag{3}$$

An ideal six-leg VSI transforms gating signals into stator voltages which can be projected to $(\alpha-\beta)$ and $(x-y)$ planes and defined in $\mathbf{U}_{(t)}$, determined with the following equation:

$$\mathbf{U}_{(t)} = V_{dc}\,\mathbf{T}\,\mathbf{M}_{[\mathbf{S}]} \tag{4}$$

The output vector, $\mathbf{Y}$, is:

$$\mathbf{Y}_{(t)} = \mathbf{C}\,\mathbf{X}_{(t)} + \nu_{(t)} \tag{5}$$

being $\nu_{(t)}$ is the measurement noise and

$$\mathbf{C} = \begin{bmatrix} 1 & 0 & 0 & 0 & 0 & 0 \\ 0 & 1 & 0 & 0 & 0 & 0 \\ 0 & 0 & 1 & 0 & 0 & 0 \\ 0 & 0 & 0 & 1 & 0 & 0 \end{bmatrix}$$

The mechanical variables of the SIM are related by the following equations:

$$T_e = 3\,P\,(\psi_{\alpha s} i_{\beta s} - \psi_{\beta s} i_{\alpha s}) \tag{6}$$

$$J_i\,\dot{\omega}_m + B_i\,\omega_m = (T_e - T_L) \tag{7}$$

$$\omega_r = P\omega_m \tag{8}$$

where B_i is the friction coefficient, J_i the inertia coefficient, T_e defines the produced torque, T_L is the load torque, ω_r is the rotor electrical speed, ω_m the rotor mechanical speed, $\psi_{\alpha s}$ and $\psi_{\beta s}$ are the stator fluxes and P the number of pole pairs.

III. PROPOSED NONLINEAR CONTROLLERS

A. *Outer Control Loop*

The outer loop is designed for control the speed. A PI controller, designed in [22] is implemented. The PI speed controller is selected to obtain the dynamic reference current $i^*_{qs[k]}$. Then, the process of the slip frequency $(\omega_{sl[k]})$ estimation is executed in the same way as the IRFOC methods, from the reference currents $(i^*_{ds[k]}, i^*_{qs[k]})$ in the dynamic reference frame and the electrical parameters of the SIM.

B. *M2PC*

1) Classic MPC: This technique uses the mathematical model of the discrete system to predict at time $[k]$ the future values $[k+1]$, by using the measured variables such as stator currents and the mechanical rotor speed.

$$\hat{\mathbf{X}}_{[k+1|k]} = \mathbf{X}_{[k]} + T_s\,f\left(\mathbf{X}_{[k]},\,\mathbf{U}_{[k]},\,\omega_{r[k]}\right) \tag{9}$$

where T_s is the sample time. In the state-space model (9), only the stator currents, voltages and mechanical speed are measured. The stator voltages are predicted from the switching commands issued to the VSI, however, the rotor currents cannot be directly measured. This fact can be solved through a reduced order observer where it provides an estimation for only the rotor currents. This method was proposed in [7] by using a reduced order estimator based on a KF. By considering a zero-mean Gaussian measurement and uncorrelated process noises, the system's equations can be written as:

$$\hat{\mathbf{X}}_{[k+1|k]} = \mathbf{A}_{[k]}\mathbf{X}_{[k]} + \mathbf{B}_{[k]}\mathbf{U}_{[k]} + \mathbf{H}\varpi_{[k]} \tag{10}$$

$$\mathbf{Y}_{[k+1|k]} = \mathbf{C}\,\mathbf{X}_{[k+1]} + \nu_{[k+1]} \tag{11}$$

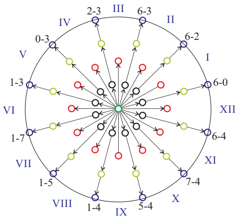

Fig. 3. Available sectors for the six-leg VSI.

where $\mathbf{A}_{[k]}$ and $\mathbf{B}_{[k]}$ are discretized matrices from the model. $\mathbf{A}_{[k]}$ depends on the present value of $\omega_{r[k]}$ and must be considered at every sampling time. A detailed description of the dynamics of the reduced order KF can be found in [7], [23] which has not been presented for the sake of conciseness.

2) Cost Function: The MPC performs an optimization process at every sampling time. This process consists on the evaluation of a cost function (12) for all possible stator voltages to achieve the control objective. The cost function is selected to minimize the current tracking error, defined as the following equation:

$$\begin{aligned} J_{[k+2|k]} =& \parallel i^*_{\alpha s[k+2]} - \hat{i}_{\alpha s[k+2|k]} \parallel^2 + \parallel i^*_{\beta s[k+2]} - \hat{i}_{\beta s[k+2|k]} \parallel^2 \\ &+ \lambda_{xy}\left(\parallel i^*_{xs[k+2]} - \hat{i}_{xs[k+2|k]} \parallel^2 + \parallel i^*_{ys[k+2]} - \hat{i}_{ys[k+2|k]} \parallel^2\right) \end{aligned} \tag{12}$$

being $i^*_{s[k+2]}$ the vector containing the reference for the stator currents and $\hat{i}_{s[k+2]}$ the vector containing the predictions based on the second-step ahead state and a tuning parameter (λ_{xy}) is used [7], [23] to prioritize the $(\alpha - \beta)$ stator currents.

3) Modulation method: It can be determined each available vector for the six-leg VSI in the $(\alpha - \beta)$ plane, which defines 48 sectors, which are given by two adjacent vectors, as shown in Fig. 3. The proposed technique, based on SVM, evaluates the prediction of two active vectors that conform the 12 outside sectors at every sampling time and evaluates the cost function separately. Each prediction is evaluated based on (9) and the only difference is in the calculation of the input vector $\mathbf{U}_{[k]}$ [8].

The duty cycles, for the two active vectors d_1 and d_2, are calculated by solving the next equations:

$$d_0 = \frac{\sigma}{J_0} \qquad d_1 = \frac{\sigma}{J_1} \qquad d_2 = \frac{\sigma}{J_2} \tag{13}$$

$$d_0 + d_1 + d_2 = T_s \tag{14}$$

where d_0 corresponds to the duty cycle of a null vector. Then, it is possible to obtain the expression for σ and the duty cycles for each vector given as:

$$d_0 = \frac{T_s J_1 J_2}{J_0 J_1 + J_1 J_2 + J_0 J_2} \tag{15}$$

$$d_1 = \frac{T_s J_0 J_2}{J_0 J_1 + J_1 J_2 + J_0 J_2} \tag{16}$$

$$d_2 = \frac{T_s J_0 J_1}{J_0 J_1 + J_1 J_2 + J_0 J_2} \tag{17}$$

Considering these expressions, the new cost function, which is evaluated at every T_s, is defined as:

$$G_{[k+2|k]} = d_1 J_1 + d_2 J_2 \tag{18}$$

The two vectors which minimize $G_{[k+2|k]}$ are selected and applied to the six-phase VSI at the next sampling time. After obtaining the duty cycles and selecting the optimal two vectors to be applied, a switching pattern procedure, shown in [24], is adopted with the goal of applying the two active vectors $(v_1 - v_2)$ and two zero vectors (v_0), considering the calculated duty cycles obtaining a fixed-switching frequency.

C. DTSM with TDE

The combination of DTSM control with TDE method will be designed to force the stator current in the $(\alpha-\beta)$ and $(x-y)$ sub-spaces to converge to their desired references in finite-time with high accuracy even in presence of unmeasurable states (rotor currents) and uncertainties. The discrete model of (2) can be expressed as follows:

$$\mathbf{x}_{1[k+1]} = \mathbf{A}_1\,\mathbf{x}_{1[k]} + \mathbf{A}_2\,\mathbf{x}_{3[k]} + \mathbf{B}_1\,\mathbf{v}_{1[k]} + \mathbf{n}_{1[k]} \tag{19}$$

$$\mathbf{x}_{2[k+1]} = \mathbf{A}_3\,\mathbf{x}_{2[k]} + \mathbf{B}_2\,\mathbf{v}_{2[k]} + \mathbf{n}_{2[k]} \tag{20}$$

$$\mathbf{x}_{3[k+1]} = \mathbf{A}_4\,\mathbf{x}_{1[k]} + \mathbf{A}_5\,\mathbf{x}_{3[k]} + \mathbf{B}_3\,\mathbf{v}_{1[k]} + \mathbf{n}_{3[k]} \tag{21}$$

with:

$$\mathbf{x}_{1[k]} = \left[i_{\alpha s[k]},\, i_{\beta s[k]}\right]^T \tag{22}$$

$$\mathbf{x}_{2[k]} = \left[i_{xs[k]},\, i_{ys[k]}\right]^T \tag{23}$$

$$\mathbf{x}_{3[k]} = \left[i_{\alpha r[k]},\, i_{\beta r[k]}\right]^T \tag{24}$$

while the stator voltages represents the input vectors:

$$\mathbf{v}_{1[k]} = \left[v_{\alpha s[k]},\, v_{\beta s[k]}\right]^T \tag{25}$$

$$\mathbf{v}_{2[k]} = \left[v_{xs[k]},\, v_{ys[k]}\right]^T \tag{26}$$

and $\mathbf{H}\,\varpi_{[k]} = \left[\mathbf{n}_{1[k]},\, \mathbf{n}_{2[k]},\, \mathbf{n}_{3[k]}\right]^T \in R^6$. The matrices $\mathbf{A}_1$, $\mathbf{A}_2$, $\mathbf{A}_3$, $\mathbf{A}_4$, $\mathbf{A}_5$, $\mathbf{B}_1$, $\mathbf{B}_2$ and $\mathbf{B}_3$ are discrete forms of sub-matrices from $\mathbf{A}$ and $\mathbf{B}$ defined as follows:

$$\mathbf{A}_1 = \begin{bmatrix} a_{11} & a_{12} \\ a_{21} & a_{22} \end{bmatrix}, \mathbf{A}_2 = \begin{bmatrix} a_{15} & a_{16} \\ a_{25} & a_{26} \end{bmatrix}, \mathbf{A}_3 = \begin{bmatrix} a_{33} & 0 \\ 0 & a_{44} \end{bmatrix}$$

$$\mathbf{A}_4 = \begin{bmatrix} a_{51} & a_{52} \\ a_{61} & a_{62} \end{bmatrix}, \mathbf{A}_5 = \begin{bmatrix} a_{55} & a_{56} \\ a_{65} & a_{66} \end{bmatrix}$$

$$\mathbf{B}_1 = \begin{bmatrix} b_{11} & 0 \\ 0 & b_{22} \end{bmatrix}, \mathbf{B}_2 = \begin{bmatrix} b_{33} & 0 \\ 0 & b_{44} \end{bmatrix}, \mathbf{B}_3 = \begin{bmatrix} b_{55} & 0 \\ 0 & b_{66} \end{bmatrix}$$

where:

$$\begin{array}{ll}
a_{11} = a_{22} = 1 - T_s\,c_2\,R_s & a_{12} = -a_{21} = T_s\,c_4 L_m\,\omega_{r[k]} \\
a_{15} = a_{26} = T_s\,c_4\,R_r & a_{16} = -a_{25} = T_s\,c_4 L_r\,\omega_{r[k]} \\
a_{33} = a_{44} = 1 - T_s\,c_3\,R_s & a_{51} = a_{62} = -T_s\,c_4\,R_s \\
a_{52} = -a_{61} = -T_s\,c_5\,L_m\,\omega_{r[k]} & a_{55} = a_{66} = 1 - T_s\,c_5\,R_r \\
h_{56} = -h_{65} = -c_5\,\omega_{r[k]}\,T_s\,L_r & b_{11} = b_{22} = T_s\,c_2 \\
b_{33} = b_{44} = T_s\,c_3 & b_{55} = b_{66} = -T_s\,c_4
\end{array}$$

1) Control of Stator Current in $(\alpha - \beta)$ Sub-Space: To quantify the control objective, let $\mathbf{x}^d_{1[k]} = \left[i^*_{\alpha s[k]},\, i^*_{\beta s[k]}\right]^T$ to be the desired reference and $e_{\phi[k]} = \mathbf{x}_{1[k]} - \mathbf{x}^d_{1[k]} \in R^2$ be the tracking error with $\phi \in \{\alpha, \beta\}$. Then, it is selected the sliding surface [18] to be the error variable as:

$$\sigma_{[k]} = e_{\phi[k]} \tag{27}$$

An ideal sliding motion is ensured if the following conditions is verified:

$$\sigma_{[k]} = 0,\;\; \sigma_{[k+1]} = 0 \tag{28}$$

where $\sigma_{[k+1]}$ is obtained using the nominal model of (19) as:

$$\begin{aligned} \sigma_{[k+1]} &= e_{\phi[k+1]} = \mathbf{x}_{1[k+1]} - \mathbf{x}^d_{1[k+1]} \\ &= \mathbf{A}_1\,\mathbf{x}_{1[k]} + \mathbf{B}_1\,\mathbf{v}_{1[k]} - \mathbf{x}^d_{1[k+1]} \end{aligned} \tag{29}$$

As the classical sliding motion is not enough to ensure robustness, the following reaching law is chosen:

$$\sigma_{[k+1]} = \lambda\,\sigma_{[k]} - T_s\rho\,\mathrm{sign}(\sigma_{[k]}) \tag{30}$$

where $\lambda = \mathrm{diag}(\lambda_1, \lambda_2)$ with $0 < \lambda_i < 1$ for $i = 1, 2$, $\rho \in R^{2\times 2}$ is a diagonal positive matrix that will be fixed later and $\mathrm{sign}(\sigma_{[k]}) = \left[\mathrm{sign}(\sigma_{1[k]}), \mathrm{sign}(\sigma_{2[k]})\right]^T$ with:

$$\mathrm{sign}(\sigma_{i[k]}) = \begin{cases} 1, & \text{if } \sigma_{i[k]} > 0 \\ 0, & \text{if } \sigma_{i[k]} = 0 \\ -1, & \text{if } \sigma_{i[k]} < 0 \end{cases} \tag{31}$$

Hence, the DTSM controller for the stator current in $(\alpha - \beta)$ sub-space described in (19) is obtained using the nominal model as:

$$\mathbf{v}_{1[k]} = \mathbf{B}_1^{-1}\left[\mathbf{x}^d_{1[k+1]} - \mathbf{A}_1\mathbf{x}_{1[k]} + \lambda\,\sigma_{[k]} - T_s\rho\,\mathrm{sign}(\sigma_{[k]})\right] \tag{32}$$

Since the rotor currents $\mathbf{x}_{3[k]}$ are not measurable and the vector $\mathbf{n}_{1[k]}$ is unknown, the control performance might not be satisfactory. Then, assuming that $\mathbf{x}_{3[k]}$ and $\mathbf{n}_{1[k]}$ do not vary largely between two consecutive sampling time. Then, using (19), they can be estimated using TDE [25], [26] method as:

$$\begin{aligned} \mathbf{A}_2\hat{\mathbf{x}}_{3[k]} + \hat{\mathbf{n}}_{1[k]} &\cong \mathbf{A}_2\mathbf{x}_{3[k-1]} + \mathbf{n}_{1[k-1]} \\ &= \mathbf{x}_{1[k]} - \mathbf{A}_1\mathbf{x}_{1[k-1]} - \mathbf{B}_1\mathbf{v}_{1[k-1]} \end{aligned} \tag{33}$$

Definition 3.1: For a discrete system, a quasi sliding mode is considered in the vicinity of the sliding surface, such that $|\sigma_{[k]}| < \varepsilon$, with ε is a positive constant called the quasi-sliding-mode bandwidth. To guarantee a convergent quasi sliding mode, the following sufficient and necessary conditions given in [25], [27] must be verified for $i = 1, 2$:

$$\begin{cases} \sigma_{i[k]} > \varepsilon & \Rightarrow \;\; -\varepsilon \leq \sigma_{i[k+1]} < \sigma_{i[k]} \\ \sigma_{i[k]} < -\varepsilon & \Rightarrow \;\; \sigma_{i[k]} < \sigma_{i[k+1]} \leq \varepsilon \\ |\sigma_{i[k]}| \leq \varepsilon & \Rightarrow \;\; |\sigma_{i[k+1]}| \leq \varepsilon \end{cases} \tag{34}$$

Theorem 3.1: The DTSM control with TDE for the stator currents in the $(\alpha - \beta)$ sub-space given in (10) is given by:

$$\begin{aligned} \mathbf{v}_{1[k]} = \mathbf{B}_1^{-1}\big[&\mathbf{x}_{1d[k+1]} - \mathbf{A}_1\mathbf{x}_{1[k]} - \mathbf{A}_2\hat{\mathbf{x}}_{3[k]} \\ &-\hat{\mathbf{n}}_{1[k]} + \lambda\,\sigma_{[k]} - T_s\rho\,\mathrm{sign}(\sigma_{[k]})\big] \end{aligned} \tag{35}$$

ensures a quasi sliding mode if the following condition is met:

$$\rho_i > T_s^{-1}\delta_i \quad for\ i = 1, 2 \tag{36}$$

Proof. The proof and the control applied to stator currents in $(x - y)$ sub-space are detailed on [28] thus it has not been presented for the sake of conciseness.

2) PWM Modulation: After DTSM generates the voltage reference in $(\alpha - \beta)$ and $(x - y)$ sub-spaces, it is used a Clark Transformation to obtain the corresponding references per phase. Then it is performed an unipolar voltage PWM to manage the activation of the six-leg VSI.

IV. SIMULATION RESULTS

A MATLAB/Simulink program has been developed for a SIM in order to compare the proposed methods. A numerical integration using first-order Euler's discretization technique has been applied to compute the evolution of the analyzed system. The parameters of the SIM are: $R_r = 6.9\ \Omega$, $R_s = 6.7\ \Omega$, $L_m = 614$ mH, $P = 1$, $L_{lr} = 12.8$ mH, $L_{ls} = 5.3$ mH, $B_i = 0.0004$ kg.m^2/s, $J_i = 0.07$ kg.m^2, 2 kW of nominal power and 3000 rpm of nominal speed.

In the simulation, V_{dc} is 600 V, the sampling frequency is 16 kHz, a torque load of 2 Nm is connected to the SIM and a d current reference ($i_{ds}^* = 1$ A) has been applied. The PI gains are designed to be $K_P = 0.1050$ and $K_I = 0.1058$. For M2PC, λ_{xy} = 0.01, which is defined in (12), giving more priority to the $(\alpha-\beta)$ stator current tracking. The values of the process noise and the measurement noise can be determined by using the method proposed in [23], being $\hat{Q}_w = 0.0022$ and $\hat{R}_v = 0.0022$. As for DTSM with TDE, these values are considered for stator currents tracking in $(\alpha - \beta)$ sub-space:

$$\lambda = \mathrm{diag}(0.5, 0.5),\ \ \rho_1 = \rho_2 = 30$$

While the gains of the DTSM for $(x - y)$ currents are:

$$\Gamma = \mathrm{diag}(0.9, 0.9),\ \ \varrho_1 = \varrho_2 = 30$$

Table I and Table II show a steady state analysis for stator currents, rotor speed and electromagnetic torque under different rotor speed references (ω_r^*) for M2PC and DTSM respectively.

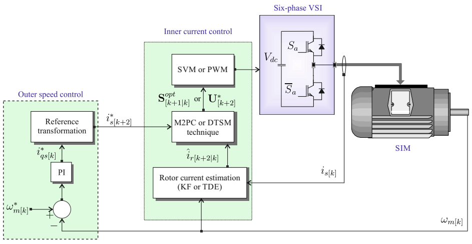

Fig. 4. Speed control with an inner current control based on M2PC or DTSM.

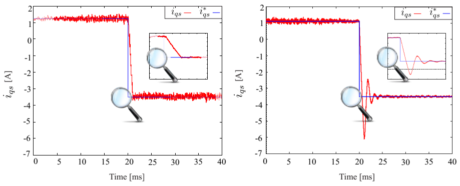

(a)

(b)

Fig. 5. Transient response in q-axis stator current for rotor speed of 500 [rpm] to -500 [rpm] and a sampling frequency of 16 [kHz]: (a) M2PC; (b) DTSM.

The results show a good performance at low speed and an average performance at high rotor speed for M2PC, in terms of speed and stator currents tracking (MSE), stator currents THD and torque ripple RMS. As for DTSM, the results denote an better performance, except for speed tracking, at different rotor speeds, compared to M2PC. Fig. 5 exposes the transient response for q stator current in a reversal test (speed reference changes from 500 [rpm] to -500 [rpm]) where M2PC and DTSM have an overshoot of 5 and 71 % and a settling time (5 % criterion) of 10 and 2.9 ms respectively.

TABLE I

STATOR CURRENTS $(\alpha - \beta)$, $(x - y)$, MSE [A], THD [%], RMS RIPPLE OF T_e [NM], MSE ω_r [RPM] FOR M2PC AT DIFFERENT SPEEDS [RPM].

		Speed ω_r^*	500 [rpm]	
MSE$_\alpha$	MSE$_\beta$	MSE$_x$	MSE$_y$	THD$_\alpha$
0.0949	0.0900	0.3251	0.3651	6.69
THD$_\beta$	MSE$_{\omega_r}$	RMS ripple T_e	RMS ripple T_e %	
6.30	0.1843	0.1001	5.01	
		Speed ω_r^*	1500 [rpm]	
MSE$_\alpha$	MSE$_\beta$	MSE$_x$	MSE$_y$	THD$_\alpha$
0.1869	0.1597	0.4062	0.4485	9.97
THD$_\beta$	MSE$_{\omega_r}$	RMS ripple T_e	RMS ripple T_e %	
9.32	0.8826	0.2042	10.09	

TABLE II

STATOR CURRENTS $(\alpha - \beta)$, $(x - y)$, MSE [A], THD [%], RMS RIPPLE OF T_e [NM], MSE ω_r [RPM] FOR DTSM AT DIFFERENT SPEEDS [RPM].

		Speed ω_r^*	500 [rpm]	
MSE$_\alpha$	MSE$_\beta$	MSE$_x$	MSE$_y$	THD$_\alpha$
0.0545	0.0547	0.1846	0.1776	5.27
THD$_\beta$	MSE$_{\omega_r}$	RMS ripple T_e	RMS ripple T_e %	
5.31	0.9625	0.0521	2.58	
		Speed ω_r^*	1500 [rpm]	
MSE$_\alpha$	MSE$_\beta$	MSE$_x$	MSE$_y$	THD$_\alpha$
0.0642	0.0651	0.2343	0.2350	5.28
THD$_\beta$	MSE$_{\omega_r}$	RMS ripple T_e	RMS ripple T_e %	
5.41	1.1929	0.0579	2.81	

At last, the behavior of the stator currents in the $(\alpha-\beta)$ and $(x - y)$ sub-spaces are shown in Fig. 6 for M2PC and DTSM

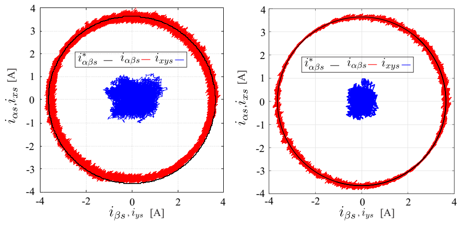

(a)

(b)

Fig. 6. Stator currents in $(\alpha - \beta)$ and $(x - y)$ sub-spaces for a sampling frequency of 16 kHz with an amplitude of 3.5 A (a) M2PC; (b) DTSM.

in steady-state response. It can be seen a better performance in the $(x - y)$ currents reduction for DTSM.

V. CONCLUSION

A comparative study of two nonlinear current controllers with fixed switching frequency applied to a SIM is presented. The results were compared between M2PC and DTSM and showed a better performance in terms of current tracking, current THD and torque ripple for DTSM. At the same time, M2PC presented a better capability at lower speed than higher speed. In terms of speed tracking (MSE), M2PC had a slightly better performance than DTSM and in the current transient analysis, M2PC presented a better response than DTSM. It can be stated that both techniques are good options to classic controllers with their corresponding characteristics.

ACKNOWLEDGMENT

Financial support came from CONACYT (Paraguayan Government) through research project 14-INV-101.

REFERENCES

[1] F. Barrero and M. J. Duran, "Recent advances in the design, modeling, and control of multiphase machines: Part I," *IEEE Trans. Ind. Electron.*, vol. 63, no. 1, pp. 449–458, 2016.

[2] M. J. Duran and F. Barrero, "Recent advances in the design, modeling, and control of multiphase machines: Part II," *IEEE Trans. Ind. Electron.*, vol. 63, no. 1, pp. 459–468, 2016.

[3] E. Levi, "Advances in converter control and innovative exploitation of additional degrees of freedom for multiphase machines," *IEEE Trans. Ind. Electron.*, vol. 63, no. 1, pp. 433–448, 2016.

[4] I. Subotic, N. Bodo, E. Levi, B. Dumnic, D. Milicevic, and V. Katic, "Overview of fast on-board integrated battery chargers for electric vehicles based on multiphase machines and power electronics," *Electric Power Applications*, vol. 10, no. 3, pp. 217–229, 2016.

[5] E. Levi, R. Bojoi, F. Profumo, H. Toliyat, and S. Williamson, "Multiphase induction motor drives–a technology status review," *Electric Power Applications*, vol. 1, no. 4, pp. 489–516, 2007.

[6] A. G. Yepes, A. Vidal, J. Malvar, O. López, and J. Doval-Gandoy, "Tuning method aimed at optimized settling time and overshoot for synchronous proportional-integral current control in electric machines," *IEEE Trans. Power Electronics*, vol. 29, no. 6, pp. 3041–3054, 2014.

[7] J. Rodas, F. Barrero, M. R. Arahal, C. Martín, and R. Gregor, "Online estimation of rotor variables in predictive current controllers: a case study using five-phase induction machines," *IEEE Trans. Ind. Electron.*, vol. 63, no. 9, pp. 5348–5356, 2016.

[8] M. Ayala, J. Rodas, R. Gregor, J. Doval-Gandoy, O. Gonzalez, M. Saad, and M. Rivera, "Comparative study of predictive control strategies at fixed switching frequency for an asymmetrical six-phase induction motor drive," in *Proc. IEMDC*, Miami, FL, 2017, pp. 1–8.

[9] J. A. Riveros, F. Barrero, E. Levi, M. J. Duran, S. Toral, and M. Jones, "Variable-speed five-phase induction motor drive based on predictive torque control," *IEEE Trans. Ind. Electron.*, vol. 60, no. 8, pp. 2957–2968, 2013.

[10] J. Riveros, B. Bogado, J. Prieto, F. Barrero, S. Toral, and M. Jones, "Multiphase machines in propulsion drives of electric vehicles," in *Proc. EPE/PEMC*. IEEE, 2010, pp. T5–201.

[11] M. A. Fnaiech, F. Betin, G.-A. Capolino, and F. Fnaiech, "Fuzzy logic and sliding-mode controls applied to six-phase induction machine with open phases," *IEEE Trans. Ind. Electron.*, vol. 57, no. 1, pp. 354–364, 2010.

[12] H. Amimeur, D. Aouzellag, R. Abdessemed, and K. Ghedamsi, "Sliding mode control of a dual-stator induction generator for wind energy conversion systems," *International Journal of Electrical Power & Energy Systems*, vol. 42, no. 1, pp. 60–70, 2012.

[13] S. Toledo, M. Rivera, J. Muñoz, R. Peña, J. Riveros, and R. Gregor, "Fixed switching frequency predictive control for a multi-drive indirect matrix converter system," in *Proc. SPEC*, pp. 1–6, 2017.

[14] Y. Kali, J. Rodas, M. Saad, R. Gregor, K. Bejelloun, and J. Doval-Gandoy, "Current control based on super-twisting algorithm with time delay estimation for a five-phase induction motor drive,," in *Proc. IEMDC*, 2017, pp. 1–8.

[15] F. Gavilan, D. Caballero, S. Toledo, E. Maqueda, R. Gregor, J. Rodas, M. Rivera, and I. Araujo-Vargas, "Predictive power control strategy for a grid-connected 2L-VSI with fixed switching frequency," in *Proc. ROPEC*, pp. 1–6, 2016.

[16] L. Comparatore, R. Gregor, J. Rodas, J. Pacher, A. Renault, and M. Rivera, "Model based predictive current control for a three-phase cascade H-bridge multilevel STATCOM operating at fixed switching frequency," in *Proc. PEDG*, pp. 1–6, 2017.

[17] M. Rivera, S. Toledo, C. Baier, L. Tarisciotti, P. Wheeler, and S. Verne, "Indirect predictive control techniques for a matrix converter operating at fixed switching frequency," in *Proc. PRECEDE*, pp. 13–18, 2017.

[18] V. Utkin, J. Guldner, and J. Shi, *Sliding mode control in electromechanical systems*. Taylor-Francis, 1999.

[19] I. Boiko and L. Fridman, "Analysis of chattering in continuous sliding-mode controllers," *IEEE Trans. Autom. Control*, vol. 50, pp. 1442–1446, 2005.

[20] Y. Kali, M. Saad, K. Benjelloun, and M. Benbrahim, *Sliding Mode with Time Delay Control for Robot Manipulators*. Singapore: Springer Singapore, 2017, pp. 135–156.

[21] Y. Zhao and T. Lipo, "Space vector PWM control of dual three-phase induction machine using vector space decomposition," *IEEE Trans. Ind. Electron.*, vol. 31, no. 5, pp. 1100–1109, 1995.

[22] L. Harnefors, S. Saarakkala, and M. Hinkkanen, "Speed control of electrical drives using classical control methods," *IEEE Trans. Ind. Appl.*, vol. 49, no. 2, pp. 889–898, 2013.

[23] J. Rodas, C. Martin, M. R. Arahal, F. Barrero, and R. Gregor, "Influence of covariance-based ALS methods in the performance of predictive controllers with rotor current estimation," *IEEE Trans. Ind. Electron.*, vol. 64, no. 4, pp. 2602–2607, 2017.

[24] O. Gonzalez, M. Ayala, J. Doval-Gandoy, J. Rodas, R. Gregor, and G. Rivas, "Variable-speed control of a six-phase induction machine using predictive-fixed switching frequency current control techniques," in *Proc. PEDG*, 2018.

[25] Y. Kali, M. Saad, K. Benjelloun, and A. Fatemi, "Discrete-time second order sliding mode with time delay control for uncertain robot manipulators," *Robotics and Autonomous Systems*, vol. 94, pp. 53 – 60, 2017.

[26] J. H. Jung, P. H. Chang, and S. H. Kang, "Stability analysis of discrete time delay control for nonlinear systems," in *Proc. ACC*, July 2007, pp. 5995–6002.

[27] S. Qu, X. Xia, and J. Zhang, "Dynamics of discrete-time sliding-mode-control uncertain systems with a disturbance compensator," *IEEE Transactions on Industrial Electronics*, vol. 61, no. 7, pp. 3502–3510, July 2014.

[28] Y. Kali, J. Rodas, M. Ayala, M. Saad, R. Gregor, K. Benjelloun, J. Doval-Gandoy, and G. Goodwin, "Discrete-time sliding mode with time delay estimation of a six-phase induction motor drive," in *Proc. IECON (under review)*, 2018.

ARTÍCULO 10

COMPARATIVE ASSESSMENT OF MODEL PREDICTIVE CURRENT CONTROL STRATEGIES APPLIED TO SIX-PHASE INDUCTION MACHINE

- Osvaldo González, **Magno Ayala**, Carlos Romero, Jorge Rodas, Raúl Gregor, Larizza Delorme, Ignacio González-Prieto, Mario Durán and Marco Rivera, ”Comparative Assessment of Model Predictive Current Control Strategies applied to Six-Phase Induction Machine”, Proc. ICIT, Buenos Aires, Argentina, pp. 1-7, 2020.

Comparative Assessment of Model Predictive Current Control Strategies applied to Six-Phase Induction Machine

O. González, M. Ayala, C. Romero, J. Rodas, R. Gregor
Lab. of Power and Control Systems
Universidad Nacional de Asunción
Luque, Paraguay
{ogonzalez, mayala, cromero, jrodas, rgregor}@ing.una.py

L. Delorme
Universidad del Cono Sur de las Américas
Asunción, Paraguay
laridelorme@gmail.com

I. González-Prieto, M.J. Durán
Dept. of Electrical Engineering
Universidad de Málaga
Málaga, Spain
ignaciogp87@gmail.com, mjduran@uma.es

M. Rivera
Lab. of Energy Conversion and Power Electronics
Universidad de Talca
Curicó, Chile
marcoriv@utalca.cl

***Abstract*—Nowadays, model predictive current control strategy has become in a viable alternative because of its fast response for high-reliability systems, such as multiphase machines. In that sense, this paper proposes a comparative assessment of four current controllers based on the model using different approaches like virtual vectors, modulation techniques and further, combining these strategies in order to at the same time deal with the regulation of the main and secondary currents components, known as (α-β) and (x-y), respectively, applied to Six-phase induction machine. Simulation results are presented so as to show the effectiveness of the four model predictive current controllers, taking into account the mean squared error and the total harmonic distortion of the stator currents in both steady and dynamic conditions.**

***Index Terms*—Multiphase machines, predictive current control, six-phase induction machine, virtual vectors.**

Nomenclature

DSP	Digital signal processing.
FOC	Field oriented control.
KF	Kalman filter.
MPC	Model predictive control.
MPCCS	Model predictive current control strategy.
MSE	Mean squared error.
PFSCCS	Predictive fixed-switching current control strategy.
SPIM	Six-phase induction machine.
THD	Total harmonic distortion.
VSD	Vector space decomposition.
VSI	Voltage source inverter.
VV	Virtual vector.

I. Introduction

Recently, the attention of the researchers community has been focused on multiphase induction machines due to their advantages over the three-phase induction machines ones, such as, better power split per phase, lower current harmonic content, less torque ripple production and fault tolerance capabilities [1]–[3]. However, the (x-y) secondary current components present in multiphase machines need a special care due to is related to copper losses. Different control strategies over the years have been proposed, one of them with promising features is MPC, described in [4]–[9], but they all present a high harmonic content in the stator currents compared to other approaches.

The PFSCCS adds a modulation stage to MPC strategy, in order to use three vectors in each sampling period. Consisting of two active vectors and the null vector, its advantages are: 1. Applying more than one vector in the sampling period helps to obtain voltages in (α-β) sub-spaces closer to the reference, in addition to avoiding large voltages at low sampling rates that would be obtained by applying a single vector throughout sampling period. 2. The selected active vectors are the largest, thus decreasing their components in the (x-y) sub-spaces. 3. A fixed switching pattern is applied so that the frequency spectrum of harmonics is reduced [10], [11].

Another control technique that uses modulation in combination with MPC, is the Model Predictive Control Using Two Virtual Voltage Vectors for Six-Phase Induction Motor Drives, proposed in [12]. This technique cancels the components in the (x-y) sub-spaces by combining two vectors, one large medium and one large vector in the (α-β) sub-spaces, with the same common direction, and opposite in the secondary sub-spaces, to form a vector called VV [12], [13]. Although the application of the VV ensures zero production of average voltage (x-y), and the combination of two VVs provides greater accuracy in the voltage supply, the tracking in the main sub-space can still be improved, for example by increasing the amount of vectors to be used taking advantage of the computational capabilities left over from the digital controllers, such as DSPs.

Two predictive control models are proposed in this article, the first one called 5V-PFCCS, is a variant of the PFSCCS control model, with the difference that it uses 5 vectors to obtain the desired voltage in the (α-β) sub-spaces while trying to reduce the voltage in the (x-y) sub-spaces through their strategic selection. The second predictive control model called PFSCCS-VVs is a variant of the VV-MPC, and it hopes to take advantage of the voltage cancellation at (x-y) of this method and at the same time increase the voltage accuracy in the main sub-spaces. In that context, the main contribution of this paper is the comparative assessment of four model predictive control strategies by employing modulation techniques through simulation results applied to SPIM taking into account the main and secondary sub-spaces, termed as, (α-β) and (x-y), from now on, respectively. The effectiveness of the four current controllers are analyzed by means the MSE and the THD so as to compare the advantages and limitations of each current control strategy. The four current controllers are examined for different speeds in steady state operation. Further, each strategy has been tested under transient operation to prove the system behavior.

This paper is structured as follows. Modeling of the SPIM including the two-level six-phase VSI employed in this study are analyzed in Section II. The comparative assessment of current controllers based on the laws of the MPC to the presented system is described in Section III. Section IV presents the proposed predictive currents controllers, explaining the behavior of the modulation strategies used in the predictive control. Simulations results of each MPCCS in both steady and dynamic operations are depicted in Section V in order to present their benefits and limitations. Finally, the conclusions are summarized and discussed in Section VI.

II. MODELING OF THE SPIM AND VSI

In this Section the main characteristics of the used SPIM drive is presented. The SPIM employed in this comparative assessment is fed by two-level six-phase VSI. A simplified topology is presented in Fig. 1. Each switching configuration of the VSI is represented by S_p, where S_p it can take two possible values that belong to 0 or 1, i.e., $S_p = 1$ if the upper switch is up and the lower switch is down and it takes place the opposite if $S_p = 0$. Hence, it is feasible to represent the switching configurations per leg of the two-level six-phase VSI like a vector: $[S_p] = [S_a, S_b, S_c, S_d, S_e, S_f]$, which produces 64 valid switching configurations that include 48 active non redundant vectors and one zero vector.

In this context, stator voltages of the considered VSI can be calculated by the DC-link voltage, known as, (V_{dc}) and the S_p vector, as shown in (1).

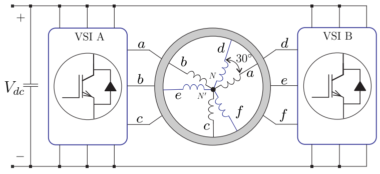

Fig. 1. SPIM fed by two-level six-phase VSI.

$$VSI_{[M]} = \frac{V_{dc}}{3} \begin{bmatrix} 2 & 0 & -1 & 0 & -1 & 0 \\ 0 & 2 & 0 & -1 & 0 & -1 \\ -1 & 0 & 2 & 0 & -1 & 0 \\ 0 & -1 & 0 & 2 & 0 & -1 \\ -1 & 0 & -1 & 0 & 2 & 0 \\ 0 & -1 & 0 & -1 & 0 & 2 \end{bmatrix} {S_p}^T \tag{1}$$

Afterwards, by combining the VSD strategy [14] and employing an invariant amplitude transformation matrix criteria [7], depicted in (2), the six-phase stator voltages of the SPIM is turned into three-two orthogonal stationary sub-spaces, which are (α-β), (x-y) and (z_1-z_2), where the first one sub-space are related to torque and flux contribution, while the second one are associated to the copper losses and the third one sub-space are not taken into account because of the isolated neutral points topology were considered.

$$T = \frac{1}{3} \begin{array}{c} \left[\begin{array}{cccccc} 1 & \frac{\sqrt{3}}{2} & -\frac{1}{2} & -\frac{\sqrt{3}}{2} & -\frac{1}{2} & 0 \\ 0 & \frac{1}{2} & \frac{\sqrt{3}}{2} & \frac{1}{2} & -\frac{\sqrt{3}}{2} & -1 \\ 1 & -\frac{\sqrt{3}}{2} & -\frac{1}{2} & \frac{\sqrt{3}}{2} & -\frac{1}{2} & 0 \\ 0 & \frac{1}{2} & -\frac{\sqrt{3}}{2} & \frac{1}{2} & \frac{\sqrt{3}}{2} & -1 \\ 1 & 0 & 1 & 0 & 1 & 0 \\ 0 & 1 & 0 & 1 & 0 & 1 \end{array} \right] \end{array} \begin{array}{c} \alpha \\ \beta \\ x \\ y \\ z_1 \\ z_2 \end{array} \tag{2}$$

Therefore, the sixty-four switching configurations in the (α-β) and (x-y) sub-spaces are represented in Fig. 2. Further, the SPIM mathematical model can be expressed by means a state-space approach, which is established by:

$$X'_{(t)} = A_{(t)}\, X_{(t)} + B_{(t)}\, U_{(t)} + Hn_{p(t)} \tag{3}$$

where the input vector of the considered state-space model is represented by $U_{(t)}$, the mentioned state vector is $X_{(t)}$ and the electrical parameters of the SPIM are represented through the matrices $A_{(t)}$ and $B_{(t)}$. While the process noise is established as $n_{p(t)}$ and the noise weight matrix by H.

According to the equation (3), which expresses the state-space model of the SPIM, and choosing the (α-β), (x-y) stator currents and (α-β) rotor currents as state vector ($x_1 = i_{\alpha s}$, $x_2 = i_{\beta s}$, $x_3 = i_{xs}$, $x_4 = i_{ys}$, $x_5 = i_{\alpha r}$ and $x_6 = i_{\beta r}$), the

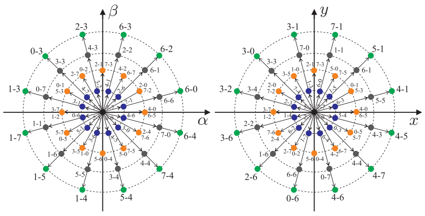

Fig. 2. Space vector representations in the (α-β) and (x-y) sub-spaces for a SPIM.

SPIM equations can be represented in the next way:

$$
\begin{aligned}
x_1' &= -R_s q_2 x_1 + q_4\left(L_m\omega_r x_2 + R_r x_5 + L_r\omega_r x_6\right) + q_2 u_1\\
x_2' &= -R_s q_2 x_2 + q_4\left(-L_m\omega_r x_1 - L_r\omega_r x_5 + R_r x_6\right) + q_2 u_2\\
x_3' &= -R_s q_3 x_3 + q_3 u_3\\
x_4' &= -R_s q_3 x_4 + q_3 u_4\\
x_5' &= R_s q_4 x_1 + q_5\left(-L_m\omega_r x_2 - R_r x_5 - L_r\omega_r x_6\right) - q_4 u_1\\
x_6' &= R_s q_4 x_2 + q_5\left(L_m\omega_r x_1 + L_r\omega_r x_5 - R_r x_6\right) - q_4 u_2
\end{aligned}
\tag{4}
$$

where the coefficients are defined as follows:

$$q_1 = L_s L_r - L_m^2,\ q_2 = \frac{L_r}{q_1} \tag{5}$$

$$q_3 = \frac{1}{L_{ls}},\ q_4 = \frac{L_m}{q_1},\ q_5 = \frac{L_s}{q_1} \tag{6}$$

being R_s, R_r, L_m, $L_r = L_{lr} + L_m$ and $L_s = L_{ls} + L_m$ the electrical parameters of the SPIM. The input vector is composed of the applied stator voltages, which are $u_1 = v_{\alpha s}$, $u_2 = v_{\beta s}$, $u_3 = v_{xs}$ and $u_4 = v_{ys}$. Further, the SPIM equations contain the rotor electrical speed ω_r.

Due to the drive of the SPIM is also composed of the VSI model, it is achievable to convert the gating signals into stator voltages which can be mapped to (α-β) and (x-y) sub-spaces represented in the vector $U_{(t)} = [u_1,\, u_2,\, u_3,\, u_4]^T$ and calculated through the next expressions:

$$U_{(t)} = V_{dc}\, T\, VSI_{[M]} \tag{7}$$

$$Y_{(t)} = \begin{bmatrix} 1 & 0 & 0 & 0 & 0 & 0\\ 0 & 1 & 0 & 0 & 0 & 0\\ 0 & 0 & 1 & 0 & 0 & 0\\ 0 & 0 & 0 & 1 & 0 & 0 \end{bmatrix} X_{(t)} + n_{m(t)} \tag{8}$$

where the output vector is expressed by $Y_{(t)}$ and the measurement noise through $n_{m(t)}$.

Finally, the mechanical expressions of the SPIM are:

$$T_e = 3P\left(\psi_{\alpha s} i_{\beta s} - \psi_{\beta s} i_{\alpha s}\right) \tag{9}$$

$$J_i \omega_m' + B_i \omega_m = \left(T_e - T_L\right) \tag{10}$$

where the variables B_i, J_i, T_e, T_L, ω_m, ω_r, $\psi_{\alpha s}$, $\psi_{\beta s}$ and P are, the friction coefficient, the inertia coefficient, the generated torque, the load torque, the rotor mechanical speed, the rotor electrical speed, the stator fluxes and the number of pole pairs, respectively.

III. ASSESSMENT OF CURRENT CONTROLLERS

A. *Classic MPCCS*

The MPCCS has been developed in the paper for the SPIM control and the VSI drive. A comprehensive block diagram of the strategy is shown in Fig. 3. In order to follow the reference stator current it employs a discrete mathematical model of SPIM to predict the future action of the considered output variables using the measurable variables, which are the stator currents, stator voltages and the rotor mechanical speed.

$$\hat{X}_{(k+1|k)} = X_{(k)} + T_s f\left(X_{(k)},\, U_{(k)},\, \omega_{r(k)}\right) \tag{11}$$

Taking into account the state-space model represented in the equation (11), the rotor currents are not directly measured. In that sense, it has been employed a reduced order estimator so as to only estimate the unmeasured variables (rotor currents) of the state vector. This strategy has been proposed in [15], [16], which is based on KF. Hence, the SPIM mathematical model can be expressed by the equations (12) and (13), respectively, using uncorrelated process and zero-mean Gaussian measurement noises.

$$\hat{X}_{(k+1|k)} = A_{(k)} X_{(k)} + B_{(k)} U_{(k)} + H n_{p(k)} \tag{12}$$

$$Y_{(k+1|k)} = \begin{bmatrix} 1 & 0 & 0 & 0 & 0 & 0\\ 0 & 1 & 0 & 0 & 0 & 0\\ 0 & 0 & 1 & 0 & 0 & 0\\ 0 & 0 & 0 & 1 & 0 & 0 \end{bmatrix} X_{(k+1)} + n_{m(k+1)} \tag{13}$$

It is worth noting that $A_{(k)}$ and $B_{(k)}$ constitute the discretized matrices from (4), where $A_{(k)}$ depends of the present value of the rotor electrical speed. Therefore, the matrix $A_{(k)}$ must be actualized at each sampling period considering the measured rotor electrical speed.

Moreover, in the MPCCS an optimization control process at every sampling period is carried out to minimize an established cost function J. This process is done by evaluating all possible control signals (stator voltages) and then it is selected the one that reduces the cost function to be applied in the next sampling period. Due to this work deals with the current control, it has been considered the tracking error (e) in the (α-β) and (x-y) sub-spaces between the reference stator currents ($i^*_{s(k+2)}$) and their predicted values ($\hat{i}_{s(k+2)}$), which are computed by the second-step ahead prediction for delay compensation, as shown in the next equations:

$$J = (e_{\alpha s})^2 + (e_{\beta s})^2 + \lambda_{xy}[(e_{xs})^2 + (e_{ys})^2] \tag{14}$$

where

$$
\begin{aligned}
e_{\alpha s} &= i^*_{\alpha s(k+2)} - \hat{i}_{\alpha s(k+2)}\\
e_{\beta s} &= i^*_{\beta s(k+2)} - \hat{i}_{\beta s(k+2)}\\
e_{xs} &= i^*_{xs(k+2)} - \hat{i}_{xs(k+2)}\\
e_{ys} &= i^*_{ys(k+2)} - \hat{i}_{ys(k+2)}.
\end{aligned}
\tag{15}
$$

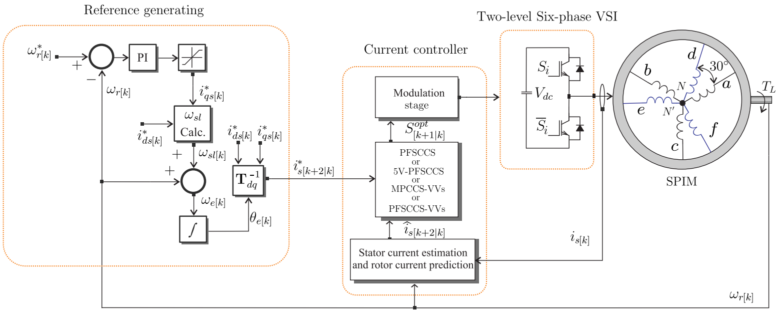

Fig. 3. Scheme of the MPCCS applied to SPIM.

Also, the tuning parameter (λ_{xy}) has been included that provides more weight on (α-β) or (x-y) sub-spaces according to the optimization control [17]–[19].

B. PFSCCS

This current control method is based on the selected sector defined by the two-level six-phase VSI in the (α-β) sub-space, which are formed by the outer 12 vectors, as depicted in Fig. 4. The current strategy computes the prediction of the two adjacent vectors that compose the considered sector at every sampling period and performs the cost function (J) individually for every prediction [10]. The performed prediction is based on (11). Nevertheless, they differ in the computation of the input vector $U_{(k)}$ [11]. The duty cycles for the adjacent vectors, d_1 and d_2, respectively, are obtained by solving the following equations:

$$d_0 = \frac{\sigma}{\sqrt{J_0}} \qquad d_1 = \frac{\sigma}{\sqrt{J_1}} \qquad d_2 = \frac{\sigma}{\sqrt{J_2}} \tag{16}$$

$$d_0 + d_1 + d_2 = T_s \tag{17}$$

where d_0 corresponds to the duty cycle of a zero vector. Then, it is possible to obtain the expression for σ and the duty cycles for each vector given as:

$$d_0 = \frac{T_s\sqrt{J_1}\sqrt{J_2}}{\sqrt{J_0}\sqrt{J_1} + \sqrt{J_1}\sqrt{J_2} + \sqrt{J_0}\sqrt{J_2}} \tag{18}$$

$$d_1 = \frac{T_s\sqrt{J_0}\sqrt{J_2}}{\sqrt{J_0}\sqrt{J_1} + \sqrt{J_1}\sqrt{J_2} + \sqrt{J_0}\sqrt{J_2}} \tag{19}$$

$$d_2 = \frac{T_s\sqrt{J_0}\sqrt{J_1}}{\sqrt{J_0}\sqrt{J_1} + \sqrt{J_1}\sqrt{J_2} + \sqrt{J_0}\sqrt{J_2}} \tag{20}$$

Analyzing the above mathematical expressions, a new cost function, which is evaluated at every sampling period, is defined as:

$$J_{n(k+2)} = d_1\sqrt{J_1} + d_2\sqrt{J_2} \tag{21}$$

The two vectors which minimize $J_{n(k+2)}$ are selected and applied to the VSI at the next sampling period. After computing the duty cycles and selecting the optimal two vectors to be applied, a switching pattern diagram, detailed in [7], [11], is adopted with the aim of applying the active vectors ($v_1 - v_2$) and zero vector (v_0), considering the calculated duty cycles achieving a fixed-switching frequency.

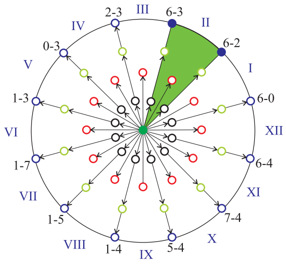

Fig. 4. Space sectors in the (α-β) sub-space for PFSCCS.

C. MPCCS-VVs

The implementation of MPCCS-VVs consists on the use of two active voltage vectors, one is the large vector and another is the mid-large vector as shown in Fig. 5, in every sampling time. This virtual vector is applied as follows:

$$VV = d_1 V_{large} + d_2 V_{mid-large} \tag{22}$$

where $d_1 = 0.73T_s$ and $d_2 = 0.27T_s$ which generate approximately 93% of the actual value of the large vector in (α-β) sub-space but it also obtains zero average value of the (x-y) currents due to the fact that those two vectors are opposite in (x-y) sub-space [12].

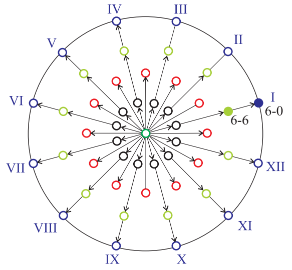

Fig. 5. Space sectors in the $(\alpha\text{-}\beta)$ sub-space for MPCCS-VVs.

IV. Proposed Predictive Current Controllers

A. 5V-PFSCCS

This technique is based on PFSCCS, so the duty cycles are calculated in the same way, with the difference that this technique has five vectors per sector, as shown in Fig. 6.

The duty cycles, for the five vectors d_0, d_1, d_2, d_3 and d_4, are obtained by solving the following equations:

$$d_i = \frac{\sigma}{\sqrt{J_i}} \tag{23}$$

$$d_0 + d_1 + d_2 + d_3 + d_4 = T_s \tag{24}$$

where $i = \{0, 1, 2, 3, 4\}$ and J_i are the corresponding cost functions (14) for the vectors in the selected sector. As PFSCCS, it is possible to obtain the expression for σ and the duty cycles for each vector given as:

$$J_{T0} = \sqrt{J_1}\sqrt{J_2}\sqrt{J_3}\sqrt{J_4} \tag{25}$$

$$J_{T1} = \sqrt{J_0}\sqrt{J_2}\sqrt{J_3}\sqrt{J_4} + \sqrt{J_0}\sqrt{J_1}\sqrt{J_3}\sqrt{J_4} \tag{26}$$

$$J_{T2} = \sqrt{J_0}\sqrt{J_1}\sqrt{J_2}\sqrt{J_4} + \sqrt{J_0}\sqrt{J_1}\sqrt{J_2}\sqrt{J_3} \tag{27}$$

$$d_1 = \frac{T_s\sqrt{J_0}\sqrt{J_2}\sqrt{J_3}\sqrt{J_4}}{J_{T0} + J_{T1} + J_{T2}} \tag{28}$$

$$d_2 = \frac{T_s\sqrt{J_0}\sqrt{J_1}\sqrt{J_3}\sqrt{J_4}}{J_{T0} + J_{T1} + J_{T2}} \tag{29}$$

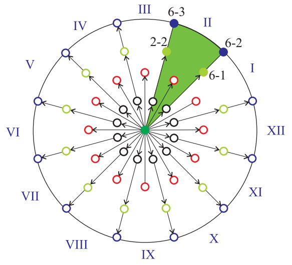

Fig. 6. Space sectors in the $(\alpha\text{-}\beta)$ sub-space for 5V-PFSCCS.

$$d_3 = \frac{T_s\sqrt{J_0}\sqrt{J_1}\sqrt{J_2}\sqrt{J_4}}{J_{T0} + J_{T1} + J_{T2}} \tag{30}$$

$$d_4 = \frac{T_s\sqrt{J_0}\sqrt{J_1}\sqrt{J_2}\sqrt{J_3}}{J_{T0} + J_{T1} + J_{T2}} \tag{31}$$

$$d_0 = T_s - d_1 - d_2 - d_3 - d_4 \tag{32}$$

B. PFSCCS-VVs

In this strategy a combination between PFSCCS and MPCCS-VVs has been proposed so as to improve the current tracking in the $(\alpha\text{-}\beta)$ sub-space and also reducing the $(x\text{-}y)$ currents. Hence, to reduce the $(x\text{-}y)$ currents, the equation presented in (22) has been employed while for $(\alpha\text{-}\beta)$ currents tracking, the V_1, V_2 and V_0 vectors, which in turn are composed by (v_1^a, v_1^b) and (v_2^a, v_2^b) for the active vectors, respectively, and according to the selected sector, the duty cycles for these vectors are computed as (18), (19) and (20). Finally, once the vectors are selected and before they are applied to the two-level six-phase VSI, a modulation diagram depicted in Fig. 7 is performed to guarantee a fixed-switching frequency at every sampling period.

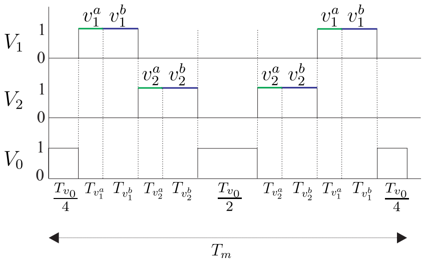

Fig. 7. Switching diagram of each selected sector in the $(\alpha\text{-}\beta)$ sub-space for PFSCCS-VVs.

V. Simulation Results

The SPIM is powered by two-level six-phase VSI, using a constant DC voltage of 200 V. The simulation results are analyzed and processed through MATLAB R2014a employing the electrical and mechanical parameters of the SPIM (Table I).

In Table II, Table III, Table IV and Table V, a steady state analysis for stator currents under different rotor speed references (ω_m^*), are shown with PFSCCS, 5V-PFSCCS, MPCCS-VVs and PFSCCS-VVs, respectively. The MSE for $(\alpha\text{-}\beta)$ and $(x\text{-}y)$ stator currents as well as the THD for (α) stator currents are included.

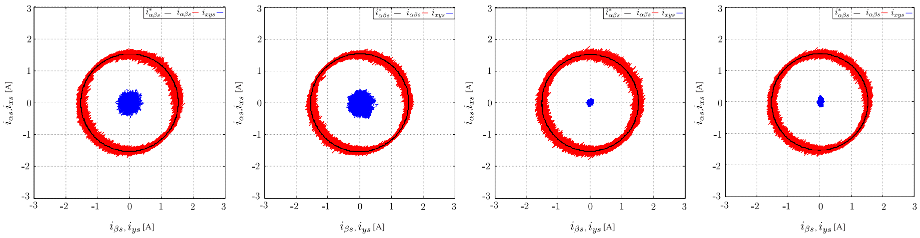

(a) (b) (c) (d)

Fig. 8. Comparative performance of stator currents in (α-β) and (x-y) sub-spaces for a rotor speed of 500 [rpm] at 10 [kHz] of sampling frequency: (a) PFSCCS; (b) 5V-PFSCCS; (c) MPCCS-VVs and (d) PFSCCS-VVs.

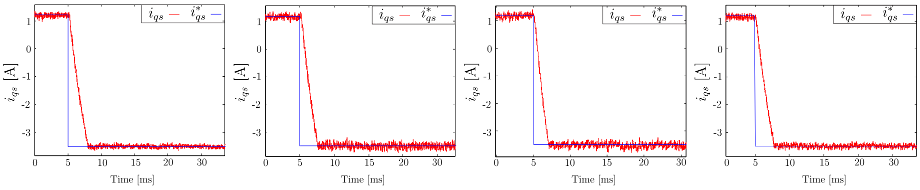

(a) (b) (c) (d)

Fig. 9. Dynamic response in q-axis of stator current for a rotor speed change from 500 [rpm] to -500 [rpm] and a sampling frequency of 10 [kHz]: (a) PFSCCS; (b) 5V-PFCCS; (c) MPCCS-VVs and (d) PFSCCS-VVs.

TABLE I
ELECTRICAL AND MECHANICAL CHARACTERISTICS OF THE SPIM

R_r	6.9 Ω	L_s	654.4 mH
R_s	6.7 Ω	P	1
L_{ls}	5.3 mH	P_w	2 kW
L_{lr}	12.8 mH	J_i	0.07 kg.m^2
L_m	614 mH	B_i	0.0004 kg.m^2/s
L_r	626.8 mH	ω_{r-nom}	3000 rpm

Fig. 8 exposes the (α-β) and (x-y) stator currents tracking, for PFSCCS, 5V-PFSCCS, MPCCS-VVs and PFSCCS-VVs, in steady state for a rotor speed of 500 rpm and a sampling frequency of 10 kHz. Fig. 9 shows the transient response for q stator current in a reversal test (speed reference changes from 500 [rpm] to -500 [rpm]) where PFSCCS, 5V-PFSCCS, MPCCS-VVs and PFSCCS-VVs show similar response speed which are denoted on Table VI.

TABLE II
ASSESSMENT OF STATOR CURRENTS IN (α-β) AND (x-y) SUB-SPACES, CONSIDERING MSE [A] AND THD [%] FOR PFSCCS AT 500 [RPM] AND 1000 [RPM].

	PFSCCS	at	f_s = 10 [kHz]		
ω^*_m	MSE$_\alpha$	MSE$_\beta$	MSE$_x$	MSE$_y$	THD$_\alpha$
500	0.0628	0.0602	0.0999	0.1013	5.58
1000	0.0982	0.0966	0.1438	0.1403	5.41

TABLE III
ASSESSMENT OF STATOR CURRENTS IN (α-β) AND (x-y) SUB-SPACES, CONSIDERING MSE [A] AND THD [%] FOR 5V-PFSCCS AT 500 [RPM] AND 1000 [RPM].

	5V-PFSCCS	at	f_s = 10 [kHz]		
ω^*_m	MSE$_\alpha$	MSE$_\beta$	MSE$_x$	MSE$_y$	THD$_\alpha$
500	0.0571	0.0544	0.1151	0.1194	4.68
1000	0.0999	0.0954	0.1558	0.1554	5.14

TABLE IV
ASSESSMENT OF STATOR CURRENTS IN (α-β) AND (x-y) SUB-SPACES, CONSIDERING MSE [A] AND THD [%] FOR MPCCS-VVS AT 500 [RPM] AND 1000 [RPM].

	MPCCS-VVs	at	f_s = 10 [kHz]		
ω^*_m	MSE$_\alpha$	MSE$_\beta$	MSE$_x$	MSE$_y$	THD$_\alpha$
500	0.0662	0.0616	0.0381	0.0395	6.14
1000	0.0772	0.0676	0.0455	0.0488	6.41

TABLE V
ASSESSMENT OF STATOR CURRENTS IN (α-β) AND (x-y) SUB-SPACES, CONSIDERING MSE [A] AND THD [%] FOR PFSCCS-VVS AT 500 [RPM] AND 1000 [RPM].

	PFSCCS-VVs	at	f_s = 10 [kHz]		
ω^*_m	MSE$_\alpha$	MSE$_\beta$	MSE$_x$	MSE$_y$	THD$_\alpha$
500	0.0594	0.0529	0.0372	0.0776	5.04
1000	0.0690	0.0630	0.0331	0.0405	5.94

TABLE VI

Response analysis of PFSCCS, 5V-PFSCCS, MPCCS-VVs and PFSCCS-VVs, considering overshoot (%) and settling time (ms) in a reversal test (500 [rpm] to −500 [rpm]).

MPCCS	Overshoot	Settling time
PFSCCS	4.85 %	3 ms
5V-PFSCCS	4.8 %	3.2 ms
MPCCS-VVs	3.3 %	2.7 ms
PFSCCS-VVs	4.9 %	3 ms

VI. Conclusion

In this paper a comparative assessment of four model predictive current control strategies applied to SPIM are presented. The simulation results show a good performance on the four analyzed techniques, highlighting MPCCS-VVs and PFSCCS-VVs for its (x-y) currents reduction. At the same time, PFSCCS-VVs presents a better (α-β) stator currents tracking and a better THD, presenting an excellent performance as a predictive current controller.

Acknowledgment

The authors would like to thank the financial support from the Paraguayan Science and Technology National Council (CONACYT) through program POSG16-5.

References

[1] E. Levi, R. Bojoi, F. Profumo, H. A. Toliyat, and S. Williamson, “Multiphase induction motor drives - A technology status review,” *IET Electr. Power Appl.*, vol. 1, no. 4, pp. 489–516, 2007.

[2] F. Barrero and M. J. Duran, “Recent advances in the design, modeling, and control of multiphase machines: Part I,” *IEEE Trans. Ind. Electron.*, vol. 63, no. 1, pp. 449–458, 2016.

[3] M. J. Duran and F. Barrero, “Recent advances in the design, modeling, and control of multiphase machines: Part II,” *IEEE Trans. Ind. Electron.*, vol. 63, no. 1, pp. 459–468, 2016.

[4] S. Kouro, M. A. Perez, J. Rodriguez, A. M. Llor, and H. A. Young, “Model Predictive Control: MPC’s Role in the Evolution of Power Electronics,” *IEEE Ind. Electron. Mag.*, vol. 9, no. 4, pp. 8–21, 2015.

[5] J. Rodriguez, M. P. Kazmierkowski, J. R. Espinoza, P. Zanchetta, H. Abu-Rub, H. A. Young, and C. A. Rojas, “State of the Art of Finite Control Set Model Predictive Control in Power Electronics,” *IEEE Trans. Ind. Informat.*, vol. 9, no. 2, pp. 1003–1016, 2013.

[6] C. S. Lim, E. Levi, M. Jones, N. A. Rahim, and W. P. Hew, “FCS-MPC-Based Current Control of a Five-Phase Induction Motor and its Comparison with PI-PWM Control,” *IEEE Tran. Ind. Electron.*, vol. 61, no. 1, pp. 149–163, 2014.

[7] M. Ayala, J. Rodas, R. Gregor, J. Doval-Gandoy, O. Gonzalez, M. Saad, and M. Rivera, “Comparative study of predictive control strategies at fixed switching frequency for an asymmetrical six-phase induction motor drive,” in *Proc. IEMDC*, 2017, pp. 1–8.

[8] M. Ayala, O. Gonzalez, J. Rodas, R. Gregor, and J. Doval-Gandoy, “A speed-sensorless predictive current control of multiphase induction machines using a Kalman filter for rotor current estimator,” in *Proc. ESARS-ITEC*, 2016, pp. 1–6.

[9] M. Ayala, J. Doval-Gandoy, J. Rodas, O. Gonzalez, and R. Gregor, “Current control designed with model based predictive control for six-phase motor drives,” *ISA Trans.*, 2019.

[10] M. Ayala, O. Gonzalez, J. Rodas, R. Gregor, and M. Rivera, “Predictive control at fixed switching frequency for a dual three-phase induction machine with Kalman filter-based rotor estimator,” in *Proc. ICA-ACCA*, 2016, pp. 1–6.

[11] O. Gonzalez, M. Ayala, J. Doval-Gandoy, J. Rodas, R. Gregor, and M. Rivera, “Predictive-fixed switching current control strategy applied to six-phase induction machine,” *Energies*, vol. 12, no. 12, p. 2294, 2019.

[12] I. Gonzalez-Prieto, M. J. Duran, J. J. Aciego, C. Martin, and F. Barrero, “Model predictive control of six-phase induction motor drives using virtual voltage vectors,” *IEEE Trans. Ind. Electron.*, vol. 65, no. 1, pp. 27–37, 2017.

[13] J. J. Aciego, I. G. Prieto, and M. J. Duran, “Model predictive control of six-phase induction motor drives using two virtual voltage vectors,” *IEEE J. Emerg. Sel. Top. Power Electron.*, vol. 7, no. 1, pp. 321–330, 2018.

[14] Y. Zhao and T. Lipo, “Space vector PWM control of dual three-phase induction machine using vector space decomposition,” *IEEE Trans. Ind. Electron.*, vol. 31, no. 5, pp. 1100–1109, 1995.

[15] J. Rodas, F. Barrero, M. R. Arahal, C. Martin, and R. Gregor, “On-line estimation of rotor variables in predictive current controllers: A case study using five-phase induction machines,” *IEEE Trans. Ind. Electron.*, vol. 63, no. 9, pp. 5348–5356, 2016.

[16] J. Rodas, C. Martin, M. R. Arahal, F. Barrero, and R. Gregor, “Influence of covariance-based ALS methods in the performance of predictive controllers with rotor current estimation,” *IEEE Trans. Ind. Electron.*, vol. 64, no. 4, pp. 2602–2607, 2017.

[17] C. S. Lim, E. Levi, M. Jones, N. A. Rahim, and W. P. Hew, “FCS-MPC-based current control of a five-phase induction motor and its comparison with PI-PWM control,” *IEEE Trans. Ind. Electron.*, vol. 61, no. 1, pp. 149–163, 2013.

[18] M. Novak, T. Dragicevic, and F. Blaabjerg, “Weighting factor design based on Artificial Neural Network for Finite Set MPC operated 3L-NPC converter,” in *Proc. APEC*, 2019, pp. 77–82.

[19] B. Majmunović, T. Dragičević, and F. Blaabjerg, “Multi objective modulated model predictive control of stand-alone voltage source converters,” *IEEE J. Emerg. Sel. Top. Power Electron.*, 2019.